

University of Nottingham
UK | CHINA | MALAYSIA

EPSRC
Engineering and Physical Sciences Research Council



# Halometallate-based ionic liquid catalysts

Meike Katharina Leu

Thesis submitted to the University of Nottingham for the degree of Doctor of Philosophy

September 2019

# Abstract

This work focuses on the synthesis and characterisation of halometallate ionic liquids (ILs), including Co(II), Ni(II), Cu(II), Zn(II), In(III), and Fe(III) metal halides. Due to their Lewis acidic nature, halometallate ILs are promising candidates as catalysts. In addition, ILs show advantageous properties (*e.g.* low vapour pressure and good ionic conductivity) for their use in catalytic applications using inductive heating methods such as microwave (MW) radiation or magneto-thermal heating. As for any catalyst the understanding of the catalytically active species and the properties of the respective catalyst are fundamental to explain the catalytic process. As to the best of our knowledge, no phase diagram has been reported for mixtures of $[C_1C_4Im]Cl/CoCl_2$ and $[C_1C_4Im]Cl/NiCl_2$, these were prepared to further understanding of discrete anion formation. Thermogravimetric analysis (TGA) and differential scanning calorimetry (DSC) were used to prepare the phase diagram and it is demonstrated how small changes in mole fraction lead to significant changes in thermal behaviour. In addition, Raman spectroscopy and X-ray photoelectron spectroscopy (XPS) were used to find additional evidence for anions formed. However only the formation of $[MCl_4]^-$ could be observed.

Furthermore, dielectric properties are investigated as they are crucial to a future application of halometallate IL catalysts in MW radiation. The data was analysed and showed dependency regarding change with temperature and frequency. Conductivity was calculated from the obtained data and was

confirmed by impedance spectroscopy. The observed dielectric constants vary depending on the metal and are in a range from ε' = 3.4-13.9.

Finally, mechanistic and kinetic studies were carried out to determine the catalytically active species of the novel IL $[C_1C_4Im][Fe(NO)_2Cl_2]$, which was used as a catalyst for carbon dioxide ($CO_2$) conversion. Full conversion with good selectivity to the desired product was observed at optimised reaction parameters (neat, 40°C, 2 bar $CO_2$, 24h, 5 mol% catalyst loading).

# Declaration

This thesis is the result of my own investigations and is not being concurrently submitted in candidature for any degree.

Signed_____

Date_____

# Publications

- Meike K. Leu, Isabel Vicente, Jesum Alves Fernandes, Imanol de Pedro, Jairton Dupont, Victor Sans, Peter Licence, Aitor Gual, Israel Cano, On the real catalytically active species for $CO_2$ fixation into cyclic carbonates under near ambient conditions: Dissociation equilibrium of [BMIm][$Fe(NO)_2Cl_2$] dependant on reaction temperature, Applied Catalysis B: Environmental, 245 (2019) 240-250, DOI: 10.1016/j.apcatb.2018.12.062.

- Sergi Cot, Meike K. Leu, Alexis Kalamiotis, Georgios Dimitrakis, Victor Sans Sangorrin, Imanol de Pedro, Israel Cano, An Oxalate-Bridged Binuclear Iron(III) Ionic Liquid for the Highly Efficient Glycolysis of Polyethylene Terephthalate under Microwave Irradiation, ChemPlusChem, 84 (2019) 786-793, DOI: 10.1002/cplu.201900075.

# Acknowledgements

First of all, I would like to thank my principal supervisor Pete Licence for his supervision and continuous encouragement during my PhD. I am very grateful to have been able to count on his support, even more so as he was not my principal supervisor from the beginning of my PhD. I would also like to take this opportunity to thank Jesum Alves Fernandes, Georgios Dimitrakis, and Jairton Dupont for their supervision and open door for any research queries.

I thank the School of Chemistry for providing the facilities to successfully complete this PhD. Also, I recognize the NMRC for providing access and support to their instruments. I am indebted to the CDT in Sustainable Chemistry and the EPSRC for funding and providing me with the opportunity to carry out this PhD, especially Perislava Williams, Amanda Broniewski, and Chris Moody.

A PhD is not always easy and I would not have been able to succeed without the love and support from my husband Daniel, my parents Angelika and Karl, my sister Anna, my grandparents Roswitha and Walter, and all my friends from home that have not forgotten about me while I was away. Four years is a long time and I was lucky to have also found my Nottingham family, special thanks to Zé, Vera, Stelios, Astrid, and Neelam.

Even though in the end a PhD project is a solitary project, it would not have been possible without the countless discussions with my colleagues at the CNL and my past and current group members. I would like to thank everyone for their open ear and enthusiasm in scientific discussions.

# Abbreviations and Symbols

| | |
|---|---|
| % | Per cent |
| $\pi$ | Pi |
| $\phi$ | Phase angle |
| $A$ | Area |
| $A^+$ | Acid |
| AC | Alternating current |
| arb. | arbitrary |
| ATR FT-IR | Attenuated total reflectance Fourier transformed infrared |
| $B_0$ | Magnitude of applied magnetic field |
| BASIL | Biphasic acid scavenging ionic liquid |
| $[BF_4]^-$ | Tetrafluoroborate |
| β | Bohr magneton |
| °C | Degree Celsius |
| °C/min | Degree Celsius per minute |
| $cm^{-1}$ | Reciprocal centimetre |
| $[C_1C_4Im]$ | 1-butyl-3-methylimidazolium |
| $[C_1C_1C_4Im]$ | 1-butyl-2,3-dimethylimidazolium |
| Cat. | Catalyst |
| $CO_2$ | Carbon dioxide |
| Conv. | Conversion |
| CCD | Charge coupled device |
| $d$ | Distance |

| | |
|---|---|
| DC | Direct current |
| DSC | Differential scanning calorimetry |
| DPPH | 2,2-diphenyl-1-picrylhydrazyl |
| DNIC | Dinitrosyl iron complex |
| EIS | Electrochemical impedance spectroscopy |
| exp | exponential |
| $\varepsilon^*$ | Complex permittivity |
| $\varepsilon'$ | Real permittivity |
| $\varepsilon''$ | Imaginary permittivity |
| $\varepsilon_0$ | Permittivity in vacuum |
| EA | Elemental analysis |
| ESI-MS | Electron spray ionization mass spectrometry |
| $E_a$ | Activation energy |
| $E_{app}$ | Apparent activation energy |
| ESR | Electron spin resonance |
| EPR | Electron paramagnetic resonance |
| $[Et_4N]$ | Tetraethylammonium |
| FLP | Frustrated Lewis pair |
| $G$ | Conductance |
| GHz | Gigahertz |
| GC | Gas chromatography |
| $h$ | Planck constant |
| $\hbar$ | Reduced Planck constant |

| | |
|---|---|
| Hz | Hertz |
| HOMO | Highest occupied molecular orbital |
| $I$ | current |
| $I_0$ | Amplitude current |
| $i$ | Imaginary number |
| ISM | Industrial, scientific, and medical |
| IL | Ionic liquid |
| IFP | Institute of French Petroleum |
| ICP-OES | Inductively coupled plasma optical emission spectroscopy |
| $\kappa$ | Cell constant |
| K | Kelvin |
| $k_{obs}$ | Apparent kinetic constant |
| $k_B$ | Boltzmann constant |
| $k$ | Kinetic constant |
| Kcal/mol | Kilocalories per mol |
| kOe | Kilo Oersted |
| kHz | Kilohertz |
| LUMO | Lowest unoccupied molecular orbital |
| log | Logarithm |
| $m$ | Mass |
| $M$ | Molar mass |
| mg | Milligram |
| MHz | Megahertz |

| | |
|---|---|
| mmol | Millimol |
| 2-MeTHF | 2-methyltetrahydrofuran |
| MOF | Metal organic framework |
| MW | Microwave |
| MAOS | Microwave assisted organic synthesis |
| mT | Millitesla |
| *n* | number of moles |
| Nu | Nucleophile |
| NP | Nanoparticle |
| NMR | Nuclear magnetic resonance |
| NR | Non-reactive |
| [*n*-$Bu_4N$] | Tetrabutylammonium |
| $\sigma$ | Conductivity |
| *P* | Pressure |
| PO | Propylene oxide |
| PEG | Polyethylene glycol |
| *R* | Resistance |
| R./ref. | Reference |
| r.t. | Room temperature |
| SO | Styrene oxide |
| S/C% | Catalyst loading |
| Subst. | Substrate |
| SPR | Surface plasmon resonance |

| | |
|---|---|
| sin | Sinus |
| Sel. | Selectivity |
| STDEV | Standard deviation |
| *S* | Siemens |
| *t* | Time |
| *T* | Temperature |
| THF | Tetrahydrofuran |
| TGA | Thermogravimetric analysis |
| $T_m$ | Melting temperature |
| $T_c$ | Crystallisation temperature |
| $T_g$ | Glass transition temperature |
| $U_0$ | Amplitude potential |
| *U(t)* | Potential |
| $\upsilon$ | Frequency |
| $\omega$ | Angular frequency |
| $\chi$ | Mole fraction |
| XPS | X-ray photoelectron spectroscopy |
| Y | Yield |
| $\hat{Z}$ | Complex impedance |
| *Z'* | Real impedance |
| *Z''* | Imaginary impedance |

# Table of Contents

## Chapter 1


1. Introduction ..... 17

1.1 Ionic liquids ..... 17

1.2 Halometallate ionic liquids ..... 17

1.2.1 Iron containing ionic liquids ..... 18

1.2.2 Indium containing ionic liquids ..... 19

1.2.3 Copper containing ionic liquids ..... 21

1.2.4 Zinc containing ionic liquids ..... 21

1.2.5 Cobalt containing ionic liquids ..... 22

1.2.6 Nickel containing ionic liquids ..... 23

1.3 Lewis acidity of halometallate ionic liquids ..... 24

1.3.1 How to influence Lewis acidity? ..... 25

1.3.2 Nitrosyl ligands for improved reactivity ..... 25

1.3.3 How is Lewis acidity determined? ..... 28

Gutmann Acceptor Number ..... 29

1.4 Halometallate ionic liquids and the challenge of anion speciation ..... 31

1.4.1 Phase diagram of chloroaluminate(III) ionic liquids ..... 31

1.4.2 Phase diagram of chloroindate(III) ionic liquids ..... 33

1.4.3 Phase diagram of chlorozincate(II) ionic liquids ..... 35

1.5 Halometallate ionic liquids as catalysts ..... 35

1.6 Industrial processes using halometallate ionic liquids ..... 38

1.7 Aims and objectives ..... 39


## Chapter 2


2. Synthesis and characterisation of halometallate ionic liquids ..... 41

2.1. Synthetic procedures ..... 41

2.1.1 Synthesis of $[C_1C_4Im]Cl$ ..... 41

2.1.2 Synthesis of $[C_1C_4Im]Br$ ..... 42

2.1.3 Synthesis of $[C_1C_4Im][FeCl_4]$ ..... 43

2.1.4 Synthesis of $[C_1C_4Im][FeBr_4]$ ..... 43
2.1.5 Synthesis of $[C_1C_4Im][InCl_4]$ ..... 44
2.1.6 Synthesis of $[C_1C_4Im]_2[CuCl_4]$ ..... 44
2.1.7 Synthesis of $[C_1C_4Im]_2[ZnCl_4]$ ..... 44
2.1.8 Synthesis of $[C_1C_4Im]_2[NiCl_4]$ ..... 45
2.1.9 Synthesis of $[C_1C_4Im]_2[CoCl_4]$ ..... 45
2.1.10 Synthesis of $[Fe(NO)_2Cl]_2$ ..... 46
2.1.11 Synthesis of $[C_1C_4Im][Fe(NO)_2Cl_2]$ ..... 47
2.1.12 Synthesis of $[n\text{-}Bu_4N][Fe(NO)_2Cl_2]$ ..... 47
2.1.13 Synthesis of $[C_1C_1C_4Im]Cl$ ..... 48
2.1.14 Synthesis of $[C_1C_1C_4Im][Fe(NO)_2Cl_2]$ ..... 49
2.2 Halometallate ionic liquids with substituted ligands using nitrosyl ..... 49
2.2.1 $[C_1C_4Im][Fe(NO)_2Cl_2]$ ..... 49
2.2.2 $[C_1C_1C_4Im][Fe(NO)_2Cl_2]$ and $[(n\text{-}Bu)_4N][Fe(NO)_2Cl_2]$ ..... 58
2.2.3 $[C_1C_4Im][FeBr_4]$ ..... 62
2.3 Conventional halometallate ionic liquids ..... 63
2.3.1 $[C_1C_4Im][FeCl_4]$ ..... 63
2.3.2 $[C_1C_4Im][InCl_4]$ ..... 66
2.3.3 $[C_1C_4Im]_2[ZnCl_4]$ ..... 69
2.3.4 $[C_1C_4Im]_2[CuCl_4]$ ..... 72

# Chapter 3

3. Halometallate ionic liquids as catalysts for the cycloaddition of carbon dioxide into epoxides ..... 76
3.1. Experimental procedures ..... 81
3.1.1 Formation of carbonates ..... 81
3.1.2 Formation of diols ..... 81
3.1.3 Kinetic studies ..... 82
3.1.4 Recycling experiments ..... 82
3.1.5 Radical scavenger experiments ..... 83
3.2 Selection of catalyst ..... 84
3.3 Optimisation of reaction conditions ..... 85
3.4 Substrate scope ..... 88
3.5 Recycling studies ..... 89

3.5 Study of the catalytic reaction mechanism ..... 94
3.6.1 Control experiments ..... 94
3.6.2 Radical scavenger experiments ..... 96
3.6.3 Use of $H_2O$ as nucleophile and optically pure substrates ..... 96
3.6.4 Kinetic studies ..... 98
3.7 Proposed catalytic cycle ..... 101
3.8 Conclusion ..... 104

## Chapter 4

4. Dielectric spectroscopy studies ..... 106
4.1 Fundamentals of non-conventional heating approaches ..... 106
4.2 Ionic liquid catalysts in microwave synthesis ..... 109
4.3 Dielectric spectroscopy ..... 112
4.3.1 Dielectric spectroscopy studies on ionic liquids ..... 113
4.4 Impedance spectroscopy ..... 115
4.5 Real and imaginary permittivity ..... 117
4.5.1 Measurement of dielectric properties at different frequency and temperature ..... 119
4.5.2 Variation with increasing temperature ..... 131
4.5.3 Calculation of conductivity ..... 140
4.5.4 Conductivity and phase transitions ..... 146
4.5.5 Fitting of Arrhenius plot ..... 152
4.6 Comparison of conductivity using impedance spectroscopy ..... 153
4.7 Mechanism of relaxation ..... 163
4.8. Evaluation of ILs for MW application ..... 165
4.9 Conclusion ..... 166

## Chapter 5

5. Thermal properties of cobalt and nickel chloride mixtures with $[C_1C_4Im]Cl$ ..... 168
5.1 Experimental techniques used for the preparation of the phase diagram ..... 169
5.1.1 Thermal analysis ..... 169

5.1.2 Raman spectroscopy ..... 170
5.2 Synthesis and characterisation of $[C_1C_4Im]Cl/ CoCl_2$ and $[C_1C_4Im]Cl/ NiCl_2$ mixtures ..... 172
5.2.1 Preparation of $[C_1C_4Im]Cl/CoCl_2$ mixtures ..... 172
5.2.2 Preparation of $[C_1C_4Im]Cl/NiCl_2$ mixtures ..... 172
5.3 Phase diagram for $[C_1C_4Im]Cl/CoCl_2$ ..... 173
5.3.1 Thermal analysis ..... 173
5.3.2 Raman spectra for mixtures of $[C_1C_4Im]Cl/CoCl_2$ ..... 182
5.4 Phase Diagram for $[C_1C_4Im]Cl/[NiCl_2]$ ..... 187
5.4.1 Thermal analysis ..... 187
5.4.2 X-ray photoelectron spectroscopy ..... 195
5.5 Conclusion ..... 198

6. Conclusion and future work ..... 200
6.1 Conclusion ..... 200
6.2 Future work ..... 201

7. Methods and materials ..... 203
7.1 Analytical methods ..... 203
7.1.1 Dielectric spectroscopy ..... 203
7.1.2 Impedance spectroscopy ..... 203
7.1.3 Nuclear magnetic resonance (NMR) ..... 203
7.1.4 Gas chromatography (GC) ..... 204
7.1.5 Thermogravimetric analysis (TGA) ..... 204
7.1.6 Differential scanning calorimetry (DSC) ..... 204
7.1.7 Inductively coupled plasma optical emission spectrometry (ICP-OES) ..... 204
7.1.8 Electrospray ionization mass spectrometry (ESI-MS) ..... 205
7.1.9 Fourier transform infrared spectroscopy (ATR FT-IR) ..... 205
7.1.10 Raman spectroscopy ..... 205
7.1.11 Electron paramagnetic resonance (EPR) ..... 205
7.1.12 X-ray photoelectron spectroscopy (XPS) ..... 205
7.1.13 Magnetization measurements ..... 206

8. Appendix ..... 207
8.1 Phase diagram ..... 207
8.1.1 Differential scanning calorimetry ..... 209
8.1.2 Thermogravimetric analysis ..... 228
8.2 Crystal structure ..... 245
8.3 ESI-MS spectroscopy ..... 247
8.4 Nuclear magnetic resonance spectroscopy ..... 248
8.5 Dielectric spectroscopy ..... 249
8.5.1 Arrhenius fit – conductivity versus inverse temperature ..... 249
8.6 Impedance spectroscopy ..... 255
8.7 Magnetization measurements ..... 280
8.8 GC chromatograms ..... 281
8.9 Kinetic experiments ..... 283

9. References ..... 285

# Chapter 1

## 1. Introduction

### 1.1 Ionic liquids

Ionic liquids (ILs) are liquid salts consisting solely of ions and often are defined to have a melting point below an arbitrary temperature of 100°C.[1-5] They possess desirable characteristics such as high polarity, low vapour pressure, high ionic conductivity, large electrochemical window, and thermal stability[6-8] which make them interesting candidates for many different fields in chemistry[9] such as analytical chemistry and separation science,[10, 11] reaction media,[12] electrochemistry,[13] enzyme-mediated reactions,[14] catalysis[1], soft and composite materials, pharmaceutical ILs,[15] gas storage and gas sorption,[16, 17] and computer simulations.[18]

Furthermore, these characteristics have been exploited for applications such as specialized solvents,[19] lubricants,[20] thermal fluids,[21, 22] magnetic fluids, [22] optical fluids[23] and propellants.[24]

### 1.2 Halometallate ionic liquids

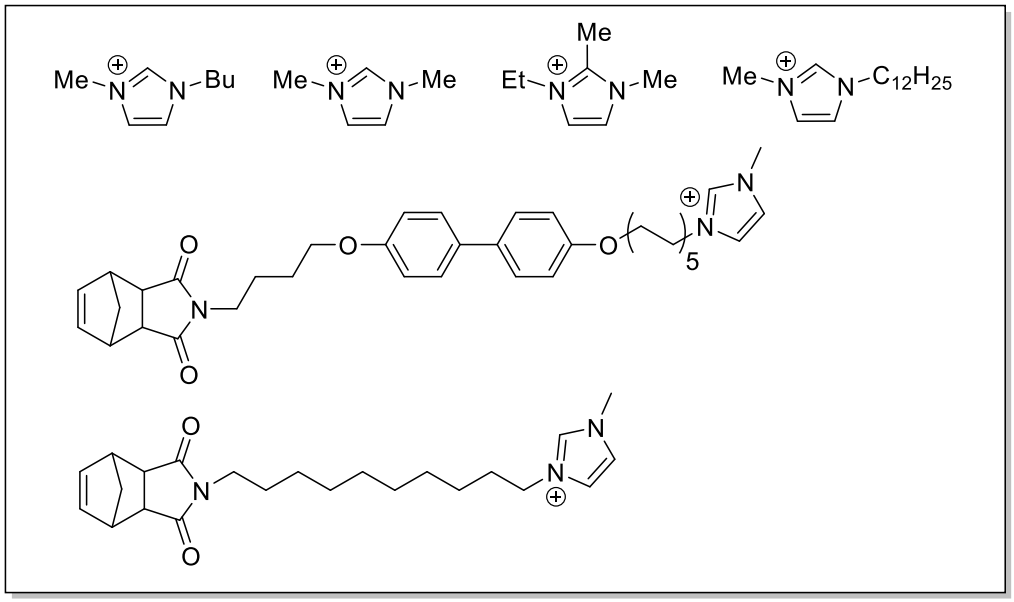
Halometallate ILs are typically prepared using an organic cation and a metal halide salt ($MCl_x$). Initially, the main focus was on chloroaluminate(III) ILs, especially through the development of low temperature thermal batteries by the U.S. Air Force.[25] Through the work of Wilkes,[25] Osteryoung[26] and Hussey[27] chloroaluminate(III) ILs were also used as liquid Lewis acid catalysts to stabilise and form transition metal catalysts. Current research has widened its focus to

incorporating almost all metals of the periodic table and new applications have evolved such as electroplating, polishing treatments, new gas scrubbing processes, new inorganic semiconductor materials, and the transformation of biomass to energy products.[16] The scope of metals has widened to other group III metals (Ga, In), group IV (Sn, Pb), transition metals (Ti, Zr, Hf, Nb, Mn, Fe, Co, Ni, Cu, Au, Zn, Cd, Hg, ), and all Lanthanides.[28]

Some of the early research interests, regarding halometallates, have continuously developed such as battery research and electrodeposition. The field of battery research has moved on from chloroaluminate(III) ILs to lithium, sodium, and magnesium ILs,[29-31] while electrodeposition research still focuses on halometallate ILs, however not solely on aluminium based ILs, but also on transition metals such as iron, zinc and copper.[32, 33]

### 1.2.1 Iron containing ionic liquids

Haloferrate ILs have been reported with a variety of cations, generally containing the anions $[FeCl_4]^-$, $[FeBr_4]^-$, or $[Fe_2Cl_7]^-$. However, ILs with $\chi FeCl_3 >$ 0.6 are not capable of dissolving more $FeCl_3$ and in conclusion an IL containing only the anion $[Fe_2Cl_7]^-$ is not being formed. An explanation is that the energy of formation is lower than the lattice energy of $FeCl_3$. At $\chi FeCl_3 = 0.6$ $[FeCl_4]^-$ and $[Fe_2Cl_7]^-$ coexist.[16] Scheme 1-1 displays some structures of cations found in the literature, which were used in the preparation of haloferrate ILs.[34-38]

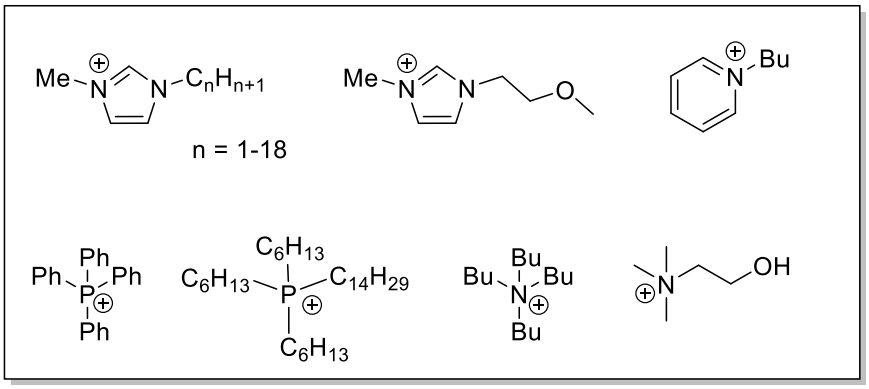


*Scheme 1-1 Some cations present in the Literature used for the preparation of iron containing ILs.*

Hamaguchi and co-worker first measured the magnetic susceptibility of the IL $[C_1C_4Im][FeCl_4]$[39], which was followed by further investigation of the magnetic properties of iron containing ILs by the group of Fernandez and de Pedro.[34-36, 40-43] An example for an application is the work of Taubert and co-workers, which have reported thermomorphic behaviour for the ILs $[C_1C_4Im][FeCl_4]$ and $[C_1C_{12}Im][FeCl_4]$ and were furthermore able to prepare an ion-conducting, paramagnetic and transparent ionogel using $[C_1C_4Im][FeCl_4]$.[37, 44]

### 1.2.2 Indium containing ionic liquids

Indium has been shown to only form monomeric anion species which is further elucidated in section 1.4.2 Phase diagram of chloroindate(III) ionic liquids. Scheme 1-2 presents some cations found in the literature, which form ILs containing the anion $[InCl_4]^-$.[45-52]




*Scheme 1-2 Some cations found for indium containing ILs in the current literature.*

The most common appearance of indium in an IL as an anion is in the form of $[InCl_4]^-$, however it is coordinatively unsaturated and hence reacts with a base as a mild Lewis acid.[28] Examples for the usefulness of the mild Lewis acidity of indium ILs in catalysis will be given in section 1.5 Halometallate ionic liquids as catalysts. In addition, indium ILs are hydrolytically stable as was reported previously.[53]

$$[InCl_4]^- + 2L \longrightarrow [InCl_4L_2]$$

*Scheme 1-3 Expansion of the indium coordination sphere.[28]*

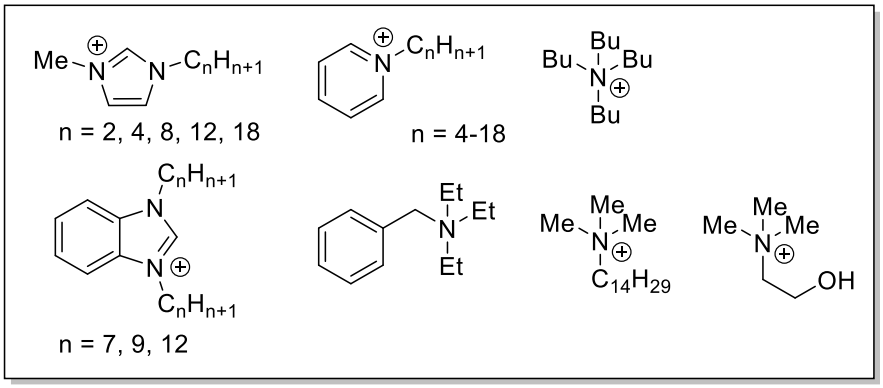
A recent example utilising the ability of ILs to form metal complexes is shown by the group of Binnemans, who have investigated the recovery of transition metals from LEDs including indium, arsenic, and gallium where the metal is recovered with a tribromide IL which is able to form a metal complex (Scheme 1-4).[54]

$$M^{3+} + 3Br^- + [P_{44410}][Br] \rightleftharpoons [P_{44410}][MBr_4]$$

*Scheme 1-4 Metal complexation using a tribromide IL.[54]*

### 1.2.3 Copper containing ionic liquids

The most common copper IL contains a Cu(II) species in the form $[cation]_2[CuCl_4]$.[55] Scheme 1-5 shows cations present in the literature utilized for the formation of copper containing ILs.[56-62]



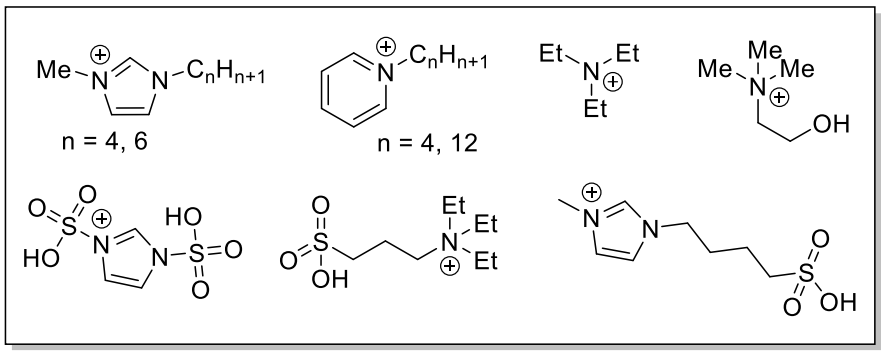

*Scheme 1-5 Commonly used cations in copper containing ILs.*

Axtell *et al.* have investigated Cu(I) chloride mixed with phosphonium or ammonium chloride and observed the formation of conducting oils. Through IR and Raman spectroscopy they confirmed the formation of $[CuCl_2]^-$ for an equimolar mixture. After further addition of CuCl the species $[Cu_2Cl_3]^-$ was observed and other complex anions are suspected.[63]

EPR and EXAFS was used to further investigate copper(II) complexes in a chlorobenzene solution and the species observed were $[CuCl_4]^{2-}$ and $[Cu_2Cl_6]^{2-}$.[64] Thiel *et al.* furthermore confirmed the $[CuCl_4]^{2-}$ as a distorted tetrahedron through EPR and DFT calculations.[65]

### 1.2.4 Zinc containing ionic liquids

The most common zinc IL contains a Zn(II) species in the form $[cation]_2[ZnCl_4]$.[66] Scheme 1-6 shows cations present in the literature utilized for the formation of zinc containing ILs.[67-71]




*Scheme 1-6 Some cations used for the preparation of zinc containing ILs.*

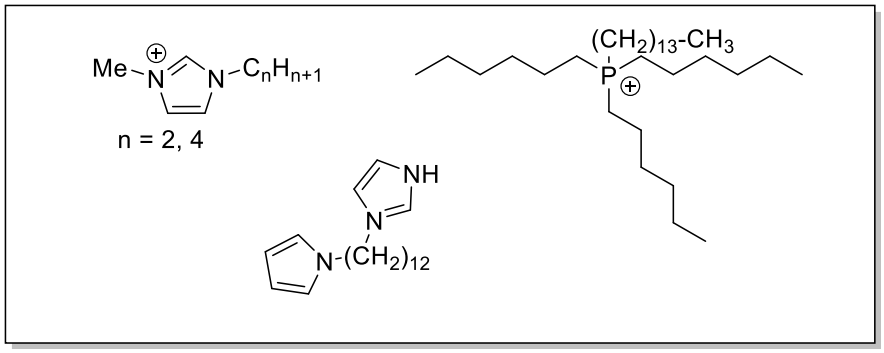
X-ray photoelectron spectroscopy (XPS) was used to give further insight to the speciation of $[C_1C_8Im]Cl$ and $ZnCl_2$. At $\chi ZnCl_2 = 0.25$ and 0.33 a single anion was observed ($[ZnCl_4]^{2-}$) and for $\chi ZnCl_2 = 0.5$ and 0.6 bridging and terminal chlorides in $[Zn_xCl_{(2x+2)}]^{2-}$.Furthermore, free chloride was noted at $\chi ZnCl_2 = 0.25$.[72] EXAFS investigation confirmed the existence of a tetrahedral $[ZnCl_4]^{2-}$ anion.[73]

Chlorozincate ILs have been reported to be moisture-stable in comparison to chloroaluminate ILs which easily hydrolyse. This makes them desirable catalysts e.g. for reactions of alcohols or phenols.[53]

Lovejoy *et al.* proposed the use of $ZnCl_2$ and ILs for pharmaceutically active materials as they increase their shelf life and show antibiofilm activity.[74]

### 1.2.5 Cobalt containing ionic liquids

The most common cobalt IL contains a Co(II) species in the form $[cation]_2[CoCl_4]$.[75] Scheme 1-7 shows cations present in the literature utilized for the formation of cobalt containing ILs.[76-78]




*Scheme 1-7 Commonly used cations for cobalt containing ILs.*

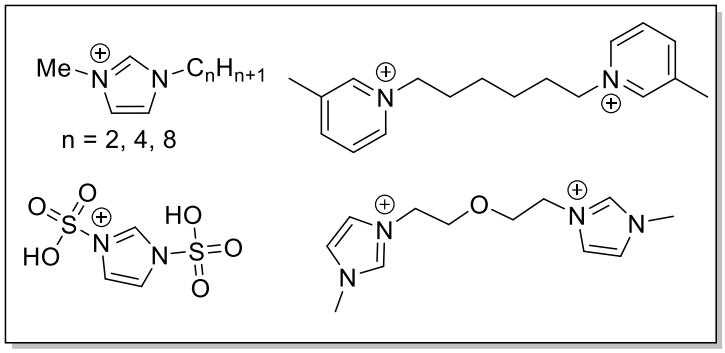
UV/Vis spectroscopy was utilised to further investigate $[C_1C_4Im]Cl$ and $CoCl_2$ speciation. The tetrahedral anion $[CoCl_4]^{2-}$ was observed at $\chi CoCl_2 \leq 0.33$ and at $\chi CoCl_2 \geq 0.33$ different complexes were postulated ($[CoCl_2(CoCl_4)_2]^{4-}$ and $[Co(CoCl_4)_3]^{4-}$).[79] In addition, Wellens *et al.* monitored the extraction of cobalt with UV/Vis spectroscopy through the formation of $[P_{66614}]_2[CoCl_4]$.[80]

Santra *et al.* investigated magnetic ILs, including cobalt containing ILs, for their applicability to isolate oligonucleotides with the help of Fluorescence spectroscopy.[77]

$[C_1C_4Im][CoCl_4]$ was also used as an electrochemical exfoliation electrolyte and as active dopant for catalyst preparation. The catalyst was then used for the synthesis of nanosheets with metallic cobalt starting from coal, which was used as a carbon source.[75]

### 1.2.6 Nickel containing ionic liquids

The most common nickel IL contains a Ni(II) species in the form $[cation]_2[NiCl_4]$.[81] Scheme 1-8 shows cations present in the literature utilized for the formation of zinc containing ILs.[81-85]




*Scheme 1-8 Commonly used cations for nickel containing ILs.*

EXAFS showed that $NiCl_2$ dissolved in chloroaluminate ILs formed $[NiCl_4]^{2-}$ and $[AlCl_4]^-$ when $\chi AlCl_3 < 0.5$. However, for $\chi AlCl_3 > 0.5$ bidentate complexes of the type $[Ni(AlCl_4)_3]^-$ were observed, which are known to be of importance as catalysts and have found an application with the Difasol process.[82, 86]

Fernandes *et al.* developed a thermochromic and thermoresistive material using the IL $[C_1C_4Im]_2[NiCl_4]$. The material is printable and demonstrates a colour change from transparent to dark blue due to the formation of the nickel anion upon dehydration.[83]

## 1.3 Lewis acidity of halometallate ionic liquids

Lewis acidic halometallate IL catalysts are a continuously evolving field and now includes not just chloroaluminate(III) ILs, but also metal chloride eutectics and ILs with Lewis acidic cations.[28] Lewis acidity in ILs is dependent on the anion speciation and therefore generally only influenced by the halometallate anion, as the organic cation is believed to only influence physical properties (e.g. viscosity, density, and melting point).[16] Speciation reported in the literature for different halometallate ILs has shown that they can differ significantly hence careful investigation needs to be carried out for each metal halide. Like

speciation, also Lewis acidity can vary significantly depending on the metal halide. For example $[AlCl_4]^-$ has been shown to be neutral, as the chloride ligands prevent further coordination. Yet, $[InCl_4]^-$ is a mild Lewis acid as it is coordinatively unsaturated.[87]

### 1.3.1 How to influence Lewis acidity?

As seen in "1.3.3 How is Lewis acidity determined?" the Lewis acidity of halometallate ILs can be influenced through the mole fraction of the metal chloride. In addition, ligands can have an influence on the Lewis acidity of a metal complex depending on their donor and acceptor properties.

### 1.3.2 Nitrosyl ligands for improved reactivity

In the 1980's nitrogen monoxide (nitric oxide, NO) was discovered to be an important signaling molecule within several biological processes, hence the research into metal nitrosyl complexes increased. The colorless gas has been known since the thirteenth century but only its importance in signaling mechanisms and coordination to enzymes initiated a deeper understanding of its geometric ambivalence.[88] Figure 1-1 shows the molecular orbital diagram for the NO molecule, where the antibonding $\pi^*$ orbital is occupied by an unpaired electron and the formal bond order is 2.5.

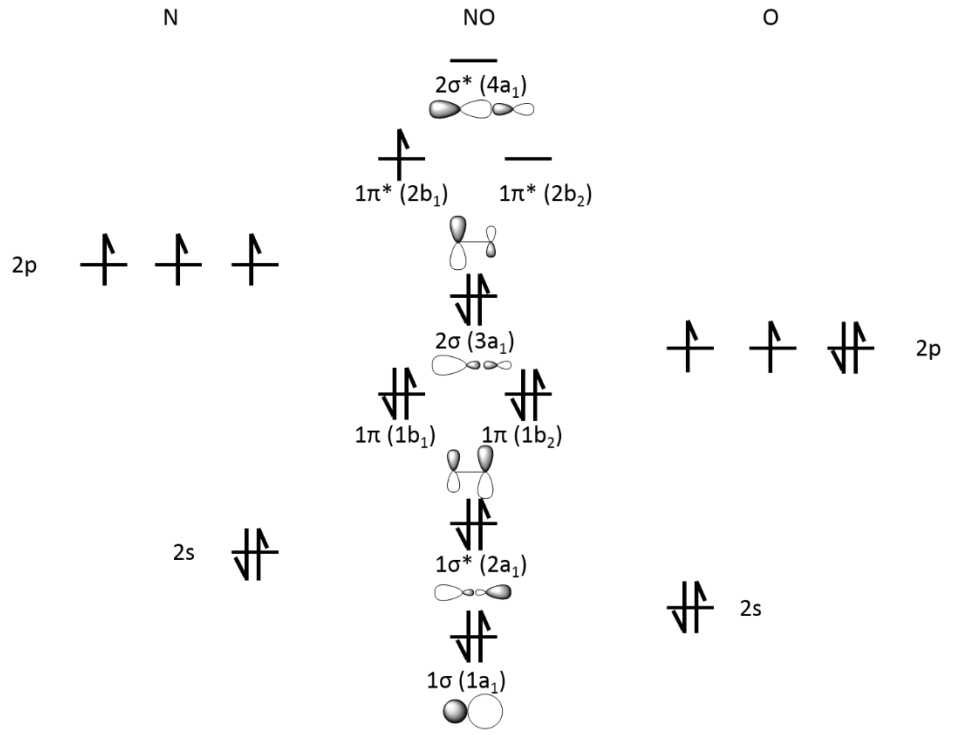



*Figure 1-1 Molecular orbital diagram for the NO molecule.*[89]

NO is a strong π-acceptor ligand and can bind to d-metal ions either in a bent or linear way. Ligands of this type are then referred to as nitrosyl. In the case of the linear bond, the ligand is considered as $NO^+$ (Figure 1-2) and is isoelectronic to CO.

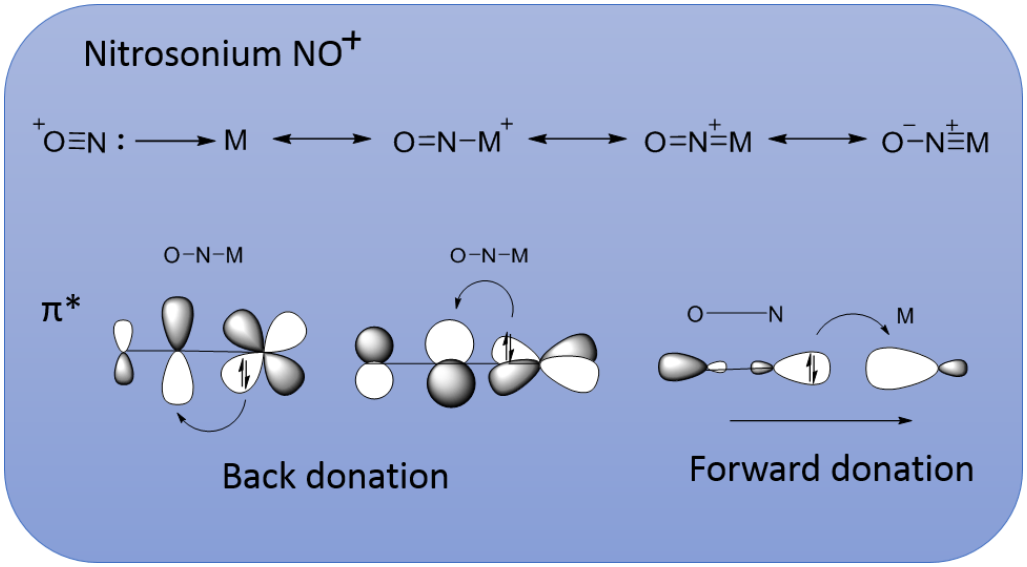



*Figure 1-2 Bond formation of nitrosonium ligand with a d-metal.*

As depicted in Figure 1-2 $NO^+$ is a two-electron σ donor and has a strong π-acceptor ability. The bond between the metal and the nitrosyl ligand is described using valence bond terms and molecular orbital terms. Initially an electron is transferred to the metal centre and hence the coordination of $NO^+$ to the reduced metal centre follows. When bound linearly to the metal centre it has been shown that the nitrosyl ligand can be seen as a neutral three electron donor.[90]

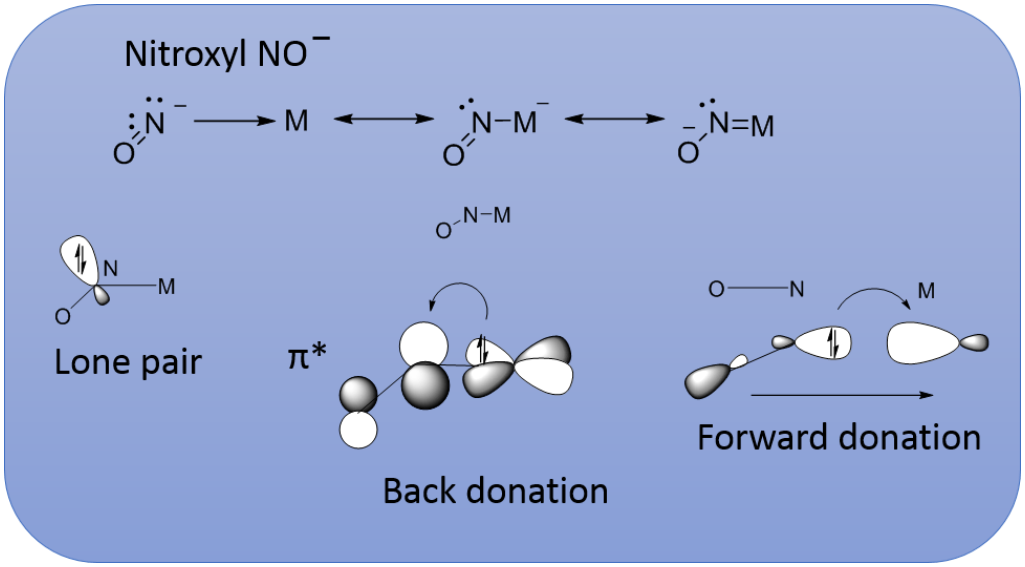



*Figure 1-3 Bond formation of nitroxyl ligand with a d-metal.*

Figure 1-3 shows the valence bond and molecular orbital description of the bond formed between a bent nitrosyl ligand and a metal centre. Due to changes in hybridisation and the increased repulsion from the lone pair a bent geometry is present. The $NO^-$ ligand is considered a one electron donor and the angle generally found in metal complexes is 120°.[90]

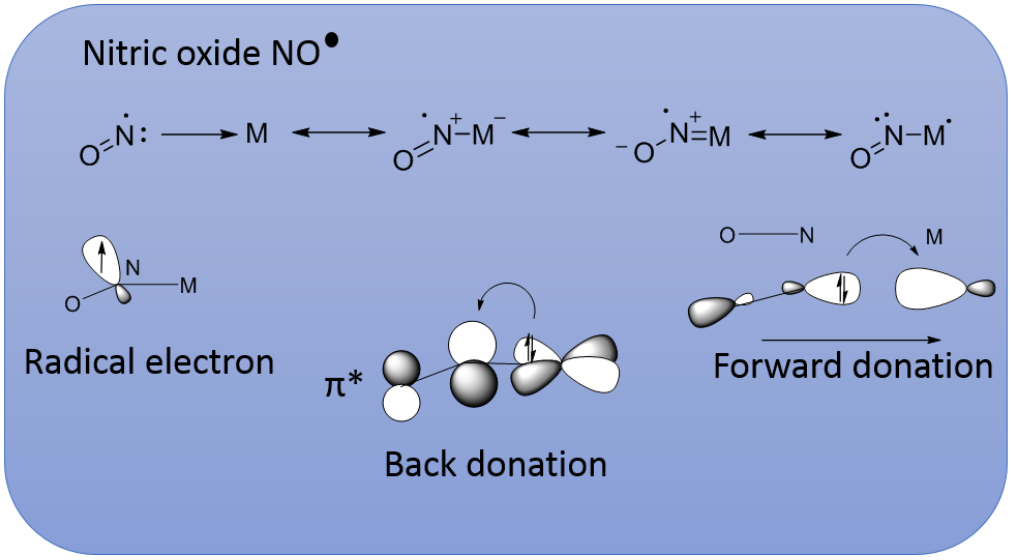



*Figure 1-4 Bond formation between nitric oxide and a d-metal.*

Nitric oxide is a radical and has been shown to have a geometry in between linear and bent. Therefore, the nitrogen might be associated with a lone pair but the electron might also be on the metal itself (Figure 1-4).

An important tool to determine the type of nitrosyl ligand is vibrational spectroscopy. Depending on the type of ligand, the shift in wavenumber can be significantly. Generally, linear M–N–O groups absorb in the range 1650–1900 $cm^{-1}$ and bent M–N–O species in the range 1525–1690 $cm^{-1}$. The IR stretching frequency depends on other ligands present in the complex, electronic configuration, overall charge of the complex, and the geometry of the complex. Due to these many factors it is difficult to draw a distinct conclusion from the type of IR stretching frequency and determine the exact structure of the M-N-O bond and a more extensive variety of spectroscopic methods is needed.[91]

### 1.3.3 How is Lewis acidity determined?

The strength of the interaction between a Lewis acid-base pair is dependent on its base, as it is influenced by the size, shape, steric effects, and relative

energies of the LUMO of the acid and the HOMO of the base.[92] Contrary to Brønsted acids, where the strength is quantified regarding the proton. There are a variety of methods, which allow indirect probing of Lewis acidity, each with a specific scale. These methods use a basic probe molecule or ion to determine the strength of the interaction between the acid-base pair. Methods for quantification include computational calculations,[93, 94] physical measurement (*e.g.* Gutmann Acceptor Number),[95-97] and reaction rate of a model reaction catalysed by the respective acid.[28, 98, 99]

*Gutmann Acceptor Number*

The Gutmann Acceptor Number (AN) was the first method used for estimating Lewis acidity in ILs. It was initially developed for investigation of donor/acceptor properties before expanding to liquid acids. The Gutmann AN is a spectroscopic NMR method using triethylphosphine oxide (TEPO) as a $^{31}P$ NMR spectroscopic probe. TEPO was chosen as a probe due to its good sensitivity, good solubility in different solvents, low steric hindrance and stability towards acids.[87, 96, 100-102]

The scale was defined arbitrarily based on the change in $^{31}P$ NMR shift due to the coordination of the Lewis acid to phosphine oxide. Hexane was defined to have AN = 0 and $SbCl_5$ in 1,2-dichloroethane as AN = 100.[103] To estimate the AN several spectra at different concentrations are recorded and the chemical shift extrapolated to infinite dilution ($\delta_{inf}$). Then the data is normalized with respect to infinite dilution of TEPO in hexane ($\Delta\delta_{inf}$) and then values are calculated with the following equation,[28]

$$AN = 2.348\ x\ \Delta\delta_{inf} \quad \text{1-1}$$

Brown *et al.* have summarised some AN for halometallate ILs of the type $[C_1C_8Im]Cl/MCl_x$ (M = Al, Ga, In, Zn and Sn) and the interesting metals for this work are highlighted in Table 1-1.[28]

*Table 1-1 AN values for M = In and Zn in the IL $[C_1C_8Im]/MCl_x$ at varying mole fraction.*

| **$\chi MCl_x$** | **AN (M = In)** | **AN (M = Zn)** |
|---|---|---|
| **0.00** | 19.86 | 19.86 |
| **0.10** | | 20.14 |
| **0.20** | 32.53 | 20.50 |
| **0.30** | | 22.51 |
| **0.33** | 49.25 | 25.63 |
| **0.40** | 51.22 | 63.09 |
| **0.46** | | 64.01 |
| **0.48** | | 65.24 |
| **0.50** | 57.11 | 67.26 |
| **0.55** | | 70.55 |
| **0.60** | 56.53 | 70.86 |
| **0.67** | 58.36 | 72.49 |
| **0.70** | | 73.57 |
| **0.75** | | 83.50 |
| **1.00** | 74.30 | 66.00 |

Non-metal containing ILs have also been investigated using this technique and other solid state techniques (*e.g.* Raman spectroscopy) have been used, which could be useful also for evaluating halometallate ILs containing a paramagnetic metal.[104-108]

## 1.4 Halometallate ionic liquids and the challenge of anion speciation

During the 1990s, when interest in ILs took hold, the main focus was on halometallate ILs, typically chlorometallates. The reaction of a metal halide and an organic cation leads to a well-defined cation and one or more halometallate anions in dynamic equilibrium, therefore the speciation of the anion can be a complex task.[9] Especially for the preparation of an IL catalyst the speciation is of utmost importance to define the catalytically active species.

### 1.4.1 Phase diagram of chloroaluminate(III) ionic liquids

To date, the most studied metal for halometallate ILs is aluminium and will be explored here as an example for a well-defined IL system. As previously mentioned, several industrial applications of chloroaluminate ILs have been reported in the past, the most notable being the Difasol process, which contributed to Chauvin's Nobel Prize win.[7, 109] More importantly, a significant part of research on chloroaluminate ILs has focused on the speciation of the anion. As demonstrated previously, speciation is a tremendous part of the formation of halometallate ILs. In fact, a change in mole fraction can lead to a different IL displaying distinct physical and chemical properties.[28] In the case of chloroaluminate ILs three different species can be observed with Raman spectroscopy; $[AlCl_4]^-$ at mole fraction $\chi AlCl_3 = 0.5$, and $[Al_2Cl_7]^-$ at mole fraction

$\chi AlCl_3$ = 0.67 in equilibrium with $[Al_3Cl_{10}]^-$.[26, 110] Fannin *et al*. reported a phase diagram for $[C_1C_2Im]Cl/AlCl_3$ (Figure 1-5) using differential scanning calorimetry (DSC) as well as visual observation (using a standard melting point apparatus) for the determination of melting, freezing, and glass transition temperatures.[111]

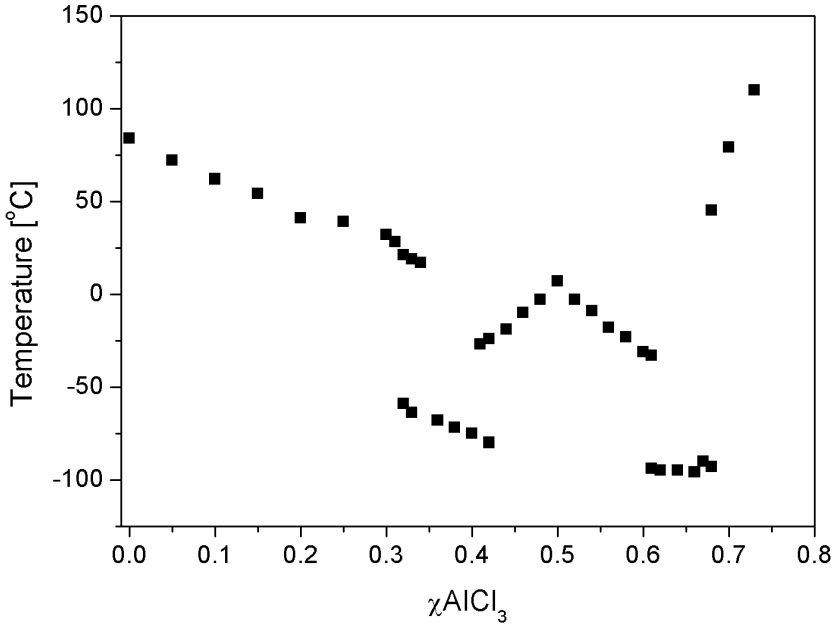



*Figure 1-5 Phase diagram for $[C_1C_2Im]Cl/[AlCl_3]$ including melting, freezing and glass transition temperatures (adapted from reference [111]).*

A peritectic can be observed at $\chi AlCl_3$ = 0.5, suggesting the melting of a pure compound $[C_1C_2Im][AlCl_4]$. Eutectic regions around $\chi AlCl_3$ = 0.33 and 0.67 are consistent with the formation of mixtures containing $[C_1C_2Im][AlCl_4]$ and $[C_1C_2Im]Cl$ ($\chi AlCl_3$ = 0.33) or $[C_1C_2Im][Al_2Cl_7]$ ($\chi AlCl_3$ = 0.67).[16, 111]

Additionally, $^{27}Al$ NMR spectroscopy has been used to characterise chloroaluminate ILs. However, care must be taken as results can change significantly depending on whether the IL is neat or in solvent. Furthermore,

temperature can also influence results for samples with high viscosities, which is often the case for halometallate ILs.[112, 113]

Phase diagrams for other halometallate ILs have been reported, such as $InCl_3$, $ZnCl_2$, and $SnCl_2$.[73, 114, 115] Significant differences in anion speciation were found, for example In does not form any dimeric anions like Al does. Thus, highlighting the importance of investigating each metal halide individually. The known phase diagrams for $InCl_3$, $ZnCl_2$, and $SnCl_2$ will be discussed further in the following sections.

### 1.4.2 Phase diagram of chloroindate(III) ionic liquids

Figure 1-6 shows the phase diagram for $InCl_3$ and $[C_1C_4Im]Cl$ prepared from data obtained with DSC. The observations were supported by Raman spectroscopy and computational methods. At mole fraction $\chi InCl_3$ = 0.5 a eutectic point was observed and the species was confirmed as $[C_1C_4Im][InCl_4]$ by Raman and ab initio calculations. Furthermore, the existence of the anions $[InCl_6]^{3-}$ and $[In_2Cl_7]^-$ was suggested by theoretical calculations.[116]

However, Apperley *et al.* have investigated mixtures of $InCl_3$ with $[C_1C_8Im]Cl$ and $[C_1C_4Im]Cl$ to propose a phase diagram and in their research they found that no dimeric species could be confirmed for indium.[114]

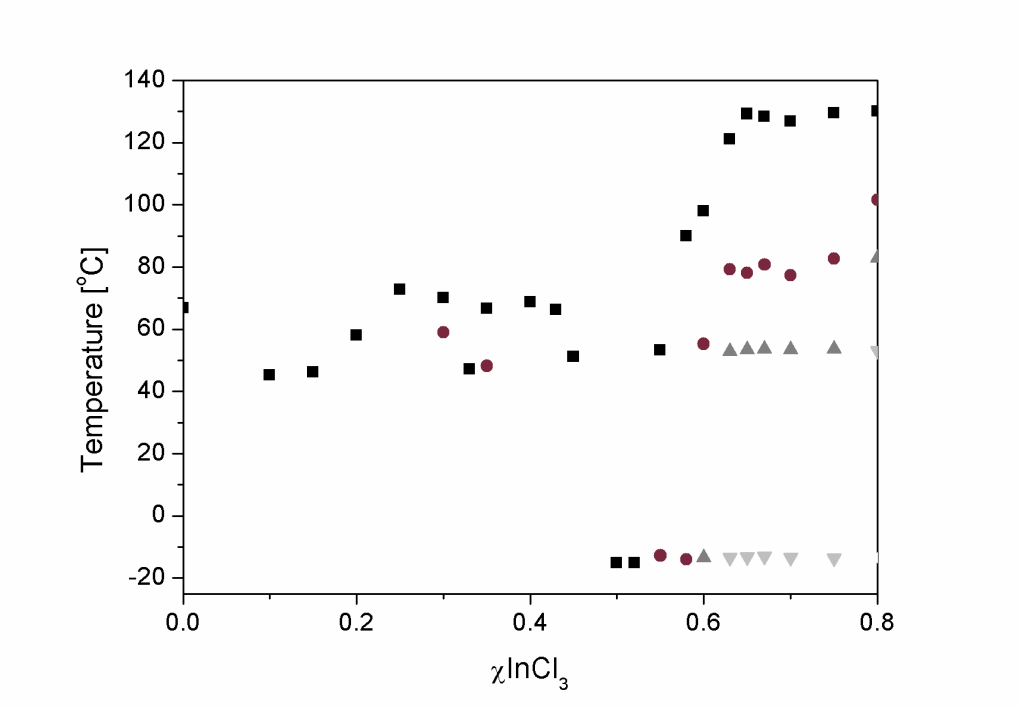



*Figure 1-6 Phase diagram for $[C_1C_4Im]Cl/InCl_3$ obtained with DSC.*[116]

The formation of $[InCl_6]^{3-}$ at $\chi InCl_3 = 0.25$ is confirmed and in addition at $\chi InCl_3 = 0.33$ the existence of $[InCl_5]^{2-}$ is suggested (Scheme 1-9).

$$[cation]Cl + 3InCl_3 \longrightarrow [cation]_3[InCl_6]$$

$$4Cl^- + 2InCl_3 \longrightarrow 2[InCl_5]^{2-} \rightleftharpoons [InCl_6]^{3-} + [InCl_4]^-$$

*Scheme 1-9 Formation chloroindate(III) anions with up to six chlorides and the suggested formation of an equilibrium.*[28]

At a molar fraction $\chi InCl_3 > 0.5$ a biphasic suspension was observed with a solid suspended in a liquid and was confirmed as $InCl_3$ in the neutral $[C_1C_4Im][InCl_4]$ IL. Molar fraction $\chi InCl_3 \leq 0.5$ was observed to be liquid and for $\chi InCl_3 < 0.5$ the anions $[InCl_6]^{3-}$, $[InCl_5]^{2-}$, and $[InCl_4]$ were confirmed to be present depending on the molar fraction.[114, 117]

### 1.4.3 Phase diagram of chlorozincate(II) ionic liquids

A phase diagram for $ZnCl_2$ with $[C_1C_4Im]Cl$ was prepared by Alves *et al.* using DSC and Raman spectroscopy. Complex behaviour was observed displaying four maxima and minima, likely corresponding to eutectic and isoplectic points. The group suggested the following anion speciation at different mole fractions $[ZnCl_4]^{2-}$ for $\chi ZnCl_2 = 0.35$; $[Zn_2Cl_6]^{2-}$ for $\chi ZnCl_2 = 0.64$ and $[Zn_4Cl_{10}]^{2-}$ for $\chi ZnCl_2 = 0.50$; and $[Zn_3Cl_8]^{2-}$ for $\chi ZnCl_2 = 0.70$.[118, 119]

Estager *et al.* carried out further investigation into the different anion formation depending on the mole fraction. They reviewed two speciation models present in the Literature[120-123] and concluded that the speciation present for $ZnCl_2$ is in agreement with the previously reported anions from Alves *et al.* only differing in the species present at certain mole fraction. In their research Raman spectroscopy, DSC, and Crystallography was used to confirm the anions present (Table 1-2).[73, 119]

*Table 1-2 Anion speciation present at different mole fraction of $ZnCl_2$ with $[Zn_xCl_{2x+2}]^{2-}$ being a postulated polynuclear species.*

| $\chi ZnCl_2$ | 0.33 | 0.5 | 0.6 | 0.67 |
|---|---|---|---|---|
| $Cl^-$<br>$[ZnCl_4]^{2-}$ | $[ZnCl_4]^{2-}$<br>$[Zn_2Cl_6]^{2-}$ | $[Zn_2Cl_6]^{2-}$<br>$[Zn_3Cl_8]^{2-}$ | $[Zn_3Cl_8]^{2-}$<br>$[Zn_4Cl_{10}]^{2-}$ | $[Zn_4Cl_{10}]^{2-}$<br>$[Zn_xCl_{2x+2}]^{2-}$ |

## 1.5 Halometallate ionic liquids as catalysts

Halometallate ILs are of particular interest for catalysis due to their easily tuneable Lewis acidity, achieved simply by changing the speciation of the metal complex.[124] Some of the most studied metals are the group III halometallates, with an increasing Lewis acidity in the following order In < Al < Ga.[87] It has been stated that the main influence on the Lewis acidity comes from the metal itself

and the mole fraction of metal halide in respect to the organic moiety of the IL.[112-114, 117, 125-127] The main advantages of halometallate ILs as catalysts are controllable acidity, ability to dissolve a variety of materials, facile product isolation, and dual functionality as both a catalyst and a solvent. These generally outweigh their drawbacks, which include viscosity, and moisture sensitivity.[124] Group III halometallate ILs have been successfully used for a plethora of reactions, which include alkylation,[128-135] acylation,[131, 136] oligomerization,[137-139] Diels-Alder reaction,[140-142] hydrogenation,[143] esterification,[144-146] condensation,[147-149] isomerization,[150-152] and oxidation.[153]

An early example of a chlorometallate IL used in a catalytic reaction is presented by Parshall in 1972, where chlorostannate(II) or germanate(II) anions were used as solvent and to form coordinating complexes with platinum for olefin hydrogenation. The coordination complex formed showed higher stability towards hydrogen reduction and increased selectivity was observed.[154]

In 1995 the Nobel Prize in Chemistry was awarded to Yves Chauvin not only but in part due to the development of the Difasol process which uses $NiCl_2$ dissolved in an chloroaluminate IL ($[C_2mim]Cl\text{-}NiCl_2\text{-}AlEtCl_2$).[155]

Special interest for halometallate IL catalysts has always been on the group III elements (Al, Ga, In). A review from Rogers *et al.* highlights the many applications group III halometallate ILs have found (*e.g.* alkylation, acylation, oligomerization, Diels-Alder reactions, hydrogenation, oxidation, isomerization, condensation, and esterification). Different anion speciation has

been used in catalytic applications with a focus on anions showing an increased Lewis acidity.[124]

Indium for example has been used as a Lewis acidic catalyst for etherification[156], alkylation[53], and conversion of $CO_2$ to form cyclic carbonates[157] by several research groups.

Several examples exist in the literature, where halometallate ILs have been used for the glycolysis of poly(ethyleneterephthalate) (PET). The reaction has been carried out with thermal heating and microwave assisted heating with good selectivity to form the monomer bis(hydroxyethyl)terephthalate (BHET).[66, 158-160]

Srivastava *et al.* prepared a Zeolite functionalised with a manganese based halometallate IL as a catalyst for the reduction of olefins at mild reaction conditions using hydrazine as a reducing agent.[161]

Maciejewski *et al.* reported an IL type catalyst with a chloroplatinate anion and imidazolium or pyridinium cation. However, melting points over 100°C were observed classifying the catalyst as anionic platinum complexes. The catalysts were successfully used for hydrosilylation of olefins with high recyclability through easy catalyst separation.[162]

Rogers *et al.* developed a mixed metal species IL with aluminium and gallium for Friedel-Crafts acylation and alkylation. Higher yields and better selectivity was noted in comparison to single metal IL due to the liquid Lewis acid catalyst which presented a dynamic anionic species.[163]

The same group had previously reported a Lewis acidic aluminium and zinc mixed species IL, which was applied as a catalyst for a Beckmann rearrangement with good conversion and selectivity.[164]

Tiong *et al.* very recently reported the use of a Brønsted-Lewis acidic indium IL, $InCl_3$-[HMIM][$HSO_4$], which was used to prepare levulinic acid from cellulose and then further upgrade it to ethyl levulinate.[165]

Another recent example utilizes a propylphosphonium tetrachloroindate IL supported on silica as a heterogeneous, reusable catalyst under solvent free conditions for the formation of symmetric and unsymmetric pyrido quinolines.[166]

## 1.6 Industrial processes using halometallate ionic liquids

In addition ILs are also found in industrial processes like the BASIL process (BASF), which uses an IL as an acid scavenger in the production of alkylphenylphosphines. BASF uses these as photoinitiators for UV curing of double-bonded resins, which are often found in printing inks and coatings.[167]

The Difasol process (IFP) uses a chloroaluminate IL as a solvent for a nickel catalyst in a dimerisation reaction. The process is a biphasic system, where the catalyst stays in one phase and the products form a second phase which facilitates easy separation.[7]

HycaPure Hg (Petronas) is a technology, which uses solid-supported ILs to remove inorganic and organic mercury compounds from natural gas. The

Harbin Petroleum alkylation process (PetroChina) uses ILs for production of isobutylene from liquefied butane gas.[7, 86, 168, 169]

The ISOALKY™ process (Chevron) uses an acidic IL instead of hydrofluoric or sulphuric acids as alkylation catalyst and has shown comparable yields and good selectivity at industrial scale in a demonstration unit. A new unit will be operational by 2020.[170, 171]

## 1.7 Aims and objectives

The aim of this work is to expand the knowledge on halometallate ILs regarding a future application in inductive heating. As was previously discussed, a range of factors must be considered, when employing halometallate IL catalysts. Anion speciation, being one of these factors, influences the Lewis acidity hence phase diagrams are a necessary tool to determine the species present. In addition, further methods might be necessary to determine the active Lewis catalyst, as was shown in section 1.3 Lewis acidity of halometallate ionic liquids can vary depending on the metal halide. Thus a variation of the traditional chlormetallate anion could lead to improved activity through a change in the Lewis acidity. Furthermore, an application in inductive heating (*e.g.* MW radiation) requires further investigation on the dielectric properties of the ILs. The dielectric constant and loss are important tools to estimate a successful application of a material in a MW process. Finally, it is crucial to understand the reaction pathway and to verify the catalytically active species of a halometallate IL catalyst through mechanistic and kinetic studies.

- What is the phase diagram for $CoCl_2$ and $NiCl_2$, and which anion speciation is present?
- How viable are halometallate ILs in MW synthesis?
- Are halometallate ILs a good catalyst for $CO_2$ conversion and what is the catalytically active species?

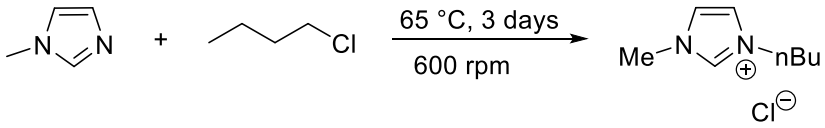
# Chapter 2

## 2. Synthesis and characterisation of halometallate ionic liquids

### 2.1. Synthetic procedures

All oxygen and moisture sensitive operations were carried out under an argon atmosphere using standard vacuum-line and Schlenk techniques. Solvents were purchased from Sigma-Aldrich as HPLC grade and dried by means of an Inert Puresolv MD purification system. All reagents were purchased from Sigma Aldrich and purified when required by literature procedures.[172] Chemical shifts of $^{1}H$ and $^{13}C$ NMR are reported in ppm, the solvent was used as internal standard. Signals are quoted as s (singlet), d (doublet), m (multiplet), dt (double triplet) and td (triplet doublet). Determination of accurate mass was performed by the Mass Spectroscopy Service of the University of Nottingham (Nottingham, UK) Elemental analysis was performed by the Elemental Analysis Service of the University of Nottingham (Nottingham, UK).

#### 2.1.1 Synthesis of $[C_1C_4Im]Cl$




1-Methylimidazolium (100 ml, 1.22 mol) was added to 1-chlorobutane (168.5 ml, 1.82 mol) and the reaction mixture was heated under reflux at 65°C for 3 days. After cooling down the solution to r.t., acetone (184 ml) was added and the solution was slowly heated again at 40°C for 10 minutes. Afterwards, methanol (*ca*. 5 mL) was added drop-wise until a clear solution was obtained.

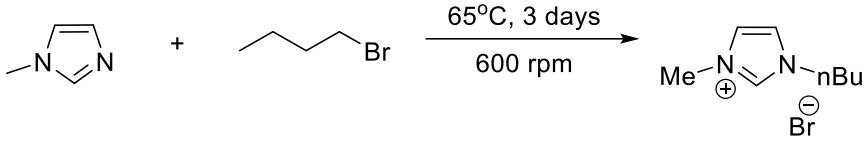
The product was crystallized in the freezer. Then, the solvent was removed by filtration via cannula and the product was dried under vacuum. The final product was washed with ethyl acetate to remove residual 1-methylimidazolium and dried under vacuum at 40°C for 2 days.

$^1$H NMR (400 MHz, $CDCl_3$): δ 0.89 (t, 3H, *J* = 7.4 Hz, $CH_2$-C*H*$_3$), 1.30 (m, 2H, $CH_2$-C*H*$_2$-$CH_3$), 1.79 (m, 2H, $CH_2$-C*H*$_2$-$CH_2$), 4.04 (s, 3H, C*H*$_3$-N), 4.22-4.27 (t, 2H, *J* = 7.4 Hz, N-$CH_2$-$CH_2$), 7.24-7.59 (d, 2H, *J* = 1.8 Hz, N-C*H*-C*H*-N), 10.59 (s, 1H, N-C*H*-N) ppm.

$^1$H NMR data was consistent with those previously reported. [173]

Accurate mass $[M]^+$: Calc. 139.1230, Obs.: 139.1252.

### 2.1.2 Synthesis of $[C_1C_4Im]Br$




1-Methylimidazolium (100 ml, 1.22 mol) was added to 1-bromobutane (195 ml, 1.82 mol) and the reaction mixture was heated under reflux at 65°C for 3 days. After cooling down the solution to r.t., acetone (184 ml) was added and the solution was slowly heated again at 40°C for 10 minutes. Afterwards, methanol (*ca*. 5 mL) was added drop-wise until a clear solution was obtained. The product was crystallized in the freezer. Then, the solvent was removed by filtration via cannula and the product was dried under vacuum. The final product was washed with ethyl acetate to remove residual 1-methylimidazolium and dried under vacuum at 40°C for 2 days.

$^1$H NMR (400 MHz, $CDCl_3$): δ 0.80-0.93 (t, 3H, *J* = 7.4 Hz, $CH_2$-C*H*$_3$), 1.25-1.45 (m, 2H, $CH_2$-C*H*$_2$-$CH_3$), 1.68-1.91 (m, 2H, $CH_2$-C*H*$_2$-$CH_2$), 4.06 (s, 3H, C*H*$_3$-N), 4.26-4.29 (t, 2H, *J* = 7.4 Hz, N-$CH_2$-$CH_2$), 7.46-7.60 (d, 2H, *J* = 1.8 Hz, N-C*H*-C*H*-N), 10.25 (s, 1H, N-C*H*-N) ppm.

$^1$H NMR data was consistent with those previously reported.[174]

Accurate mass $[M]^+$: Calc. 139.1230, Obs.: 139.1223.

### 2.1.3 Synthesis of $[C_1C_4Im][FeCl_4]$

1-Butyl-3-methylimidazolium chloride (2.15 g, 0.0123 mol) was weighed into a Schlenk flask in an inert atmosphere. An equimolar amount of anhydrous $FeCl_3$ (2 g, 0.0123 mol) was added and the mixture stirred for five minutes. The product is a green brown liquid.

Raman: 111, 334 $cm^{-1}$.

Accurate mass $[M]^+$: Calc. 139.1230, 140.1263; Obs.: 139.1232, 140.1258.

Elemental Analysis: Calc. C, 28.52; H, 4.49; N, 8.32; Obs.: C, 28.41; H, 4.54; N, 8.15.

### 2.1.4 Synthesis of $[C_1C_4Im][FeBr_4]$

1-Butyl-3-methylimidazolium bromide (1.48 g, 0.00677 mol) was weighed into a Schlenk flask in an inert atmosphere. An equimolar amount of anhydrous $FeBr_3$ (2 g, 0.00677 mol) was added and the mixture stirred for five minutes. The product is an orange brown liquid.

Raman: 154, 200, 300 $cm^{-1}$.

Accurate mass $[M]^+$: Calc. 139.1230; Obs. Obs.: 139.1223.

### 2.1.5 Synthesis of $[C_1C_4Im][InCl_4]$

1-Butyl-3-methylimidazolium chloride (2 g, 0.0115 mol) was weighed into a Schlenk flask in an inert atmosphere. An equimolar amount of anhydrous $InCl_3$ (2.53 g, 0.0115 mol) was added and the mixture stirred for one hour. The product is a clear liquid.

$^{115}In$ NMR (400 MHz, neat): δ 442.41 ppm (s, $[InCl_4]^-$)

Accurate mass $[M]^+$: Calc. 139.1230, 140.1263; Obs.: 139.1233, 140.1261.

Elemental Analysis: Calc. C, 24.27; H, 3.82; N, 7.08; Obs.: C, 23.72; H, 3.94; N, 6.61.

### 2.1.6 Synthesis of $[C_1C_4Im]_2[CuCl_4]$

1-Butyl-3-methylimidazolium chloride (2 g, 0.0115 mol) was weighed into a Schlenk flask in an inert atmosphere. Anhydrous $CuCl_2$ (0.77 g, 0.00575 mol) was added and the mixture was heated to 60°C and stirred overnight. The product is a light brown liquid.

Raman: 275 $cm^{-1}$.

Accurate mass $[M]^+$: Calc. 139.1230, 140.1263; Obs.: 139.1232, 140.1260.

Elemental Analysis: Calc. C, 39.72; H, 6.25; N, 11.58; Obs.: C, 39.07; H, 6.47; N, 11.04.

### 2.1.7 Synthesis of $[C_1C_4Im]_2[ZnCl_4]$

1-Butyl-3-methylimidazolium chloride (2 g, 0.0115 mol) was weighed into a Schlenk flask in an inert atmosphere. Anhydrous $ZnCl_2$ (0.78 g, 0.00575 mol) was added and the mixture was heated to 60°C and stirred overnight. The product is a white solid at room temperature.

Raman: 230, 275 $cm^{-1}$.

$^{1}H$ NMR (400 MHz, $CDCl_3$): δ 0.22 (s, 3H, $CH_2$-C*H*$_3$), 0.68 (s, 2H, $CH_2$-C*H*$_2$-$CH_3$), 1.24 (s, 2H, $CH_2$-C*H*$_2$-$CH_2$), 3.43 (s, 3H, C*H*$_3$-N), 3.7 (s, 2H, N-$CH_2$-$CH_2$), 7.01-707 (d, 2H, *J* = 24.7 Hz, N-C*H*-C*H*-N), 8.37 (s, 1H, N-C*H*-N) ppm.

Accurate mass $[M]^+$: Calc. 139.1230, 140.1263; Obs.: 139.1232, 140.1259.

Elemental Analysis: Calc. C, 39.57; H, 6.23; N, 11.54; Obs.: C, 39.49; H, 6.27; N, 11.41.

### 2.1.8 Synthesis of $[C_1C_4Im]_2[NiCl_4]$

1-Butyl-3-methylimidazolium chloride (2 g, 0.0115 mol) was weighed into a Schlenk flask in an inert atmosphere. Anhydrous $NiCl_2$ (0.745 g, 0.00575 mol) was added and the mixture was heated to 80°C and stirred overnight. The product is a blue solid at room temperature.

Accurate mass $[M]^+$: Calc. 139.1230, 140.1263; Obs.: 139.1232, 140.1262.

Accurate mass $[M]^-$: Calc. 239.03; Obs.: 239.0564.

Elemental Analysis: Calc. C, 40.13; H, 6.31; N, 11.70; Obs.: C, 39.16; H, 6.54; N, 11.74.

### 2.1.9 Synthesis of $[C_1C_4Im]_2[CoCl_4]$

1-Butyl-3-methylimidazolium chloride (2 g, 0.0115 mol) was weighed into a Schlenk flask in an inert atmosphere. Anhydrous $CoCl_2$ (0.747 g, 0.00575 mol) was added and the mixture was heated to 80°C and stirred overnight. The product is a blue solid at room temperature.

Raman: 350 $cm^{-1}$ ($[CoCl_4]^-$).

Accurate mass $[M]^+$: Calc. 139.1230, 140.1263; Obs.: 139.1234,

140.1263.

Elemental Analysis: Calc. C, 40.11; H, 6.31; N, 11.69; Obs.: C, 39.81; H, 6.43; N, 11.50.

### 2.1.10 Synthesis of $[Fe(NO)_2Cl]_2$

$$2\,FeCl_3 + Fe + 12\,NO \xrightarrow[90\,^\circ C,\ 600\ rpm]{THF,\ 1h} 3\,[Fe(NO)_2Cl]_2 \quad (Yield\ 43\ \%)$$

Iron (III) chloride ($FeCl_3$, 2 g, 12.3 mmol) and iron (Fe, 3 g, 53.8 mmol) were mixed in 30 mL of dry tetrahydrofuran (THF) in a Schlenk flask under Ar atmosphere. The solution was heated at 90°C under reflux for 1 h.

$$6\,FeSO_4 + 12\,NaNO_2 \xrightarrow{r.t.,\ 600\ rpm} 2\,Fe_2O_3 + Fe_2O_3 \cdot N_2O_5 + 10\,NO + 6\,Na_2SO_4$$

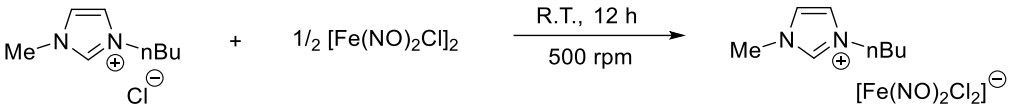
The continuous flow of NO gas was produced by the above shown reaction. Iron sulphate ($FeSO_4$) (75 g) was dissolved in diluted sulfuric acid (74 ml, ratio $H_2SO_4$:$H_2O$ 1:1) and sodium nitrite ($NaNO_2$) (25 g) was dissolved in $H_2O$ (37 ml). The solution of $NaNO_2$ was slowly added to the solution of $FeSO_4$ through a dropping funnel. The generated NO gas was dried over molecular sieves and bubbled into the solution of Fe and $FeCl_3$ mixture. Afterwards, the solvent was removed, and the final product was obtained by sublimation under vacuum at *ca*. 100°C.

IR, v ($cm^{-1}$): 1722 $cm^{-1}$, 1815 $cm^{-1}$.

EPR: g = 2.012 (2-MeTHF, 77K).

IR and EPR were consistent with previously reported data.[175]

### 2.1.11 Synthesis of $[C_1C_4Im][Fe(NO)_2Cl_2]$




1-Butyl-3-methylimidazolium chloride (2 g, 11.5 mmol) and $[Fe(NO)_2Cl]_2$ (1.74 g, 5.75 mmol) were mixed in a Schlenk flask under Ar atmosphere. After stirring for 12 h at room temperature (r.t.), a black liquid was obtained.

IR, ν ($cm^{-1}$): 1700 $cm^{-1}$, 1779 $cm^{-1}$.

Raman: 311 $cm^{-1}$, 507 $cm^{-1}$.

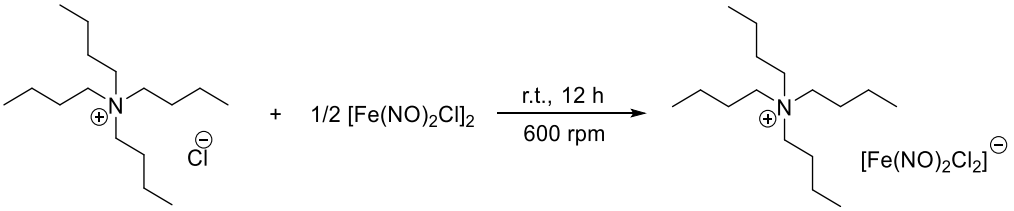
EPR: g = 2.012 (2-MeTHF, 77K).

Accurate mass $[M]^+$: Calc. 139.1230, Obs.: 139.1232.

Elemental Analysis: Calc. C, 29.48; H, 4.64; N, 17.19. Obs. C, 30.28; H, 4.62; N, 13.74.

ICP-OES (%weight): Calc. Fe, 17.13. Obs. Fe, 16.88.

### 2.1.12 Synthesis of $[n\text{-}Bu_4N][Fe(NO)_2Cl_2]$




Tetrabutylammonium chloride (100 mg, 0.912 mmol) and $[Fe(NO)_2Cl]_2$ (138.1 mg, 0.456 mmol) were mixed in a Schlenk flask under Ar atmosphere. After stirring overnight at r.t., a black liquid was obtained.

IR, ν ($cm^{-1}$): 1685 $cm^{-1}$, 1755 $cm^{-1}$.

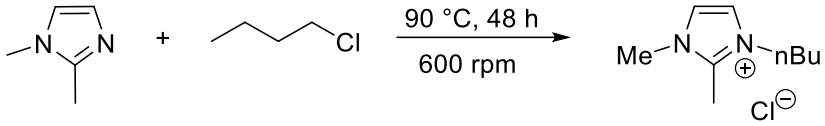
EPR: g = 2.014 (2-MeTHF, r.t.).

Accurate mass $[MH]^+$: Calc. 242.2842, Obs.: 242.2865.

Elemental Analysis: Calc. C, 44.77; H, 8.45; N, 9.79. Obs. C, 43.77; H, 8.37; N, 8.28.

ICP-OES (%weight): Calc. Fe, 13.01. Obs. Fe, 11.88.

### 2.1.13 Synthesis of $[C_1C_1C_4Im]Cl$



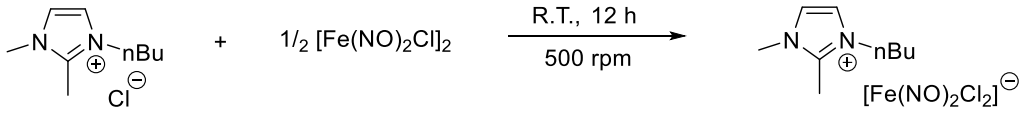

1,2-Dimethylimidazolium (99 ml, 1.02 mol) was added to 1-chlorobutane (117 ml, 1.12 mol) and the reaction mixture was heated under reflux at 90°C for 48 hours. Afterwards, the solution was cooled to r.t. and the volatile materials were evaporated under vacuum. The remaining orange oil was re-dissolved in 100 mL of dry acetonitrile and added dropwise via cannula to a well-stirred solution of ethyl acetate and one crystal seed of 1-butyl-2,3-dimethylimidazolium chloride. After the addition of the acetonitrile solution was completed, the mixture was cooled at -30°C in the freezer to crystallize. Then, the solvent was removed by filtration via cannula and the final product was washed with ethyl acetate to remove residual 1,2-dimethylimidazolium and dried under vacuum, obtaining a white powder.

$^1$H NMR (400 MHz, $CDCl_3$): δ 0.93-0.97 (3H, t, *J* = 7.4 Hz, $CH_2$-C*H*$_3$), 1.33-1.42 (2H, m, $CH_2$-C*H*$_2$-$CH_3$), 1.75-1.83 (2H, m, $CH_2$-C*H*$_2$-$CH_2$), 2.80 (3H, s, C-C*H*$_3$-N),

4.03 (3H, s, NC*H*$_3$), 4.20 (2H, t, *J* = 7.5 Hz, N-C*H*$_2$-CH$_2$), 7.49-7.50 (1H, d, *J* = 2.1 Hz, N-C*H*-CH-N), 7.80-7.81 (1H, d, *J* = 2.1 Hz, N-CH-C*H*-N).

$^1$H NMR data was consistent with those previously reported.[176]

### 2.1.14 Synthesis of $[C_1C_1C_4Im][Fe(NO)_2Cl_2]$




1-Butyl-2,3-dimethylimidazolium chloride (100 mg, 0.530 mmol) and $[Fe(NO)_2Cl]_2$ (80.2 mg, 0.265 mmol) were mixed in a Schlenk flask under Ar atmosphere. After stirring for 12 h at r.t., a black liquid was obtained.

IR, ν (cm$^{-1}$): 1534 cm$^{-1}$, 1584 cm$^{-1}$.

EPR: g = 2.014 (2-MeTHF, r.t.).

Accurate mass $[M]^+$: Calc. 153.1386, Obs.: 153.1396.

Elemental Analysis: Calc. C, 31.79; H, 5.04; N, 16.48. Obs. C, 32.58; H, 5.13; N, 14.31.

ICP-OES (%weight): Calc. Fe, 16.98. Obs. Fe, 16.43.

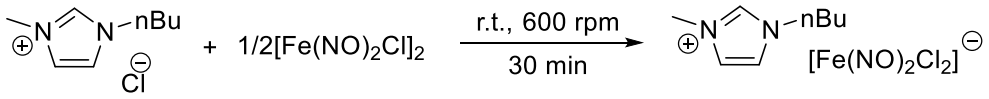
## 2.2 Halometallate ionic liquids with substituted ligands using nitrosyl

### 2.2.1 $[C_1C_4Im][Fe(NO)_2Cl_2]$

$[C_1C_4Im]Cl$ was synthesized through a nucleophilic addition of 1-chlorobutane to 1-methylimidazole,[27] whereas μ-dichloro-tetranitrosyl-diiron ($[Fe(NO)_2Cl]_2$) was prepared in a two-step synthesis (2.1.10 Synthesis of $[Fe(NO)_{2Cl}]_2$). Firstly, $FeCl_3$ and Fe(0) were heated under reflux in THF for 1 hour, followed by NO gas which, was bubbled into the solution.[175] The final step in the preparation is a

sublimation to purify the iron complex. However, this is also the step most limiting to the yield, which generally was quite low, making this a very challenging synthesis. The sublimation was carried out using a cold finger with a circulating cooling liquid (ethylene glycol) and a heating block to keep the temperature constant. As an alternative acetone and liquid nitrogen was used as a cooling agent to improve the overall yield, though this was not successful.

The new halometallate IL, $[C_1C_4Im][Fe(NO)_2Cl_2]$, was prepared through reaction of $[Fe(NO)_2Cl]_2$ with $[C_1C_4Im]Cl$ (Scheme 2-1).




*Scheme 2-1 Synthesis of $[C_1C_4Im]$ $[Fe(NO)_2Cl_2]$.*

The IL $[C_1C_4Im][Fe(NO)_2Cl_2]$ was fully characterised using a wide range of techniques, including TGA, EA, ICP-OES, ESI-MS, EPR, XPS, magnetic susceptibility measurements (8.7 Magnetization measurements), and ATR FT-IR and Raman spectroscopies.

*Table 2-1 Experimental and theoretical (in brackets) values for ICP-OES and ESI-MS for $[C_1C_4Im][Fe(NO)_2Cl_2]$.*

| **Sample** | **ICP-OES** | **ESI-MS** |
|---|---|---|
| **$[C_1C_4Im][Fe(NO)_2Cl_2]$** | 16.9% (17.1%) | 139.1232 (139.1230) |

Table 2-1 shows experimentally measured and theoretical values for ICP-OES and ESI-MS for $[C_1C_4Im][Fe(NO)_2Cl_2]$. All values are in good agreement with the theoretical value, which confirms the Fe content within the IL. In addition, the ESI-MS shows a very intense peak in the positive mode corresponding to the cation, namely the imidazolium moiety, confirming that the cation of the IL

precursor remains intact after the reaction with the iron complex. Furthermore, a low intensity peak with m/z = 464.1152 corresponding to $\{[C_1C_4Im]_2[Fe(NO)_2Cl_2]\}^+$ was observed (Appendix, 8.3 ESI-MS spectroscopy). Unfortunately, no significant information can be extracted from the ESI-MS spectrum in the negative mode with only a single peak corresponding to the $[Fe(NO)Cl_2]$ species being observed (Appendix, 8.3 ESI-MS spectroscopy). However, Estager *et al.* demonstrated, in a review on halometallate ILs, that mass spectrometry can often lead to wrong conclusions for anion speciation, as the measurement is carried out in gas phase and therefore does not represent the actual environment of the metal anion in its liquid form.[16]

$[C_1C_4Im][Fe(NO)_2Cl_2]$ (Figure 2-1) was analysed by Raman at room temperature using excitation wavelength of 785 nm. The presence of the iron-nitrosyl moiety in $[C_1C_4Im][Fe(NO)_2Cl_2]$ was confirmed by the Raman spectrum, which displayed a narrow peak at *ca*. 507 $cm^{-1}$ identified as the Fe–NO stretch vibration.[177-179] A second peak was present at *ca.* 311 $cm^{-1}$ that, is found to be a vibration frequency consistent of the symmetric stretching mode of the Fe–Cl bond.[41, 43, 180] The peak is shifted slightly to lower wavenumber, possibly due to a not perfectly symmetrical environment of the iron complex when compared to the $[FeCl_4]^-$.[181]

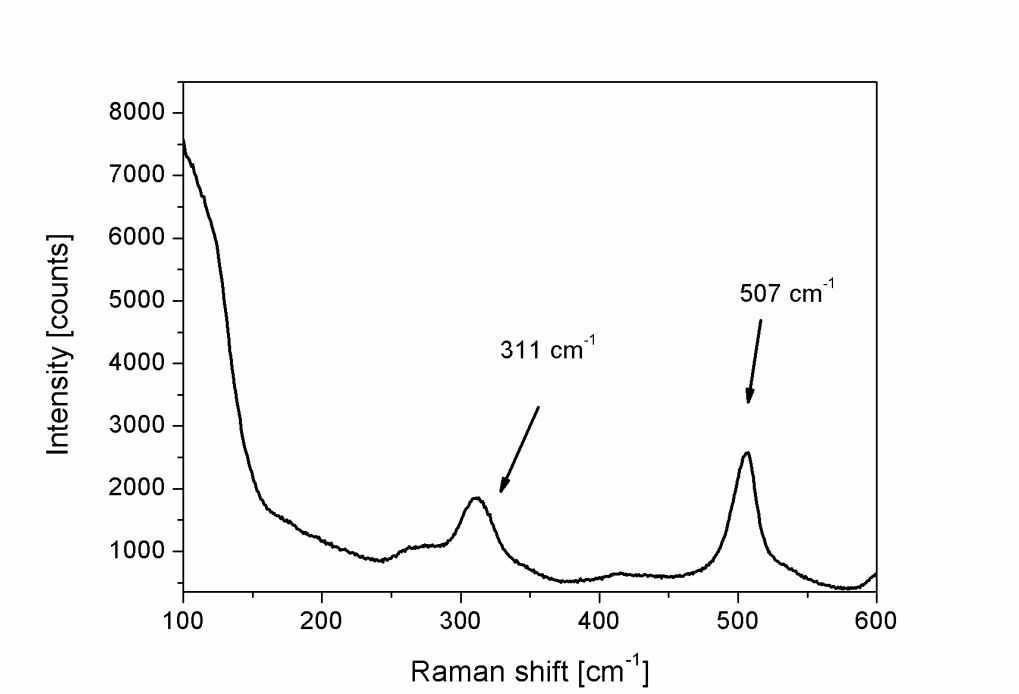



*Figure 2-1 Raman spectrum for $[C_1C_4Im][Fe(NO)_2Cl_2]$ measured at room temperature using excitation wavelength 785 nm.*

Vibrational spectroscopy is an important class of experimental techniques that can be used to probe the structure and bonding in metal-nitrosyl based complexes. Subtle shifts in the observed frequency of characteristic bands can be used to differentiate between binding modes, as a general guide, linear M–N–O groups absorb in the range 1650–1900 $cm^{-1}$ and bent M–N–O species in the range 1525–1690 $cm^{-1}$. The IR stretching frequency depends on the environment around the probe group which is sensitive to the nature of other ligands present in the complex, the overall electronic configuration of the metal, overall charge of the complex, and the geometry of the complex. In practice, it is often very difficult to draw a distinct conclusion from the type of IR stretching frequency and hence assign the absolute geometry of the M-N-O bond and a more extensive variety of spectroscopic methods could be necessary.[91]

The iron complex $[Fe(NO)_2Cl]_2$ and the corresponding IL $[C_1C_4Im][Fe(NO)_2Cl_2]$ were characterised by IR spectroscopy (Figure 2-2). Distinct peaks were found at 1722 $cm^{-1}$ and 1815 $cm^{-1}$ for $[Fe(NO)_2Cl]_2$ corresponding to NO valence vibrations.[175] The spectrum of $[C_1C_4Im][Fe(NO)_2Cl_2]$ shows peaks within the same region (1700 and 1779 $cm^{-1}$) but the vibrations were observed with higher intensity. $[Fe(NO)_2Cl]_2$ on its own is not stable for a very long time in air. However, decomposition of $[Fe(NO)_2Cl]_2$ seems to be hindered after reaction with $[C_1C_4Im]Cl$. In addition, comparable IR frequencies were reported for the compound $(Et_4N)[Fe(NO)_2Cl_2]$ (1765 and 1692 $cm^{-1}$) and therefore suggesting that a comparable dinitrosyl iron complex (DNIC) $[Fe(NO)_2Cl_2]^-$ is present in both complexes.[91, 182, 183]

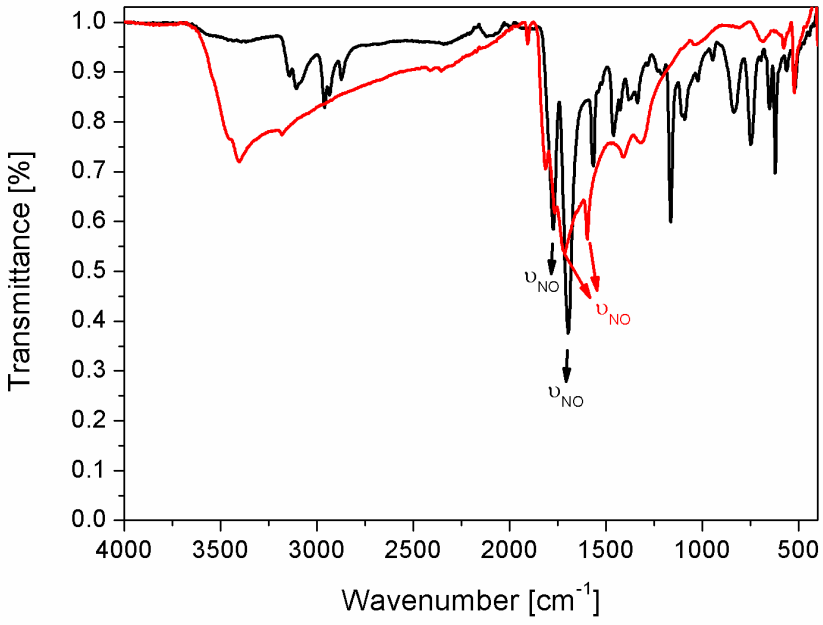



*Figure 2-2 Overlay of FT-IR spectra of $[Fe(NO)_2Cl]_2$ (red) and $[C_1C_4Im][Fe(NO)_2Cl_2]$ ( black).*

The decomposition temperature of $[C_1C_4Im][Fe(NO)_2Cl_2]$ was evaluated with TGA under nitrogen flow and a heating ramp of 10°C/min from room

temperature until 1000°C. Figure 2-3 shows the thermogram for $[C_1C_4Im][Fe(NO)_2Cl_2]$. The decomposition onset temperature was found to be 125°C and the final mass loss at 1000°C was found to be 81.4 wt%. The decomposition appeared in a two-step mass loss. The remaining 18.6 wt% corresponds to the expected iron content (17.1 wt%) for the $[C_1C_4Im][Fe(NO)_2Cl_2]$ IL.

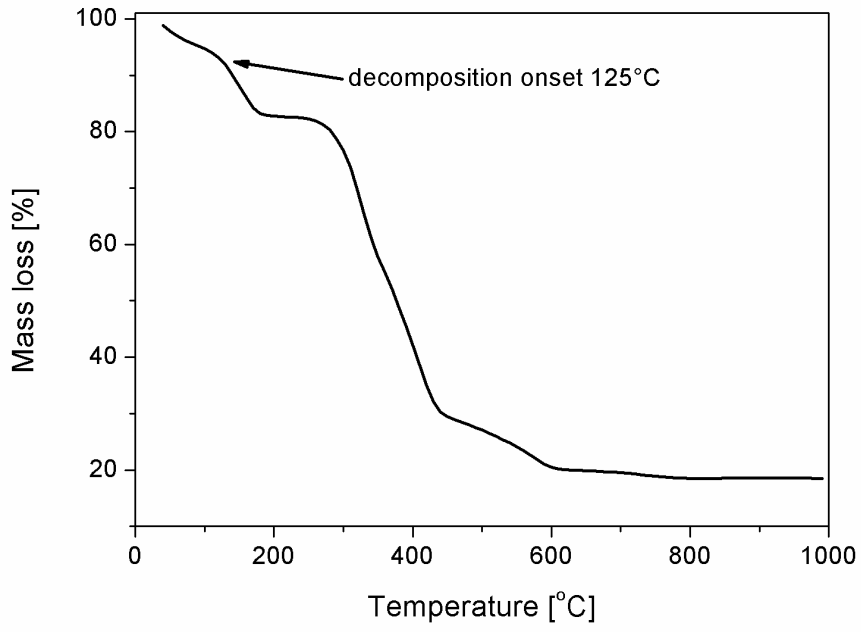



*Figure 2-3 Thermogram obtained with TGA under nitrogen flow for $[C_1C_4Im][Fe(NO)_2Cl_2]$ at a ramp of 10°C/min.*

Electron paramagnetic resonance spectroscopy (EPR), often also referred to as electron spin resonance spectroscopy (ESR), is used to investigate paramagnetic centres. Each paramagnetic species has its own distinct spectrum with well-defined spin Hamiltonian parameters.[184] EPR measurements were carried out for the iron complex $[Fe(NO)_2Cl]_2$ and the IL $[C_1C_4Im][Fe(NO)_2Cl_2]$ in 2-methyltetrahydrofuran (2-MeTHF), to confirm the

existence of unpaired electrons as well as the formation of a monomer $[Fe(NO)_2Cl_2]$ from the dimer $[Fe(NO)_2Cl]_2$ after reaction with $[C_1C_4Im]Cl$.

Figure 2-4 shows the EPR spectrum of $[Fe(NO)_2Cl]_2$ at 77K dissolved in 2-MeTHF. Ballivet-Tkatchenko *et al.* reported an EPR spectrum of the same complex dissolved in THF which is comparable to the signal shape of Figure 2-4.[175] However, under this condition no hyperfine structure was visible but new peaks were observed at a lower field. Van Eldik *et al.* reported a similar spectrum of an iron nitrosyl species dissolved in an IL.[185]

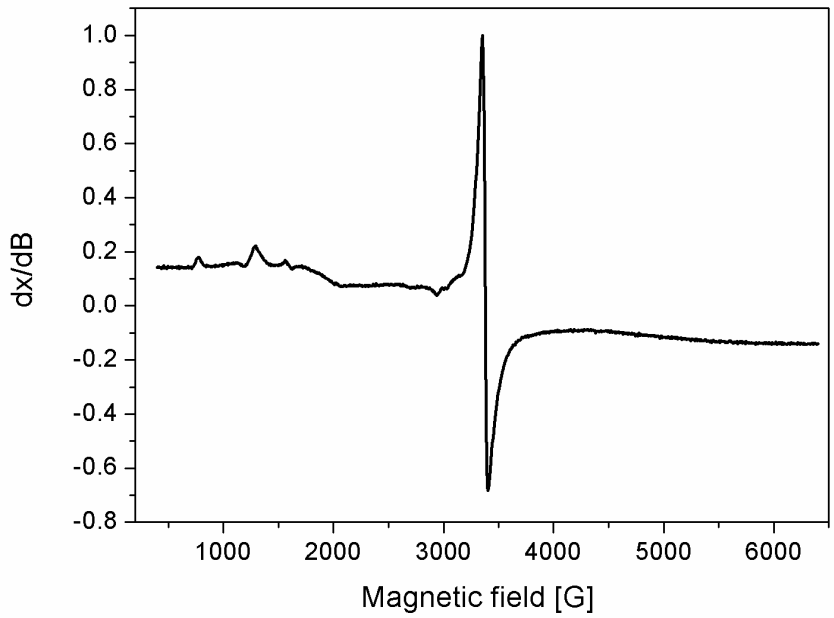



*Figure 2-4 EPR spectrum of $[Fe(NO)_2Cl]_2$ at 77K dissolved in 2-MeTHF.*

The EPR spectrum for $[C_1C_4Im][Fe(NO)_2Cl_2]$ (Figure 2-5) shows a similar g-value and shape as $[Fe(NO)_2Cl]_2$ (Figure 2-4). Furthermore, at lower field, an additional peak was observed for $[C_1C_4Im][Fe(NO)_2Cl_2]$ (Figure 2-6) similarly to $[Fe(NO)_2Cl]_2$ (Figure 2-4).

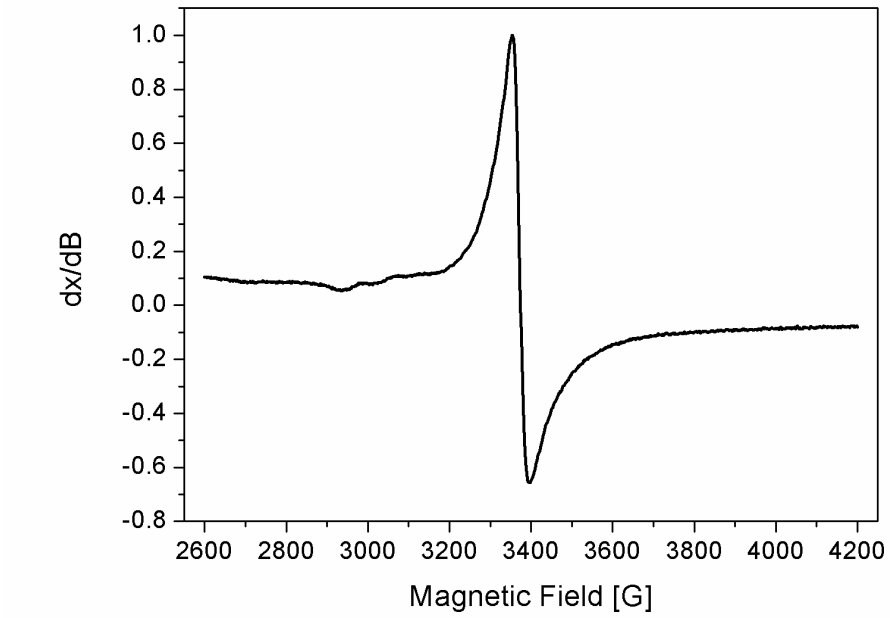



*Figure 2-5 EPR spectrum for $[C_1C_4Im][Fe(NO)_2Cl_2]$ at 77K and dissolved in 2-MeTHF.*

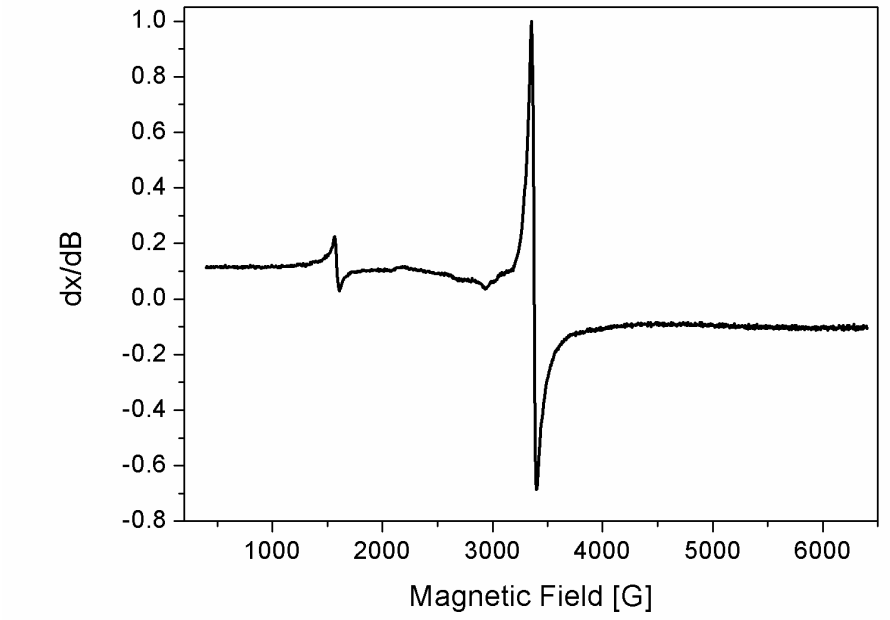



*Figure 2-6 EPR spectrum of $[C_1C_4Im][Fe(NO)_2Cl_2]$ at 77K dissolved in 2-MeTHF measured at a wide magnetic field.*

Even though 2-MeTHF is a less coordinating solvent than for example THF, due to steric hindrance, it is not possible to completely rule out potential

coordination of the solvent with the iron complex. Therefore, an EPR spectrum of the IL $[C_1C_4Im][Fe(NO)_2Cl_2]$ diluted in $[C_1C_4Im]Cl$ was recorded (Figure 2-7). The spectrum shows a signal like the previously shown spectra and a similar g-value was calculated. All g-values are summarized in Table 2-2 and no significant difference can be detected comparing the different samples. All g-values were calculated using the following Equation,

$$hv = g\beta B \qquad [2\text{-}1]$$

where *ß* is the Bohr Magnetron, *h* the Planck constant and *υ* the frequency.

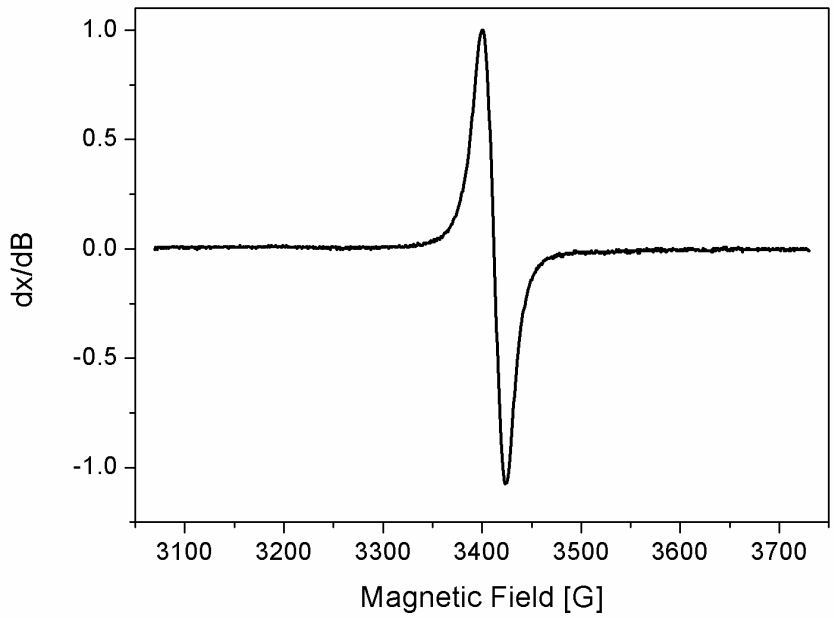



*Figure 2-7 EPR spectrum of $[C_1C_4Im][Fe(NO)_2Cl_2]$ at room temperature diluted in $[C_1C_4Im]Cl$.*

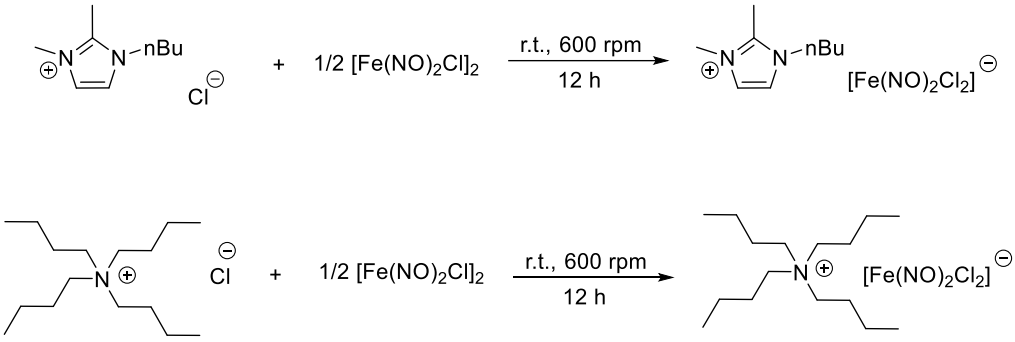
*Table 2-2 g-values from EPR spectroscopy for metal-containing ILs.*

| Sample | B (mT) | MF (GHz) | g |
|---|---|---|---|
| **$[Fe(NO)_2Cl]_2$/2-MeTHF 77 K** | 336.976 | 9.49 | 2.012 |
| **$[C_1C_4Im][Fe(NO)_2Cl_2]$/2-MeTHF 77 K** | 336.976 | 9.49 | 2.012 |

| | | | |
|---|---|---|---|
| **$[C_1C_4Im][Fe(NO)_2Cl_2]$ diluted in $[C_1C_4Im]Cl$ r.t.** | 341.128 | 9.716 | 2.035 |

## 2.2.2 $[C_1C_1C_4Im][Fe(NO)_2Cl_2]$ and $[(n\text{-}Bu)_4N][Fe(NO)_2Cl_2]$

$[C_1C_1C_4Im][Fe(NO)_2Cl_2]$ and $[(n\text{-}Bu)_4N][Fe(NO)_2Cl_2]$ were prepared (Scheme 2-2) at room temperature and stirring until a homogeneous solution was obtained (approximately 12h).




*Scheme 2-2 Synthesis of $[C_1C_1C_4Im][Fe(NO)_2Cl_2]$ and $[(n\text{-}Bu)_4N][Fe(NO)_2Cl_2]$.*

$[C_1C_1C_4Im][Fe(NO)_2Cl_2]$ and $[(n\text{-}Bu)_4N][Fe(NO)_2Cl_2]$ are new compounds and characterisation included ATR FT-IR spectroscopy, EPR, EA, ICP-OES, and ESI-MS.

*Table 2-3 Experimental and theoretical (in parenthesis) values for ICP-OES and ESI-MS for $[C_1C_1C_4Im][Fe(NO)_2Cl_2]$, and $[(n\text{-}Bu)_4N][Fe(NO)_2Cl_2]$.*

| Sample | ICP-OES | ESI-MS |
|---|---|---|
| **$[C_1C_1C_4Im][Fe(NO)_2Cl_2]$** | 16.4% (17.0%) | 153.1396 (153.1386) |
| **$[n\text{-}Bu_4N][Fe(NO)_2Cl_2]$** | 11.9% (13.0%) | 242.2865 (242.2842) |

Table 2-3 shows experimentally measured and theoretical values for ICP-OES and ESI-MS for $[C_1C_1C_4Im][Fe(NO)_2Cl_2]$ and $[(n\text{-}Bu)_4N][Fe(NO)_2Cl_2]$. All values

are in good agreement with the theoretical value, which confirms the Fe content within the IL. In addition, the ESI-MS shows a very intense peak in the positive mode corresponding to the cation, namely the imidazolium and tetrabutylammonium moiety, and therefore suggests that the cationic part of the IL precursor stays intact after the dissolution of the iron complex.

Figure 2-8 and Figure 2-9 show the FT-IR spectra with the NO vibrations for $[(n\text{-Bu})_4N][Fe(NO)_2Cl_2]$ at 1684 and 1754 $cm^{-1}$ and for $[C_1C_1C_4Im][Fe(NO)_2Cl_2]$ at 1592 and 1541 $cm^{-1}$. The difference observed in the IR frequencies are associated to the distinct cation, as the electron charge distribution of the MNO moiety is very sensitive regarding the geometry of the coordination sphere, the total charge of the complex, and the surrounding ligands.[91]

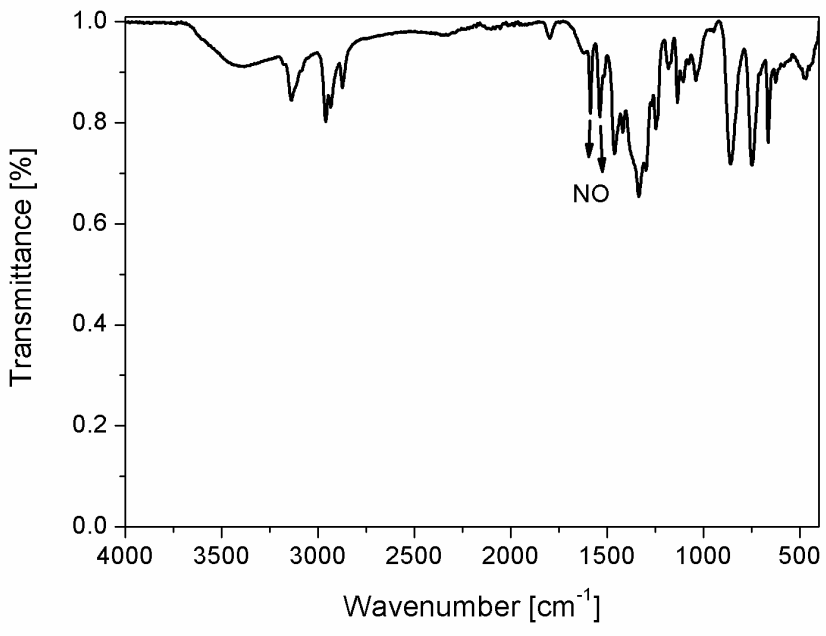



*Figure 2-8 FT-IR spectrum of $[C_1C_1C_4Im][Fe(NO)_2Cl_2]$ measured at room temperature.*

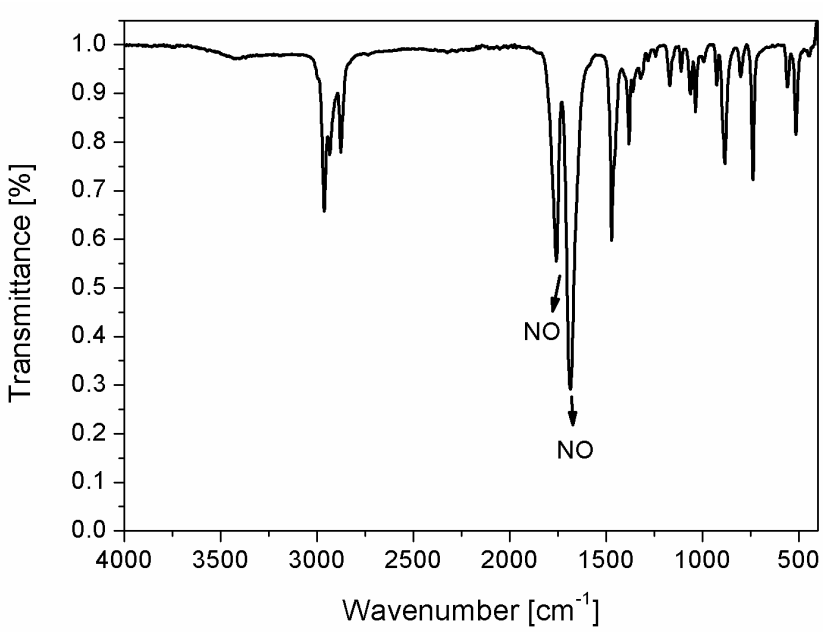



*Figure 2-9 FT-IR spectrum of [(n-Bu)$_4$N][Fe(NO)$_2$Cl$_2$] measured at room temperature.*

Figure 2-10 and Figure 2-11 display EPR spectra for [(*n*-Bu)$_4$N][Fe(NO)$_2$Cl$_2$] and [C$_1$C$_1$C$_4$Im][Fe(NO)$_2$Cl$_2$] respectively. Both signal shapes and g-values match that of the previously discussed IL [C$_1$C$_4$Im][Fe(NO)$_2$Cl$_2$] (Figure 2-5) hence suggesting the presence of the same DNIC [Fe(NO)$_2$Cl$_2$]. All g-values, calculated using Equation [2-1], are displayed in Table 2-4.

*Table 2-4 g-values from EPR spectroscopy for metal containing ILs.*

| **Sample** | **B (mT)** | **MF (GHz)** | **g** |
|---|---|---|---|
| **[(*n*-Bu)$_4$N][Fe(NO)$_2$Cl$_2$]/2-MeTHF r.t.** | 345.663 | 9.743 | 2.014 |
| **[C$_1$C$_1$C$_4$Im][Fe(NO)$_2$Cl$_2$]/ 2-MeTHF r.t.** | 345.724 | 9.745 | 2.014 |

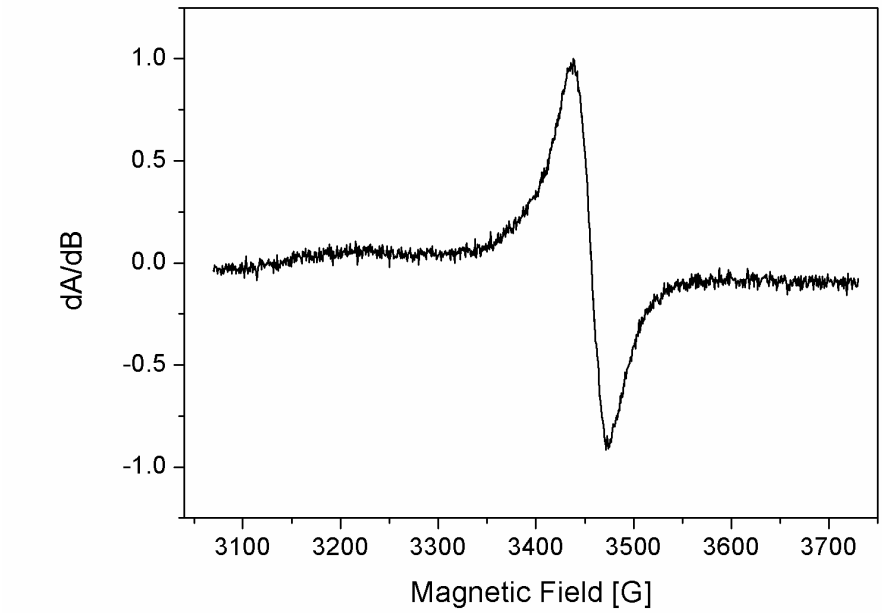



*Figure 2-10 EPR spectrum of $[C_1C_1C_4Im][Fe(NO)_2Cl_2]$ recorded in 2-MeTHF at room temperature.*

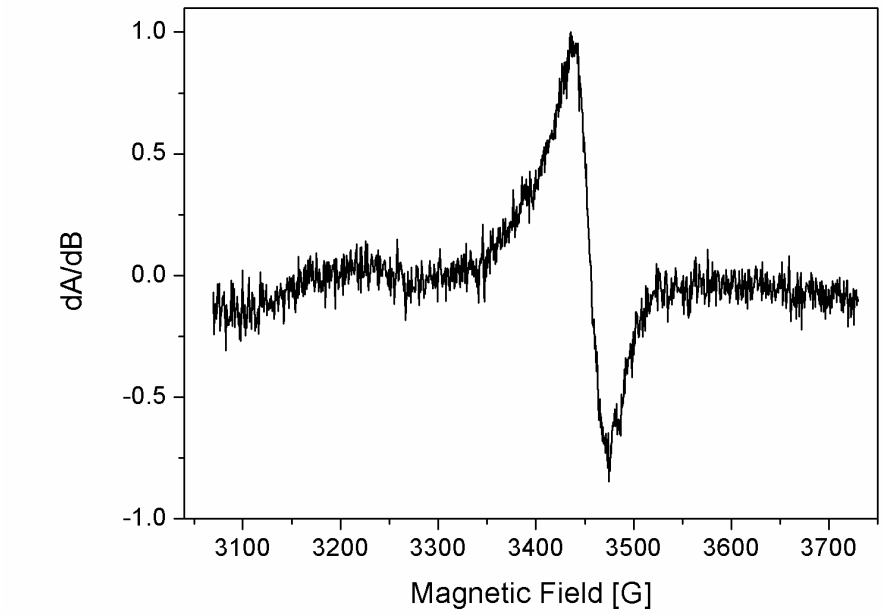
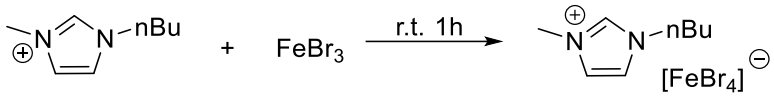



*Figure 2-11 EPR spectrum of $[(n\text{-}Bu)_4N][Fe(NO)_2Cl_2]$ recorded in 2-MeTHF at room temperature.*

### 2.2.3 $[C_1C_4Im][FeBr_4]$

$[C_1C_4Im]Br$ was prepared according to literature procedures[173] (see Appendix, 2.1.2 Synthesis of [C1C4Im]Br) and $[C_1C_4Im][FeBr_4]$ (Scheme 2-3) was obtained by mixing $[C_1C_4Im]Br$ and $FeBr_3$ under an inert atmosphere for approximately 1h until a homogeneous solution was achieved. The synthesis was adapted from the procedure used for $[C_1C_4Im][FeCl_4]$ (2.3.1 [C1C4Im][FeCl4]).




*Scheme 2-3 Synthesis of $[C_1C_4Im][FeBr4]$ at room temperature and under inert atmosphere.*

$[C_1C_4Im][FeBr_4]$ is a known compound and synthesis was confirmed by ATR FT-IR spectroscopy, EA, and ESI-MS.

*Table 2-5 Experimental and theoretical (in parenthesis) values for ESI-MS for $[C_1C_4Im][FeBr_4]$.*

| **Sample** | **ESI-MS** |
|---|---|
| **$[C_1C_4Im][FeBr_4]$** | 139.1223 (139.1230) |

Figure 2-12 displays the FT-IR spectrum for $[C_1C_4Im][FeBr_4]$ measured at room temperature. Low field bands appearing around 780 $cm^{-1}$ correspond to the butyl and methyl chain of the imidazolium moiety. Three sharp bands at 1560, 1675 and 1780 $cm^{-1}$ correspond to the imidazolium moiety as well as broader bands around 2800 $cm^{-1}$. A very broad peak at 3400 $cm^{-1}$ belongs to the aromatic =NH vibration.

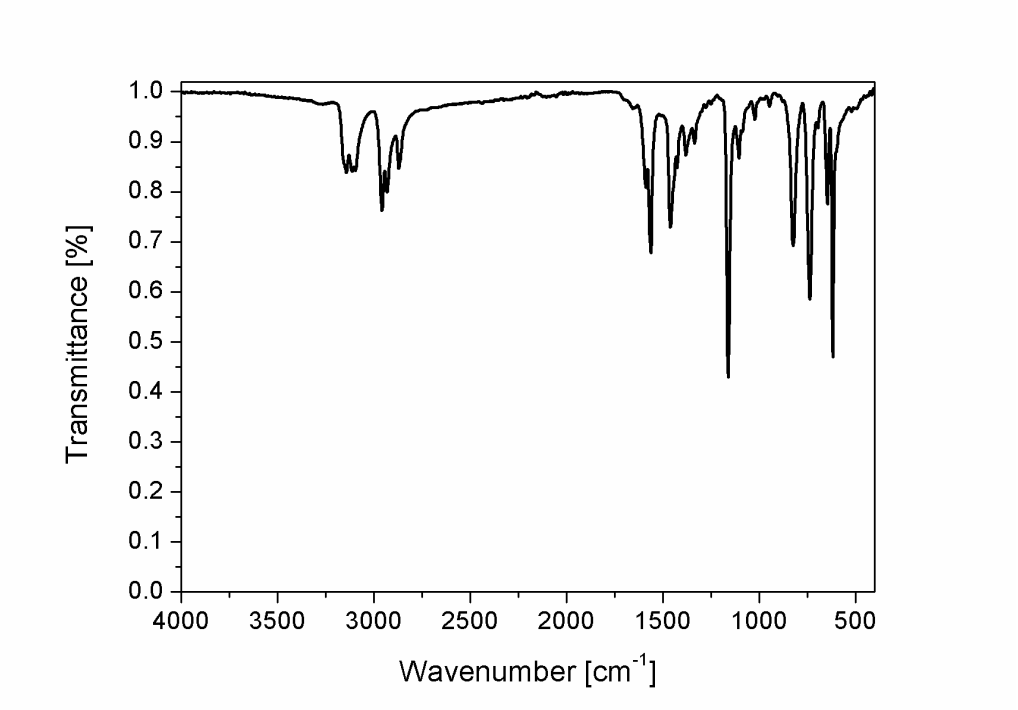
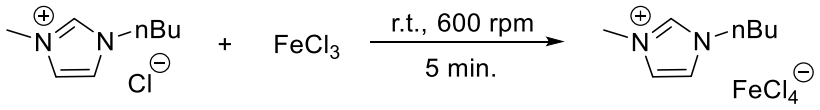



*Figure 2-12 FT-IR spectrum for $[C_1C_4Im][FeBr_4]$ measured at room temperature.*

## 2.3 Conventional halometallate ionic liquids

### 2.3.1 $[C_1C_4Im][FeCl_4]$

For the preparation of $[C_1C_4Im][FeCl_4]$ (Scheme 2-4), $[C_1C_4Im]Cl$ was stirred with an equimolar amount of anhydrous $FeCl_3$ for five minutes under an inert atmosphere. The reaction occurs spontaneously upon bringing the two solids together and is exothermic, as also shown by Taubert *et al.*.[37]




*Scheme 2-4 Synthesis of $[C_1C_4Im][FeCl_4]$ at room temperature and under an inert atmosphere.*

Figure 2-13 shows the Raman spectrum for $[C_1C_4im][FeCl_4]$ measured at room temperature using excitation wavelength 785 nm displaying a distinct peak at 334 $cm^{-1}$. Comparison with literature data[186] confirmed this peak as the symmetrical stretch vibration of the $[FeCl_4]^-$ anion. A second peak was detected

at 111 $cm^{-1}$ which was reported by Garcia-Saiz *et al*.[36] as symmetrical bending vibration corresponding to the Fe-Cl bond.

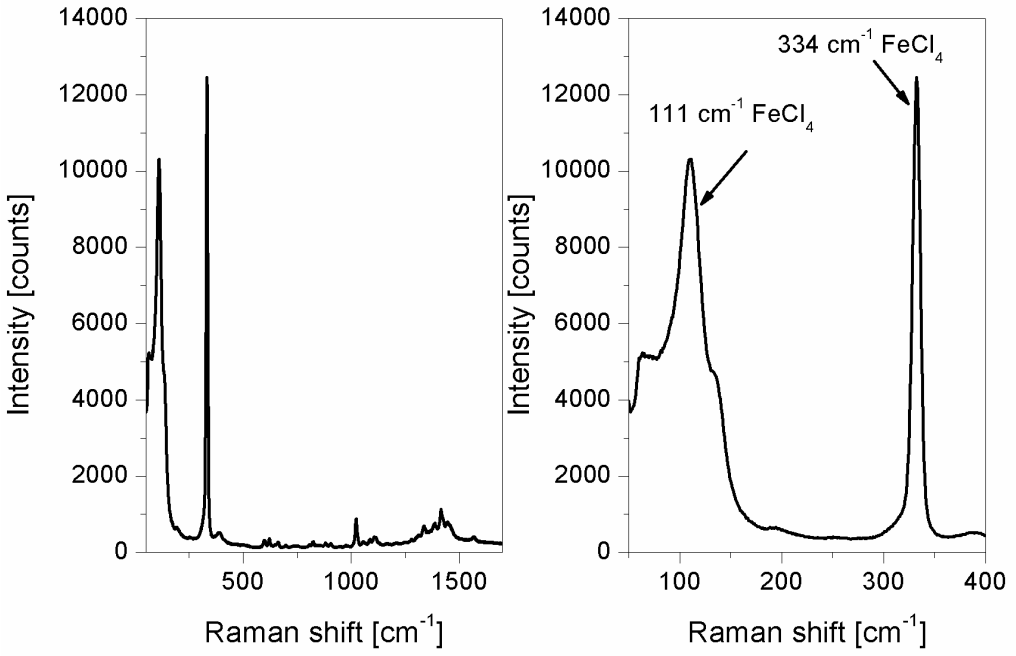



*Figure 2-13 Raman spectrum of [$C_1C_4$Im][ $FeCl_4$] measured at room temperature and excitation wavelength 785 nm. On the left a full range spectrum is displayed and, on the right, the same spectrum in the range 50 to 400 $cm^{-1}$.*

The decomposition temperature of [$C_1C_4$im][$FeCl_4$] (Figure 2-14) was obtained using TGA. The decomposition onset temperature was found to be 371°C and the residual mass at 1000°C was found to be 10 wt%.

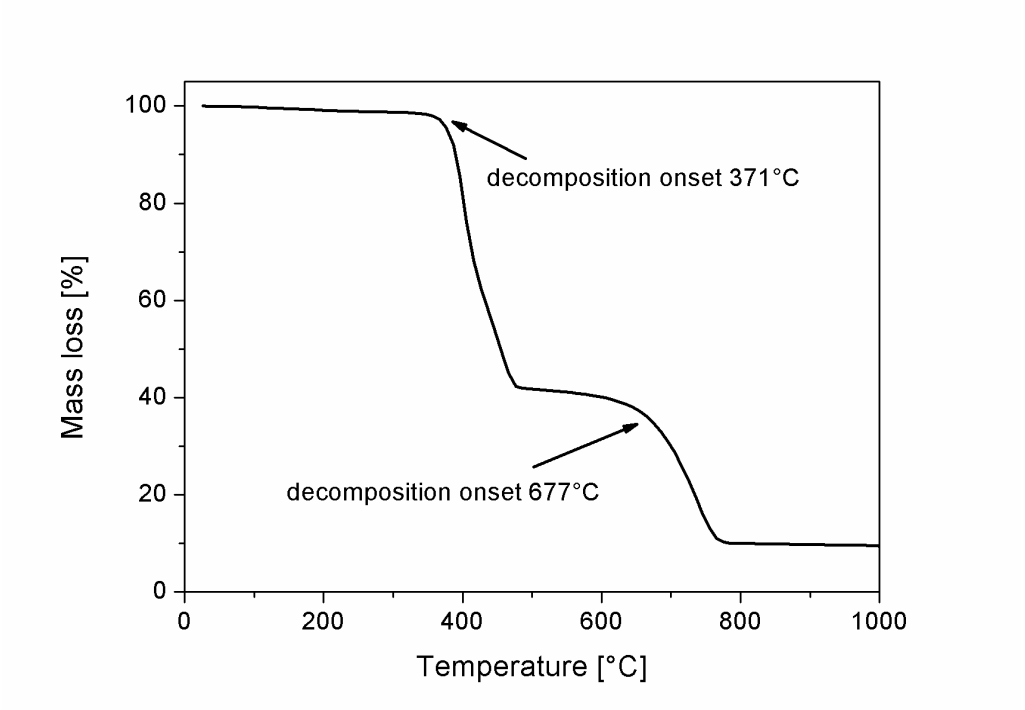



*Figure 2-14 Thermogram obtained from TGA under nitrogen flow gas for [$C_1C_4$Im][$FeCl_4$].*

Figure 2-15 shows the thermogram obtained from DSC for [$C_1C_4$Im][$FeCl_4$] at a heating rate of 10°C/min and two cycles. After cooling the sample and starting the first heating ramp a crystallisation peak is observed at -60°C, which is followed by melting of the sample at 0°C. This behaviour repeats itself in the second cycle.

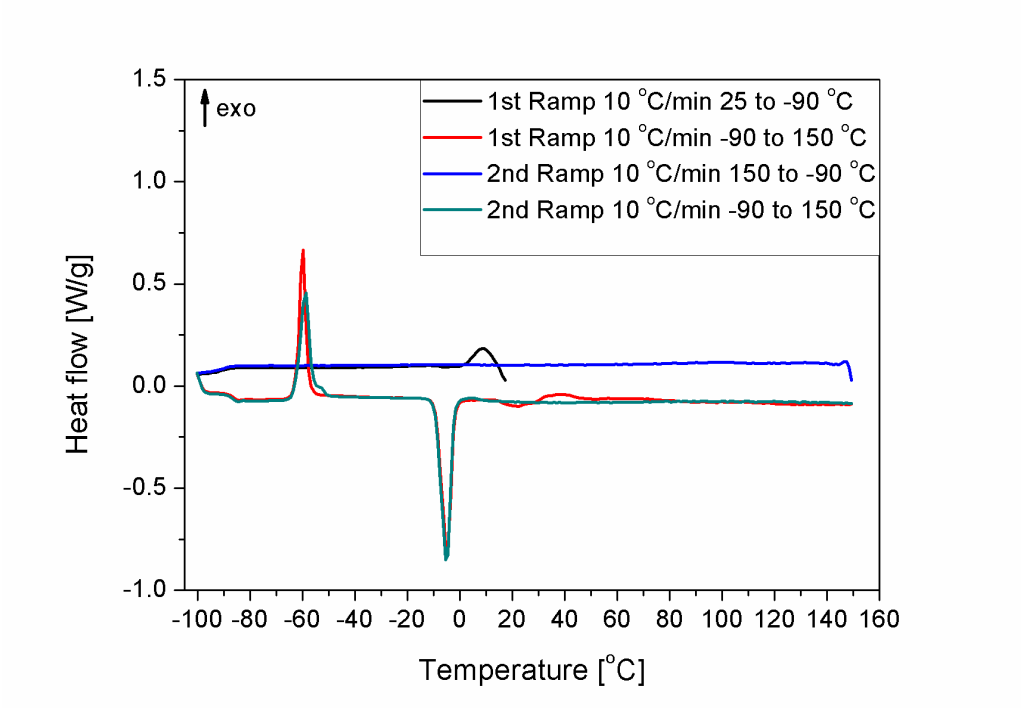


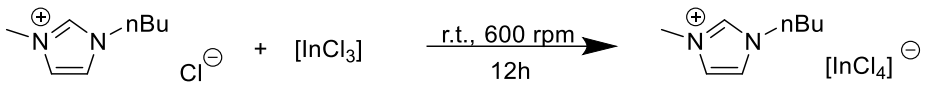

*Figure 2-15 Thermogram obtained from DSC for $[C_1C_4Im][FeCl_4]$ at a heating rate of 10°C/min and in a range from -90°C to 150°C.*

*Table 2-6 Crystallisation $T_c$, melting $T_m$ and glass transition temperatures $T_g$ for $[C_1C_4Im][FeCl_4]$.*

| | $T_c$ [°C] | $\Delta H(T_c)$ [J/g] | $T_m$ [°C] | $\Delta H(T_m)$ [J/g] | $T_g$ [°C] |
|---|---|---|---|---|---|
| **1st cooling ramp** | | | | | |
| **1st heating ramp** | -60 | 35 | 0 | 47 | |
| **2nd cooling ramp** | | | | | |
| **2nd heating ramp** | -60 | 49 | 0 | 47 | |

### 2.3.2 $[C_1C_4Im][InCl_4]$

For the preparation of $[C_1C_4Im][InCl_4]$ (Scheme 2-5), $[C_1C_4Im]Cl$ was stirred with an equimolar amount of anhydrous $InCl_3$ for 12 hours under an inert atmosphere to yield a clear liquid.[114]




*Scheme 2-5 Synthesis of [$C_1C_4$Im][$InCl_4$] at room temperature and under an inert atmosphere.*

Unfortunately, it was not possible to obtain a satisfactory Raman spectrum. Although a $^{115}$In NMR was obtained and confirmed the formation of [$C_1C_4$Im][$InCl_4$] (Appendix, 8.4 Nuclear magnetic resonance spectroscopy).[114]

Figure 2-16 depicts the thermogram for [$C_1C_4$Im][$InCl_4$] obtained from TGA. Decomposition appears in a one-step process with an onset decomposition temperature of 357°C. A residual of 2 wt% was observed at 1000°C. Similar thermal behaviour was also observed by Varma *et al.*.[157]

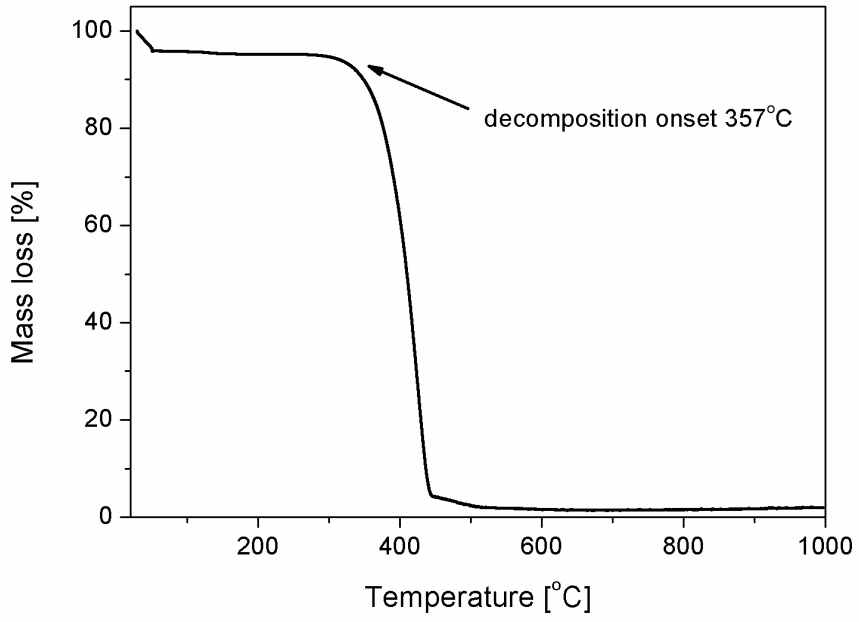



*Figure 2-16 Thermogram obtained from TGA under nitrogen flow gas for [$C_1C_4$Im][$InCl_4$].*

A thermogram (Figure 2-17) for [$C_1C_4$Im][$InCl_4$] was obtained from DSC with a heating rate of 10°C/min and a temperature range of -90 to 150°C. Upon cooling a crystallisation peak ($T_c$ = 11°C) is noted and a corresponding melting

peak ($T_m$ = -14°C) was observed upon heating. A glass transition appeared at -83°C in both heating ramps. The second heating ramp shows an endothermic peak again at -14°C, demonstrating a reversible system. However, it is noted that the enthalpy of melting is much higher than the enthalpy of crystallization indicating that the sample is amorphous and did not crystallize.

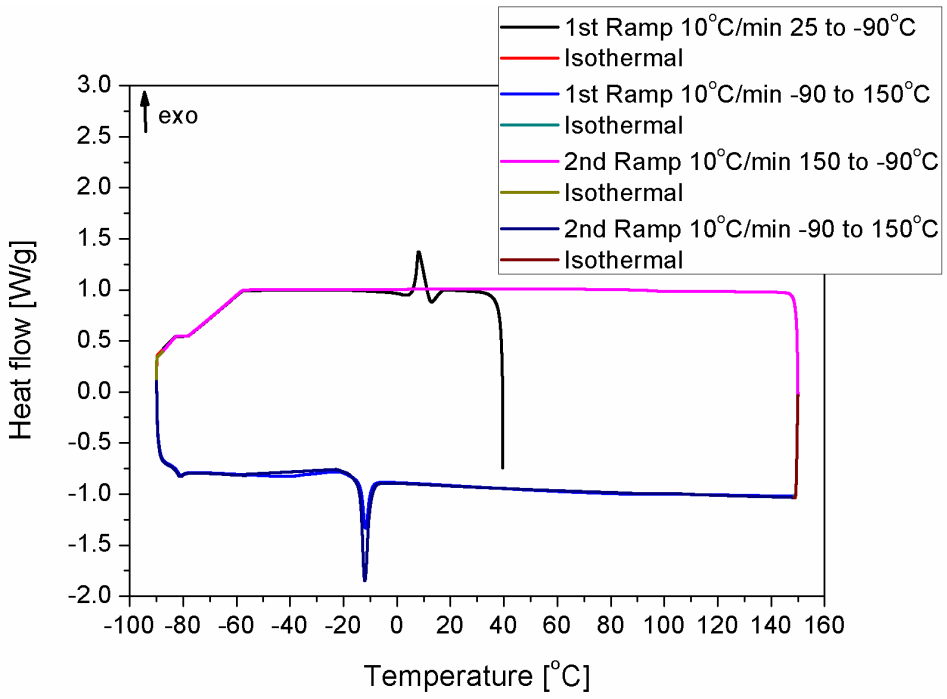


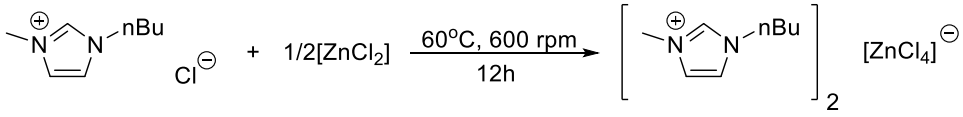

*Figure 2-17 Thermogram obtained from DSC for $[C_1C_4Im][InCl_4]$ at a heating rate of 10°C/min and in a range from -90°C to 150°C.*

*Table 2-7 Crystallisation $T_c$, melting $T_m$ and glass transition temperatures $T_g$ for $[C_1C_4Im][InCl_4]$.*

| | $T_c$ [°C] | $\Delta H(T_c)$ [J/g] | $T_m$ [°C] | $\Delta H(T_m)$ [J/g] | $T_g$ [°C] |
|---|---|---|---|---|---|
| **1st cooling ramp** | 11 | 2 | | | |
| **1st heating ramp** | | | -14 | 10 | -83 |
| **2nd cooling ramp** | | | | | |
| **2nd heating ramp** | | | -14 | 19 | -83 |

### 2.3.3 $[C_1C_4Im]_2[ZnCl_4]$

$[C_1C_4Im]_2[ZnCl_4]$ (Scheme 2-6) was prepared using $[C_1C_4Im]Cl$ and 0.5 mol equivalents of $ZnCl_2$, which were mixed together in an inert atmosphere and stirred at 60°C for 12 hours to yield a white solid. The preparation method was adapted from the literature.[114]




*Scheme 2-6 Preparation of $[C_1C_4Im]_2[ZnCl_4]$ at 60°C under an inert atmosphere.*

Figure 2-18 shows a full range Raman spectrum (left) from 200-2000 $cm^{-1}$ and a smaller range of (right) 190-320 $cm^{-1}$ highlighting significant bands for $[C_1C_4Im]_2[ZnCl_4]$. The spectrum was recorded at room temperature and excitation wavelength of 785 nm. Roisnel *et al.* described three bands corresponding to the Zn-Cl vibration frequencies at 230, 263 and 278 $cm^{-1}$ for $[C_7H_{16}N_2][ZnCl_4]$.[187] For $[C_1C_4Im]_2[ZnCl_4]$ vibration frequencies at 230 and 275 $cm^{-1}$ consistent with tetrahedral $[ZnCl_4]^{2-}$ were observed. In addition, Tyrrell *et al.* found a band for $[C_1C_8Im]_2[ZnCl_4]$ at 275 $cm^{-1}$ attributing to $[ZnCl_4]^{2-}$.[73] Furthermore, Rubim *et al.* described $[C_1C_4Im]_2[ZnCl_4]$ coherent with the bands observed in this work.[118]

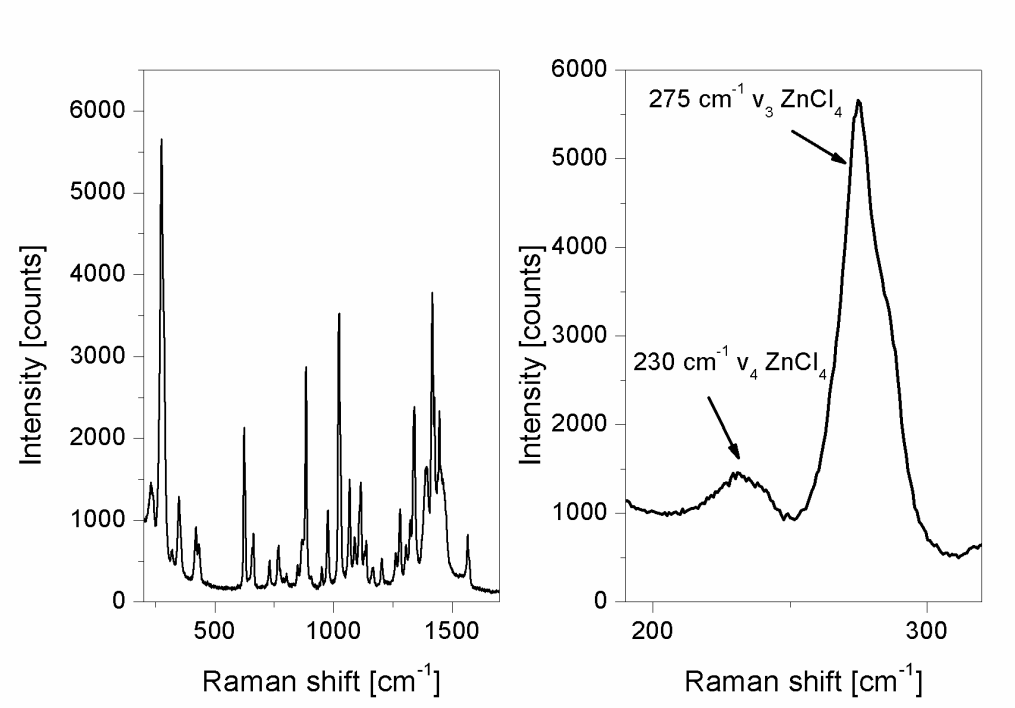



*Figure 2-18 Raman spectrum for $[C_1C_4Im]_2[ZnCl_4]$ at excitation wavelength 785 nm and room temperature. On the left a full range spectrum is displayed and, on the right, the same spectrum in the range 150 to 350 $cm^{-1}$.*

The decomposition temperature for $[C_1C_4Im]_2[ZnCl_4]$ was determined using TGA (Figure 2-19) and was measured to be 291°C. Decomposition appeared in a one-step process, coinciding with the melting temperature of pure $ZnCl_2$.[188] A residual of 4 wt% was observed, possibly due to the formation of zinc oxide or residual zinc metal.

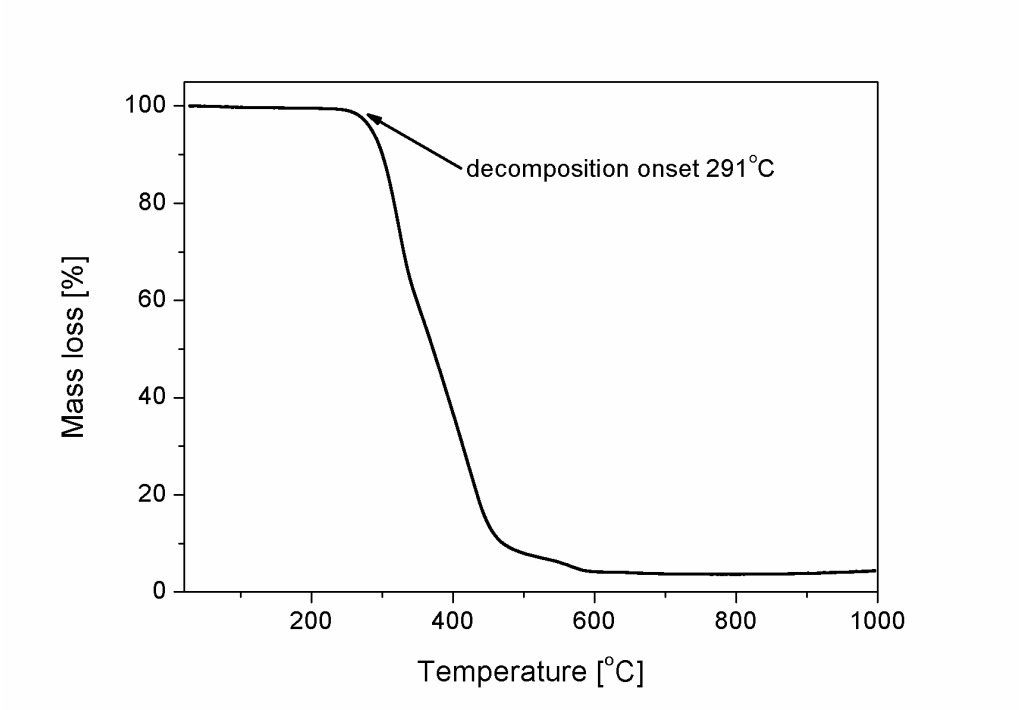



*Figure 2-19 Thermogram obtained from TGA under nitrogen flow gas for $[C_1C_4Im]_2[ZnCl_4]$.*

Figure 2-20 shows the thermogram obtained from DSC for $[C_1C_4Im]_2[ZnCl_4]$. Upon cooling a peak is observed at 11°C, which has a corresponding melting peak upon heating at 53°C. It can be noted that the enthalpy of melting is much higher than the enthalpy of crystallization indicating that the sample is amorphous and did not crystallize. The second heating ramp also displays a glass transition at -49°C. All phase transitions are presented in Table 2-8.

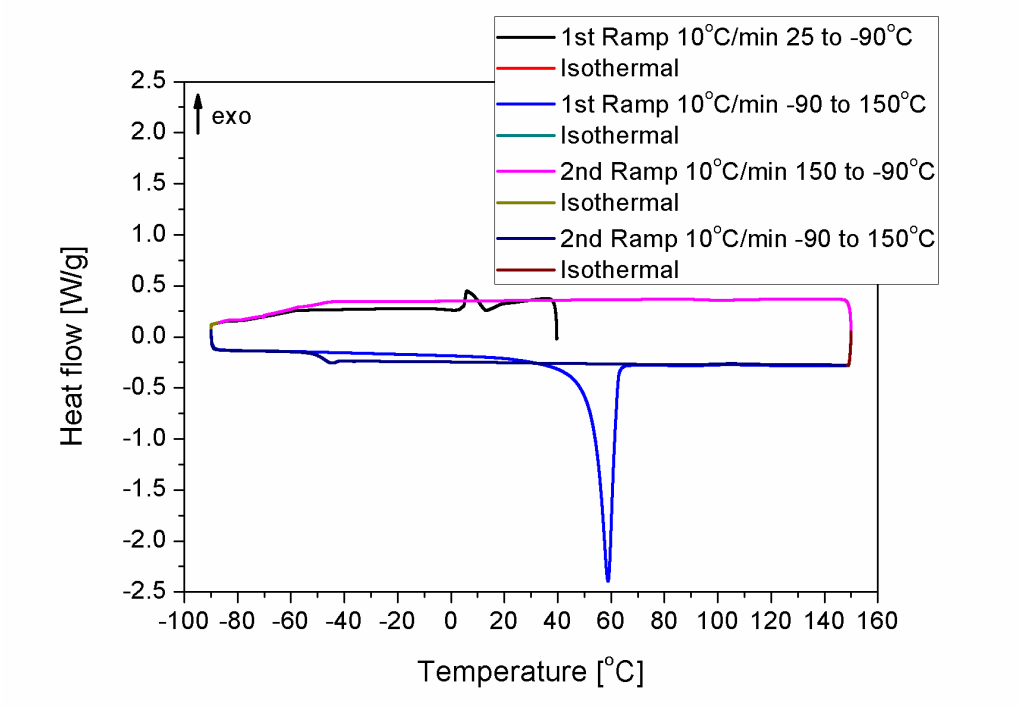


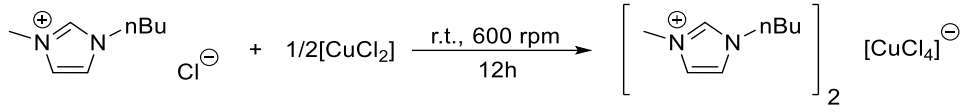

*Figure 2-20 Thermogram obtained from DSC for $[C_1C_4Im]_2[ZnCl_4]$ at a heating rate of 10°C/min and in a range from -90°C to 150°C.*

*Table 2-8 Crystallisation Tc, melting Tm and glass transition temperatures Tg for $[C_1C_4Im]_2[ZnCl_4]$.*

| | $T_c$ [°C] | $\Delta H(T_c)$ [J/g] | $T_m$ [°C] | $\Delta H(T_m)$ [J/g] | $T_g$ [°C] |
|---|---|---|---|---|---|
| **1st cooling ramp** | 11 | 1 | | | |
| **1st heating ramp** | | | 53 | 96 | |
| **2nd cooling ramp** | | | | | |
| **2nd heating ramp** | | | | | -49 |

### 2.3.4 $[C_1C_4Im]_2[CuCl_4]$

The synthesis of $[C_1C_4Im]_2[CuCl_4]$ (Scheme 2-7) was carried out using 0.5 mol equivalents of $CuCl_2$ which were mixed with $[C_1C_4Im]Cl$ in an inert atmosphere and stirred at room temperature for 12 hours. A brown, viscous liquid was obtained. The preparation method was adapted from the literature.[114]




*Scheme 2-7 Preparation of $[C_1C_4Im]_2[CuCl_4]$ at room temperature under an inert atmosphere.*

Figure 2-21 shows the Raman spectrum for $[C_1C_4Im]_2[CuCl_4]$ in the range 200-2000 $cm^{-1}$ (left) and 200-400 $cm^{-1}$ (right). The spectrum was measured at room temperature and excitation wavelength of 785 nm. On the right, the band for the symmetric ($\upsilon_1$) and asymmetric ($\upsilon_3$) stretching mode of the tetrahedral $[CuCl_4]^{2-}$ are observed at 275 and 300 $cm^{-1}$. Both bands overlap noticeably through a shoulder towards higher wavenumber. Rhaiem *et al.* reported a Raman spectrum for $[N(CH_3)_3H]_2[CuCl_4]$ displaying similar bands for the tetrahedral anion.[189] Above 400 $cm^{-1}$ (Figure 2-21, left) bands for $[C_1C_4Im]^+$ are visible, as previously reported in the literature.[190, 191]

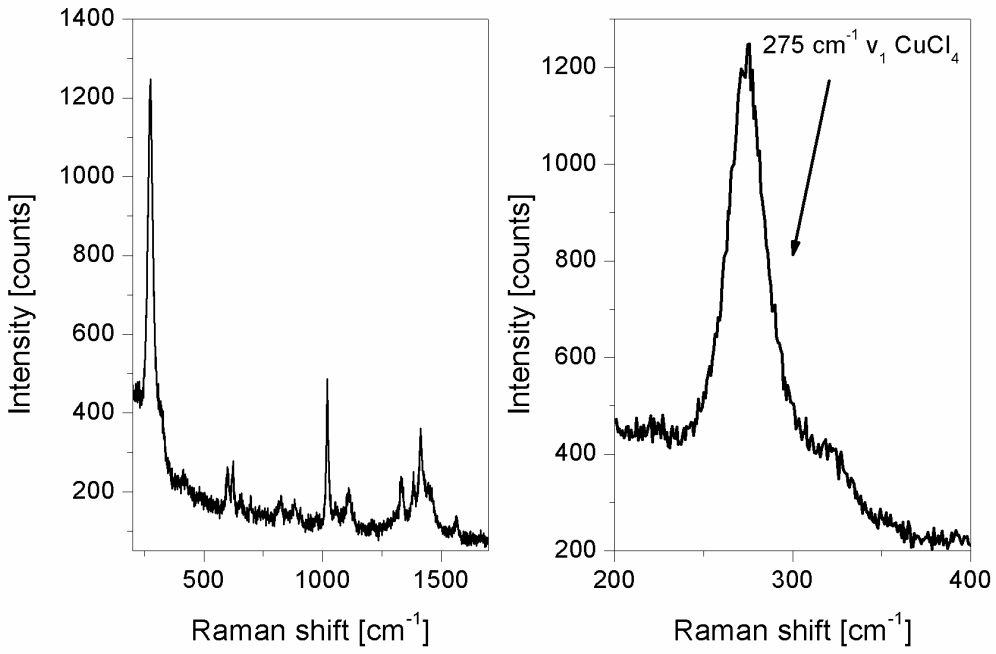



*Figure 2-21 Raman spectrum for $[C_1C_4Im]_2[CuCl_4]$ at excitation wavelength 785 nm and room temperature. On the left a full range spectrum is displayed and, on the right, the same spectrum in the range 200 to 400 $cm^{-1}$.*

The decomposition temperature for $[C_1C_4Im]_2[CuCl_4]$ was obtained from TGA (Figure 2-22) and was found to be 214°C. In comparison, Zhang *et al.* reported a decomposition temperature of 270°C.[66] However, they do not elucidate how the decomposition temperature was obtained. Therefore, a certain difference in values could be expected depending on the measurement method (*e.g.* onset point or endpoint).

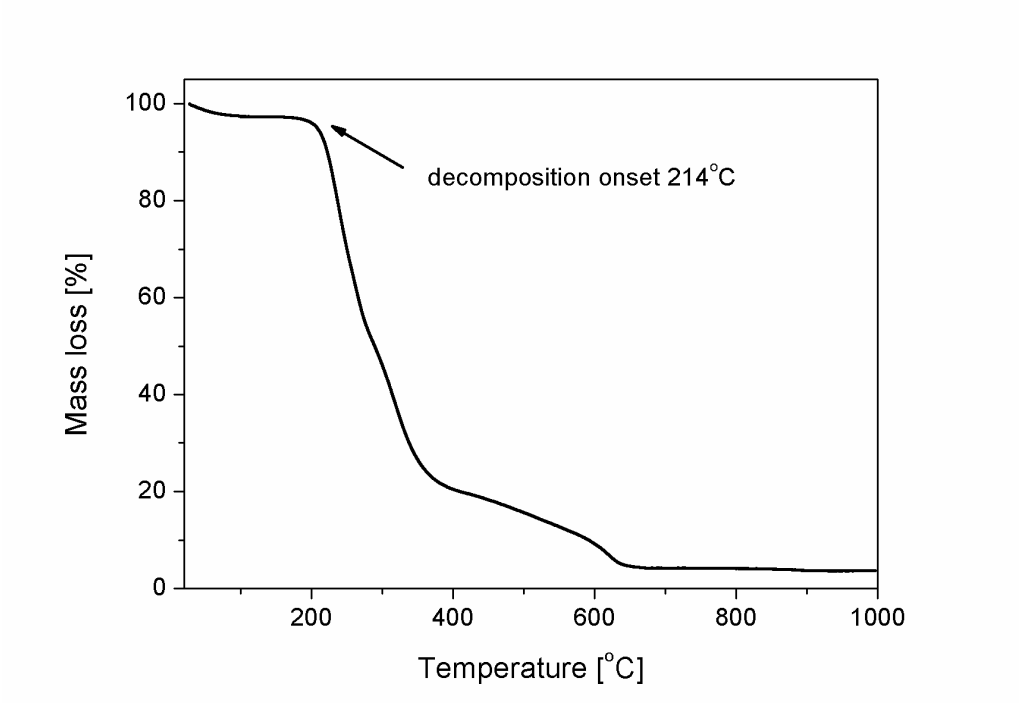



*Figure 2-22 Thermogram obtained from TGA under nitrogen flow gas for $[C_1C_4Im]_2[CuCl_4]$.*

Figure 2-23 shows the thermogram obtained from DSC at a heating rate of 10°C/min. Upon cooling a broad exothermic peak ($T_c$ = 11°C) is observed which corresponds to the crystallisation of the sample with an enthalpy of ΔH = 1 J/g. However, upon heating no corresponding melting peak to the crystallisation peak can be observed, which means that the sample solidified in a glassy amorphous state.[192] Glass transitions occur upon on heating and cooling at

around -54 and 112°C and are observed for all cycles in the same temperature range (Table 2-9) except for the first cooling ramp.

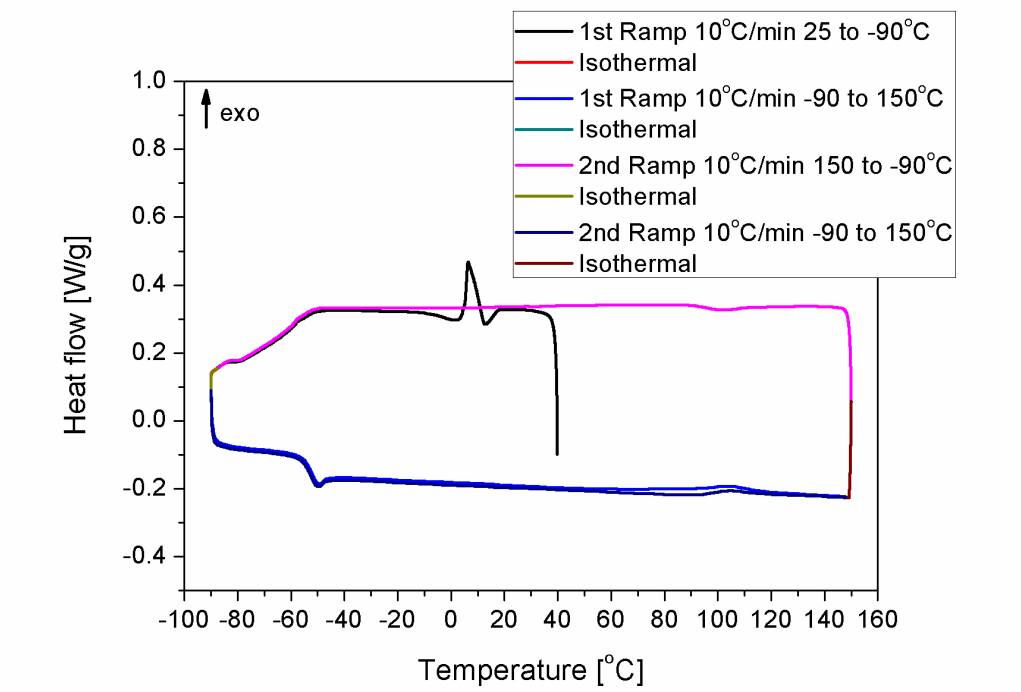



*Figure 2-23 Thermogram obtained from DSC for $[C_1C_4Im]_2[CuCl_4]$ at a heating rate of 10°C/min and in a range from -90°C to 150°C.*

*Table 2-9 Crystallisation $T_c$, melting $T_m$ and glass transition temperatures $T_g$ for $[C_1C_4Im]_2[CuCl_4]$.*

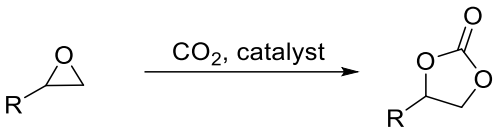
| | $T_c$ [°C] | $\Delta H(T_c)$ [J/g] | $T_m$ [°C] | $\Delta H(T_m)$ [J/g] | $T_g$ [°C] |
|---|---|---|---|---|---|
| **1st cooling ramp** | 11 | 1 | | | |
| **1st heating ramp** | | | | | -54<br>113 |
| **2nd cooling ramp** | | | | | 90 |
| **2nd heating ramp** | | | | | -54<br>111 |

# Chapter 3

The work presented in this chapter led to a publication in Applied Catalysis B: Environmental, Volume 245, 15 May 2019, Pages 240-250.

## 3. Halometallate ionic liquids as catalysts for the cycloaddition of carbon dioxide into epoxides

Carbon dioxide ($CO_2$) capture and utilisation is a widely investigated topic[193-195] and as it is a primary greenhouse gas this is a very important matter in light of the climate change crisis. Consequently, greener and more sustainable methodologies for the $CO_2$ fixation with more efficient energy consumption are required for drastically reducing the $CO_2$ footprint. Considering $CO_2$ is a very abundant, non-toxic and cheap reagent, it would be a good C1 building block in organic synthesis. However, in this context the high stability of $CO_2$ is a disadvantage. The carbon atom of $CO_2$ is in its most oxidised state and thus a high energy input is necessary for its activation. For example, cyclic carbonates can be formed through the insertion of $CO_2$ into epoxides (Scheme 3-1). Carbonates show applications as electrolytes for batteries, aprotic polar solvents, valuable starting materials for polymerisation reactions and intermediates in organic syntheses.[196]




*Scheme 3-1 Synthesis of cyclic carbonates from epoxides by conversion of $CO_2$.[174]*

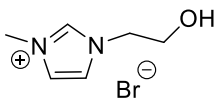
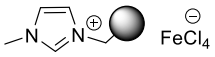
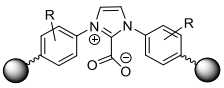
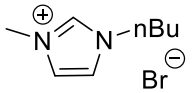
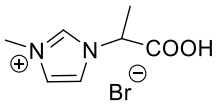
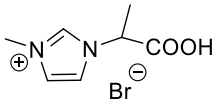
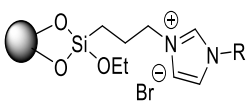
Homogeneous catalytic systems (for instance, Fe-based metal complexes) have been developed for the cycloaddition of $CO_2$ to epoxides, but they often show various challenges and disadvantages, with respect to the separation of the catalyst or low-cost effectiveness. In comparison, heterogeneous catalysts can overcome those difficulties but suffer from other disadvantages such as low catalytic activity and/or selectivity and high pressure requirements.[197] As previously described, ILs offer various advantageous properties and therefore are an excellent alternative to classic solvents and catalysts. The catalytic activity of ILs in this type of process has already been reported, as well as catalytic transformations using ILs as a reaction medium. Indeed, the beneficial effect of the use of ILs in processes involving $CO_2$ transformations has been extensively reported.[196]

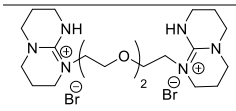
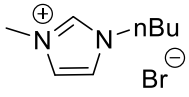
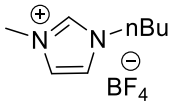
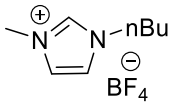
Girard *et al.* reported the formation of cyclic carbonates by reaction of epoxides with $CO_2$ under mild pressure conditions (5-8 bar) using halide imidazolium salts as catalysts. They investigated various cations and anions, and through structural modifications they detected that the ring opening step is the most important one towards reactivity.[174]

Table 3-1 shows examples from the literature describing the use of ILs as a catalyst. To the best of our knowledge, only a few examples have been described in which a metal-containing IL was used as a catalyst for the conversion of $CO_2$ into cyclic carbonates from epoxides. For example, Xiao *et al.* used an IL supported on $FeCl_3$ for the conversion of $CO_2$ with propylene oxide

as a substrate, obtaining a yield of 31%. In general, all examples required relatively high pressures to achieve good activity.[198]

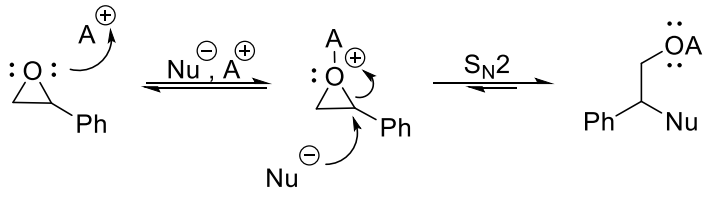
*Table 3-1 Literature comparison of $CO_2$ conversion with ILs as catalysts. S/C% = catalyst loading, SO = styrene oxide, PO = propylene oxide, P = pressure, T = temperature, t = time, Y = yield, Subst. = substrate, and R. = reference.*

| **Catalyst** | **S/C%** | **Support** | **Subst.** | **P [bar]** | **T [°C]** | **t [h]** | **Y [%]** | **R.** |
|---|---|---|---|---|---|---|---|---|
|  | 1.6 | - | SO | 20 | 125 | 1 | 99 | 199 |
|  | 1 | Polystyrene | SO | 80 | 120 | 12 | 84 | 200 |
|  | 1 | Mesoporous material | SO | 20 | 120 | 48 | 87 | 201 |
|  | 20 | - | SO | 140 | 120 | 2 | 69 | 202 |
|  | 0.5 | $ZnBr_2$ (0.03 mol%) | SO | 15 | 110 | 1 | 59 | 198 |
|  | 0.235 | $FeCl_3$ (0.0168 mol%) | PO | 15 | 110 | 1 | 31 | 198 |
| $PPh_3BuI$ | 0.5 | $H_2O$ (0.0335 mol%) | SO | 20 | 125 | 1 | 83 | 203 |
|  | 0.5 | Silica | SO | 16.2 | 115 | 5 | 96 | 204 |

| | | | | | | | | |
|---|---|---|---|---|---|---|---|---|
|  | 1 | PEG | SO | 10 | 120 | 3 | 94 | [205] |
|  | 0.18 | $ZnCl_2$ (0.0286 mol%) | SO | 15 | 100 | 1 | 90 | [206] |
|  | 2.5 | $ZnBr_2$ | SO | 140 | 80 | 1 | 93 | [207] |
|  | 2.5 | - | PO | 25 | 110 | 6 | 100 | [208] |

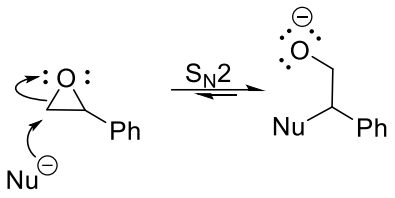
Epoxides are 3-membered rings with a bond angle of 60° rendering them unstable due to ring strain. Nevertheless, they need an acid catalyst or a strong nucleophile to react properly. Epoxides are not good leaving groups in a $S_N2$ reaction since their reactivity is only due to the ring strain. In addition, the regiochemistry depends strongly on the reaction conditions.

An acid-catalysed ring opening is favoured at the most substituted position of the ring (Scheme 3-2). The epoxide is activated by the acid, which leads to a positively charged intermediate.[209] A substituted carbon facilitates the charge build-up (a tertiary carbon would be even more stable) and therefore the nucleophile attacks at this carbon. A loose $S_N2$ transition state is formed, followed by the ring opening, and generation of the new product.




*Scheme 3-2 Acid-catalysed ring opening of an epoxide demonstrating the ring opening at the substituted carbon.[209]*

A base-catalysed ring opening (Scheme 3-3) is only possible with a strong nucleophile. There is no activation at the oxygen and thus no build-up of charge is possible. Therefore, the steric hindrance is the controlling factor in the reaction and the nucleophile will attack the less substituted carbon.[209]




*Scheme 3-3 Base-catalysed ring opening of an epoxide with a ring opening at the less substituted carbon.[209]*

Both homogeneous and heterogeneous catalytic systems have been developed for the cycloaddition of $CO_2$ to epoxides, such as amines and phosphines,[210-213] frustrated Lewis pairs (FLPs),[214] alkali metals,[215] metal oxides,[216, 217] organometallic complexes,[218-224] metal-organic frameworks[225-227] and carbon materials.[228-231] Nonetheless, they often exhibit various challenges and disadvantages, such as the separation of the catalyst and low-cost effectiveness for homogeneous systems. Whereas, heterogeneous catalysts can overcome those difficulties but have other disadvantages like low catalytic activity and/or selectivity as well as high pressure requirements.[197] On the other hand, ILs show various advantageous properties, including good thermal stability, high catalytic activity, ease of catalyst recovery and product purification, high capability for $CO_2$ capture and solvation, and easy fine-tuning basicity-nucleophilicity by simple modification of the IL structure (anion and cation)[197, 207, 221, 232-237] and therefore are an excellent alternative to classic solvents and catalysts. In addition, the use of metal halides or metal complexes

with Lewis acid properties as co-catalyst improves the catalytic performance of ILs.[207] These metal containing ILs function simultaneously as Lewis acid and as nucleophile therefore behaving as a bifunctional catalyst. However, the dissolution of a metal salt in an IL leads to a difficult task in identifying the real catalyst as different ionic species can be generated within the IL.[238] In the Literature only a few examples have been reported in which well-defined halometallate ILs were used as catalysts for the cycloaddition of $CO_2$ to epoxides.[200, 239-241]

## 3.1. Experimental procedures

### 3.1.1 Formation of carbonates

Catalytic experiments were carried out in a small reactor with a total volume of 2 mL. In a standard reaction, the chosen amount of Fe-based IL was mixed with the required quantity of epoxide in a glass vial with a magnetic stirrer. The reactor was flushed with $CO_2$ three times before the pressure was kept constant at the desired pressure using a reservoir and was heated at the desired temperature. After the specified time, the reactor was cooled to r.t. and slowly depressurized. The product was purified by extraction with diethyl ether and filtration with $SiO_2$ by flash chromatography. Afterwards, the solvent was evaporated to dryness at 150 mbar and r.t. using a rotary evaporator. The residue was dissolved in $CDCl_3$ and analysed by $^1H$ NMR to determine conversion and selectivity.

### 3.1.2 Formation of diols

Catalytic experiments were carried out in a small Schlenk flask. In a standard reaction, 10 mol% of the Fe-based IL was mixed with 200 mg of styrene oxide

and 1 mL of $H_2O$ in a Schlenk flask under Ar atmosphere with a magnetic stirrer. After 24 h, the product was purified by extraction with diethyl ether and filtration with $SiO_2$ by flash chromatography. Afterwards, the solvent was evaporated to dryness at 150 mbar and r.t. using a rotary evaporator. The residue was dissolved in $CDCl_3$ and analysed by $^1H$ NMR to determine conversion and selectivity.

### 3.1.3 Kinetic studies

Experiments were carried out in a Fisher-Porter reactor with the possibility to take samples during the reaction without depressurizing the reactor. In a standard reaction, 10 mL of styrene oxide, and the chosen amount of Fe-based IL were charged into the reactor equipped with a magnetic stirrer. The reactor was flushed with $CO_2$ three times before the pressure was kept constant at the desired pressure using a reservoir and was heated at the desired temperature. In the first hour of the reaction, samples were taken every 15 minutes and afterwards every hour. After the specified time, the reactor was cooled to r.t. and slowly depressurized. The product was purified by extraction with diethyl ether and filtration with $SiO_2$ by flash chromatography. Afterwards, the solvent was evaporated to dryness at 150 mbar and r.t. using a rotary evaporator. The residue was dissolved in $CDCl_3$ and analysed by $^1H$ NMR to determine conversion and selectivity.

### 3.1.4 Recycling experiments

Recycling experiments were carried out in a Fisher-Porter reactor. In a standard reaction, 5 mol% of the Fe-based IL was mixed with the chosen amount of epoxide (200 mg for styrene oxide, 283 mg for 1,2-epoxypentane) and

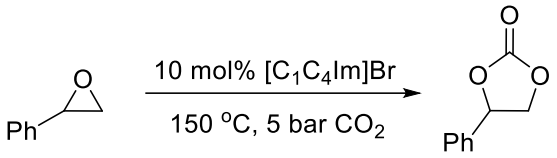
equipped with a magnetic stirrer. The reactor was flushed with $CO_2$ three times before the pressure was kept constant at 2 bar using a reservoir and was heated at the desired temperature (40 ˚C for styrene oxide, 80 ˚C for 1,2-epoxypentane). After 24 h, the reactor was cooled to r.t. and slowly depressurized. The product was purified by extraction with diethyl ether and centrifugation to recover the catalyst. Afterwards, the solvent was evaporated to dryness at 150 mbar and r.t. using a rotary evaporator. The residue was dissolved in $CDCl_3$ and analysed by $^1H$ NMR to determine conversion and selectivity. 1 was recovered through re-precipitation of the insoluble fraction, which was left after the extraction of the product with diethyl ether. The catalyst was then used for the next cycle.

### 3.1.5 Radical scavenger experiments

Radical scavenger experiments were carried out in a small reactor with a total volume of 2 mL. In a standard reaction, 5 mol% of the Fe-based IL catalyst was mixed with 400 mg of epoxide, and 2.5 mol% of a radical scavenger (galvinoxyl or 2,2-diphenyl-1-picrylhydrazyl (DPPH)) and equipped with a magnetic stirrer. The reactor was flushed with $CO_2$ three times before the pressure was kept constant at 2 bar using a reservoir and was heated to 40 ˚C. After 48 h, the reactor was cooled to r.t. and slowly depressurized. The product was purified by extraction with diethyl ether and filtration with $SiO_2$ by flash chromatography. Afterwards, the solvent was evaporated to dryness at 150 mbar and r.t. using a rotary evaporator. The residue was dissolved in $CDCl_3$ and analysed by $^1H$ NMR to determine conversion and selectivity.

## 3.2 Selection of catalyst

The reactor set-up was successfully tested with a reaction procedure reported by Girard *et al.* where $[C_1C_4Im]Br$ was found to be the best IL to catalyse the formation of a cyclic carbonate from an epoxide via the transformation of $CO_2$ (Scheme 3-4, 99% conversion at 5 bar $CO_2$ pressure, 10 mol% catalyst and 150°C).[174]




*Scheme 3-4 Catalytic transformation from an epoxide to a cyclic carbonate using $[C_1C_4Im]Br$ as a catalyst.*

Therefore, this IL was used to test the reactor set-up and a conversion of 67% at 100°C and 74% at 80°C was obtained (4 bar $CO_2$ and 10 mol% catalyst). Lower conversion was obtained with $[C_1C_4Im]Br$ than in Girard *et al.*'s work, however the reaction conditions were slightly varied as the aim in this work is to reduce the energy input.

As $[C_1C_4Im]Br$ was reported as a successful catalyst for the transformation of $CO_2$, the first halometallate IL tested in this work was $[C_1C_4Im][FeBr_4]$. The reaction was carried out at 80°C and gave a conversion of 38% (4 bar $CO_2$ and 10 mol% catalyst). Consequently, $[C_1C_4Im][FeCl_4]$ was tested as a catalyst for comparison of iron halide Lewis acidity and halide nucleophilicity. In addition, a good dielectric constant was observed previously (4.5.1 Measurement of dielectric properties at different frequency and temperature), suggesting $[C_1C_4Im][FeCl_4]$ as a viable candidate for inductive heating. Furthermore, $[C_1C_4Im][FeCl_4]$ is an already well-studied IL and Gao *et al.* reported the

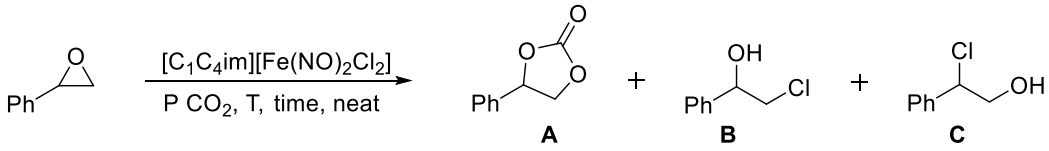
transformation of styrene oxide into cyclic carbonate using $CO_2$ and $[C_1C_1Im][FeCl_4]$ supported on polystyrene as a catalyst. They obtained a yield of 84% and a selectivity of 100% (120°C, 12h, 1 mol% catalyst loading and 80 bar $CO_2$).[200] In comparison in this work the transformation with $[C_1C_4Im][FeCl_4]$ was achieved with a conversion of 94% at 80°C and a selectivity of ≥ 99% (4 bar $CO_2$ and 10 mol% catalyst). It seems that $[FeCl_4]^-$ is a better Lewis acid than $[FeBr_4]^-$ and that this is more important than nucleophilicity, which would have been expected from the bromine. Both iron halides were tested as catalysts as well, but when added to styrene oxide an exothermic reaction was initiated. NMR showed that various species were formed before the catalytic experiment was even started, therefore these were not further tested. Additionally Coclough *et al.* reported the reaction of $FeCl_3$ and $FeBr_3$ with epoxides leading to polymerization.[242] $[C_1C_4Im][Fe(NO)_2Cl_2]$ has, to the best of our knowledge, not been reported in the literature previously. It has demonstrated good dielectric properties (4.5.2 Variation with increasing temperature) and was therefore selected as a possible catalyst. The catalytic experiment led to a conversion of 75% at 80°C. $[Fe(NO)_2Cl]_2$ was tested as well and showed a pressure increase when heated to 80°C, which indicates that it is unstable under these conditions. The conversion was determined to be 4%.

## 3.3 Optimisation of reaction conditions

The Fe-based IL catalyst $[C_1C_4Im][Fe(NO)_2Cl_2]$ was chosen from the initial screening of catalysts, due to its interesting magnetic properties (8.7 Magnetization measurements), good dielectric constant (4.5.2 Variation with

increasing temperature), and good catalytic performance for the formation of cyclic carbonates by reaction of styrene oxide with $CO_2$ under mild pressure and temperature conditions. Table 3-2 shows the results of the catalytic optimisation experiments. Further analysis of the reaction mixture revealed two side products 2-chloro-1-phenylethanol (B) and 2-chloro-2-phenylethanol (C) which are generated in addition to the desired product. Furthermore, a control experiment consisting of the reaction between styrene oxide and HCl led to the formation of 2-chloro-2-phenylethanol (C) as the only product, suggesting the in-situ formation of HCl during the catalytic process.

*Table 3-2 Optimisation parameters for the cycloaddition of $CO_2$ with styrene oxide catalysed by $[C_1C_4im][Fe(NO)_2Cl_2]$.[a] Cat. = catalyst loading, T = temperature, t = time, P = pressure, Conv. = conversion, Sel. = selectivity.*




| Entry | Cat. [mol%] | T [°C] | t [h] | P [bar] | Conv. [%][b] | Sel. [%][c] |
|---|---|---|---|---|---|---|
| **1** | 10 | r.t. | 7 | 1 | 21 | 77 : 18 : 5 |
| **2** | 10 | r.t. | 24 | 1 | 58 | 85 : 12 : 3 |
| **3** | 10 | 40 | 24 | 1 | >99 | 87 : 11 : 2 |
| **4** | 5 | 40 | 24 | 1 | 66 | 86 : 11 : 3 |
| **5** | 10 | R.T | 24 | 2 | 85 | 84 : 13 : 3 |
| **6** | 10 | 40 | 24 | 2 | >99 | 83 : 13 : 3 |
| **7** | 5 | 40 | 24 | 2 | >99 | 94 : 5 : 1 |
| **8** | 2.5 | 40 | 24 | 2 | 51 | 88 : 10 : 2 |

| | | | | | | |
|---|---|---|---|---|---|---|
| **9** | 10 | r.t. | 24 | 3 | 99 | 76 : 21 : 3 |
| **10** | 10 | 40 | 24 | 3 | >99 | 86 : 14 : 0 |
| **11**[d] | 5 | 40 | 24 | 2 | 28 | 70 : 24 : 6 |
| **12**[e] | 5 | 40 | 24 | 2 | 18 | 43 : 44 : 13 |

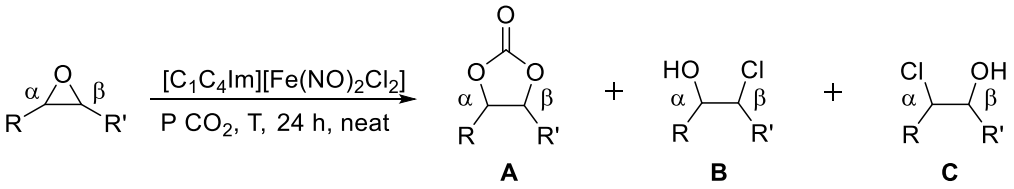
*[a] Reagents and conditions: styrene oxide (1.665 mmol), neat.[b] Conversions determined by $^1$H NMR spectroscopy and refer to the selective conversion of styrene oxide (average of two runs).[c] % selectivity referred to A : B : C. [d] 0.0832 mmol of $H_2O$ were added (1 equivalent regarding catalyst), [e] 1.665 mmol of $H_2O$ were added (1 equivalent regarding substrate).*

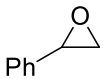
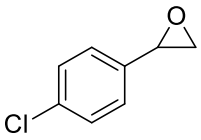
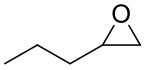
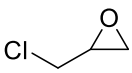
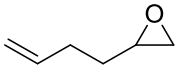
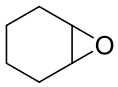
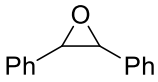
At room temperature, 10 mol% catalyst loading and 1 bar $CO_2$ pressure, low conversion was observed during 7 h reaction time (entry 1, 21%). In 24 h, 58% of conversion and a selectivity of 85% were obtained (entry 2). If the temperature is increased to 40°C, quantitative conversion of the substrate with 87% selectivity was achieved (entry 3). Increasing the pressure to 2 bar, high conversions were observed, but with a low selectivity to the expected product (entry 5 and 6). The catalyst loading was found to be crucial regarding conversion to the desired product. A decrease in the catalyst loading to 5 mol% at 1 bar led to a significant decrease in the conversion (entry 4, 66%), the same catalyst loading at 2 bar gave quantitative conversion with high selectivity (entry 7, 94%). However, a lower catalyst loading of 2.5 mol% showed a significant decline in conversion (entry 8, 51%). In addition, the use of higher pressures did not provide higher selectivities (entries 9 and 10). It is worth noting that the catalytic system does not require the use of any solvent to perform the process. With these optimized reaction parameters based on 24 h reaction time, 40°C and 2 bar of $CO_2$ pressure, quantitative conversion and 94% selectivity (entry 7) were achieved.

## 3.4 Substrate scope

After determining optimal reaction conditions (40 $^{o}$C, 2 bar, 24h), a variety of epoxides were tested in order to evaluate the potential of $[C_1C_4Im][Fe(NO)_2Cl_2]$ as a catalyst in the cycloaddition of $CO_2$ to epoxides. The IL was found to be a highly active catalyst under very mild and near ambient conditions (Table 3-3). Epoxides with electron-withdrawing substituents gave higher conversions than those with electron-donor groups (entries 1-5). Indeed, the use of 1,2-epoxypentane as substrate needed higher temperatures than styrene oxide (entries 1 and 3). However, the presence of an electron-withdrawing functionality favoured the formation of side product (B) and led to a decrease in chemoselectivity (entries 1 vs. 2, and 3 vs. 4), suggesting a nucleophilic attack at the C$\beta$ of the epoxide. In addition, aliphatic epoxides required the use of higher pressures and/or temperatures than aromatic epoxides (entries 1-5). On the other hand, the results indicate a steric influence of the substituents in the substrate, since the presence of internal and sterically hindered epoxides required the use of harder reaction conditions and led to lower conversions (entries 6 and 7). Finally, the cycloaddition of $CO_2$ to cyclohexene oxide is of particular interest as this transformation can be considered as a challenging one due to the steric hindrance posed by the substrate. The catalytic reaction was carried out with reasonable conversion (63%) at 80 $^{o}$C and 4 bar $CO_2$ (entry 6), which can still be considered as mild conditions.

*Table 3-3 Cycloaddition of $CO_2$ with various epoxides catalysed by $[C_1C_4Im][Fe(NO)_2Cl_2]$.[a]*




| Entry | Substrate | T [°C] | P [bar] | Conv. [%][b] | Sel. [%][c] |
|---|---|---|---|---|---|
| **1** |  | 40 | 2 | >99 | 94 : 5 : 1 |
| **2** |  | 40 | 2 | >99 | 73 : 23 : 4 |
| **3** |  | 80 | 2 | 99 | 100 : 0 : 0 |
| **4** |  | 80 | 4 | >99 | 76 : 24 : 0 |
| **5** |  | 40 | 4 | 92 | 88 : 12 : 0 |
| **6** |  | 80 | 4 | 63 | 96 : 4 : 0 |
| **7** |  | 80 | 4 | 3 | 100 : 0 : 0 |

*[a] Reagents and conditions: $[C_1C_4Im][Fe(NO)_2Cl_2]$ (0.832 mmol), substrate (1.665 mmol), 24 h, neat, 600 rpm.[b] Conversions determined by $^1H$ NMR spectroscopy and refer to the selective conversion of epoxide (average of two runs).[c] % selectivity referred to A : B : C.*

## 3.5 Recycling studies

A key driver towards IL-based catalytic systems is the possibility of catalyst recovery and reuse. Recycling experiments were carried out using styrene oxide as a substrate. Through extraction of the substrate and products with diethyl ether followed by re-precipitation of the insoluble fraction, the catalyst could be recovered and re-used in consecutive cycles. Still, a significant decrease in the activity was observed in the third cycle (Figure 3-1), which is due to a gradual loss and/or decomposition of the catalyst as a result of the

repeated washing cycles. In addition, this behaviour can be explained by the consumption of chloride anions associated to the formation of by-products 2-chloro-1-phenylethanol (B) and 2-chloro-2-phenylethanol (C).

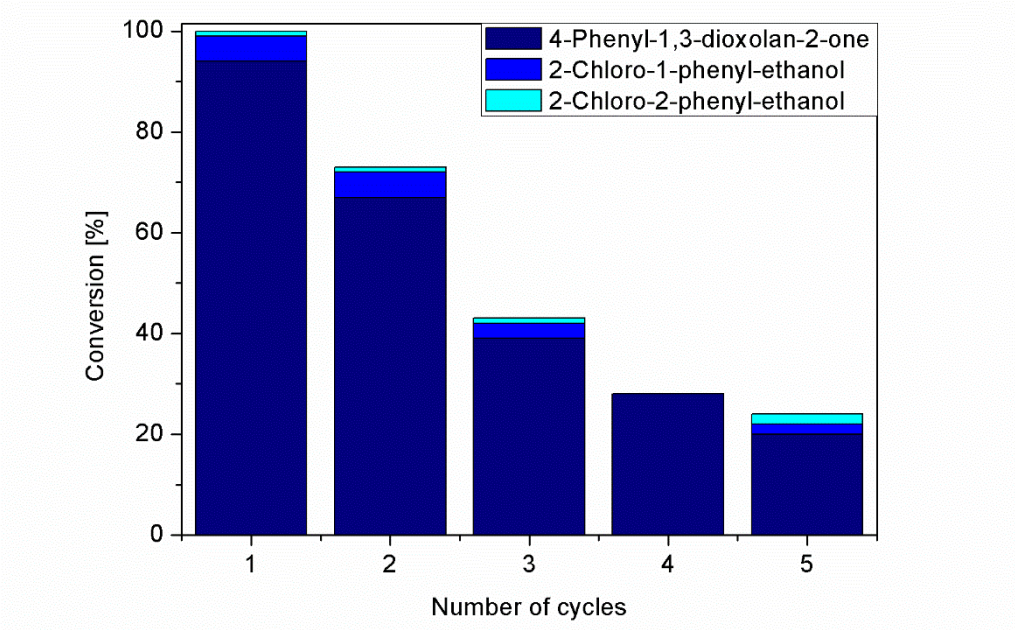



*Figure 3-1 Reuse of $[C_1C_4Im][Fe(NO)_2Cl_2]$ in the cycloaddition of $CO_2$ with styrene oxide (reagents and conditions: 5 mol% catalyst, 24 hours, 40°C, 2 bar $CO_2$).*

Indeed, the recyclability was improved using 1,2-epoxypentane as substrate, which does not generate chlorinated by-products. Only a slight decrease in the activity (14%) was observed after five cycles of catalyst recovery and reuse, whereas the catalyst remained active in the seventh cycle and the corresponding carbonate product was obtained with 74% conversion (Figure 3-2).

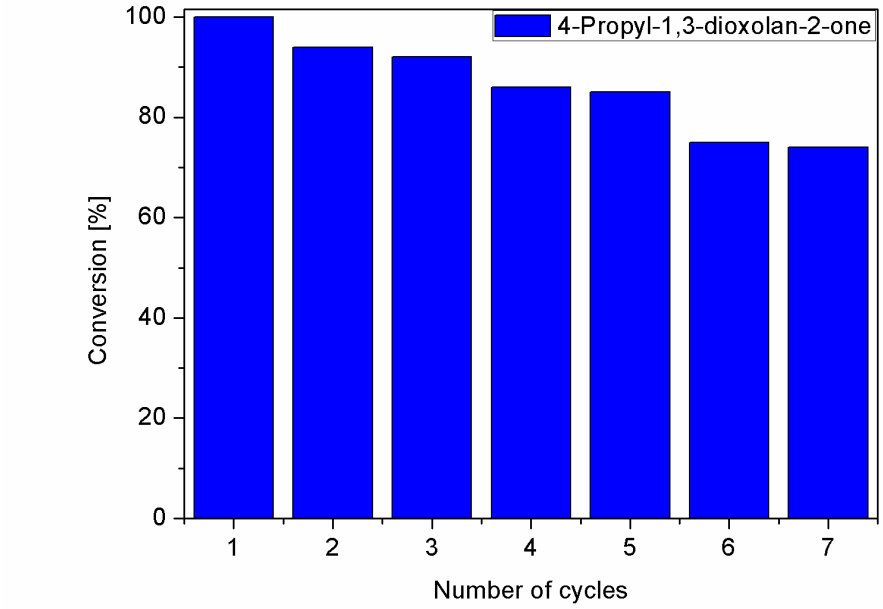



*Figure 3-2 Reuse of $[C_1C_4Im][Fe(NO)_2Cl_2]$ in the cycloaddition of $CO_2$ with 1,2-epoxypentane. Reagents and conditions: 5 mol % catalyst loading, 24 hours, 80°C, 2 bar $CO_2$.*

The catalyst was recovered after the catalytic experiments with both substrates, and analysed by FT-IR, XPS and ion chromatography ($Cl^-$). Besides the IR frequencies attributed to $[C_1C_4Im]^+$, the FT-IR spectra (Figure 3-3 and Figure 3-4) showed the bands belonging to the NO stretching absorption (1700 and 1779 $cm^{-1}$), indicating the presence of NO fragments in the recovered catalysts.

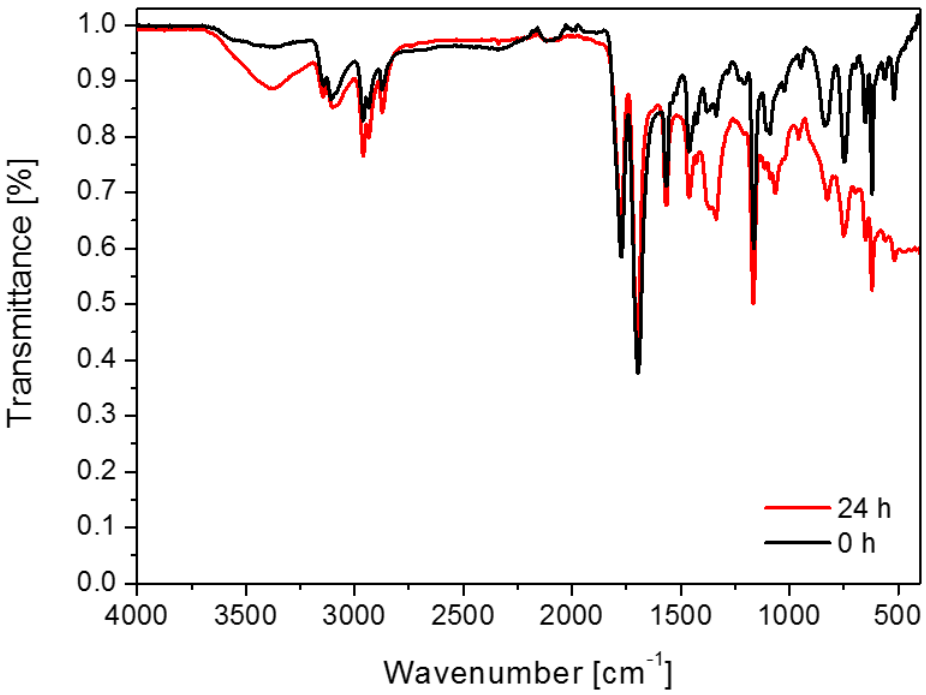



*Figure 3-3 Overlay of FT-IR spectra of the catalyst before and after reaction employing 1,2-epoxypentane as substrate.*

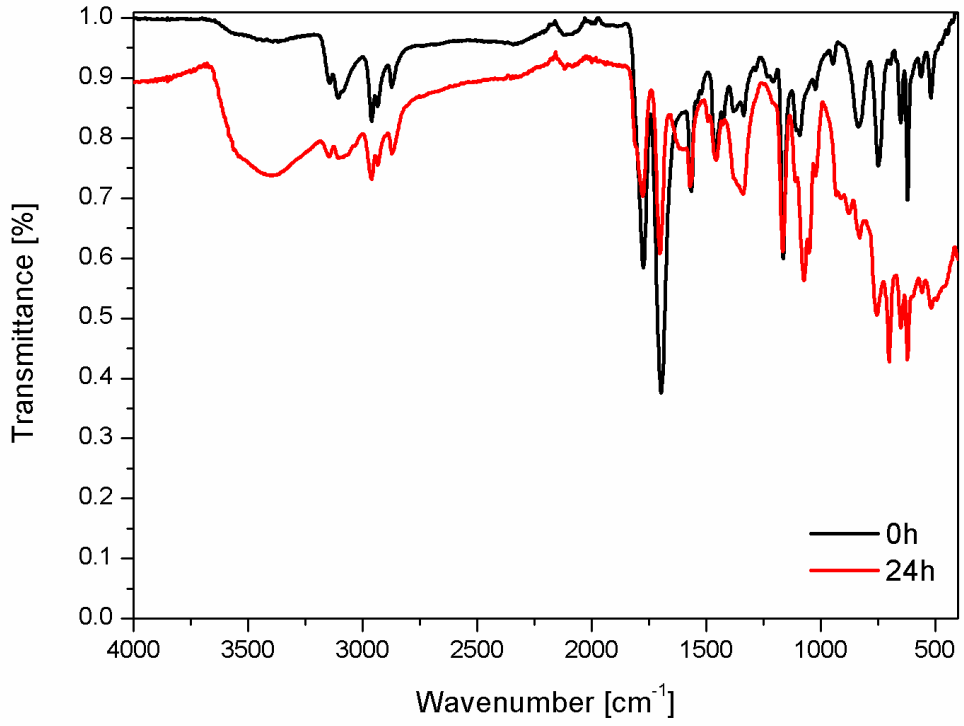



*Figure 3-4 Overlay of FT-IR spectra of the catalyst before and after reaction employing styrene oxide as substrate.*

In addition, the high resolution XP spectra of Fe 2p for $[C_1C_4Im][Fe(NO)_2Cl_2]$ before and after catalysis are very similar (Figure 3-5b and d). Interestingly, the high-resolution spectra of Cl 2p showed a new chloride species after reaction, consistent with simple chloride-based ILs, for example $[C_1C_4Im]Cl$ (Figure 3-5a and c).[243] This reveals that the initial iron-containing IL $[C_1C_4Im][Fe(NO)_2Cl_2]$ may generate the catalytically active species $[C_1C_4Im][Cl]$ + $[Fe(NO)_2Cl]$ under the reaction conditions (see 3.6.1 Control experiments and 3.6.4 Kinetic studies). Furthermore, ion chromatography gave a chloride content of *ca*. 21.0% after the reaction with 1,2-epoxypentane, in good agreement with the expected value for $[C_1C_4Im][Fe(NO)_2Cl_2]$ (21.75%). However, the observed chloride content is lower for the catalyst recovered after the experiment with styrene oxide (18.0%), consistent with the consumption of $Cl^-$ ions related with the formation of by-products 2-chloro-1-phenylethanol (B) and 2-chloro-2-phenylethanol (C). These analyses indicate that the iron-containing IL $[C_1C_4Im][Fe(NO)_2Cl_2]$ evolves during the reaction, and this change is more pronounced in the case of using styrene oxide as substrate in comparison to 1,2-epoxypentane, since a higher amount of chlorine containing by-product is formed.

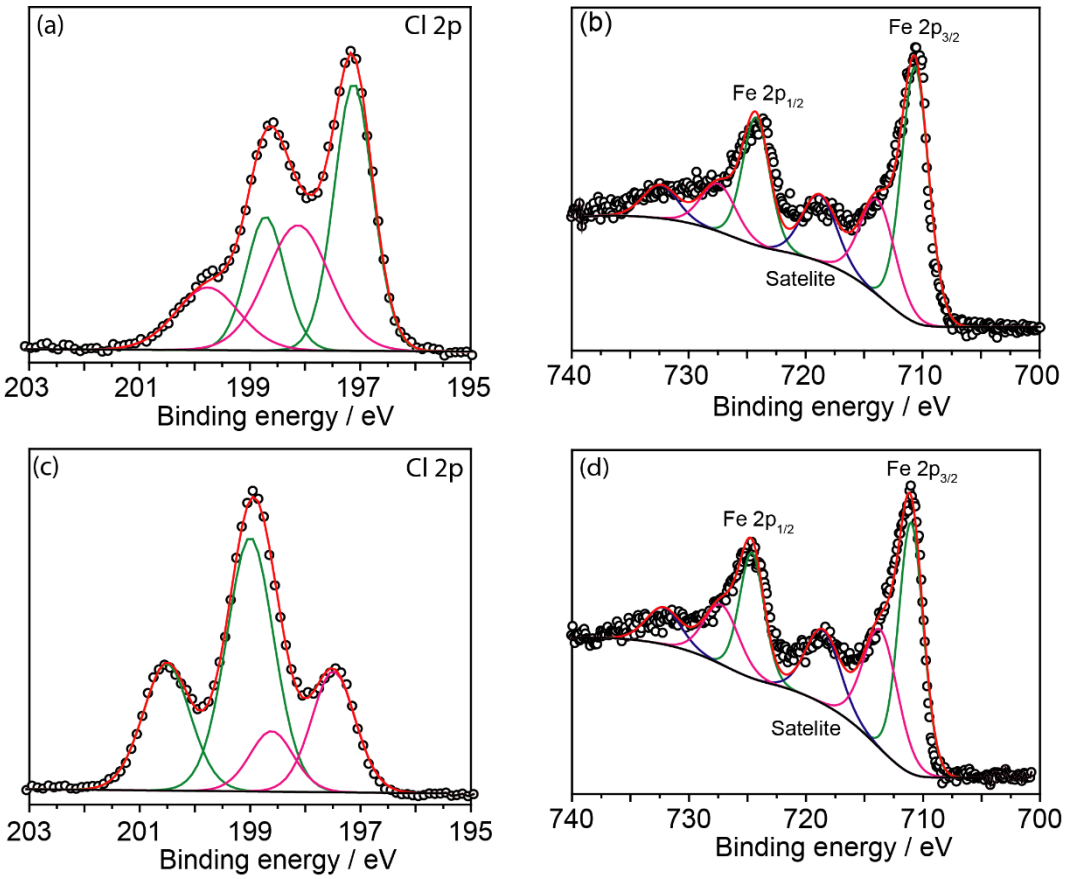



*Figure 3-5 (a) HR-XPS Cl 2p and (b) HR-XPS Fe 2p spectra of the catalyst after reaction employing 1,2-epoxypentane as substrate. (c) HR-XPS Cl 2p and (d) HR-XPS Fe 2p spectra of the catalyst after reaction employing styrene oxide as substrate.*

## 3.5 Study of the catalytic reaction mechanism

### 3.6.1 Control experiments

Mechanistic studies were carried out to investigate the formation of cyclic carbonates *via* cycloaddition of $CO_2$ to epoxides (Table 3-4). Firstly, the significance of $[C_1C_4Im][Fe(NO)_2Cl_2]$ in the catalytic reaction was examined by using the respective precursors $[C_1C_4Im]Cl$ and $[Fe(NO)_2Cl]_2$. Yet, both were inactive under the optimized reaction conditions (entries 1 and 2). These results reveal that both cation and anion belonging to the Fe-based IL $[C_1C_4Im][Fe(NO)_2Cl_2]$ play a role in the catalytic process, and thus proves the cooperative effect of the two fragments. Next, it was found that $[(n\text{-}Bu)_4N][Fe(NO)_2Cl_2]$ prepared from tetrabutylammonium chloride was less

active than $[C_1C_4Im][Fe(NO)_2Cl_2]$ (entries 3 and 4), which evidences the importance of the imidazolium cation to the observed catalytic activity. Similarly, $[C_1C_4Im][FeCl_4]$,[244] which was already examined during the selection of the catalyst (3.2 Selection of catalyst), showed less activity and much less selectivity than $[C_1C_4Im][Fe(NO)_2Cl_2]$ (entries 3 and 6), highlighting the role of the $[Fe(NO)_2Cl_2]^-$ moiety in the process.

*Table 3-4 Summary of the attempted cycloaddition of $CO_2$ to epoxides using various catalytic systems.[a]*

| Entry | Catalyst | Conversion [%][b] | Selectivity [%][c] |
|---|---|---|---|
| **1** | $[C_1C_4Im]Cl$ | 0 | -- |
| **2** | $[Fe(NO)_2Cl]_2$ | 5 | 0 : 0 : 100 |
| **3** | $[C_1C_4Im][Fe(NO)_2Cl_2]$ | >99 | 94 : 5 : 1 |
| **4** | $[(n\text{-}Bu)_4N][Fe(NO)_2Cl_2]$ | 60 | 84 : 12 : 4 |
| **5** | $[C_1C_1C_4Im][Fe(NO)_2Cl_2]$ | 59 | 80 : 17 : 3 |
| **6** | $[C_1C_4Im][FeCl_4]$ | 89 | 65 : 24 : 11 |

*[a] Reagents and conditions: catalyst (0.832 mmol), styrene oxide (1.665 mmol), 24 h, neat, 40°C, 2 bar $CO_2$, 600 rpm. [b] Conversions determined by $^1$H NMR spectroscopy and refer to the selective conversion of styrene oxide (average of two runs). [c] % selectivity referred to A : B : C.*

Previously reported mechanisms for this reaction have proposed the involvement of the C2 position of the imidazolium ring in the cycloaddition of $CO_2$ to epoxides catalysed by imidazolium-based ILs.[157, 200, 245-249] Thus, in order to determine the influence of the H–C2 of the imidazolium cation, the Fe-based IL $[C_1C_1C_4Im][Fe(NO)_2Cl_2]$ was prepared via an identical method using 1-butyl-2,3-dimethylimidazolium chloride (2.1.13 Synthesis of [C1C1C4Im]Cl), in which the C2 position is blocked by a methyl group. This catalyst displayed lower activity than $[C_1C_4Im][Fe(NO)_2Cl_2]$ (entries 3 and 5), suggesting that the H–C2

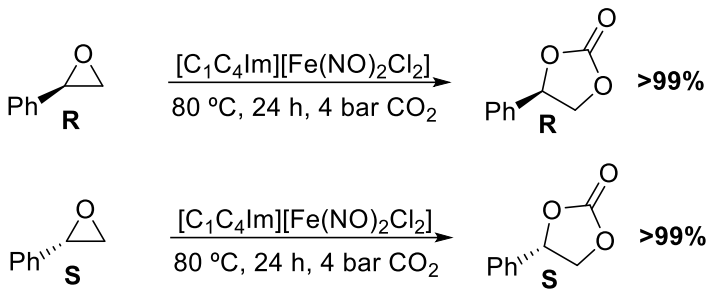
position of the imidazolium ring is participating in the reaction mechanism, possibly through the stabilisation of anionic intermediates by H-bonding interaction. The influence of this type of hydrogen bonding interaction (CH···X) on physical properties (i.e. melting point) has been described by several authors.[250-252]

### 3.6.2 Radical scavenger experiments

Another possible reaction pathway is via a radical formation. Therefore, an experiment was conducted with two different radical scavengers, namely galvinoxyl and 2,2-diphenyl-1-picrylhydrazyl (DPPH). The catalytic reaction in the presence of either galvinoxyl or DPPH still led to the formation of the desired product with moderate to good conversions (galvinoxyl: 91% conversion and 81% selectivity; DPPH: 74% conversion and 41% selectivity). Therefore, a radical mechanism can be dismissed as the catalytic pathway.

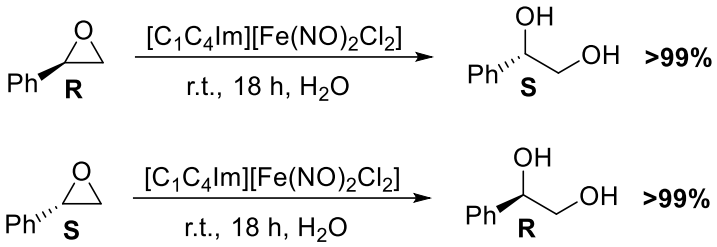
### 3.6.3 Use of $H_2O$ as nucleophile and optically pure substrates

To further investigate the mechanism optically pure (*R*)- and (*S*)-styrene oxide were used as substrates for the carbonate formation catalysed by $[C_1C_4Im][Fe(NO)_2Cl_2]$ (Scheme 3-5, 8.8 GC chromatograms). The (*R*)- and (*S*)-carbonates were obtained with high enantioselectivity (74% and 82% *ee*, respectively). This indicates that the reaction proceeds predominantly with retention of configuration, and thus through a nucleophilic attack to the Cβ of styrene oxide, which is relatively unexpected.[253-257] Indeed, the formation of 2-chloro-1-phenylethanol as by-product clearly demonstrates the epoxide ring opening through β attack.




*Scheme 3-5 Formation of optically pure carbonates by cycloaddition of $CO_2$ with R- and S-styrene oxide catalysed by $[C_1C_4Im][Fe(NO)_2Cl_2]$. Reagents: $[C_1C_4Im][Fe(NO)_2Cl_2]$, 0.1665 mmol; styrene oxide, 1.665 mmol. %ee determined by GC.*[258]

Interestingly, the reaction of the optically pure (*R*)- and (*S*)-styrene oxide with water catalysed by $[C_1C_4Im][Fe(NO)_2Cl_2]$ was mainly performed with inversion of configuration (Scheme 3-6 and 8.8 GC chromatograms ), leading to the formation of (*S*)- and (*R*)- diol products, respectively, even though with low-to-moderate enantioselectivity (54% and 40% *ee*, respectively). This result points to a nucleophilic attack on the more hindered side of the epoxide (C$\alpha$) in which the nucleophile is $H_2O$.[259] Consequently, there could be an influence of the bulkiness of the species involved in the catalytic process, which supports a role of the imidazolium moiety in the mechanism of the carbonate formation. A steric effect may avoid the attack on the C$\alpha$ of the epoxide and direct the attack of the nucleophile towards the C$\beta$. Supporting this theory, when $H_2O$ acts as the nucleophile in the diol formation, which does not show any steric impediment, the attack occurs on the more electronically favoured C$\alpha$.[257]




*Scheme 3-6 Formation of diols by reaction of styrene oxide with $H_2O$ catalysed by $[C_1C_4Im][Fe(NO)_2Cl_2]$. Reagents: $[C_1C_4Im][Fe(NO)_2Cl_2]$, 0.1665 mmol; styrene oxide, 1.665 mmol; $H_2O$, 1 mL. % ee were determined by GC.*[258]

### 3.6.4 Kinetic studies

For any reaction involving $CO_2$, the thermodynamics and kinetics of the process are of critical importance. If a large energy input is required, this will generate more $CO_2$ than is consumed by the reaction, unless the process can be linked to renewable or nuclear power. However, previous studies on the experimental determination of reaction thermodynamics and kinetics for the catalytic cycloaddition of $CO_2$ to epoxides are limited.[260] Theoretical calculations revealed that this transformation does not occur spontaneously because it is highly endothermic and requires a rather high activation energy (i.e., 30–60 kcal/mol).[257, 261-265] Therefore, a kinetic study under solvent-free conditions in which styrene oxide served simultaneously as a substrate and as a solvent was developed.[154] Reaction kinetics at different temperatures (i.e., 40, 50, 60, 70, 80 and 90 °C) were studied and the activation energy for the process was calculated by the Arrhenius Equation. The progress of these reactions was monitored by $^1$H NMR analysis of aliquots collected at regular intervals. The apparent kinetic constant ($k_{obs}$) was determined by the use of the general form of the rate Equation given by Equation [3-3] and Equation [3-4].[260] Analysis of the reaction kinetics revealed that the process followed first-order kinetics

regarding epoxide concentration (Figure 3-6), whereas $CO_2$ (present in large excess with a gas reservoir) and the concentration of $[C_1C_4Im][Fe(NO)_2Cl_2]$ were assumed to remain effectively constant during the process.

$$r = k[epoxide]^a[CO_2]^b[[C_1C_4Im][Fe(NO)_2Cl_2]^c \quad [3\text{-}1]$$

$$r = k_{obs}[epoxide]^a, where \quad [3\text{-}2]$$

$$k_{obs} = [CO_2]^b[[C_1C_4Im][Fe(NO)_2Cl_2]^c \quad [3\text{-}3]$$

$$\ln(k_{obs}) = \ln(A) - \frac{E_{a-app}}{R}\left(\frac{1}{T}\right) \quad [3\text{-}4]$$

By varying the $CO_2$ pressure (constant pressure of 2, 4 and 6 bar maintained with a gas reservoir, (8.9 Kinetic experiments) and $[C_1C_4Im][Fe(NO)_2Cl_2]$ concentration (2.5, 5.0 and 7.5% mol/mol epoxide, 8.9 Kinetic experiments), but maintaining all the other parameters constant (substrate concentration and temperature), the order of reaction for $CO_2$ and $[C_1C_4Im][Fe(NO)_2Cl_2]$ was determined to be zero and 1.5, respectively.[260] The zero–order dependence on $CO_2$ concentration is attributable to the large excess of gas present in solution due to the high solubility of $CO_2$ in the IL medium, while the 1.5–order dependence on the $[C_1C_4Im][Fe(NO)_2Cl_2]$ catalyst concentration exhibited by the rate was unexpected. This indicates that 1.5 separate molecules of $[C_1C_4Im][Fe(NO)_2Cl_2]$ are involved in the catalytic cycle before the rate-determining step occurs. It was also noted that reactions carried out at very low concentration of $[C_1C_4Im][Fe(NO)_2Cl_2]$ showed an induction period. Furthermore, a deactivation of the catalyst was observed in some catalytic experiments by the formation of chlorinated products occurring through nucleophilic attack from the chloride anion at the epoxide. However, this was

not apparent in reactions carried out at higher concentrations of $[C_1C_4Im][Fe(NO)_2Cl_2]$. Analogous behaviour was recently described for the same process mediated by Al-Lewis Acid catalysts dissolved in tetrabutylammonium bromide ILs.[260]

This dependence on the $[C_1C_4Im][Fe(NO)_2Cl_2]$ concentration was correlated with the fact that two reaction regimes were observed in the Arrhenius plot (Figure 3-6): one regime with $E_a$ = 321 Kcal/mol at low-to-mild temperature (*i.e.* 40 to 60 °C), and another one with $E_a$ = 31 Kcal/mol at mild-to-high temperatures (*i.e.* 70 to 90 °C). The presence of these two regimes suggests the existence of a fast pre-equilibrium, as it was previously observed for enzymatic systems with non-reactive (NR) and reactive (R) states.[266] This reversible pre-equilibrium determines the concentration of non-reactive (NR) and reactive (R) species in the reaction medium (i.e., NR ⇔ R, and k = [R]/[NR]), that is, the fast pre-equilibrium governs the reaction rate. Thus, the dissociated species corresponding to the reactive state predominates at high temperature, whereas the non-reactive state predominates at low temperature. And so, the reaction partners (*i.e.* $[C_1C_4Im][Fe(NO)_2Cl_2]$ ⇔ $[C_1C_4Im][Cl]$ + $[Fe(NO)_2Cl]$) are immersed in strong interactions with other species. This observation is very important to address the nature of the true-catalytically active species and understand the reaction mechanism that takes place with iron-chloride anions dissolved in ILs.

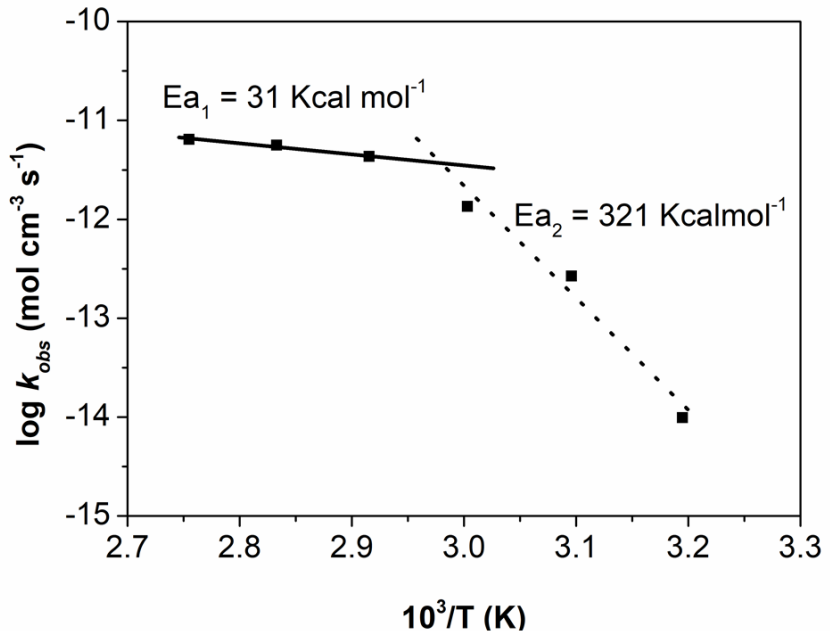
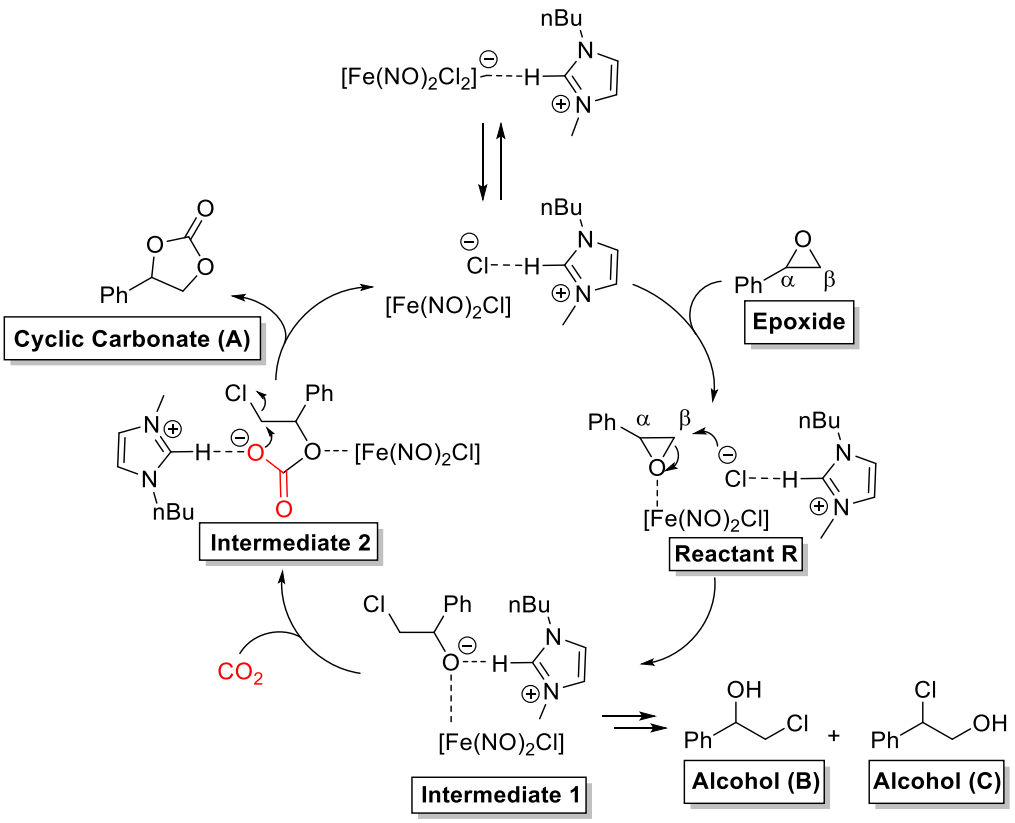



*Figure 3-6 Arrhenius plot for the cycloaddition reaction of $CO_2$ with styrene oxide catalysed by $[C_1C_4Im][Fe(NO)_2Cl_2]$.*

## 3.7 Proposed catalytic cycle

Two mechanisms are possible under the optimal reaction conditions. The first possibility is the reaction mechanism proposed for catalysts containing a good nucleophile and good leaving groups (*i.e.* bromide and iodide salts): (a) ring opening of the epoxide by the nucleophile with the formation of an alkoxide, (b) reaction of the alkoxide with $CO_2$ to give a carbonate, and (c) intramolecular displacement of the nucleophile by the carbonate to yield the five-membered ring and regenerate the catalyst.[264, 267] Alternatively, the reaction pathways observed for systems bearing a Lewis acidic metal-based catalyst (*e.g.* Co-MOF[265] and Zn-Salphen[257]) could also act under our mild reaction conditions: (a) activation of epoxide by the Lewis acidic metal-based catalyst and formation of a primary radical through cleavage of the less substituted C–O bond, and (b) $CO_2$ binding with the primary radical complex and carbonate formation by cyclization through a five-membered cyclic transition state. The radical

mechanism was examined by free-radical termination experiments under the reaction conditions. Different free radical scavengers, such as galvinoxyl and 1,1-diphenyl-2-picrylhydrazyl (DPPH),[265] were added to the mixture of the cycloaddition reaction of $CO_2$ with styrene oxide catalysed by $[C_1C_4Im][Fe(NO)_2Cl_2]$. The catalytic system described herein could be considered as a combination of these two types of catalyst. The Lewis acidic Fe-site is combined with a chloride anion, allowing the carbonate formation under mild conditions. The aim is to identify the nature of the true-catalytically active species, *i.e.*, $[C_1C_4Im][Fe(NO)_2Cl_2]$ ⇔ $[C_1C_4Im]+[Cl]^-$ + $[Fe(NO)_2Cl]$. The experimental kinetic data suggests that $[C_1C_4Im]+[Cl]^-$ ($[Cl]^-$ acting as nucleophile) and $[Fe(NO)_2Cl]$ (Fe acting as Lewis acid) are the true-catalytically reactive state, and the $[C_1C_4Im][Fe(NO)_2Cl_2]$ is the non-reactive state.



*Scheme 3-7 Proposed catalytic cycle for the formation of carbonates catalysed by $[C_1C_4Im][Fe(NO)_2Cl_2]$.*

Based on the experimental evidences, the catalytic cycle depicted in Scheme 3-7 was proposed, which is also supported by state-of-the-art DFT calculations that are focused upon similar Lewis acidic systems.[174, 268] After activation of the epoxide through coordination with the Lewis acid $[Fe(NO)_2Cl]$, the nucleophilic attack of $[C_1C_4Im]Cl$ on the epoxide promotes a ring opening reaction and the formation of the alkoxide intermediate (Intermediate 1). This nucleophilic attack is favoured on the less sterically-hindered Cβ, as is demonstrated by two facts. Firstly, the alcohol by-product (B) is formed in a significantly higher ratio than alcohol by-product (C). Secondly, in the instance when the optically pure epoxide was used as substrate, the configuration of the obtained cyclic carbonate was retained and only a slight decrease of the enantioselectivity was observed. Furthermore, the interaction from the H–C2 position of the imidazolium ring with the substrate *via* H-bonding in Intermediate 1 is supported through the control experiments (3.6.1 Control experiments) carried out with $[C_1C_1C_4Im][Fe(NO)_2Cl_2]$ and $[(n\text{-}Bu)_4N][Fe(NO)_2Cl_2]$ as catalysts, which showed lower reaction rates. Next, the insertion of $CO_2$ into the Intermediate 1 and the following ring closure by nucleophilic attack of the carbonate to the C–Cl bond yields the cyclic carbonate and regenerates the catalyst. After careful literature research, this seems to be the first case which describes the formation of alcohols (B) and (C) as by-products by protonation of the alkoxide under the near-ambient reaction conditions employed herein (2 bar and 40 °C). The formation of (B) and (C) was tried to inhibit by increasing the temperature to 80 °C in the catalytic reactions with styrene oxide and *p*-chlorostyrene oxide

(Table 3-3, entries 3 and 4), but the corresponding carbonate products were formed with identical selectivities as those observed at 40°C (Table 3-3, entries 1 and 2). Furthermore, the cycloaddition of $CO_2$ to (B) catalysed by $[C_1C_4Im][Fe(NO)_2Cl_2]$ was carried out in order to study the implication of this by-product as an intermediate in the catalytic cycle. However, no reaction was observed. Therefore, the by-products are formed through a deactivation pathway and they could be considered as a very stable dormant catalytic species, since the chloride nucleophile is trapped into their structures and, consequently, the decrease in the activity observed after each run during the recycling experiment with styrene oxide can be attributed to the loss of the $[Cl^-]$ nucleophile. Indeed, the catalyst remained active in the seventh cycle using 1,2-epoxypentane as substrate, which does not generate such by-products. The formation of these by-products is favoured for epoxides with electron-withdrawing substituents due to the higher basicity of the generated alkoxide.[269]

## 3.8 Conclusion

In this chapter, metal-containing ILs were investigated for their application as catalysts for the cycloaddition of $CO_2$ to epoxides with special focus on the catalytic pathway and the reduction of the energy input regarding temperature and pressure. The previously synthesized IL $[C_1C_4Im][Fe(NO)_2Cl_2]$ was found to be a highly active catalyst for the cycloaddition of $CO_2$ to epoxides, giving high conversions and chemoselectivities under near ambient conditions and without the need of any additive. Furthermore, the catalytic system showed a

good recycling performance and the catalyst remained active in the seventh cycle of recovery and reuse.

The complex works as a bifunctional catalyst playing a crucial double role, as Lewis acid and as nucleophile. In addition to the catalytic studies, the reaction mechanism and the nature of the different species involved in the catalytic cycle of this transformation were investigated by experimental studies. Such experiments demonstrated that the imidazolium moiety is involved in the catalytic process, whereas the reaction proceeds with retention of configuration through a nucleophilic attack to the Cβ of the epoxide. In addition, kinetic studies showed that the process followed first-order kinetics with respect to the epoxide concentration. The studies also revealed that the presence of a fast reversible pre-equilibrium in which the iron-containing IL $[C_1C_4Im][Fe(NO)_2Cl_2]$ (non-reactive state) dissociates at elevated temperature and generates the true-catalytically active species, $[C_1C_4Im]Cl + [Fe(NO)_2Cl]$.

Based on these experiments, a catalytic cycle was proposed where the $[Fe(NO)_2Cl]$ fragment operates as a Lewis acid leading to the activation of the epoxide. Whereas the chloride $[Cl]^-$, as part of $[C_1C_4Im]Cl$ moiety, acts as nucleophile and promotes the ring opening of the substrate through a nucleophilic attack on the less sterically-hindered Cβ. All in all, it is possible to conclude that the nature of the true-catalytically active species involved in the cycloaddition of $CO_2$ to epoxides mediated by halometallate ILs was determined.

# Chapter 4

## 4. Dielectric spectroscopy studies

### 4.1 Fundamentals of non-conventional heating approaches

**Magnetic heating**

The use of a magnetic field to increase the local temperature employing magnetic nanoparticles (NPs) is well known and used in medicine. The magnetic moment switching, or the Brownian motion induced by an alternative magnetic field leads to energy dissipation. Therefore, this process may constitute a simple and alternative method to increase the local temperature of catalysts based on magnetic materials. In particular, energy intensive reactions such as Fischer-Tropsch, $CO_2$ conversion or methanol production would benefit from this newly developed concept for improving heat efficiency in chemical reactions. Bordet *et al.* have described the use of composite iron carbide NPs in a magnetic heating reactor set-up for the hydrogenation of $CO_2$ (Sabatier reaction). The reactor set-up consists of a continuous flow reactor with an induction coil, which is situated around a glass vessel. An AC magnetic field oscillating at a frequency of 300 kHz and an adjustable amplitude between 0 and 64 mT is used. The reaction is carried out with a $H_2/CO_2$ ratio of 4 at atmospheric pressure. Monitoring of the reaction with an infrared camera showed a heat increase from 25°C to 350°C within 30 s (Figure 4-1). Over 80% conversion of $CO_2$ to $CH_4$ with 100% selectivity by the use of iron carbide NPs

supported on ruthenium doped SiRAlO*x*, which shows the potential of this technique.[270]

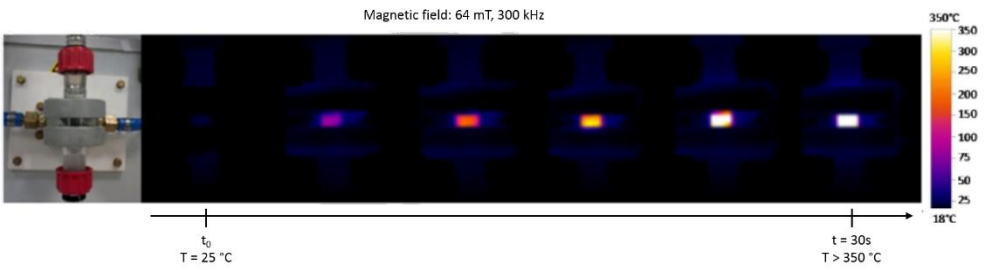



*Figure 4-1 Thermal images of the reactor being exposed to an alternating external magnetic field of 64 mT and 300 kHz.*[270]

**Photothermal heating**

Photothermal heating like magnetic heating is currently used for cancer therapy. Specifically, gold nanoparticles are widely investigated for this application. The photothermal effect arises from dissipation of photon energy into heat. Due to the excitation of the surface plasmon band of NPs and the subsequent rapid thermal relaxation of the exciton, the light energy is converted into heat.[271] This effect is induced by the surface plasmon resonance (SPR) absorption and enables the effective use of visible and near-infrared light for chemical processes.[272, 273] SPR generally means the coupling of an electromagnetic wave and a surface plasmon wave, which can occur between a metal and a dielectric medium.[274] Conduction band electrons are highly polarizable. If the electrons are hit with light whose wavelength is resonant with the wavelength of their surface plasmons, the electrons will move due to the impact of the external field. This leads to a net charge difference at the NPs boundaries and the incident light might be absorbed or scattered.

Consequently, the Photon confinement causes the generation of strong electromagnetic fields at the metal surface.[275] Meng *et al.* have reported the use of photothermal heating for the conversion of $CO_2$ into methane employing hydrogen and group VIII nanocatalysts (Ru, Rh, Ni, Co, Pd, Pt, Ir, and Fe) supported on $Al_2O_3$. Temperatures in the range of 300-400˚C were achieved using these catalytic systems. All the catalysts were active under photoirradiation, but $Ru/Al_2O_3$ and $Rh/Al_2O_3$ led to the highest conversion of $CO_2$ (96%).[276]

**Microwave irradiation**

The research field of microwave (MW) radiation/synthesis is ever growing and evolving. Material synthesis is one of the fastest growing fields in MW synthesis, including electrode materials,[277] nanoparticles,[278] metal-organic frameworks,[279] and polymer synthesis.[280] Other popular fields of MW irradiation lie in organic synthesis and biomass valorization.[281, 282] MW heating relies on the interaction of an electromagnetic wave with the dipole of a molecule, where two heating mechanisms are essential, namely dipolar polarization and ionic conduction.[283] The ions or dipoles try to align themselves with the oscillating electric field, and due to the alternating nature of the field energy is lost in form of heat, through molecular friction or dielectric loss, when the ions or dipoles attempt to realign with the field. MW reactors and kitchen MW ovens commonly use frequencies of either 0.9 or 2.45 GHz, even though MW irradiation ranges from 0.3 to 300 GHz. However, the majority of the

frequency range is reserved for radar and telecommunication to avoid interference (Industrial, Scientific, and Medical applications (ISM band)).[284, 285]

The most commonly chosen frequency of 2.45 GHz is also selected because at this frequency most polar molecules start to fall behind in their realignment with the oscillating field consequently creating resistive heat. This process is also called dielectric loss (see also 4.3 Dielectric spectroscopy), describing the amount of energy which is lost as heat. Interestingly, ionic conductivity can lead to greater heat dissipation than dipolar polarization. The ionic conduction mechanism leads to creation of heat due to, the collision of molecules when these oscillate back and forth.[286, 287]

## 4.2 Ionic liquid catalysts in microwave synthesis

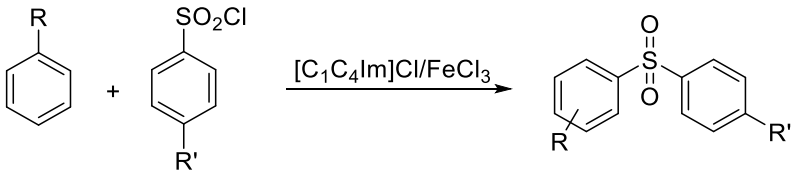
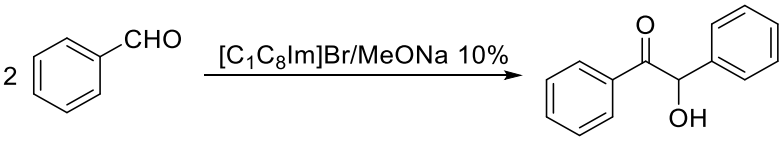
ILs are interesting candidates for MW synthesis, due to their high thermal stability, low vapour pressure, and tuneable ionic conductivity.[288] Especially, the low vapour pressure is of interest for safety reasons, as the pressure build up leading to explosions can be avoided. It has been demonstrated that it is possible to heat up ILs at a rate of 10°C/s without any noticeable pressure buildup.[286, 288] Generally, ILs have been used as solvents, catalysts, reagents, and as dopants for poor MW absorbing solvents.[289] Furthermore, MWs have been used to synthesize ILs themselves.[290, 291]

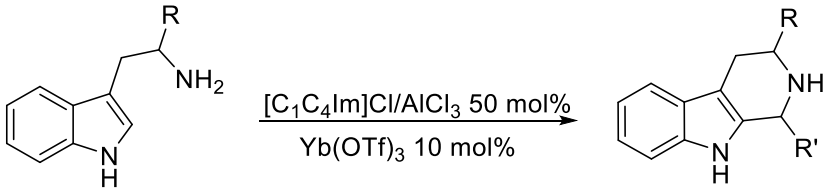
For example the group of Varma has prepared imidazolium based ILs using a household MW and in addition has prepared imidazolium based indium and gallium ILs for their application in catalysis. However, this exothermic and air sensitive synthesis has not been carried out in an inert atmosphere.

$[C_1C_4Im][InCl_4]$ was then used for the MW-assisted protection of alcohols which would be more challenging with volatile organic solvents.[292-295]

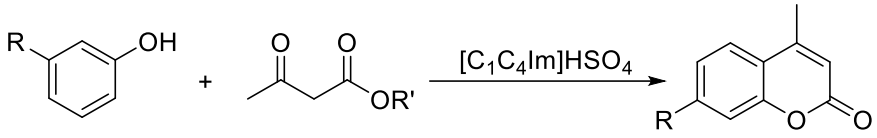
The main interest of this work lies in the use of ILs as catalysts. Therefore, the focus will be on examples from the literature describing how ILs can be used as catalysts in MW synthesis. Microwave-assisted organic synthesis (MAOS) has been known for over 30 years now, but the use of ILs as a catalyst or co-catalyst is a relatively new field. [296-298] Table 4-1 displays examples from the literature for MAOS using ILs as catalyst or co-catalyst. A variety of organic reactions has been investigated and reaction time, yield, and selectivity could be improved with the combined use of MW radiation and ILs. Many more publications can be found for ILs used as dopants and as reaction media described in the review by Martínez-Palou.[289]

*Table 4-1 Literature examples for MAOs using ILs as catalyst or co-catalyst. Ref. = reference.*

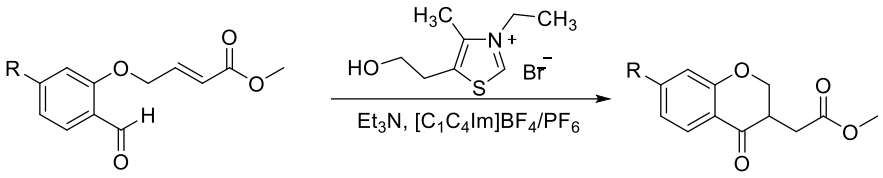
| **Reaction** | **Ref.** |
|---|---|
| **Friedel-Crafts (sulfonylation)** | 299 |
|  | |
| **Benzoin condensation** | 300 |
|  | |
| **Pictet-Spengler** | 301 |



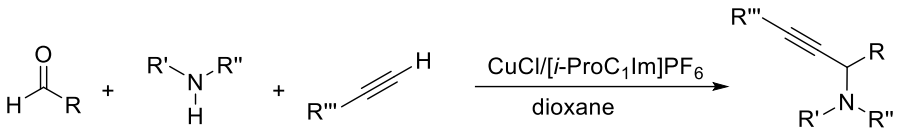

**Pechmann** [302]



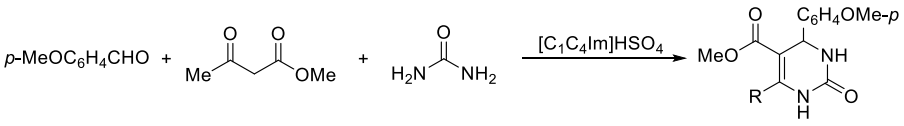

**Stetter** [303]




**Mannich condensation** [304]




**Biginelli** [305]




ILs are an interesting candidate for MW synthesis[282] and catalytic reactions using MW irradiation.[289, 306, 307] ILs containing a metal anion could be especially important as they have the ability to function as both a solvent and as a catalyst.[308] However, to date, no studies on the dielectric properties of halometallate ILs have been carried out, which is an important property to consider, due to their information provided on intermolecular interactions and

their ability to transform electromagnetic energy into heat. Indeed, the main focus has been on polymerized ILs and metal free imidazolium based ILs.[309-312]

## 4.3 Dielectric spectroscopy

Dielectric materials are an important part of everyday life and have a broad application field, mostly for high frequency circuits, insulators, and capacitators, but also in the application of MW irradiation (e. g. household MW oven or laboratory MW oven). A material that can be polarized when in proximity to an electric field is called a dielectric or dielectric material. How feasible it is to use a dielectric material for certain applications can be investigated using dielectric spectroscopy, which will provide information on how electromagnetic energy is stored and also dissipated.[313] Permittivity is a complex number and describes the polarizability of a material, which is described in the following Equation,

$$\varepsilon^*(\omega) = \varepsilon'(\omega) - i\varepsilon''(\omega) \qquad [4\text{-}1]$$

where $\omega$ is the radial frequency, $\varepsilon^*$ is the complex permittivity, $\varepsilon'$ the real part of the complex permittivity (*i. e.* the dielectric constant), and $\varepsilon''$ the imaginary part of the complex permittivity (*i. e.* the loss factor). The radial frequency is defined as followed,

$$\omega = 2\pi\nu \qquad [4\text{-}2]$$

where $\upsilon$ is the frequency. The conductivity is described through the following Equation,

$$\sigma = i\omega\varepsilon_0\varepsilon'' \qquad [4\text{-}3]$$

with $\varepsilon_0$ being the dielectric permittivity in vacuum ($\varepsilon_0 = 8.854 * 10^{-12}\ F\ m^{-1}$).

### 4.3.1 Dielectric spectroscopy studies on ionic liquids

A plethora of metal free aprotic and protic ILs has been investigated with dielectric spectroscopy, using among others broadband dielectric spectroscopy and terahertz spectroscopy.[310, 314-317] In addition, polymerizable ILs are of interest in dielectric spectroscopy.[311] The static dielectric permittivity has been extensively investigated for metal free ILs by the group of Weingärtner. In a review of the static dielectric permittivity Weingärtner highlights the challenges still to remain in the field of dielectric spectroscopy on ILs. He states the difficulty to determine a relaxation mechanism for IL systems especially in the submegahertz regime.[309, 318]

Wojnarowska and Paluch summarised the achievements on dielectric spectroscopy for protic ILs. Generally, it was found that broadband dielectric spectroscopy is a good way to gain insight into the conducting mechanism of protic ILs and especially measurements under pressure were helpful. Conductivity mechanisms observed in protic ILs are vehicular motion, proton hopping and the Grotthuss mechanism, where the charge itself moves. When using dielectric spectroscopy commonly the Grotthuss mechanism was observed for the investigated protic ILs.[316]

Turton et al. suggest to combine ultrafast optical Kerr-effect (OKE) spectroscopy with traditional dielectric spectroscopy as they observed some relaxation effects in ILs only with OKE spectroscopy but not with dielectric

spectroscopy. In their studies they observed mesoscopic clustering for ILs, which lead to a peak in the OKE spectrum but was barely visible in the dielectric spectroscopy.[319]

Buchner and Hefter highlight the importance of dielectric spectroscopy in their review, as it is the only method which reliably provides the dielectric constant for a material. An example of a well-studied IL is $[C_1C_4Im][BF_4]$ (Figure 4-2), which shows low dielectric loss however ε'' is constant over a broad frequency range due to many overlapping processes. The relaxation mechanism at low frequency is suggested to arise from reorientation of the bulky dipolar imidazolium cation. At higher frequency the relaxation mechanism poses more difficulties and is less well understood. The common understanding is that the relaxation arises from low energy vibrations.[310]

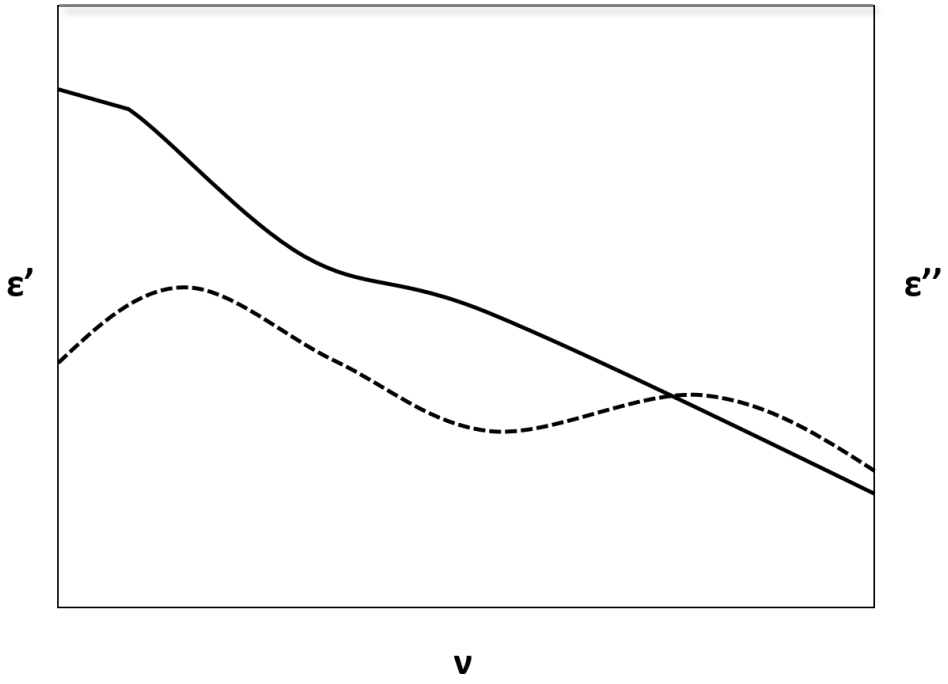



*Figure 4-2 Dielectric spectroscopy spectrum for $[C_1C_4Im]BF_4$ where the dashed line represents the imaginary part of the dielectric response.*[310]

## 4.4 Impedance spectroscopy

Electrochemical impedance spectroscopy (EIS) uses a DC bias voltage in addition to the AC voltage, which is used by AC impedance spectroscopy. The DC voltage compensates for the influence arising from the electrode potential, which is the potential difference between the electrolyte and the electrode. When an AC potential, with a DC potential superimposed on it, is applied to an electrochemical cell and there is a resultant current flow consequently, ions begin to move within the electrolyte and a relationship between the applied potential and the current flow can be determined, which is called impedance.[320] The applied potential can be described by a sinusoidal wave with a small amplitude and a defined frequency (Equation [4-4),

$$U(t) = U_0 \sin(\omega t) \qquad [4\text{-}4]$$

where $\omega$ is the angular frequency (see Equation [4-2), $U_0$ a small amplitude, $U(t)$ the applied AC potential, and $t$ the time. Then, the resulting AC current can be described by a Taylor series as followed,

$$I(t) = \left(\frac{\partial I}{\partial U}\right) U(t) + \frac{1}{2}\left(\frac{\partial^2 I}{\partial U^2}\right)\left(U(t)\right)^2 + \cdots \qquad [4\text{-}5]$$

with $(\partial I/\partial U)$ and $(\partial^2 I/\partial U^2)$ being the first and second derivative respectively, for the current-voltage relationship. However, higher order terms of the Taylor series can be disregarded when the excitation amplitude $U_0$ is small enough. In this instance, the AC current relies on the applied voltage in a linear behaviour and in this case the AC current can be described as,

$$I(t) = I_0 \sin(\omega t - \varphi) \qquad [4\text{-}6]$$

where $I_0$ is the amplitude of the AC current and $\varphi$ the phase angle between the voltage and the current (Figure 4-3a). The phase angle is defined through Equation [4-7].

$$\varphi = \omega\Delta t \qquad [4\text{-}7]$$

In consequence the complex Impedance can then be described with the following Equation,

$$\hat{Z}(\omega) \equiv \frac{U_0}{I_0} exp(i\varphi) = Z'(\omega) + iZ''(\omega) \qquad [4\text{-}8]$$

where $\hat{Z}(\omega)$ can be seen as a generalized resistance and can be displayed in a complex plane (Figure 4-3b).[321]

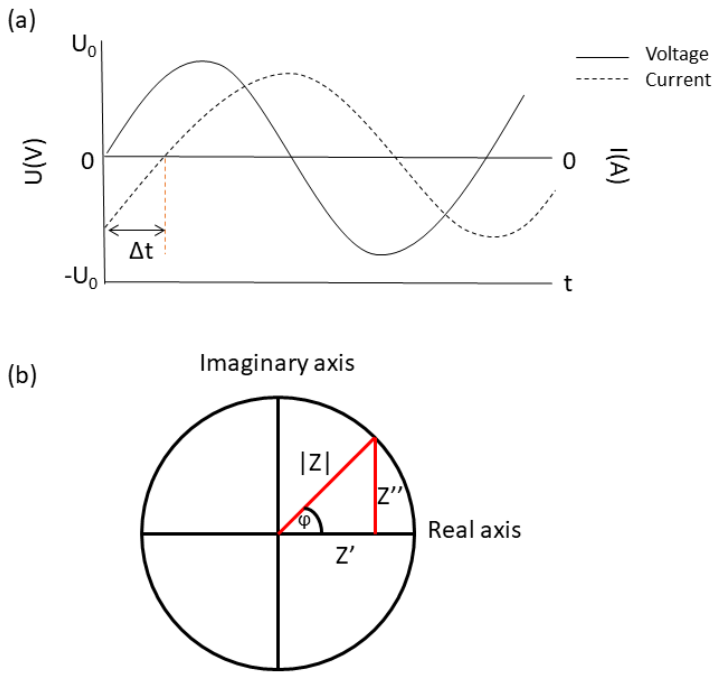



*Figure 4-3 (a) Phase shift between AC voltage and current. (b) Display of impedance in a complex plane.*[320]

Therefore, with the help of Ohm's law (Equation [4-9]) the conductivity can be calculated.

$$R = \frac{U}{I} \quad [4\text{-}9]$$

$$G = \frac{1}{R} \quad [4\text{-}10]$$

$$K = \frac{d}{A} \quad [4\text{-}11]$$

$$\sigma = G * K \quad [4\text{-}12]$$

where *G* is the conductance, *K* the cell constant, *d* the distance between the electrodes, *A* the area of the electrodes, and *σ* the conductivity. Hence, if the distance and size of the electrodes is unknown, a solution with known conductivity can be used instead.

## 4.5 Real and imaginary permittivity

Dielectric spectroscopy was carried out using a coaxial slim probe with a frequency range of 0.5 to 20 GHz, under inert atmosphere, and between a temperature range of 25 to 110°C (Figure 4-4). Further theoretical elaboration of the method can be found in the Literature.[317, 322-324] The temperature was maintained with a sand bath and verified with an external thermocouple as a temperature difference of approximately 10°C could be observed between the temperature of the hotplate and the sample. All measurements were repeated three times and the average is presented in the graphs in this chapter. Measurements were taken after the temperature had equilibrated for approximately 10 minutes.

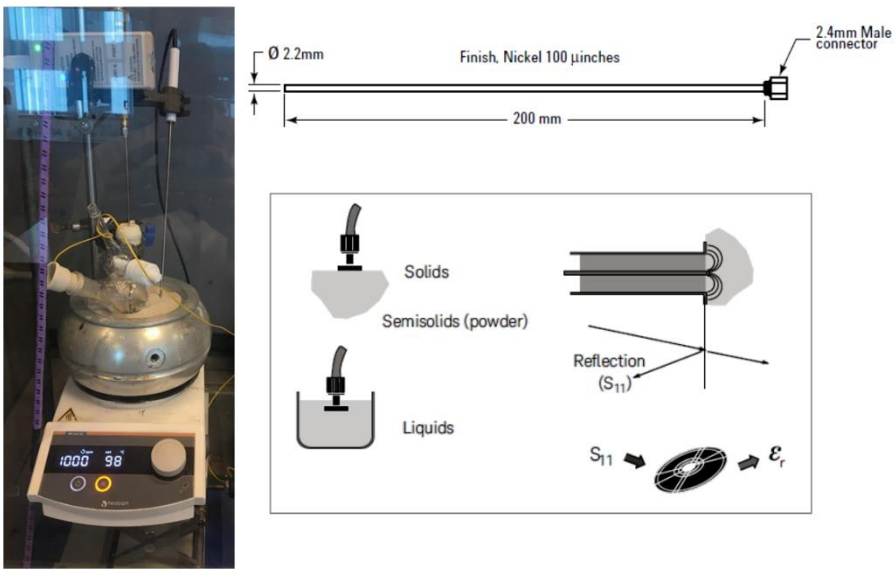



*Figure 4-4 Experimental set-up for dielectric spectroscopy using a coaxial slim probe, schematic display of a coaxial slim probe shown on the right.*[325]

Some samples displayed crystals formed around the coaxial probe, hindering a significant measurement and in some cases only a small amount of sample was available. Therefore, in these cases, a different measurement method was used. Resonance perturbation cavities are generally used for pure dielectrics but a good agreement with results from the coaxial probe could be found. The measurement has been extensively described in the Literature.[326-331] Figure 4-5 shows the set-up for the resonance perturbation cavity with a furnace, network analyser and high precision temperature control. Measurements were carried out using a quartz tube and a temperature range of 25 to 130°C. All measurements were repeated three times and the average is presented in the graphs in this chapter. Measurements were taken after the temperature had equilibrated for approximately 10 minutes.

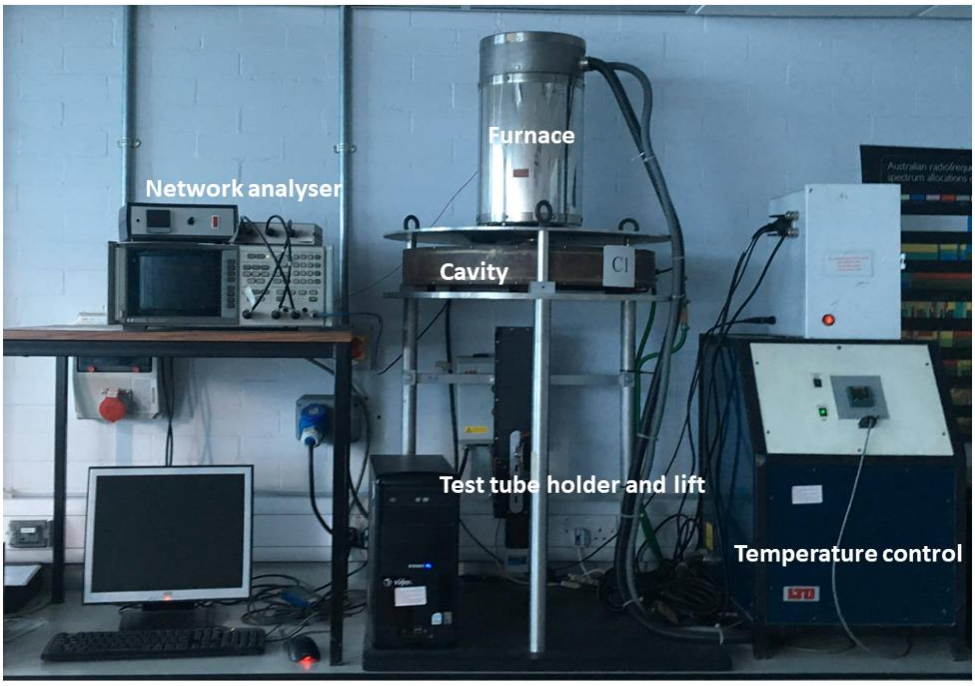



*Figure 4-5 Experimental set-up for the resonance perturbation cavity including computer, furnace and network analyser.*

### 4.5.1 Measurement of dielectric properties at different frequency and temperature

The real and imaginary part of the dielectric function ε(υ) was measured for a variety of halometallate ILs at a range of frequency (0.5-20 GHz) with increasing temperature (20-110°C) under inert conditions. All measurements were taken in the same manner to keep the data comparable. Standard deviation was calculated for all data from three repeat measurements but is omitted in these graphs for clarity but will be presented in the following section (4.5.2 Variation with increasing temperature).

Figure 4-6 shows the dielectric constant for $[C_1C_4Im][FeCl_4]$ versus the logarithm of the frequency. Measurements were taken in 10°C steps, starting from room temperature up to 110°C. A higher dielectric constant can be observed at a lower frequency and additionally an increase with increasing

temperature. The dielectric constant displays a plateau at a lower frequency range from 0.5 to 10 GHz (8.8-9.2 log(υ[Hz])) and decreases in value afterwards in a linear behaviour by approximately a factor of three.

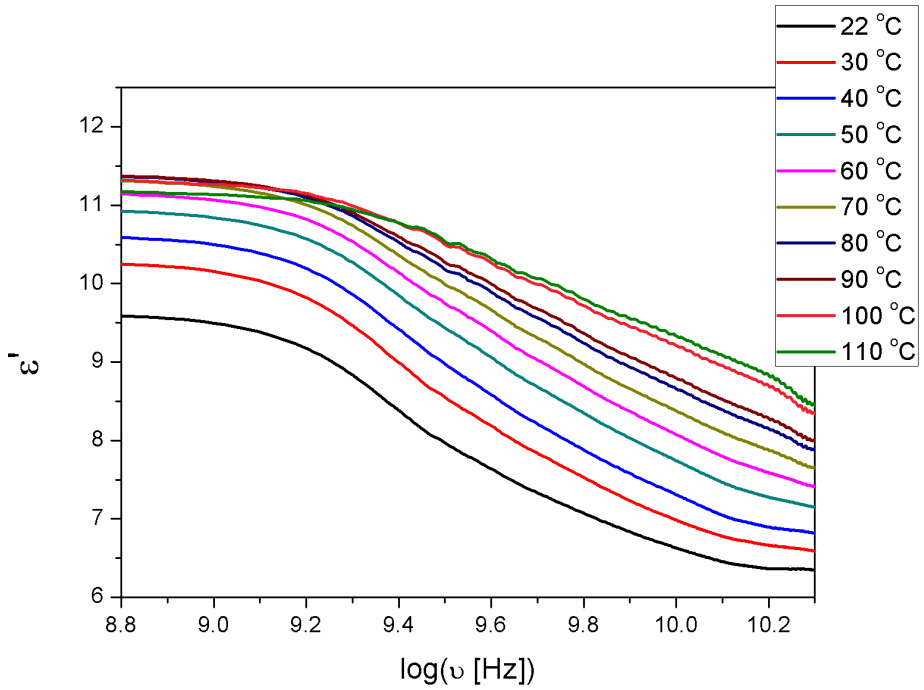



*Figure 4-6 Real part of dielectric function ε'(υ) versus frequency at different temperatures for [$C_1C_4$Im][$FeCl_4$]. The data was exponentially smoothed for clarity, STDEV 0.001-0.1.*

In Figure 4-7 the imaginary part of the dielectric function is presented. The loss factor increases significantly with increasing temperature in the low-frequency range. At higher frequency, the loss factor decreases to values between 0 and 20. Interestingly, no further temperature dependence is observed.

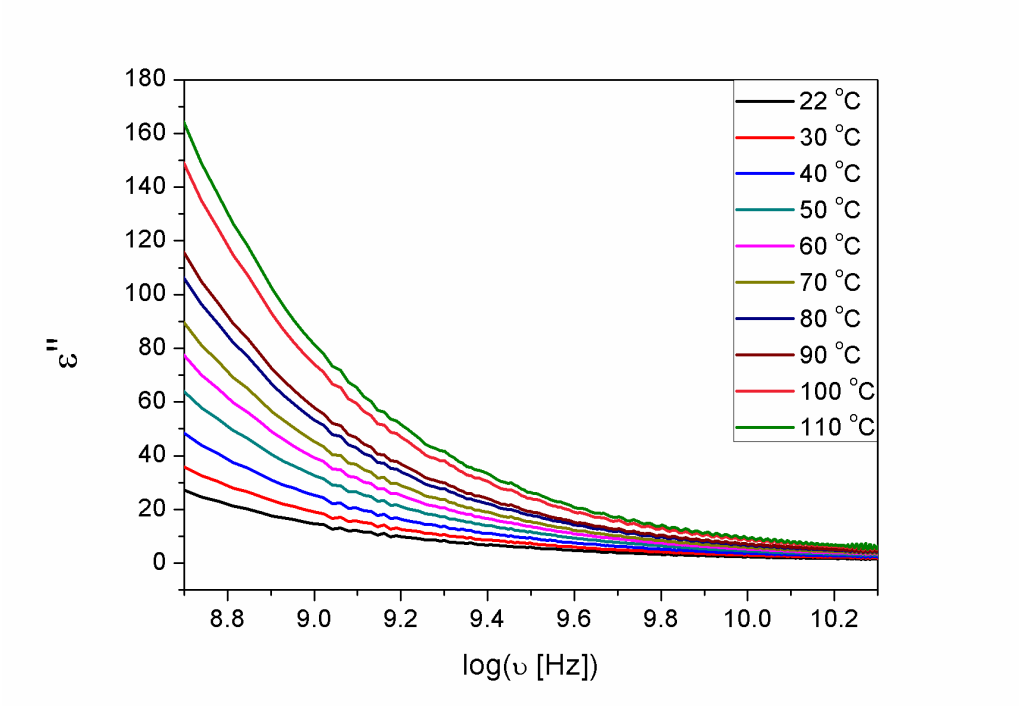



*Figure 4-7 Imaginary part of dielectric function ε''(υ) versus frequency at different temperatures for [$C_1C_4Im$][$FeCl_4$], STDEV 0.007-1.3.*

Figure 4-8 depicts the dielectric constant ε' for [$C_1C_4Im$][$InCl_4$]. A decrease in the dielectric constant with increasing frequency is observed. Temperature dependence is noticeable throughout the whole frequency range. However, at a lower frequency, a significant bend leading to a plateau is visible for values measured at a higher temperature (90-110°C).

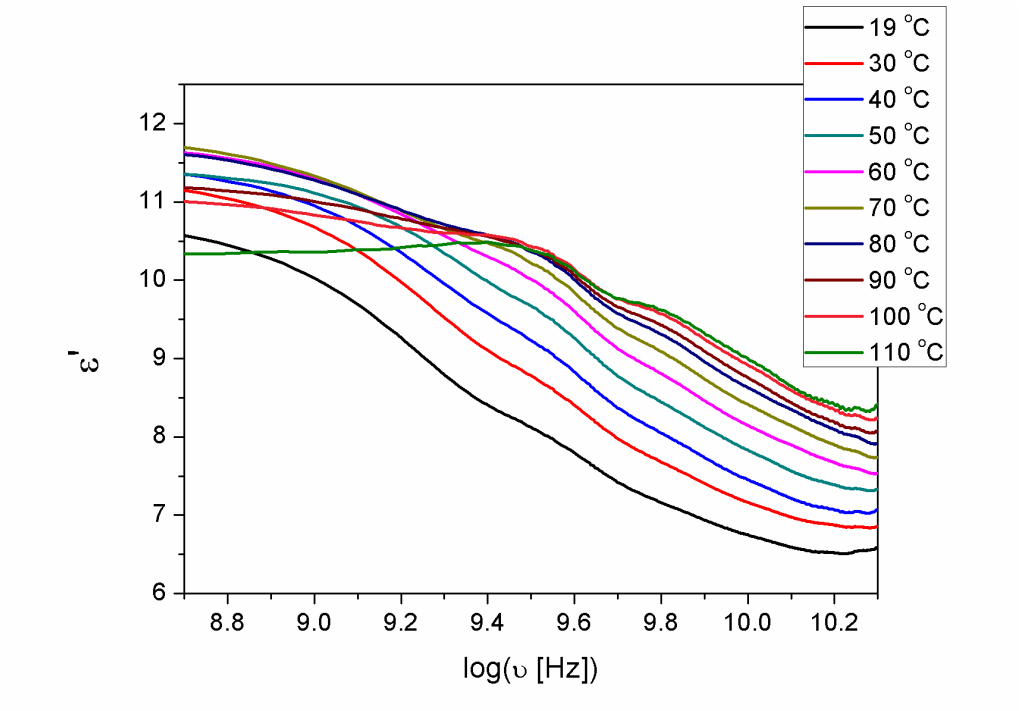



*Figure 4-8 Real part of dielectric function ε'(υ) versus frequency at different temperatures for [$C_1C_4$Im][$InCl_4$]. The data was exponentially smoothed for clarity, STDEV 0.002-0.6.*

The loss factor ε'' for [$C_1C_4$Im][$InCl_4$] (Figure 4-9) shows similar behaviour as [$C_1C_4$Im][$FeCl_4$] (Figure 4-7), where a significant increase of the loss factor can be noted at a lower frequency with increasing temperature. As well as, a decline of the loss factor at different temperatures towards higher frequencies.

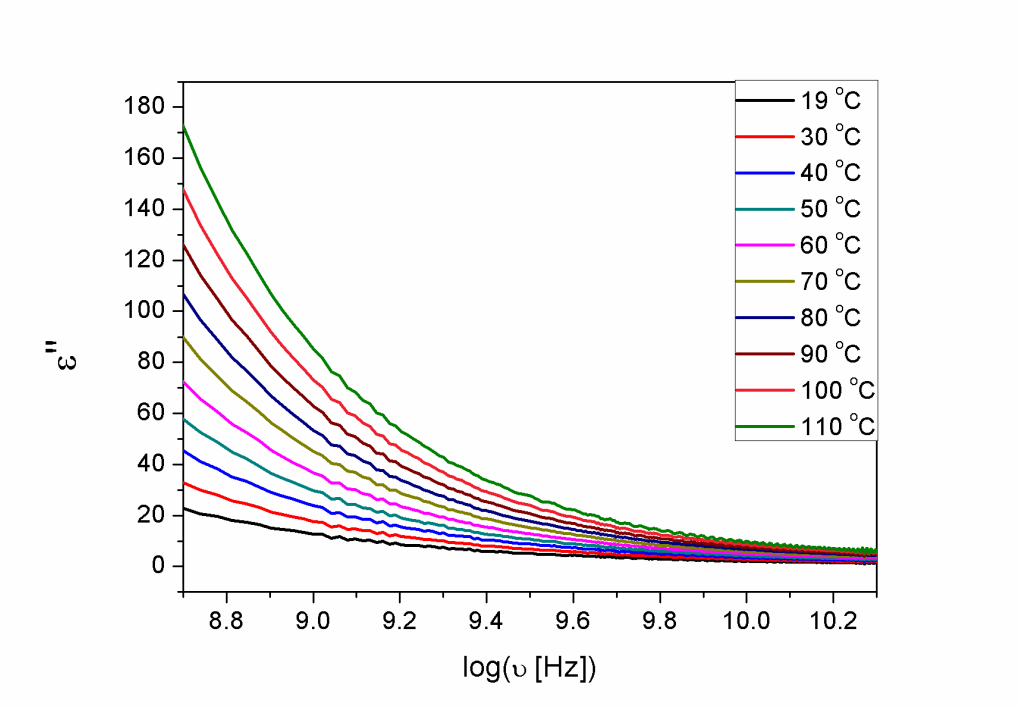



*Figure 4-9 Imaginary part of dielectric function ε''(υ) versus frequency at different temperatures for $[C_1C_4Im][InCl_4]$, STDEV 0.02-1.8.*

Figure 4-10 displays the real part of the dielectric function for $[C_1C_4Im]_2[ZnCl_4]$. As previously described for other samples the dielectric constant increases with increasing temperature. However, an exception can be noted here for ε' taken at 60°C, which displayed the lowest values measured. Interestingly, DSC (Figure 2-20) showed an endothermic melting peak around the same temperature. Overall, the dielectric constant shows temperature dependence and a decline in ε' with increasing frequency.

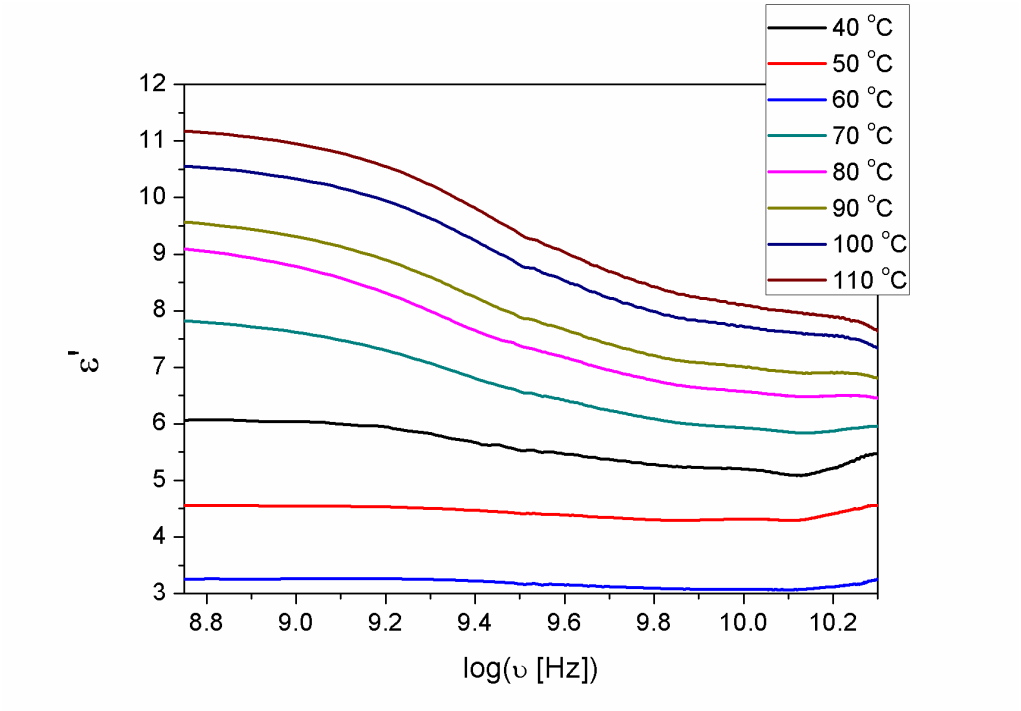



*Figure 4-10 Real part of dielectric function ε'(υ) versus frequency at different temperatures for $[C_1C_4Im]_2[ZnCl_4]$. The data was exponentially smoothed for clarity, STDEV 0.007-0.1.*

The loss factor for $[C_1C_4Im]_2[ZnCl_4]$ (Figure 4-11) displays a temperature dependence at a lower frequency but not with increasing frequency. Furthermore, it seems that at a higher frequency the slim probe is not able to give a significant measurement, as the values obtained are negative. Similarly, the imaginary part ε'' of the dielectric function displays similar behaviour, as ε' around the temperature of phase transition shown by the IL.

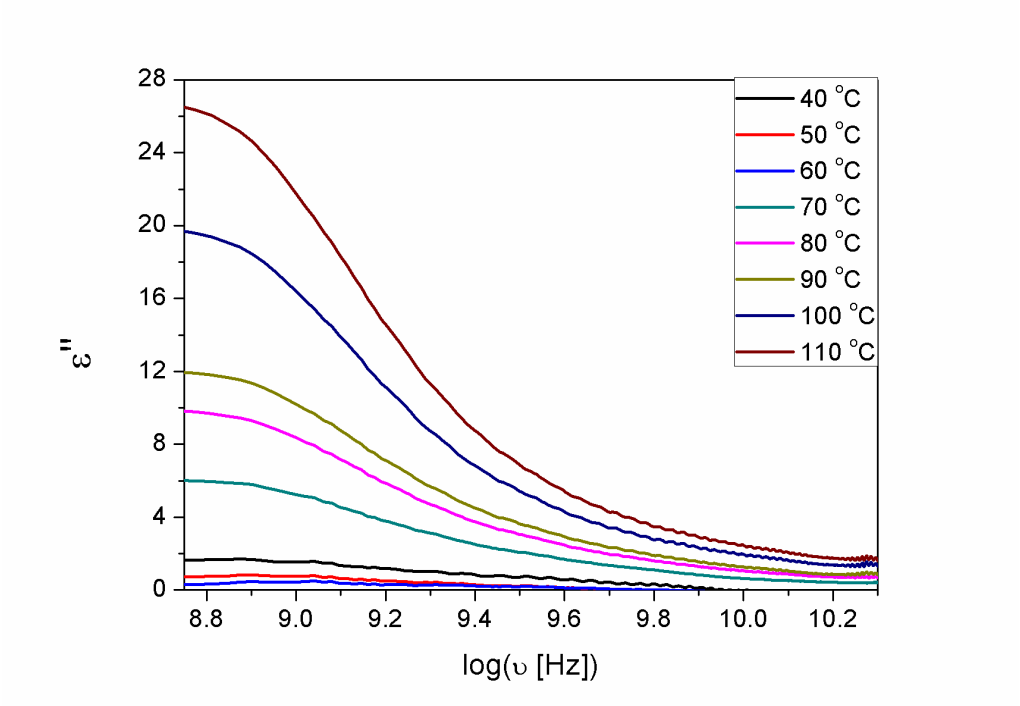



*Figure 4-11 Imaginary part of dielectric function ε''(υ) versus frequency at different temperatures for $[C_1C_4Im]_2[ZnCl_4]$. The data was exponentially smoothed for clarity, STDEV 0.004-0.5.*

The real part ε' of $[C_1C_4Im]_2[CuCl_4]$ (Figure 4-12) clearly shows a temperature and frequency dependence. Interestingly at 100°C, the dielectric constant diminishes in value below the values observed for 80 and 90°C. In other respects, ε' demonstrates analogous behaviour to the other ILs, where the dielectric constant decreases with increasing frequency.

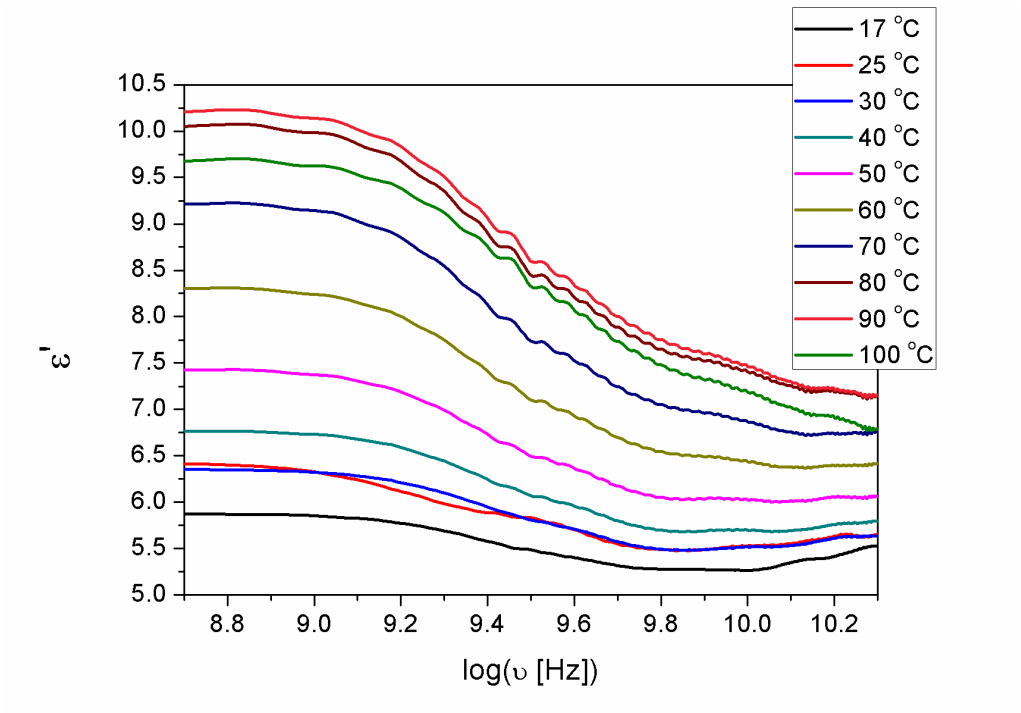



*Figure 4-12 Real part of dielectric function ε'(υ) versus frequency at different temperatures for $[C_1C_4Im]_2[CuCl_4]$. The data was exponentially smoothed for clarity, STDEV 0.0001-0.08.*

Figure 4-13 displays the imaginary part of the dielectric function ε(υ) for $[C_1C_4Im]_2[CuCl_4]$. Same as the real part ε', the imaginary part ε'' shows negative values at low temperatures and high frequencies. Generally, temperature dependence can be observed, especially in the lower frequency range. In addition, a big difference is noticeable at low frequencies with increasing temperature for the loss factor, displaying an increase of a factor of 30. At the same time, a steep decline can be detected towards higher frequency.

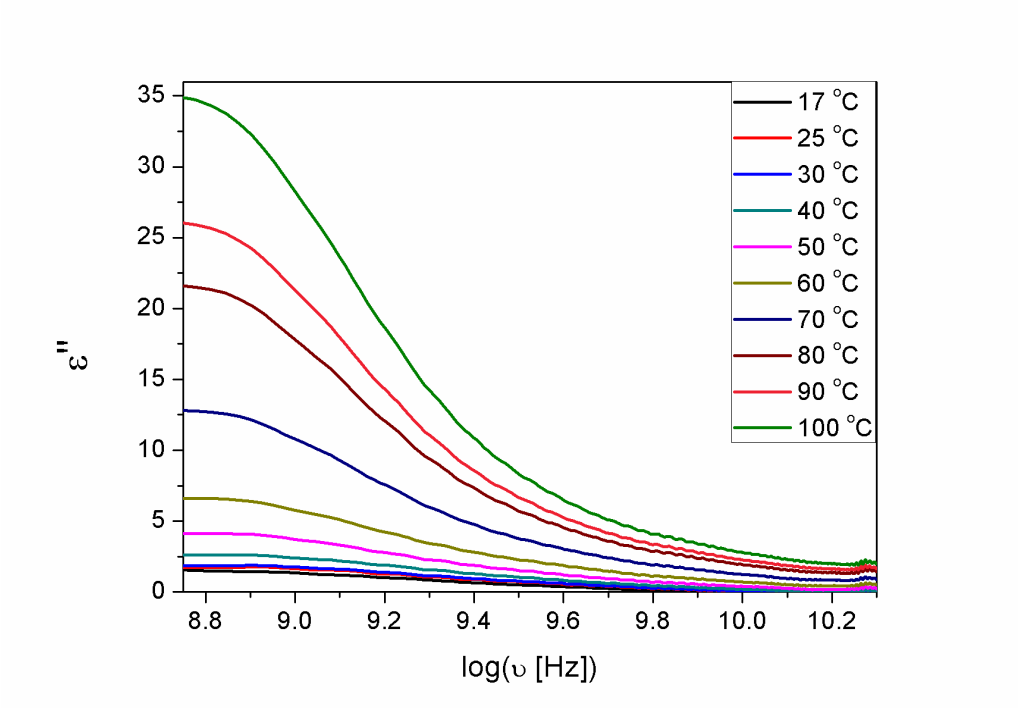



*Figure 4-13 Imaginary part of dielectric function ε''(υ) versus frequency at different temperatures for $[C_1C_4Im]_2[CuCl_4]$. The data was exponentially smoothed for clarity, STDEV 0.003-2.*

The real part ε' for $[C_1C_4Im]_2[NiCl_4]$ (Figure 4-14) again displays temperature dependence for the dielectric constant. Furthermore, the constant decreases with increasing frequency, as observed previously for the investigated ILs within this work. Nevertheless, a slight curve and incline can be observed at 19 GHz.

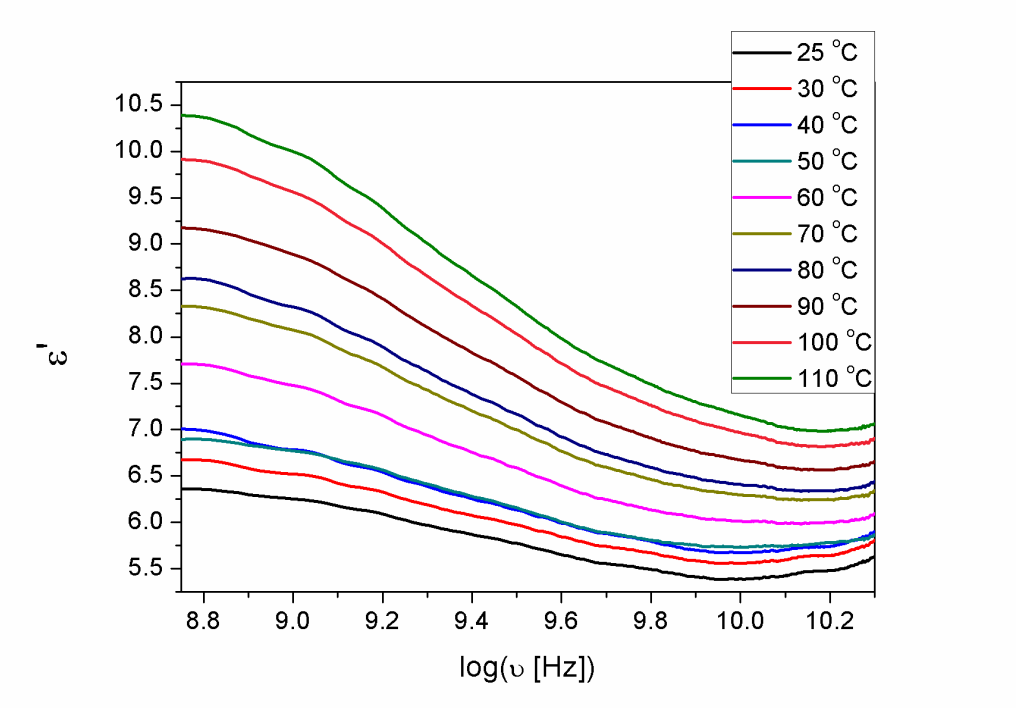



*Figure 4-14 Real part of dielectric function ε'(υ) versus frequency at different temperatures for $[C_1C_4Im]_2[NiCl_4]$. The data was exponentially smoothed for clarity, STDEV 0.003-0.2.*

Figure 4-15 displays the imaginary part of the dielectric function ε(υ) for $[C_1C_4Im]_2[NiCl_4]$. Same as the real part ε', the imaginary part ε'' shows negative values at low temperatures and high frequency. Generally, temperature dependence can be observed, especially in the lower frequency range. In addition, a big difference is noticeable at low frequency with increasing temperature for the loss factor, displaying an increase of a factor of 10. At the same time, a steep decline can be detected towards higher frequency.

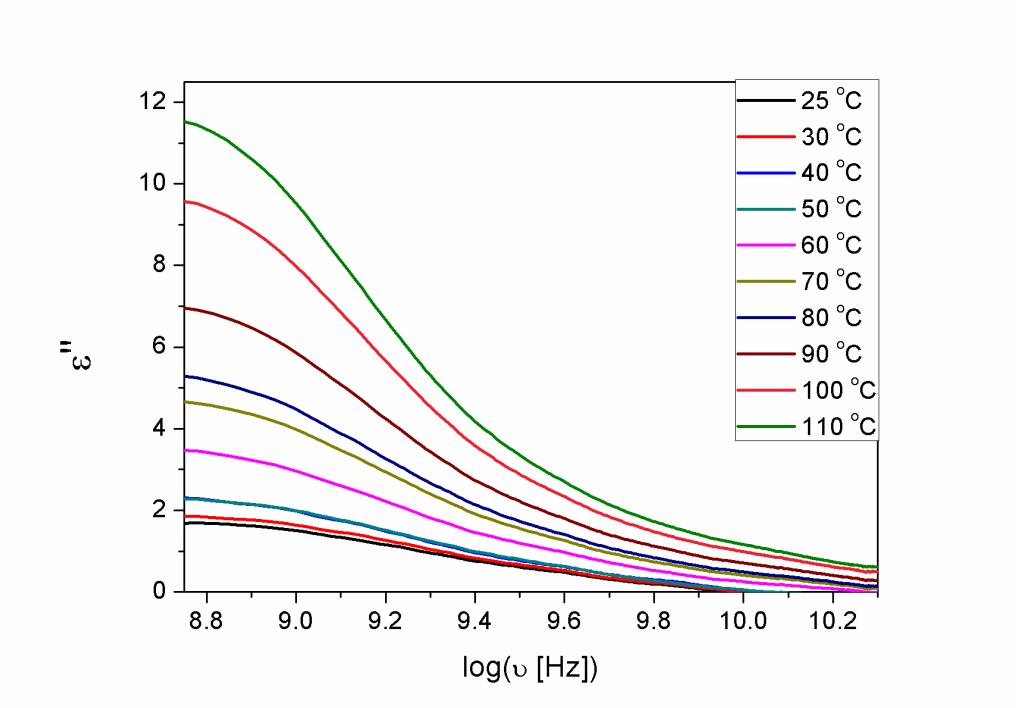



*Figure 4-15 Imaginary part of dielectric function ε''(υ) versus frequency at different temperatures for $[C_1C_4Im]_2[NiCl_4]$. The data was exponentially smoothed for clarity, STDEV 0.007-0.9.*

The real part ε' for $[C_1C_4Im]_2[CoCl_4]$ (Figure 4-16) again displays temperature dependence for the dielectric constant. Furthermore, the constant decreases with increasing frequency, as observed previously for the investigated ILs within this work. Nevertheless, a slight curve and incline can be observed at 19 GHz, which is unexpected.

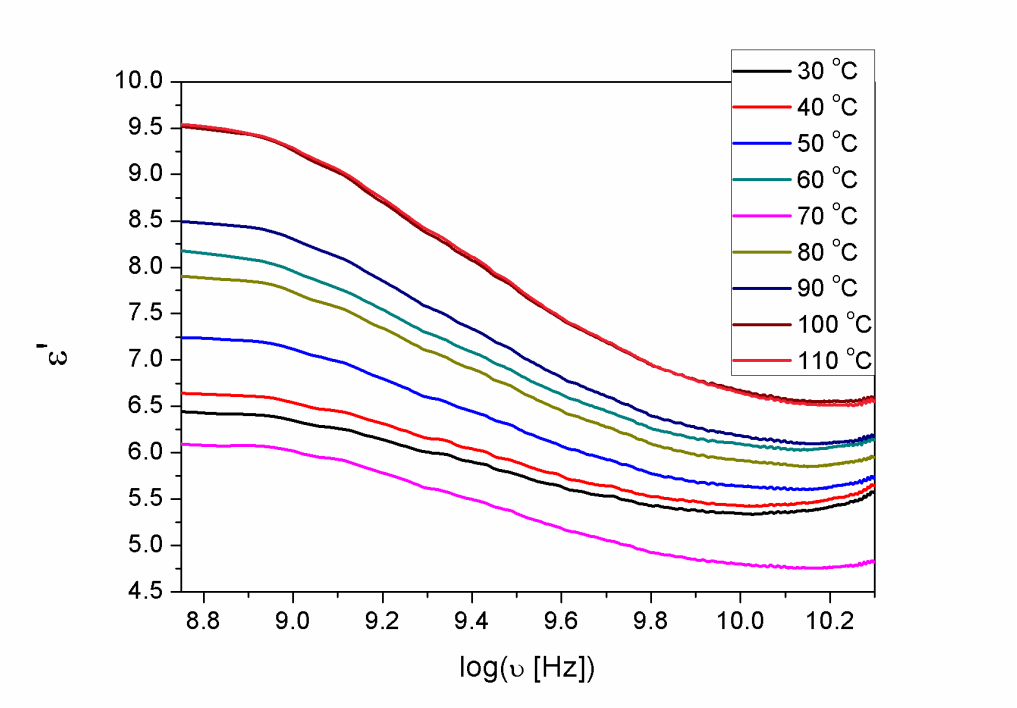



*Figure 4-16 Real part of dielectric function ε'(υ) versus frequency at different temperatures for $[C_1C_4Im]_2[CoCl_4]$. The data was exponentially smoothed for clarity, STDEV 0.01-0.3.*

Figure 4-17 displays the imaginary part of the dielectric function ε(υ) for $[C_1C_4Im]_2[CoCl_4]$. Same as the real part ε', the imaginary part ε'' shows negative values at low temperatures and high frequency. Generally, temperature dependence can be observed, especially in the lower frequency range. In addition, a large difference is noticeable at low frequency with increasing temperature for the loss factor, displaying an increase of a factor of 8. At the same time, a steep decline can be detected towards higher frequency.

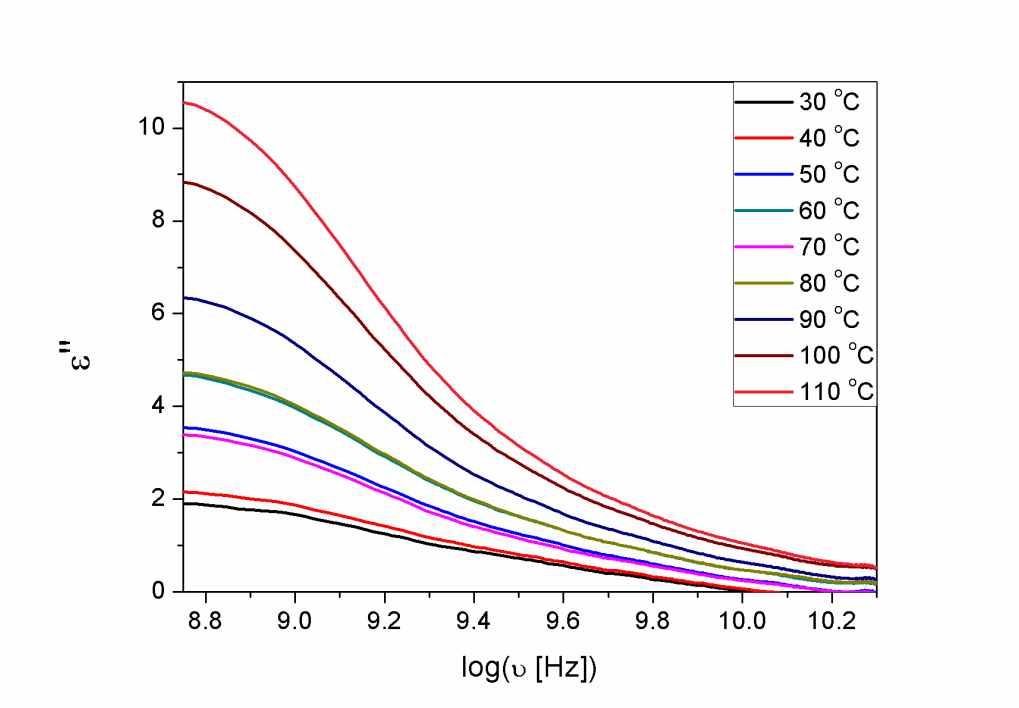



*Figure 4-17 Imaginary part of dielectric function ε''(υ) versus frequency at different temperatures for $[C_1C_4Im]_2[CoCl_4]$. The data was exponentially smoothed for clarity, STDEV 0.02-0.7.*

### 4.5.2 Variation with increasing temperature

The data obtained from dielectric spectroscopy was further analysed to explore temperature dependence. For this reason, two frequencies commonly used in MW reactions were selected for further investigation. Error bars are added to the graphs calculated from three repeat measurements for each temperature.

Figure 4-18 shows the real and imaginary part of the dielectric function ε(υ) for $[C_1C_4Im][FeCl_4]$ at the selected frequencies 0.9 and 2.45 GHz obtained with a coaxial slim probe. The imaginary part does not display any difference between the selected frequencies. A linear increase can be observed with increasing temperature. On the other hand, the real part at 0.9 GHz shows a maximum for ε' at 70°C, whereas at 2.45 GHz a maximum is reached at 100°C followed by a plateau.

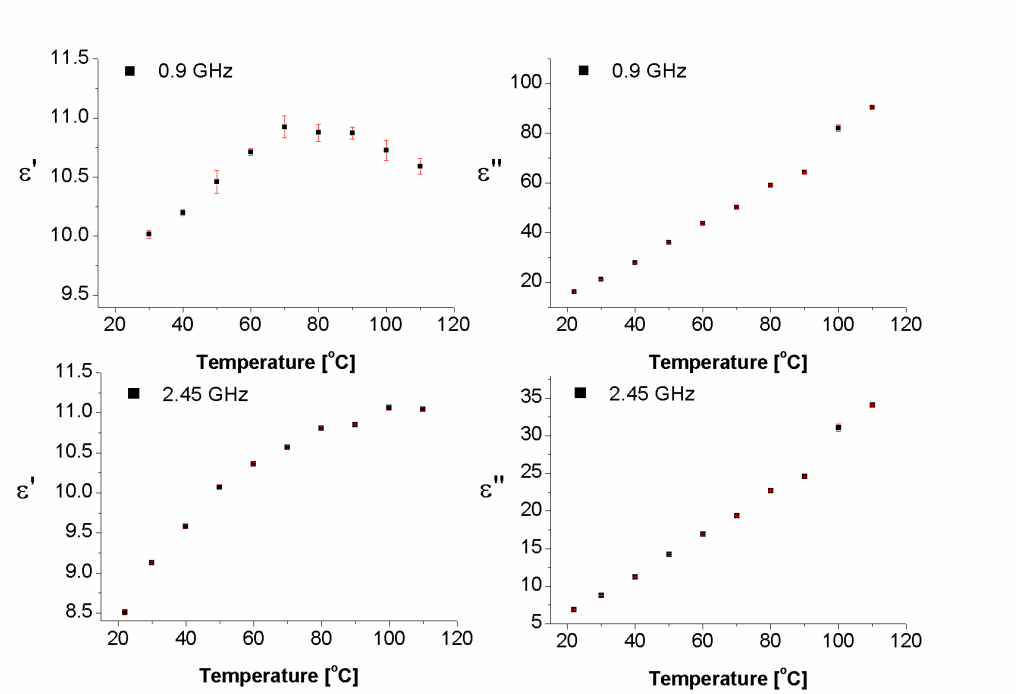



*Figure 4-18 Real ε'(υ) and imaginary ε''(υ) part of dielectric function versus temperature at 0.9 GHz and 2.45 GHz for [$C_1C_4$Im][$FeCl_4$]. The average of three measurements with a slim probe is shown.*

[$C_1C_4$Im][$InCl_4$] (Figure 4-19) demonstrates a comparable behaviour to [$C_1C_4$Im][$FeCl_4$]. The imaginary part does not display any difference between the selected frequencies, but a linear increase can be observed with increasing temperature. On the other hand, the real part at 0.9 GHz shows a maximum for ε' at 70°C, whereas at 2.45 GHz a maximum is reached at 100°C followed by a plateau.

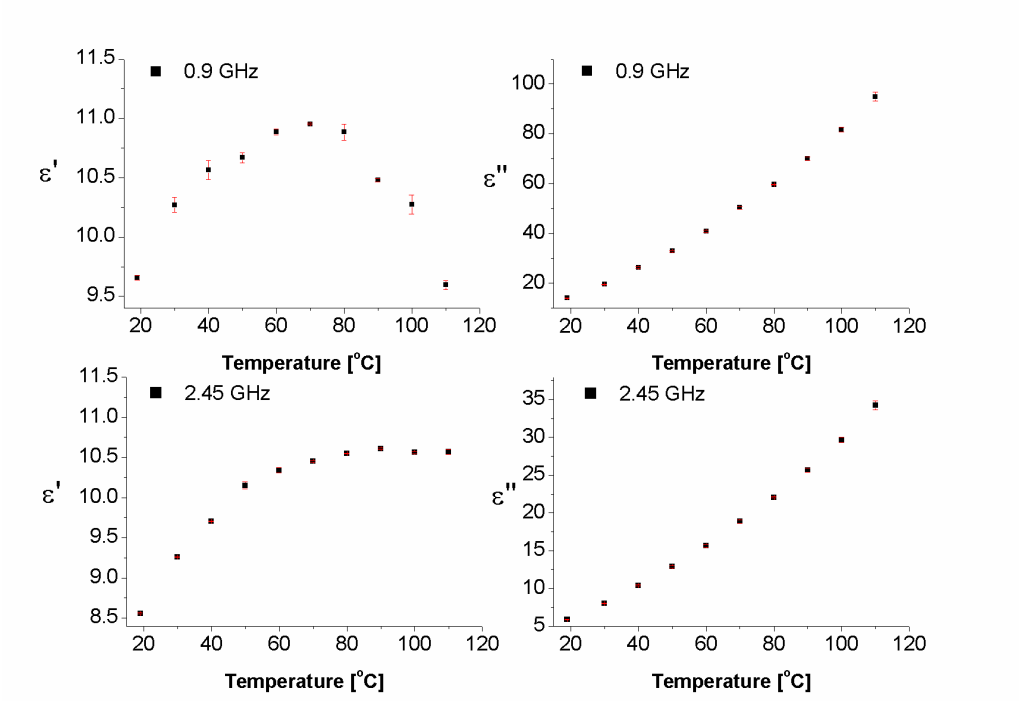



*Figure 4-19 Real ε'(υ) and imaginary ε''(υ) part of dielectric function versus temperature at 0.9 GHz and 2.45 GHz for $[C_1C_4Im][InCl_4]$. The average of three measurements with a slim probe is shown.*

Figure 4-20 shows the real and imaginary part of the dielectric function ε(υ) for $[C_1C_4Im]_2[ZnCl_4]$ at the selected frequencies 0.9 and 2.45 GHz obtained with a coaxial slim probe. Two different regimes can be observed for ε' and ε'' below and above the phase transition observed with DSC ($T_m$ = 53°C; Figure 2-20). From 40 to 60°C a decline in ε' is observed at 0.9 and 2.45 GHz, which then changes into a linear increase from 70°C onwards. For the imaginary part ε'' a similar trend can be noted. Between 40 to 60°C the loss factor is close to zero but increases linearly afterwards to over 15 at 0.9 GHz and over 7 at 2.45 GHz (110°C).

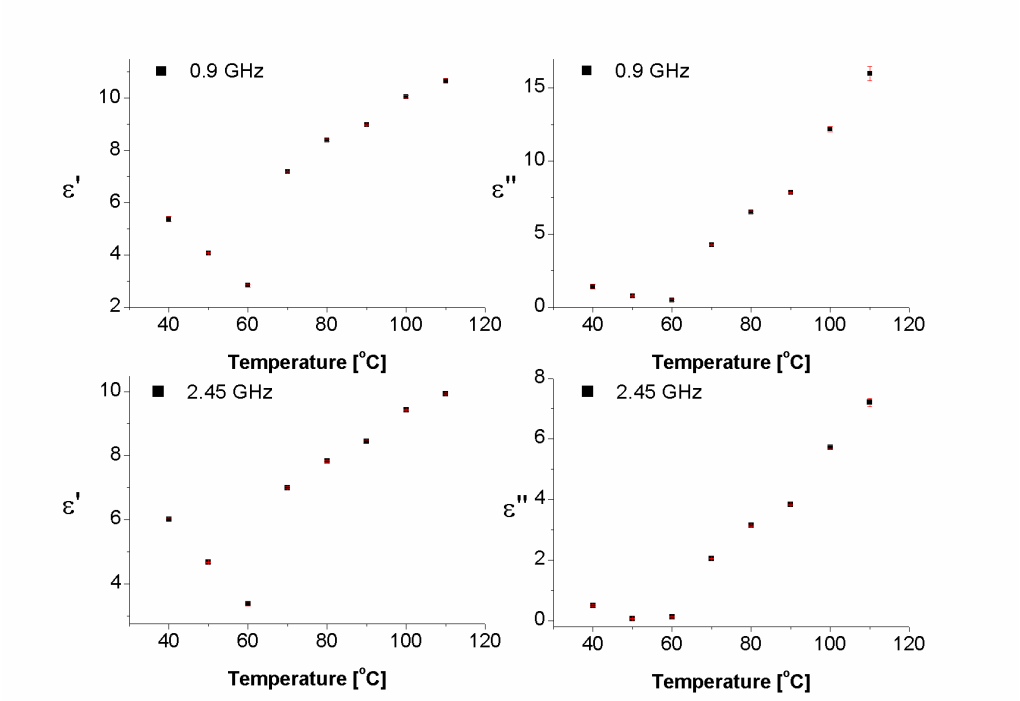



*Figure 4-20 Real ε'(υ) and imaginary ε''(υ) part of dielectric function versus temperature at 0.9 GHz and 2.45 GHz for $[C_1C_4Im]_2[ZnCl_4]$. The average of three measurements with a slim probe is shown.*

Figure 4-21 shows the real and imaginary part of the dielectric function ε(υ) for $[C_1C_4Im]_2[CuCl_4]$ at the selected frequencies 0.9 and 2.45 GHz obtained with a coaxial slim probe. The imaginary part does not display any difference between the selected frequencies. An exponential increase can be observed with increasing temperature. On the other hand, the real part ε' shows a maximum at 90°C for 0.9 and 2.45 GHz.

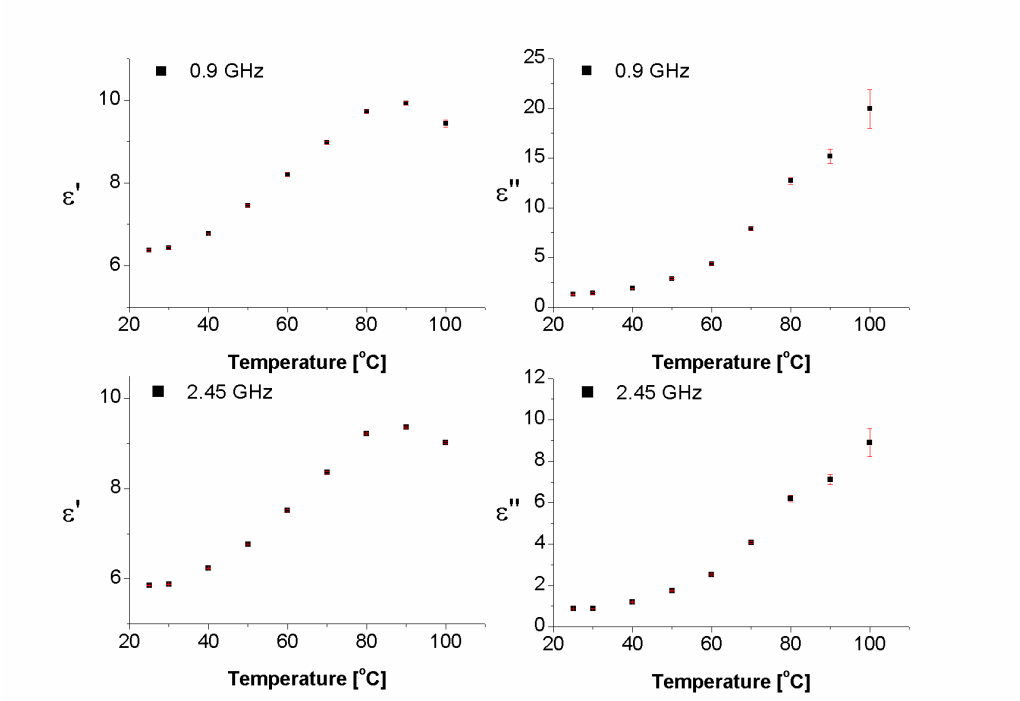



*Figure 4-21 Real ε'(υ) and imaginary ε''(υ) part of dielectric function versus temperature at 0.9 GHz and 2.45 GHz for $[C_1C_4Im]_2[CuCl_4]$. The average of three measurements with a slim probe is shown.*

$[C_1C_4Im]_2[NiCl_4]$ was probed further with a second technique, resonance perturbation cavity. Due to its many phase transitions (**5.4.1 Thermal analysis**) it was expected to show more complex relaxation mechanisms. Figure 4-22 shows the real and imaginary part of the dielectric function at 0.9 GHz measured with the coaxial slim probe and the resonance perturbation cavity. The cavity generally displays a higher sensitivity for measurements, which can make measurements of highly conductive samples challenging. Utmost care was taken for these measurements and a reproducible result was obtained when using the cavity. Again, these measurements were repeated three times for each temperature measured and the standard deviation was calculated. The real part ε' displays slightly higher values, when measured with the cavity. This could be due to the higher sensitivity towards materials presenting a high loss and a difference between measurements of large volume (probe 20 mL)

and small volume (cavity 0.01 mL). Interestingly, ε' demonstrates a drop in value around the melting point (onset $T_m$ = 57°C; **5.4.1 Thermal analysis**, **Figure 5-13**) of the sample. This could be due to the change in volume as the sample transitions from solid to liquid. In contrast, a peak in the loss factor can be noted around the same temperature. Measurements carried out with the coaxial slim probe show an almost linear increase for ε' and ε''.

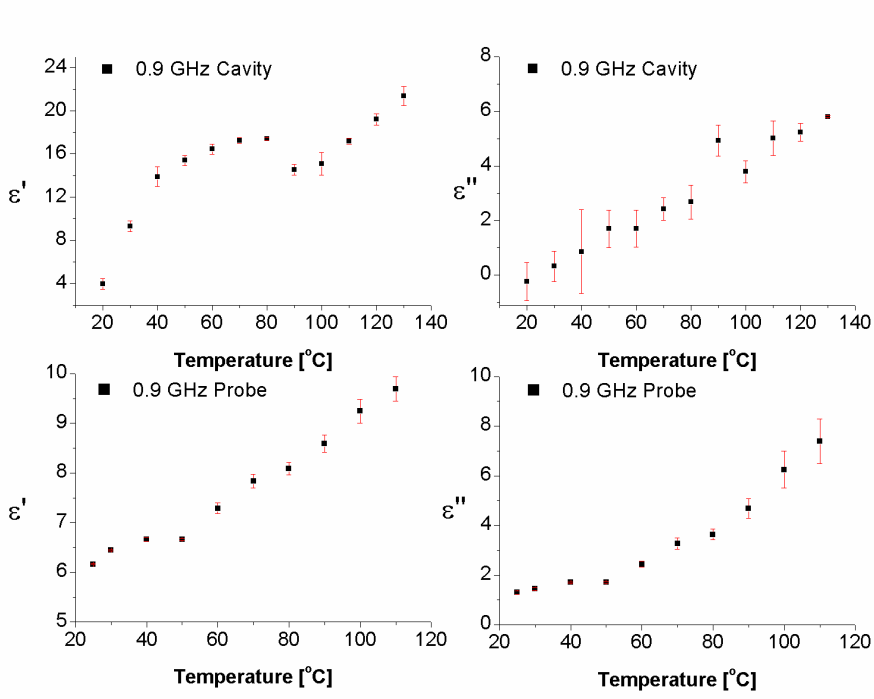



*Figure 4-22 Real ε'(υ) and imaginary ε''(υ) part of dielectric function versus temperature at 0.9 GHz for $[C_1C_4Im]_2[NiCl_4]$. The average of three measurements with a slim probe and a resonant perturbation cavity is shown.*

Figure 4-23 displays the results obtained for $[C_1C_4Im]_2[NiCl_4]$ at 2.45 GHz with the resonance perturbation cavity and the coaxial slim probe at different temperatures. The same behaviour can be observed as at 0.9 GHz but less of a difference in obtained values is noticed.

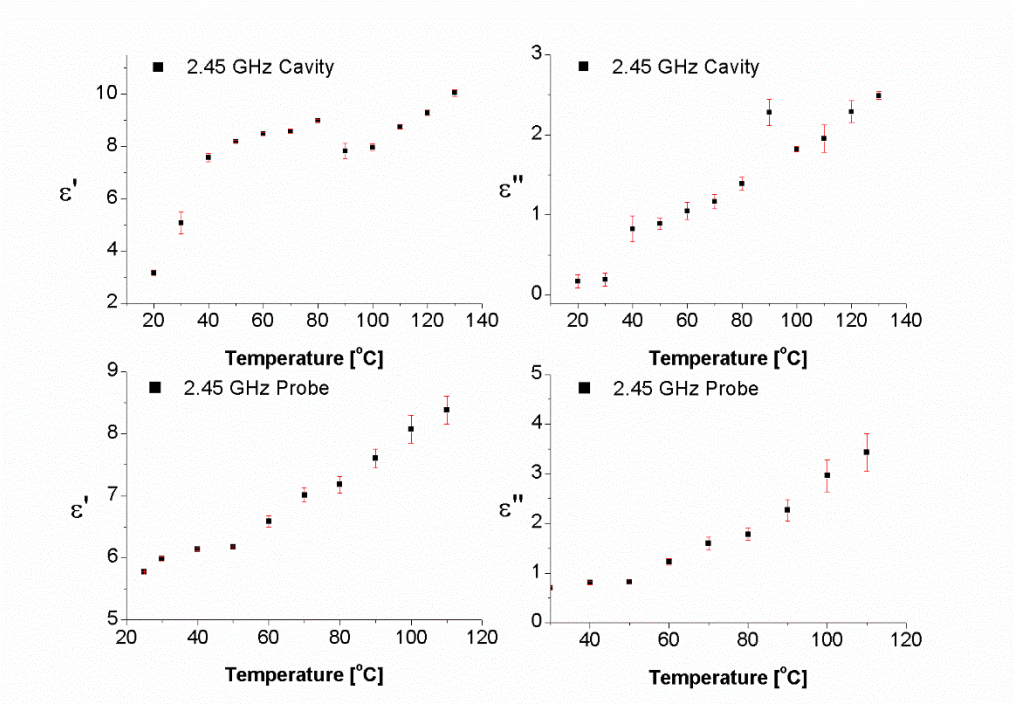



*Figure 4-23 Real ε'(υ) and imaginary ε''(υ) part of dielectric function versus temperature at 2.45 GHz for $[C_1C_4Im]_2[NiCl_4]$. The average of three measurements with a slim probe and a resonant perturbation cavity is shown.*

$[C_1C_4Im]_2[CoCl_4]$ was also selected to test the possibility of using the resonance perturbation cavity for higher loss materials. Figure 4-24 shows results at 0.9 GHz measured with the coaxial slim probe and the resonance perturbation cavity at increasing temperature. In comparison with $[C_1C_4Im]_2[NiCl_4]$ (Figure 4-23), the cavity has produced a more linear response for $[C_1C_4Im]_2[CoCl_4]$, than previously for $[C_1C_4Im]_2[NiCl_4]$. In the case of $[C_1C_4Im]_2[CoCl_4]$, the coaxial slim probe shows a drop in ε' and ε'' below the glass transition (**5.1.1 Thermal analysis**, **Figure 5-4**), indicating a change in response due to the phase transition.

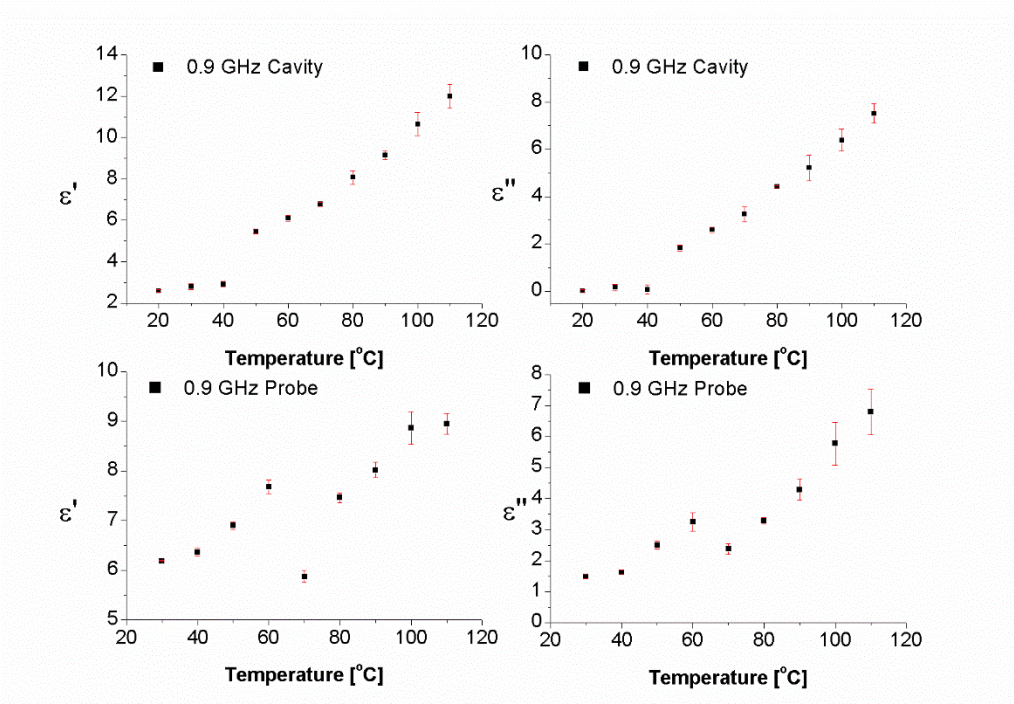



*Figure 4-24 Real ε'(υ) and imaginary ε''(υ) part of dielectric function versus temperature at 0.9 GHz for $[C_1C_4Im]_2[CoCl_4]$. The average of three measurements with a slim probe and a resonant perturbation cavity is shown.*

Figure 4-25 displays the results obtained for $[C_1C_4Im]_2[CoCl_4]$ at 2.45 GHz with the resonance perturbation cavity and the coaxial slim probe at different temperatures. The same behaviour can be observed as at 0.9 GHz and no difference in obtained values is noticed as was the case for $[C_1C_4Im]_2[NiCl_4]$.

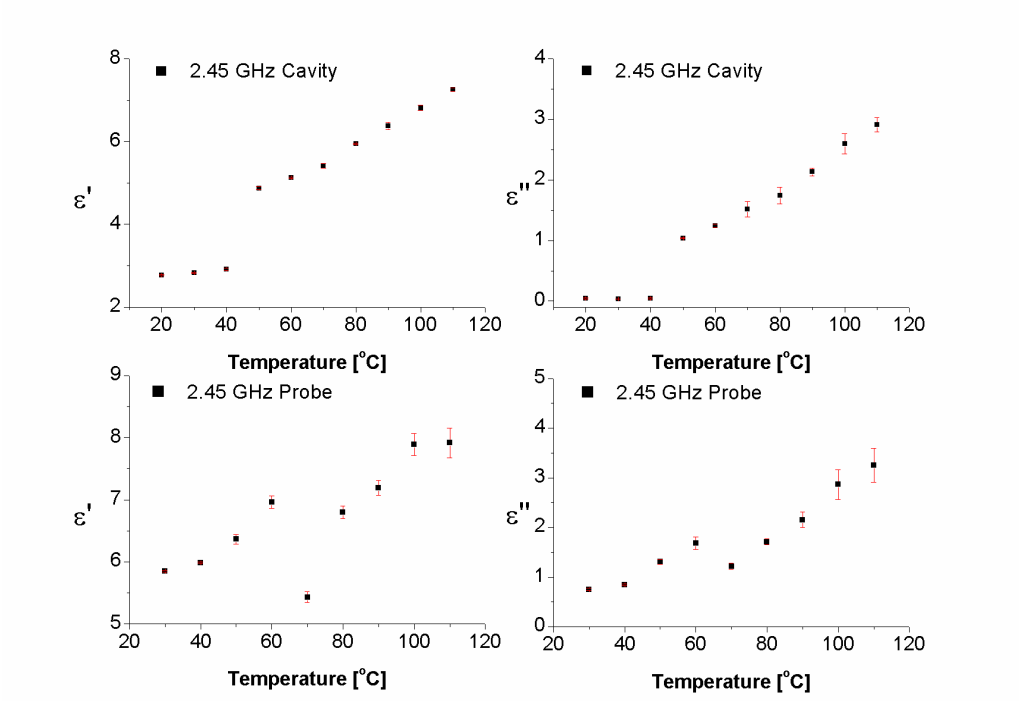



*Figure 4-25 Real ε'(υ) and imaginary ε''(υ) part of dielectric function versus temperature at 2.45 GHz for $[C_1C_4Im]_2[CoCl_4]$. The average of three measurements with a slim probe and a resonant perturbation cavity is shown.*

$[C_1C_4Im][Fe(NO)_2Cl_2]$ is a new IL and the synthesis of large quantities remains a challenge. Therefore, the use of the coaxial slim probe would be difficult as the necessary volume for measurements is approximately 20 mL. As demonstrated previously, it is possible however to use the resonance perturbation cavity for ILs. In consequence, the cavity was used to determine the real and imaginary part of the dielectric function at 0.9 and 2.45 GHz shown in Figure 4-26. As was previously determined the decomposition temperature is 125°C (Figure 2-3) hence caution was being taken to avoid decomposition during the measurements. At both frequencies, a slow incline of dielectric constant and loss can be observed with a drop at 40°C. Unfortunately, no significant phase transitions could be observed with the help of DSC.

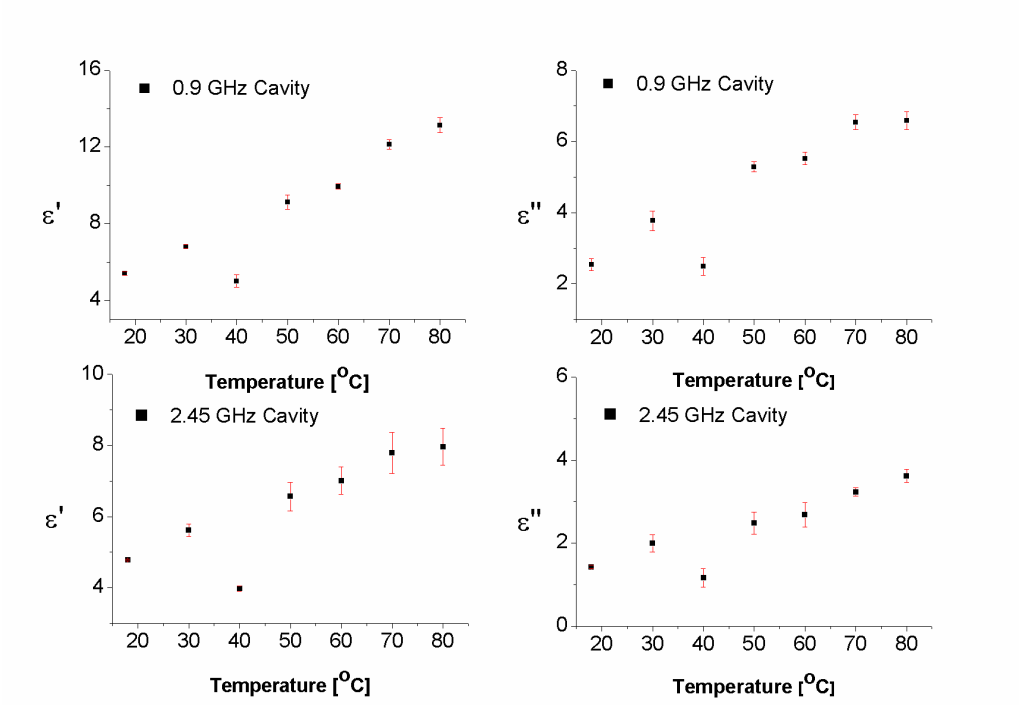



*Figure 4-26 Real ε'(υ) and imaginary ε''(υ) part of dielectric function versus temperature at 0.9 GHz and 2.45 GHz for $[C_1C_4Im][Fe(NO)_2Cl_2]$. The average of three measurements with a resonance perturbation cavity is shown.*

### 4.5.3 Calculation of conductivity

Conductivity was calculated from data obtained with the coaxial slim probe as it provides a wide frequency range and sufficient data to give significant results. The following Equation was used,

$$\sigma = 2\pi\varepsilon'\varepsilon_0 \qquad [4\text{-}13]$$

where $\sigma$ is the conductivity, $\varepsilon'$ the real part of the dielectric function, and $\varepsilon_0$ the dielectric permittivity of vacuum.

Figure 4-27 shows the dependence of the conductivity regarding frequency and temperature for $[C_1C_4Im][FeCl_4]$. It can be observed, that the conductivity stays constant for most of the frequency range measured and increases with increasing temperature. However, towards 20 GHz the conductivity begins to increase exponentially.

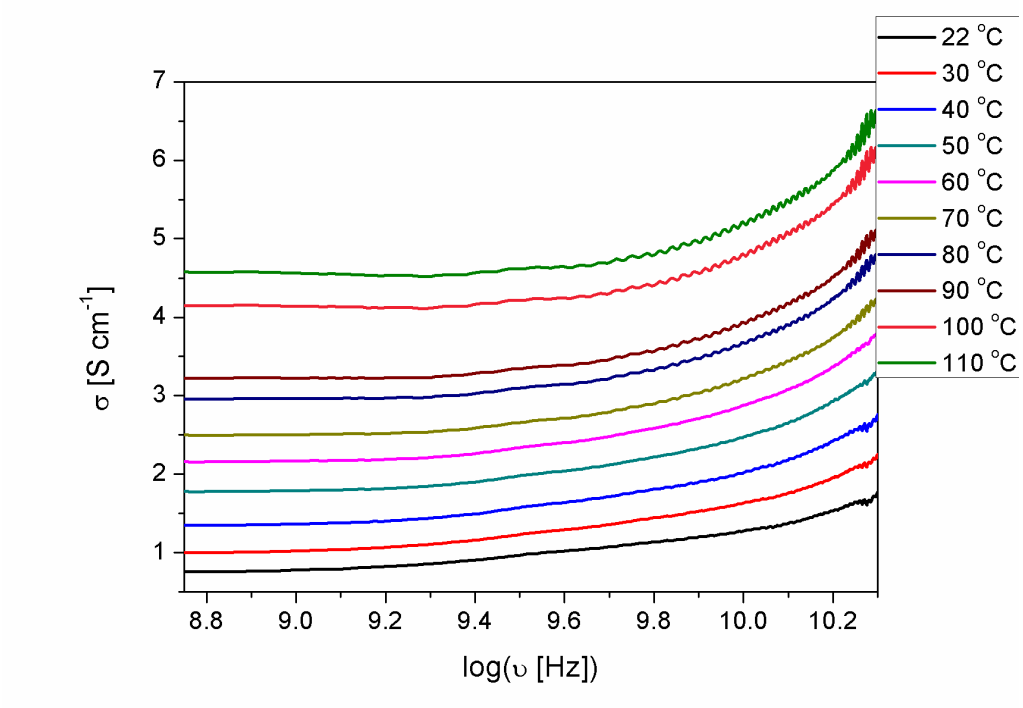



*Figure 4-27 Conductivity σ(υ) plotted against the frequency at different temperatures for [$C_1C_4$Im][$FeCl_4$]. The data was exponentially smoothed for clarity.*

[$C_1C_4$Im][$InCl_4$] (Figure 4-28) displays a similar behaviour to [$C_1C_4$Im][$FeCl_4$] (Figure 4-27). Constant values obtained for conductivity over a wide frequency range and only towards 20 GHz an increase is noticed. Furthermore, a continuous increase in conductivity with increasing temperature can be observed.

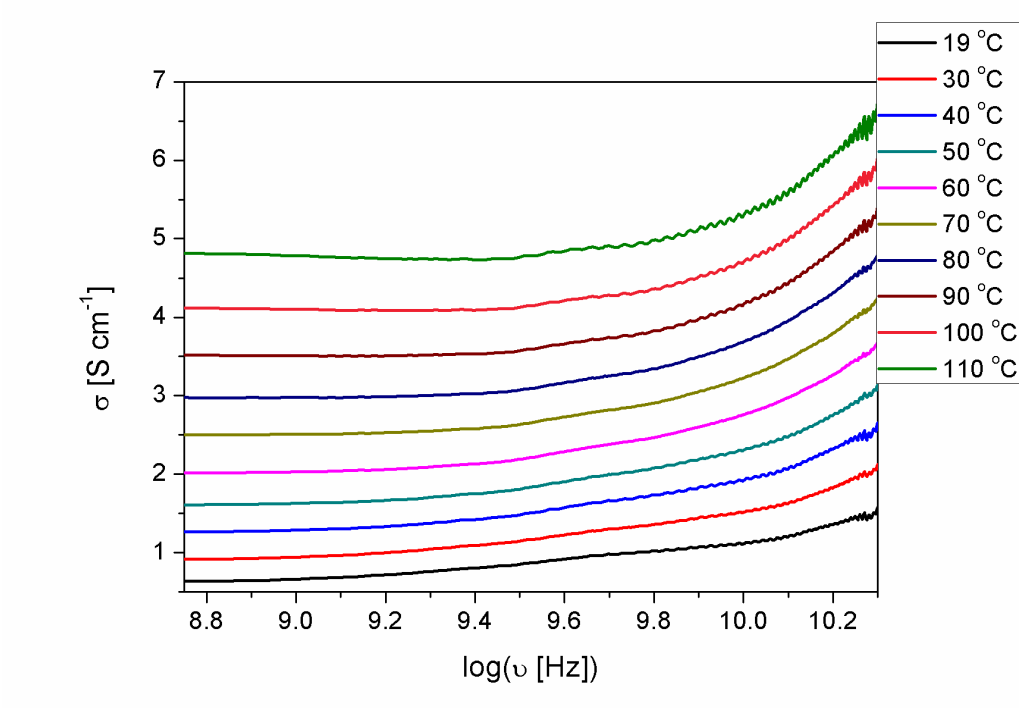



*Figure 4-28 Conductivity σ(υ) plotted against the frequency at different temperatures for $[C_1C_4Im][InCl_4]$. The data was exponentially smoothed for clarity.*

Figure 4-29 shows the conductivity calculated for $[C_1C_4Im]_2[ZnCl_4]$ at changing frequency and with increasing temperature. A difference can be observed with changing the temperature at high frequencies. Below 70°C a decrease in conductivity can be observed at higher frequencies and above 70°C an increase in conductivity is apparent. Again, this observation coincides with the end of the melting point of $[C_1C_4Im]_2[ZnCl_4]$ (Figure 2-20), indicating that this phase transition changes the behaviour of the IL.

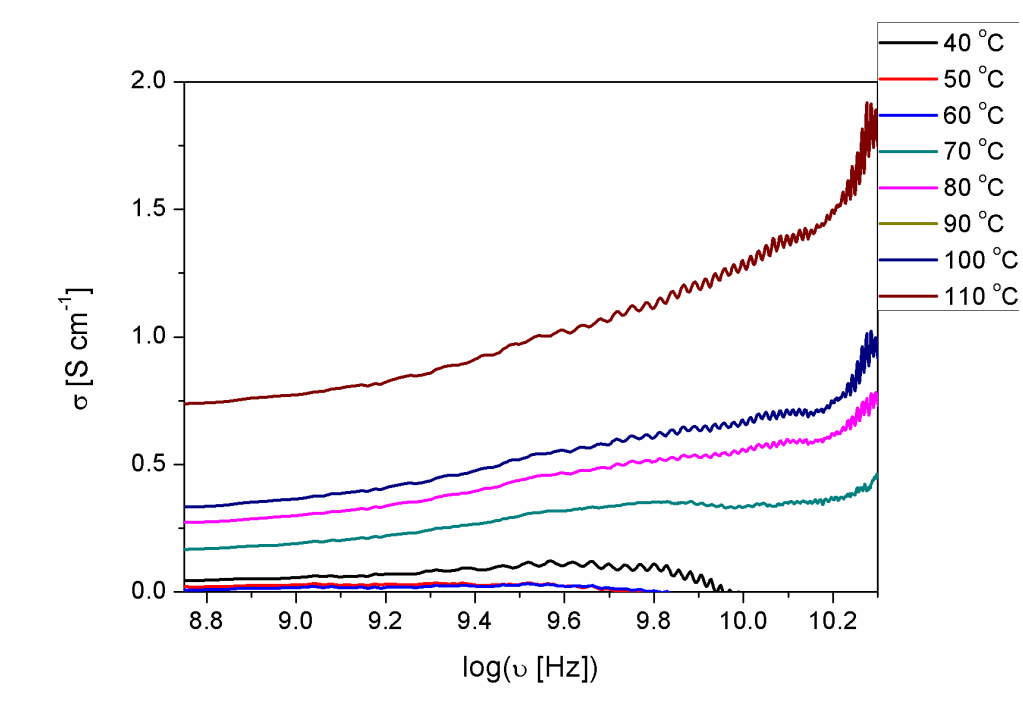



*Figure 4-29 Conductivity σ(υ) plotted against the frequency at different temperatures for $[C_1C_4Im]_2[ZnCl_4]$. The data was exponentially smoothed for clarity.*

$[C_1C_4Im]_2[CuCl_4]$ (Figure 4-30) displays a similar behaviour as $[C_1C_4Im][FeCl_4]$ and $[C_1C_4Im][InCl_4]$ but with a more linear response at low temperature (up to 60°C). In addition, a peak can be observed at approximately 20 GHz above room temperature.

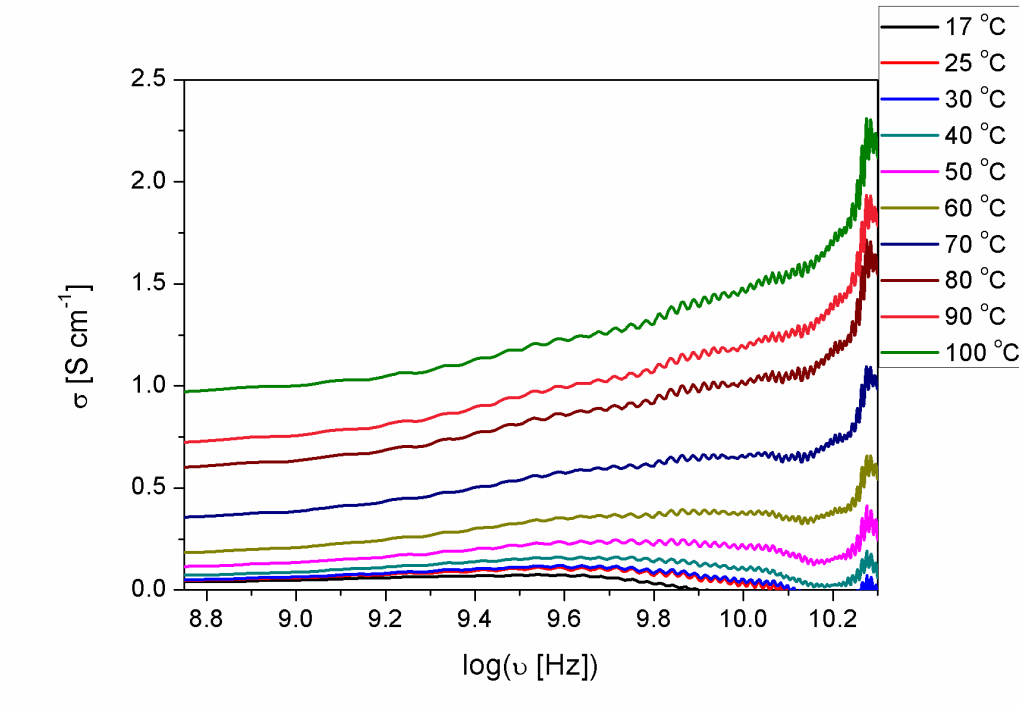



*Figure 4-30 Conductivity σ(υ) plotted against the frequency at different temperatures for $[C_1C_4Im]_2[CuCl_4]$. The data was exponentially smoothed for clarity.*

Figure 4-31 shows the conductivity calculated for $[C_1C_4Im]_2[NiCl_4]$ at changing frequency and with increasing temperature. In contrast, $[C_1C_4Im]_2[NiCl_4]$ demonstrates decreasing conductivity at increasing frequency, after a slight incline in conductivity. This can be especially observed at lower temperatures, whereas at higher temperatures a plateau is reached.

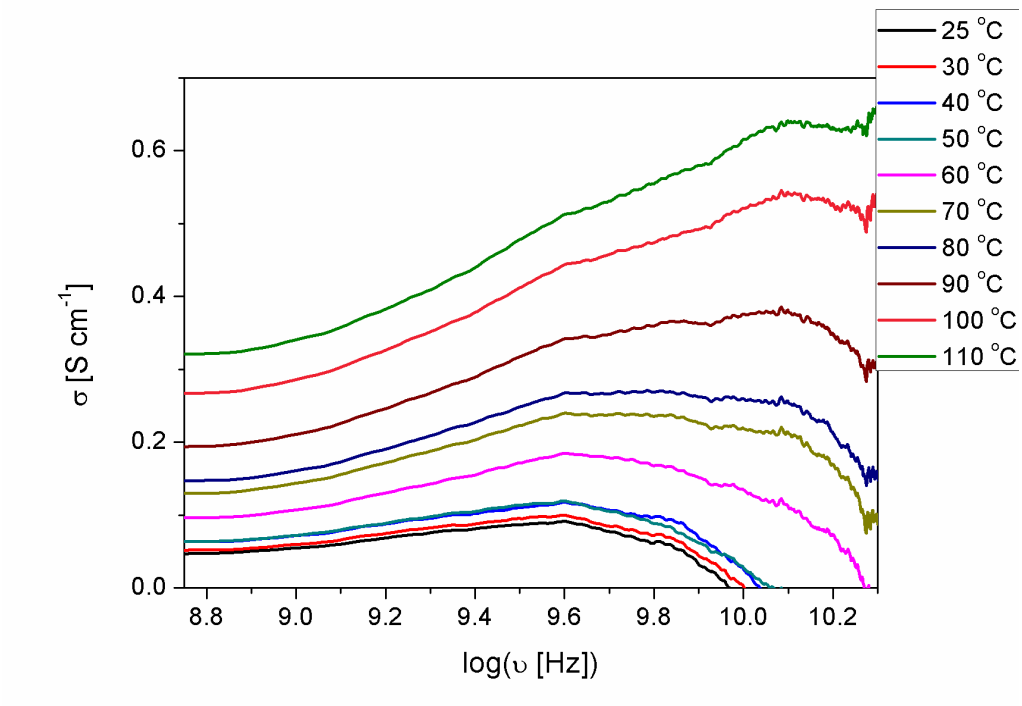



*Figure 4-31 Conductivity σ(υ) plotted against the frequency at different temperatures for $[C_1C_4Im]_2[NiCl_4]$. The data was exponentially smoothed for clarity.*

$[C_1C_4Im]_2[CoCl_4]$ (Figure 4-32) exhibits comparable conductivity and nature like $[C_1C_4Im]_2[NiCl_4]$ (Figure 4-31), where after a small increase the conductivity declines at high frequency.

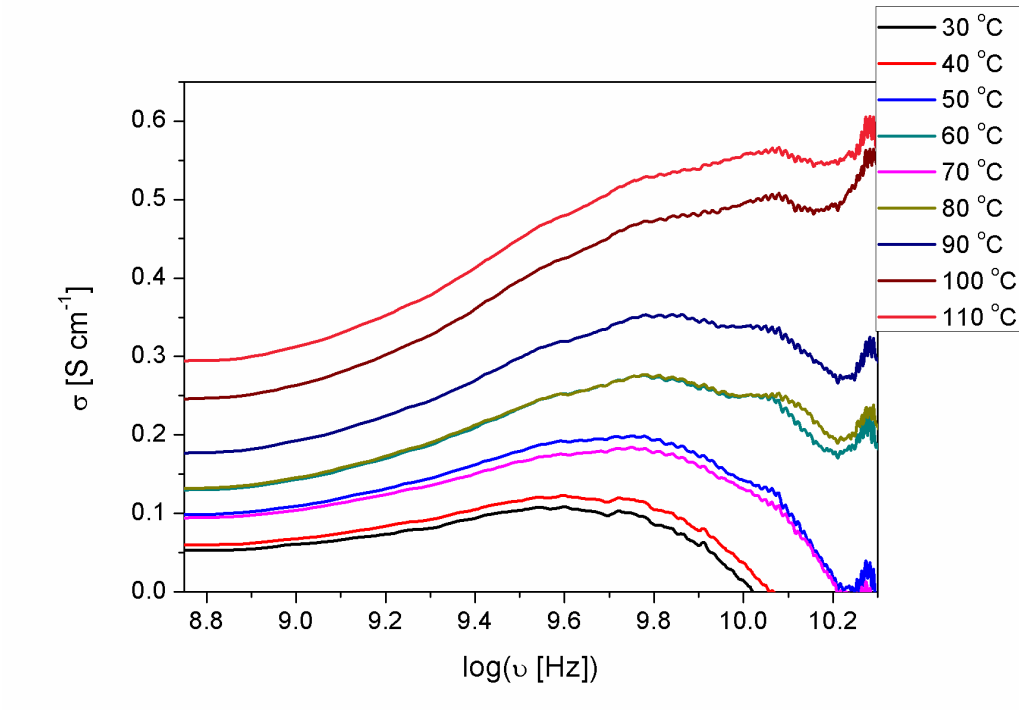



*Figure 4-32 Conductivity σ(υ) plotted against the frequency at different temperatures for $[C_1C_4Im]_2[CoCl_4]$. The data was exponentially smoothed for clarity.*

### 4.5.4 Conductivity and phase transitions

The following graphs highlight the relation between conductivity and temperature at selected frequencies (0.9, 2.45 and 10 GHz). For $[C_1C_4Im]_2ZnCl_4$ and $[C_1C_4Im]_2[CuCl_4]$ negative values were obtained at 10 GHz, as the sensitivity of the coaxial probe was exceeded. Therefore, these values were disregarded, as they did not represent a true response. Standard deviation was calculated for all values but in most cases, the error bars are smaller than the point they are corresponding to and therefore are not visible on the graph.

Figure 4-33 displays values obtained for $[C_1C_4Im][FeCl_4]$ versus inverse temperature. A linear response is observed to all frequencies, with a slight bend at 100°C. And, as previously observed an increase of conductivity is noticed with increasing frequency, especially at 10 GHz.

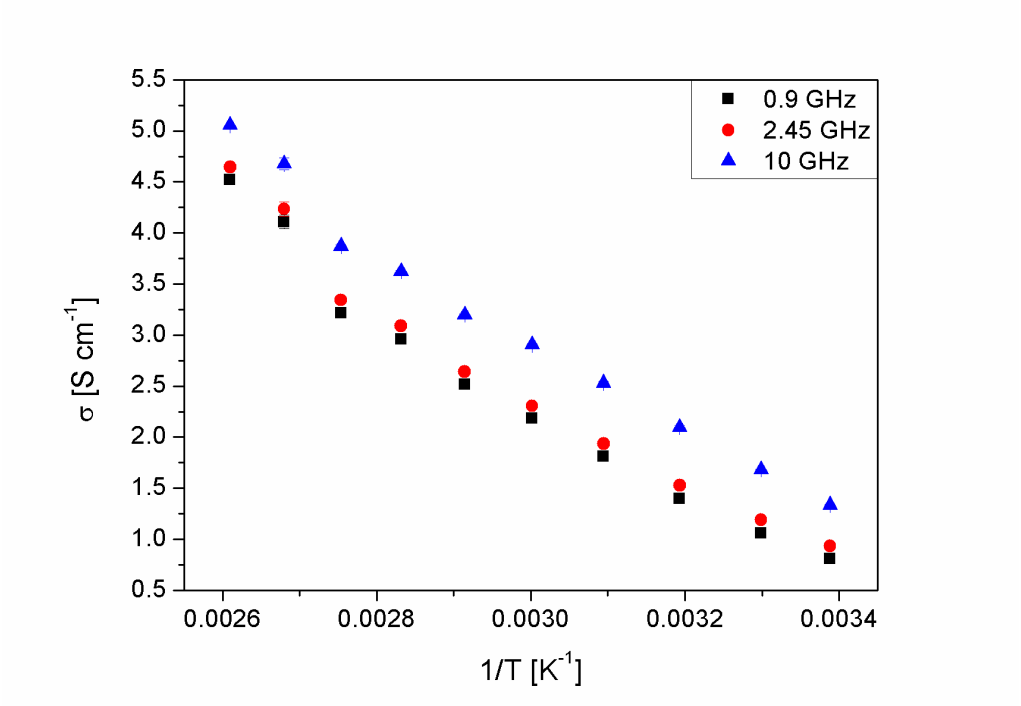



*Figure 4-33 Conductivity σ(υ) plotted versus inverse temperature at selected frequencies for [$C_1C_4$Im][$FeCl_4$].*

[$C_1C_4$Im][$InCl_4$] (Figure 4-34) shows a quasi-linear response at all frequencies against inverse temperature, similar to [$C_1C_4$Im][$FeCl_4$] (Figure 4-33) but no inflection is observed. However, an increase in conductivity with increasing frequency is visible, as could be seen for [$C_1C_4$Im][$FeCl_4$].

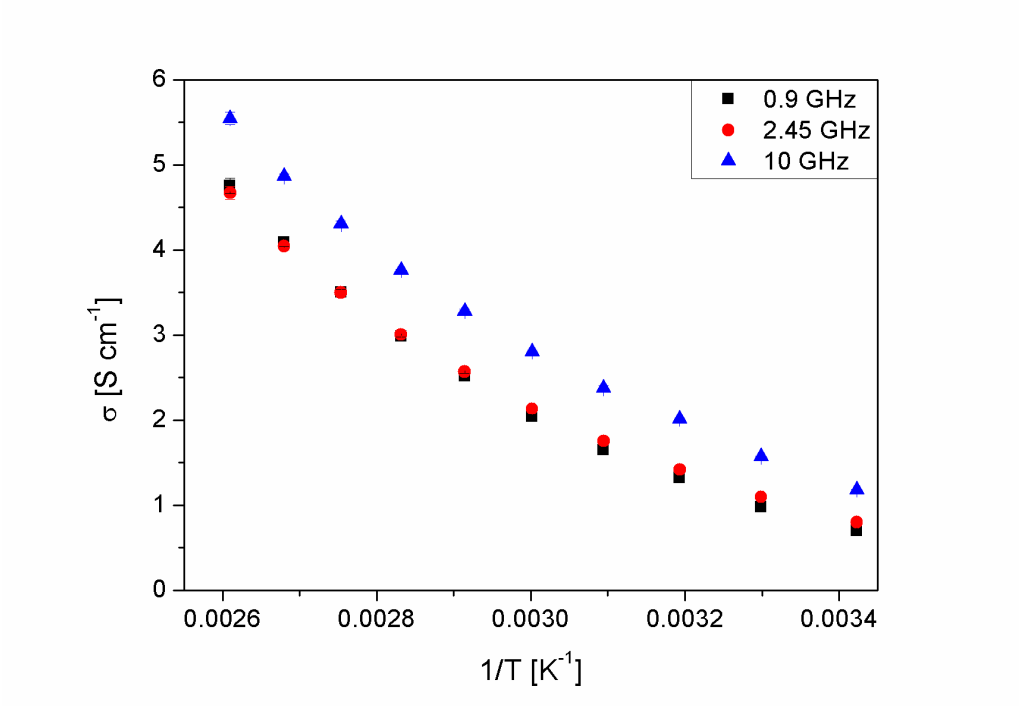



*Figure 4-34 Conductivity σ(υ) plotted versus inverse temperature at selected frequencies for $[C_1C_4Im][InCl_4]$.*

Figure 4-35 depicts the conductivity versus inverse temperature for $[C_1C_4Im]_2[ZnCl_4]$. As previously stated, no positive values were obtained at 10 GHz, therefore they will be disregarded here. A bend can be observed around 60°C, corresponding to the full melting of the sample, as was observed with DSC (Figure 2-20).

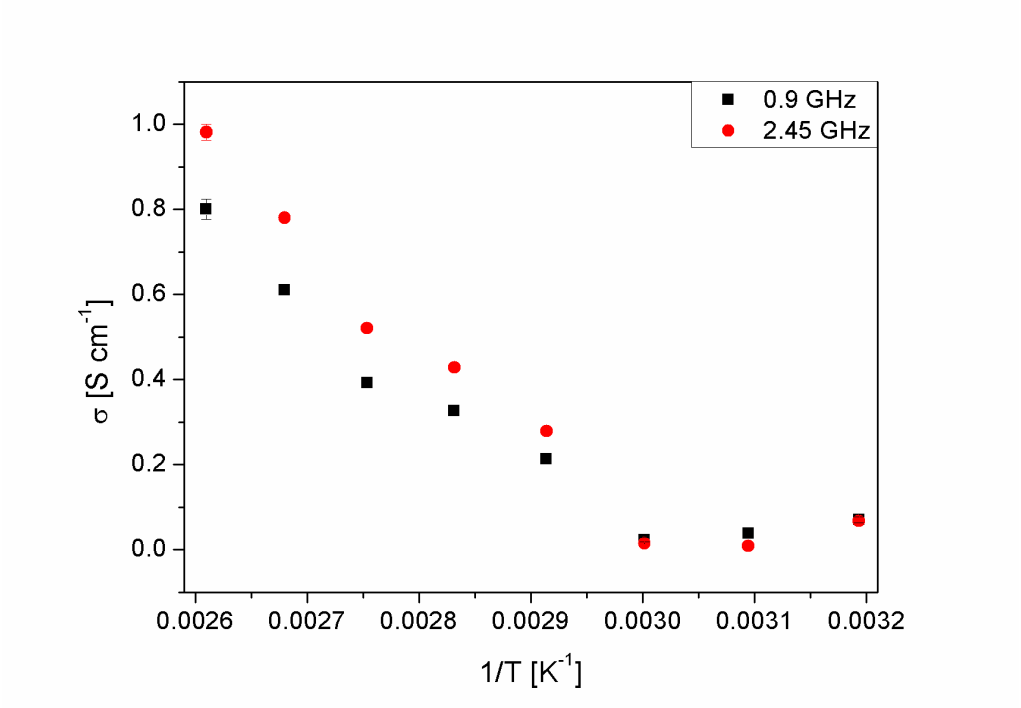



*Figure 4-35 Conductivity σ(υ) plotted versus inverse temperature at selected frequencies for $[C_1C_4Im]_2[ZnCl_4]$.*

$[C_1C_4Im]_2[CuCl_4]$ (Figure 4-36) shows an inverse exponential curve. As previously described, no values were obtained at 10 GHz due to the insufficient sensitivity of the coaxial probe. Nevertheless, a clear difference can be noticed between values obtained at 0.9 and 2.45 GHz, displaying a clear frequency dependence.

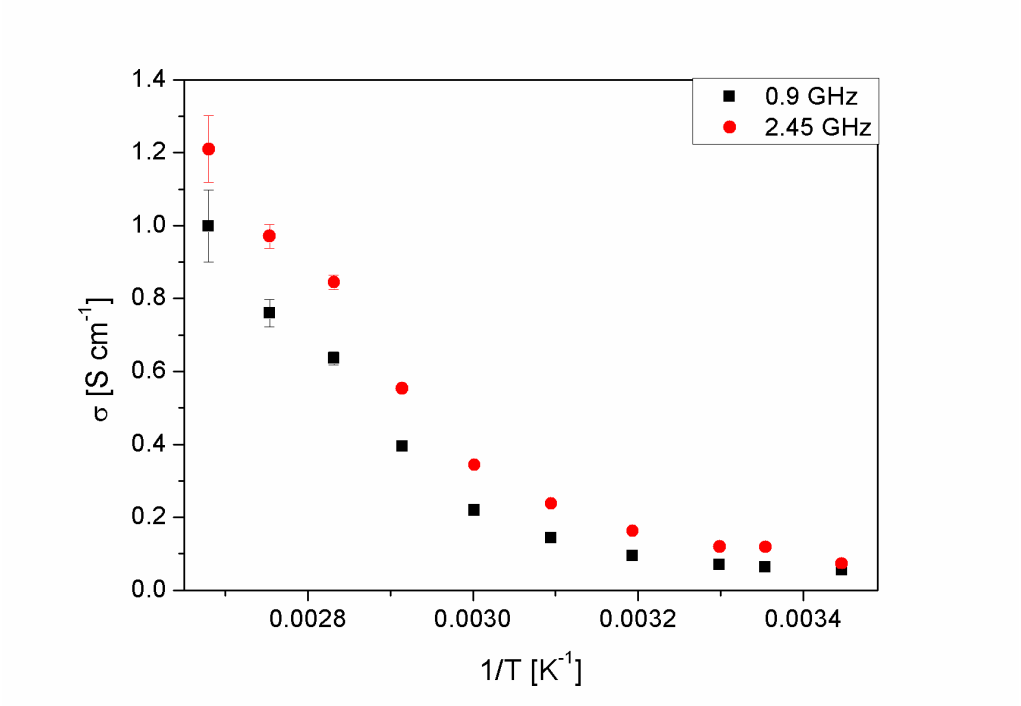



*Figure 4-36 Conductivity σ(υ) plotted versus inverse temperature at selected frequencies for $[C_1C_4Im]_2[CuCl_4]$.*

Figure 4-37 displays the conductivity against reverse temperature for $[C_1C_4Im]_2[NiCl_4]$. Non-linear behaviour can be observed and a peak around 60°C was noticed, corresponding to the fully melted sample (**5.3.1 Thermal analysis**).

At 9.4 GHz a drop in conductivity is observed, in contrast to the previously examined ILs, $[C_1C_4Im]_2[NiCl_4]$ shows lower values at high frequency than at low frequency.

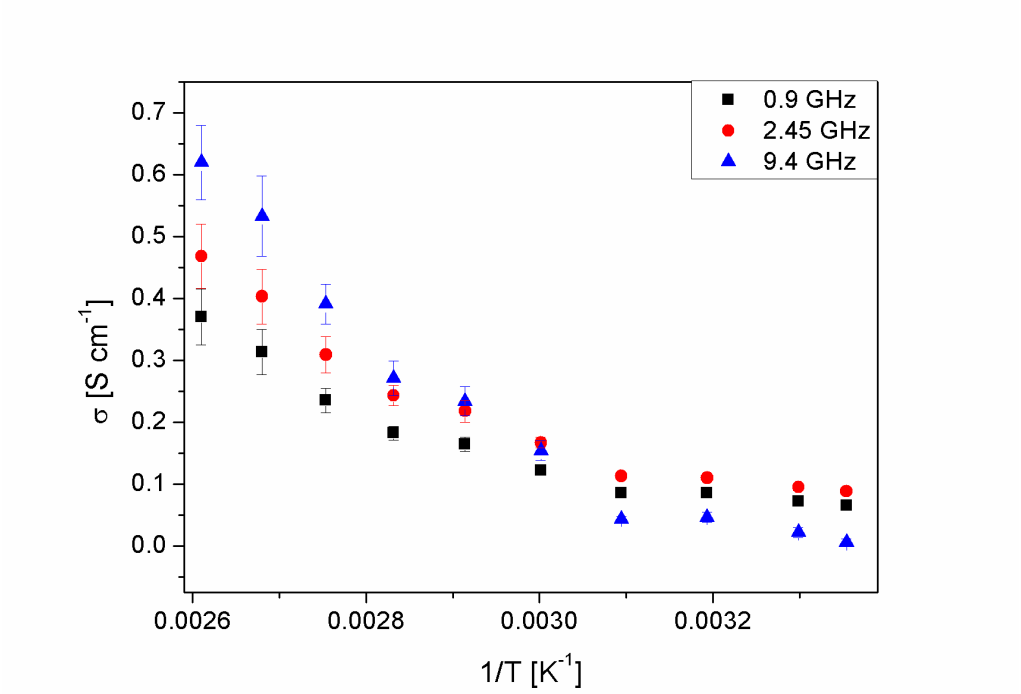



*Figure 4-37 Conductivity σ(υ) plotted versus inverse temperature at selected frequencies for $[C_1C_4Im]_2[NiCl_4]$.*

$[C_1C_4Im]_2[CoCl_4]$ (Figure 4-38) displays similar frequency dependency as $[C_1C_4Im]_2[NiCl_4]$, where a decline is observed at high frequency. Interestingly, a pronounced peak can be noticed at 60°C, which is below the glass transition observed with DSC (**5.3.1 Thermal analysis**).

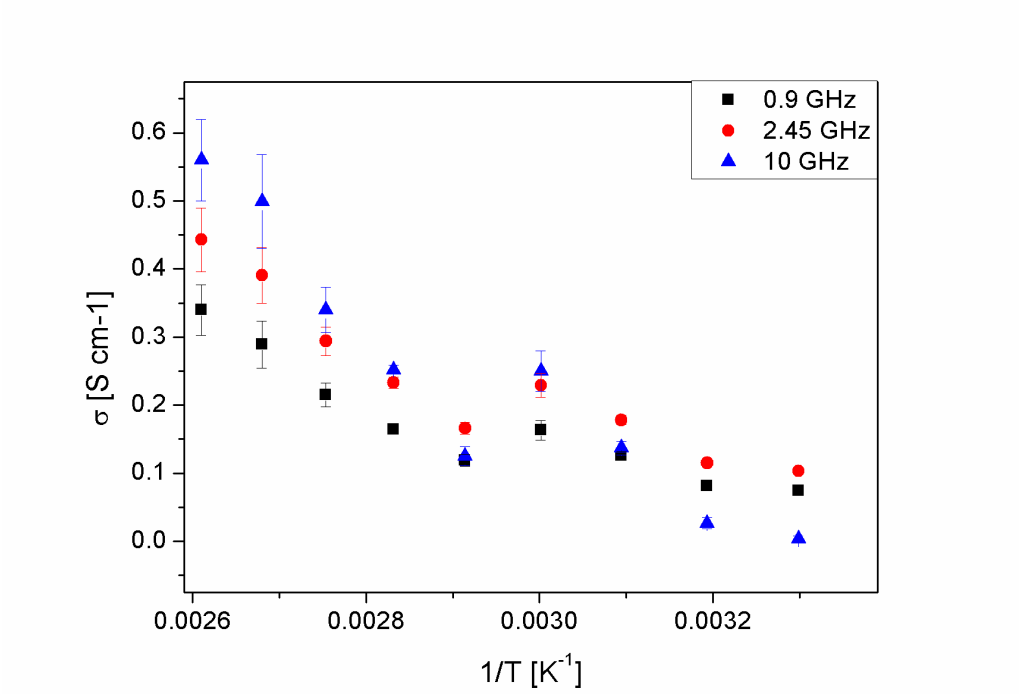



*Figure 4-38 Conductivity σ(υ) plotted versus inverse temperature at selected frequencies for $[C_1C_4Im]_2[CoCl_4]$.*

### 4.5.5 Fitting of Arrhenius plot

Data obtained with the coaxial slim probe was used to calculate the activation energy of all ILs using an Arrhenius fit. The following Equations were used,

$$\sigma = Ae^{\frac{-E_a}{k_B T}} \quad [4\text{-}14]$$

$$\ln \sigma = \ln A - \frac{E_a}{k_B}\frac{1}{T} \quad [4\text{-}15]$$

$$\ln \sigma = \frac{-E_a}{k_B}\left(\frac{1}{T}\right) + \ln A \quad [4\text{-}16]$$

where $\sigma$ is the conductivity, $A$ the pre-exponential factor, $E_a$ the activation energy, $k_B$ the Boltzmann constant and $T$ the temperature. All Arrhenius fits are presented in the Appendix (8.5.1 Arrhenius fit – conductivity versus inverse temperature). All values obtained using Equation [4-16] are presented in Table 4-2 for 0.9 and 2.45 GHz. An exception was observed for $[C_1C_4Im]_2[CoCl_4]$,

where two regions were observed at low and high temperature. For $[C_1C_4Im]_2[ZnCl_4]$ only values above 60°C were considered as this corresponds to the fully melted IL.

*Table 4-2 Activation energy $E_a$ calculated from the Arrhenius plot for 0.9 and 2.45 GHz.*

| **Ionic liquid** | **$E_{a1}$ kJ/mol (0.9 GHz)** | **$E_{a2}$ kJ/mol (0.9 GHz)** | **$E_{a1}$ kJ/mol (2.45 GHz)** | **$E_{a2}$ kJ/mol (2.45 GHz)** |
|---|---|---|---|---|
| **$[C_1C_4Im][FeCl_4]$** | 17.85 | | 16.66 | |
| **$[C_1C_4Im][InCl_4]$** | 19.36 | | 17.75 | |
| **$[C_1C_4Im]_2[ZnCl_4]$** | 35.77 | | 34.16 | |
| **$[C_1C_4Im]_2[CuCl_4]$** | 34.25 | | 31.19 | |
| **$[C_1C_4Im]_2[NiCl_4]$** | 19.66 | | 19.31 | |
| **$[C_1C_4Im]_2[CoCl_4]$** | 23.33 | 29.13 | 23.78 | 27.17 |

## 4.6 Comparison of conductivity using impedance spectroscopy

Impedance spectroscopy was selected as a method for comparison of conductivity values. A glass cell with two platinum electrodes and a potentiostat with a frequency range of 0.1 Hz to 0.1 MHz was used for the measurements (Figure 4-39). The temperature was controlled with an oil bath and the temperature of the IL was confirmed with an external thermocouple. Measurements were taken three times at each temperature and the standard deviation was calculated.

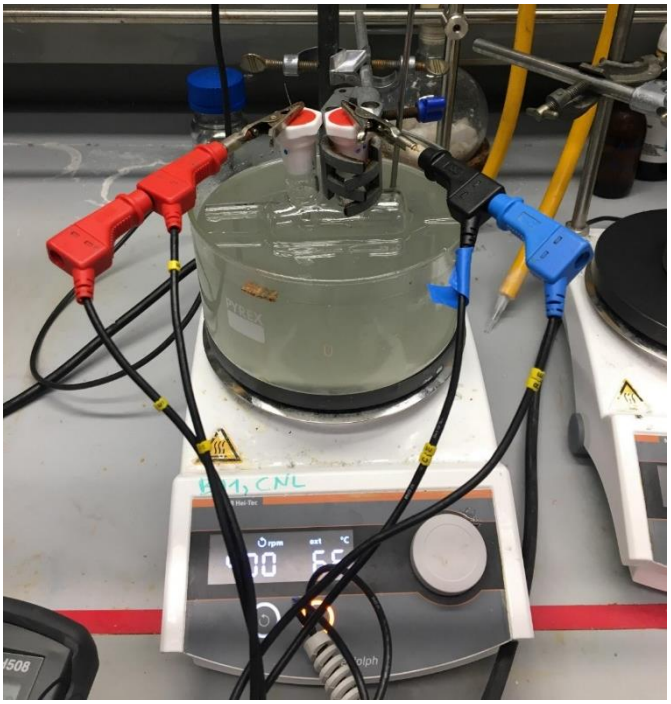


*Figure 4-39 Experimental set-up for impedance spectroscopy, using a glass cell with two platinum electrodes and an oil bath for temperature control.*

The cell was calibrated using a 0.117 M solution of KCl with a known conductivity of 15000 mS $cm^{-1}$ and the cell constant was determined using the following Equation,

$$\sigma = \frac{1}{R} K \qquad [4\text{-}17]$$

where $\sigma$ is the conductivity, $K$ cell constant and $R$ is the resistance. The derivation of Equation [4-17] can be found in the introduction of this chapter (4.4 Impedance spectroscopy).

Figure 4-40 shows a typical spectrum obtained with impedance spectroscopy for $[C_1C_4Im][InCl_4]$ at room temperature. On the left, the full spectrum is presented and, on the right, the behaviour around zero is highlighted. The data is presented as a Nyquist plot, where the imaginary part -Z'' of the impedance

is plotted against the real part Z'. Spectra for all ILs at different temperatures are presented in the Appendix (8.6 Impedance spectroscopy).

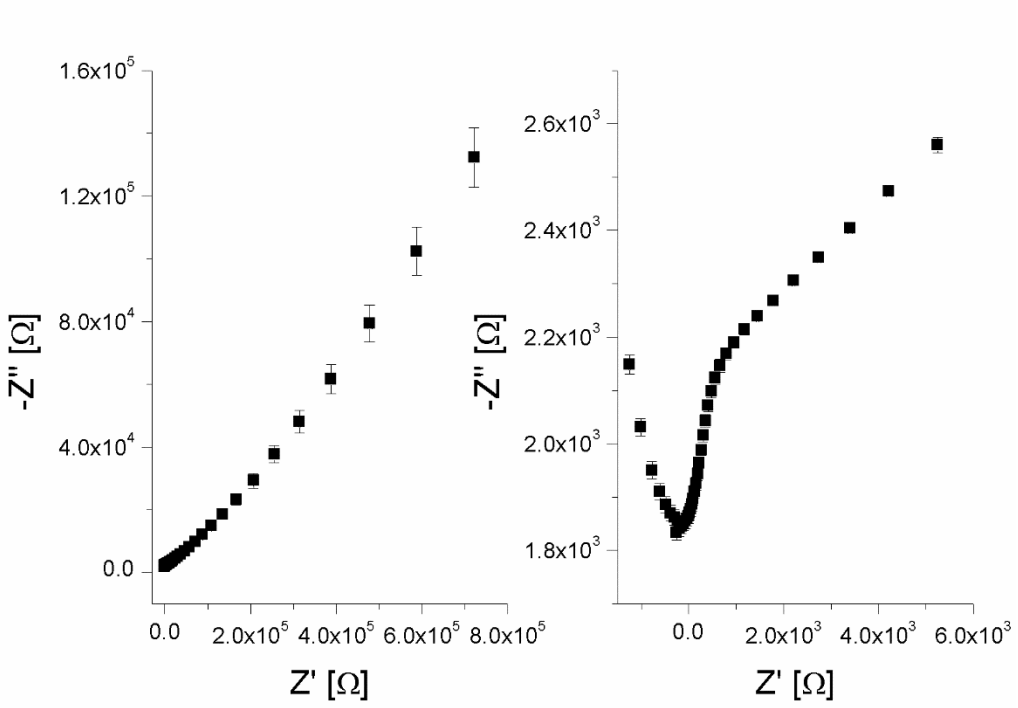



*Figure 4-40 Impedance spectroscopy of $[C_1C_4Im][InCl_4]$ at room temperature. Data from an average of three measurements is presented. On the left full-spectrum and on the right zoom into the area around zero.*

The conductivity was calculated using Equation [4-17] and is presented in the following figures. Figure 4-40 shows conductivity values obtained from impedance spectroscopy versus the inverse temperature for $[C_1C_4Im][FeCl_4]$. The same linear behaviour and temperature dependency, as was observed with dielectric spectroscopy is noticed. Conductivity values obtained are lower than were measured with the coaxial slim probe (Figure 4-27). However, a frequency dependency was present previously and the potentiostat uses a lower frequency than the coaxial slim probe. Therefore, a decline in conductivity is expected at a lower frequency.

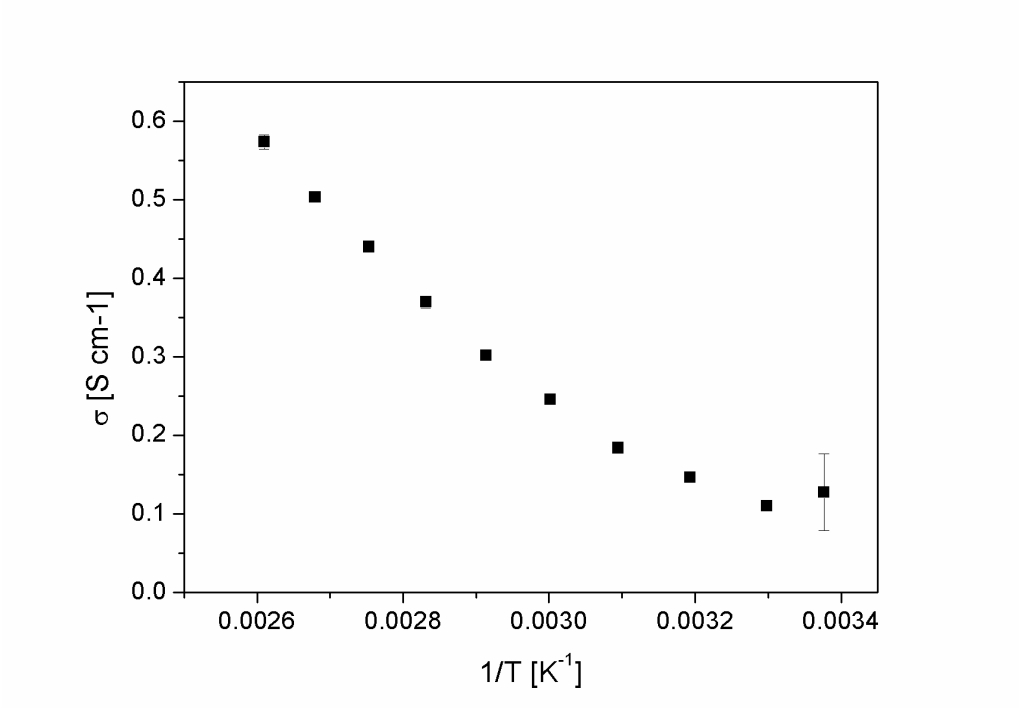



*Figure 4-41 Conductivity calculated from impedance spectroscopy at different temperatures for [$C_1C_4Im$][$FeCl_4$].*

[$C_1C_4Im$][$InCl_4$] (Figure 4-41) demonstrated similar behaviour as [$C_1C_4Im$][$FeCl_4$] (Figure 4-42) and data obtained from impedance spectroscopy is comparable with data measured with dielectric spectroscopy (Figure 4-28).

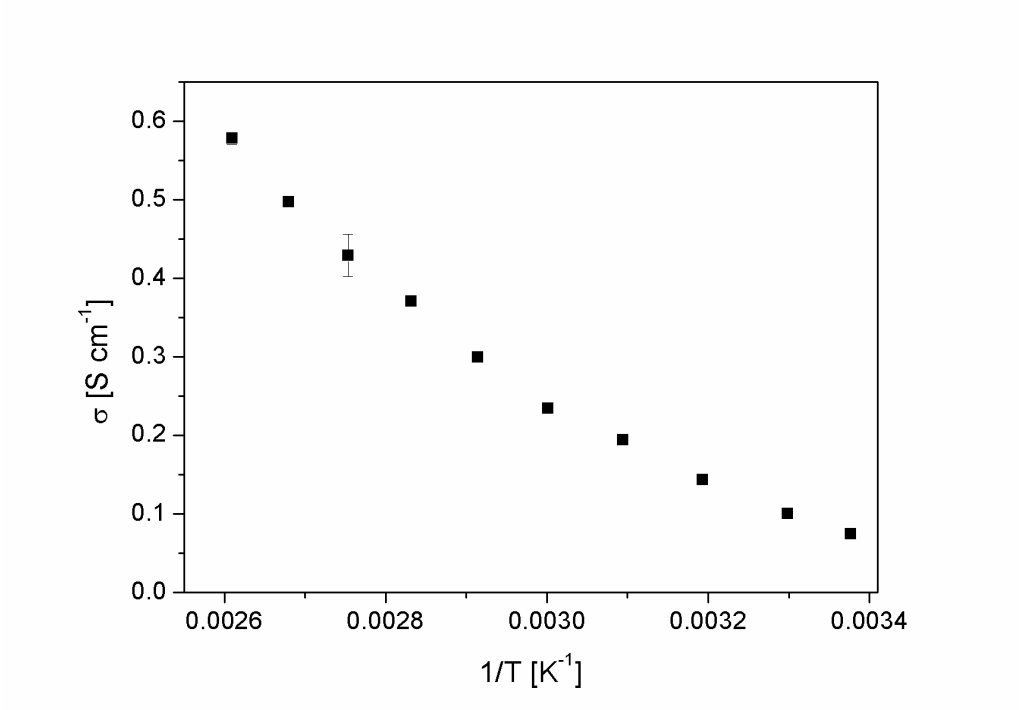



*Figure 4-42 Conductivity calculated from impedance spectroscopy at different temperatures for $[C_1C_4Im][InCl_4]$.*

Figure 4-43 displays conductivity versus inverse temperature for $[C_1C_4Im]_2[ZnCl_4]$ showing reproducible properties in comparison with dielectric spectroscopy (Figure 4-29). As was previously observed, due to a lower frequency range lower values for conductivity were measured. It was not possible to measure impedance at 40°C due to the formation of crystals around the electrode.

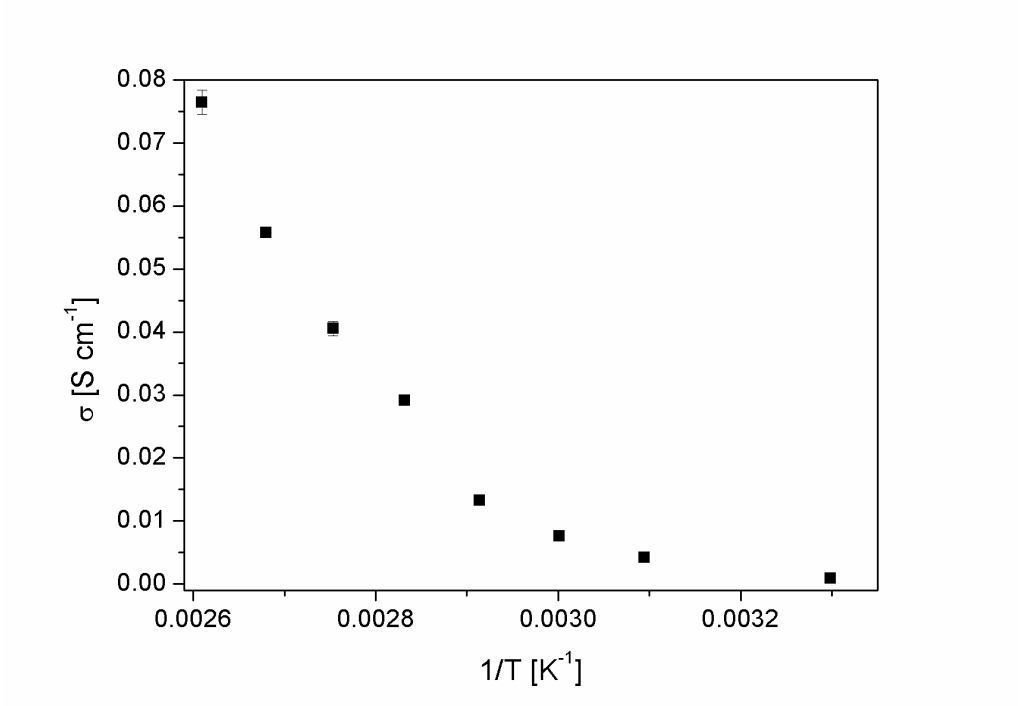



*Figure 4-43 Conductivity calculated from impedance spectroscopy at different temperatures for $[C_1C_4Im]_2[ZnCl_4]$.*

In Figure 4-44, conductivity versus inverse temperature is presented for $[C_1C_4Im]_2[CuCl_4]$. Temperature dependence occurs in a similar fashion to the measurements obtained from the coaxial slim probe and hence validates the previously observed result (Figure 4-30).

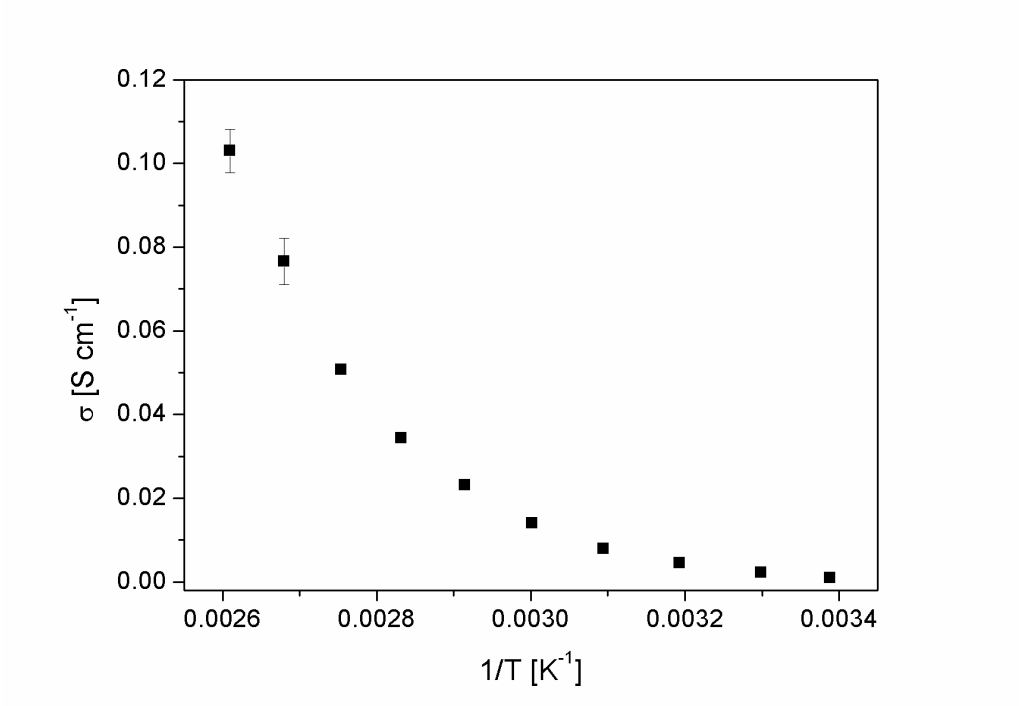



*Figure 4-44 Conductivity calculated from impedance spectroscopy at different temperatures for $[C_1C_4Im]_2[CuCl_4]$.*

Figure 4-45 shows the conductivity calculated for $[C_1C_4Im]_2[NiCl_4]$ and again the temperature dependence was noted. Only a change in conductivity could be observed, due to a change in the frequency range. In addition, a peak at 60°C is observed, which was not present in the results from dielectric spectroscopy (Figure 4-31). DSC showed a melting peak around 60°C (**5.4.1 Thermal analysis**) hence indicating a connection between the incline in conductivity and the phase transition.

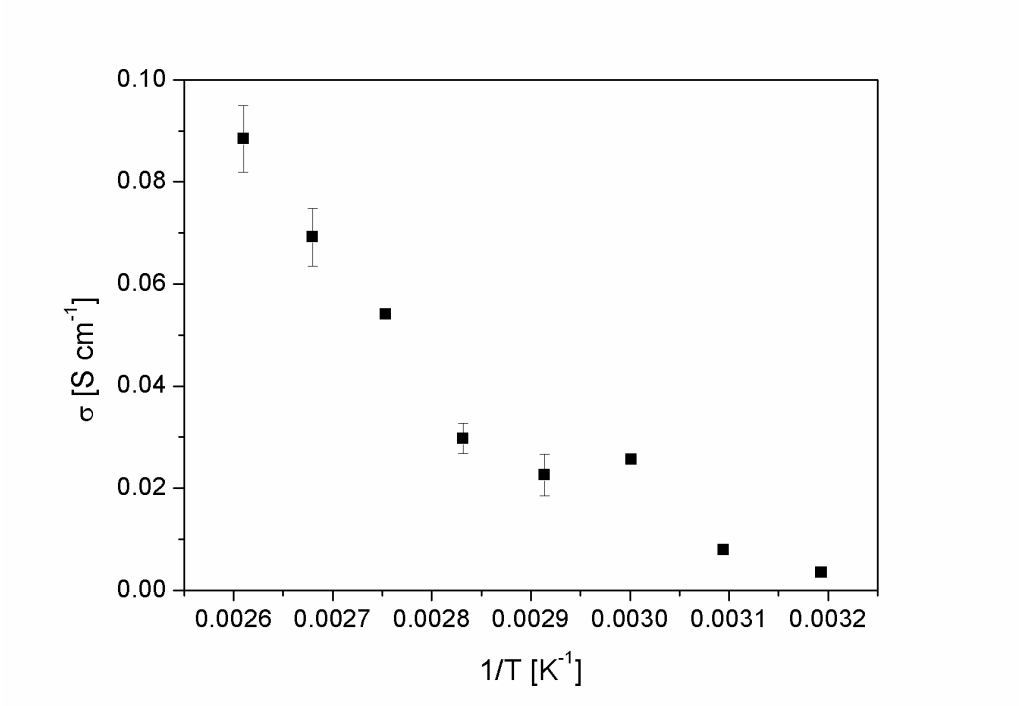



*Figure 4-45 Conductivity calculated from impedance spectroscopy at different temperatures for $[C_1C_4Im]_2[NiCl_4]$.*

For $[C_1C_4Im]_2[CoCl_4]$ only values above 60°C were measured, due to the solidification of the sample in the electrochemical glass cell. Nevertheless, values obtained at high temperature are comparable to the conductivity calculated from dielectric spectroscopy (Figure 4-32).

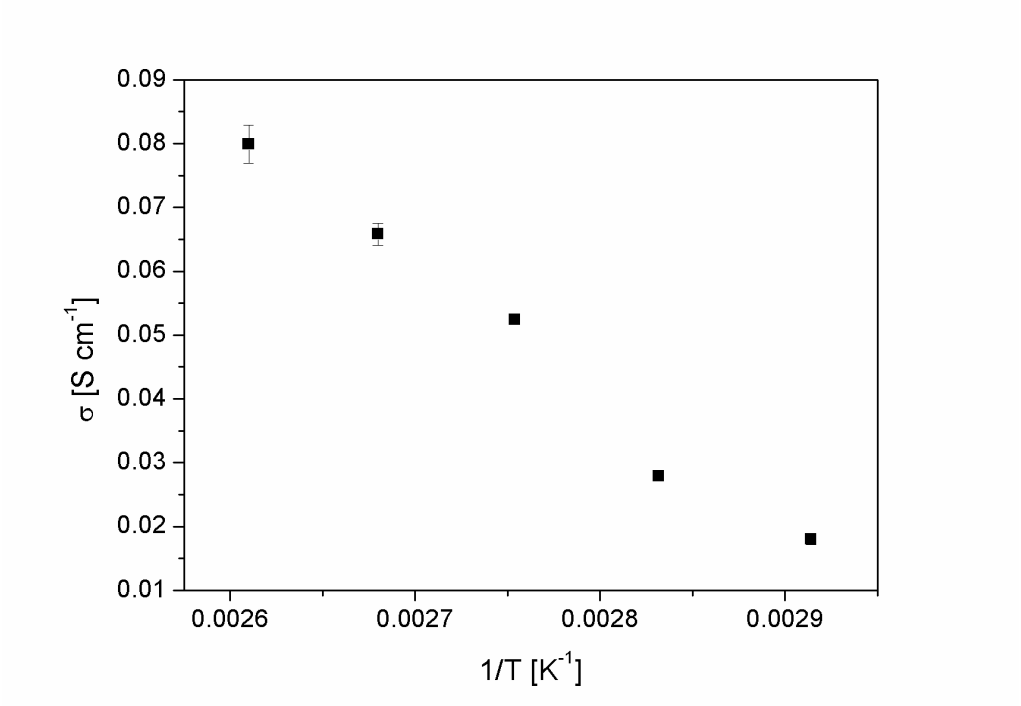



*Figure 4-46 Conductivity calculated from impedance spectroscopy at different temperatures for $[C_1C_4Im]_2[CoCl_4]$.*

Zhong *et al.* have investigated dialkylimidazolium ILs containing $CoCl_2$, $NiCl_2$, $CuCl_2$, $FeCl_2$, and $ZnCl_2$ metal halides. The group investigated crystal structures and ionic conductivities of the halometallate ILs. The following table (Table 4-3) shows a comparison of the data obtained in this work and from Zhong *et al*. The ionic conductivity was determined by Zhong *et al.* with an electrometer using an AC impedance method with a frequency of 80 Hz below 20 mS $cm^{-1}$ and 3 kHz above 20 mS $cm^{-1}$. [332]

*Table 4-3 Comparison of ionic conductivity obtained from impedance spectroscopy in this work and from Zhong et al. at 300 K. Exceptions are given in brackets behind the calculated conductivity.*

| **Ionic liquid** | **σ (this work)** | **σ (Zhong *et al.*)[332]** |
|---|---|---|
| **$[C_1C_4Im][FeCl_4]$ (this work)/$[C_1C_4Im]_2[FeCl_4]$ (Zhong *et al.*)** | 0.109 | 0.0177 |

| | | |
|---|---|---|
| **$[C_1C_4Im]_2[ZnCl_4]$** | 0.0086 | 0.00829 |
| **$[C_1C_4Im]_2[CuCl_4]$** | 0.00229 | 0.0144 |
| **$[C_1C_4Im]_2[NiCl_4]$** | 0.00348 (313 K) | 0.00998 |
| **$[C_1C_4Im]_2[CoCl_4]$** | 0.018 (343 K) | 0.00935 |

Table 4-3 shows that a difference in conductivity can be observed for $[C_1C_4Im][FeCl_4]$ (this work) and $[C_1C_4Im]_2[FeCl_4]$ (Zhong *et al.*), which is not unexpected as the two compounds differ in oxidation state. Zhong *et al.* have used iron(II) chloride with two equivalents of $[C_1C_4Im]Cl$, whereas in this work a 1:1 mixture of $[C_1C_4Im]Cl$ and iron(III) chloride was used. For $[C_1C_4Im]_2[ZnCl_4]$ a comparable result was obtained, but for $[C_1C_4Im]_2[CuCl_4]$ a difference of one decimal point could be observed. In the case of the cobalt and nickel IL, a difference in temperature hinders the accurate comparison. Nevertheless, values obtained for the conductivity are within reason, as the observed difference is less than one decimal.

The activation energy was calculated in the same manner as for data obtained from dielectric spectroscopy using Equation [4-16]. All data is presented in Table 4-4 showing values for $E_a$ in kJ/mol. Values obtained for $[C_1C_4Im][FeCl_4]$ and $[C_1C_4Im][InCl_4]$ are consistent with $E_a$ calculated from dielectric spectroscopy. However, values determined for all metal(II) species differ approximately by a factor of 20 (Table 4-2). A possible explanation could be that with the coaxial slim probe, due to the use of high frequency, a localized

motion is observed and in contrast, when using low frequency with impedance spectroscopy a long diffusion is observed.

*Table 4-4 Activation energies calculated from Arrhenius fit for all ILs using data obtained with impedance spectroscopy.*

| **Ionic liquid** | **$E_a$ kJ/mol** |
|---|---|
| **$[C_1C_4Im][FeCl_4]$** | 18.61 |
| **$[C_1C_4Im][InCl_4]$** | 21.86 |
| **$[C_1C_4Im]_2[ZnCl_4]$** | 54.73 |
| **$[C_1C_4Im]_2[CuCl_4]$** | 50.17 |
| **$[C_1C_4Im]_2[NiCl_4]$** | 43.26 |
| **$[C_1C_4Im]_2[CoCl_4]$** | 42.17 |

## 4.7 Mechanism of relaxation

In dielectric spectroscopy an interaction of a material with the applied electromagnetic field is observed, which is described through Maxwell's equation and states that a frequency dependence is present when time dependent processes take place in the material. These processes can be resonance phenomena due to molecular or atomic vibrations or relaxation phenomena due to molecular fluctuations of dipoles. Conductive contribution arises from drift motion of mobile charge carriers (*e.g.* electrons, ions, or charge defects). A time dependent process within a material leads to a difference in time dependency of the outer electrical field and results in a dielectric displacement. In other words the disturbance from a time dependent external electrical field leads to a response from the material as polarization. ε' is proportional to the energy stored reversibly in the system per period and ε''

is proportional to the energy dissipated per period. The complex dielectric function ε* is dependent on temperature and angular frequency and as mentioned before observed phenomena can have different origins. Therefore models are needed to describe dielectric relaxation phenomena.

A relaxation process has a characteristic peak in the imaginary part ε'' and for the real part ε' a step-like decrease with increasing frequency is observed. In the case of a conduction phenomenon ε'' increases with decreasing frequency. Contrary, if pure ohmic conduction is observed then ε' is independent of the frequency. However, non-ohmic conduction or polarization leads to an increase of ε' with decreasing frequency (Figure 4-47).[321]

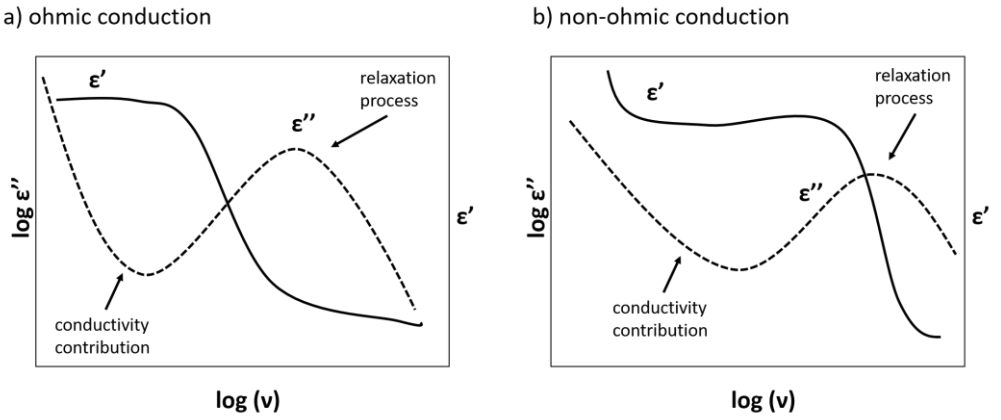



*Figure 4-47 Relaxation processes observed for ohmic and non-ohmic conduction.*[321]

Figure 4-47 displays relaxation phenomena generally observed with dielectric spectroscopy however the systems investigated in this work did not display relaxation phenomena of this type hence it could display a more disordered system which might facilitate charge transport through hopping conduction. In these types of systems the motion of charge is accompanied by an electrical relaxation and the ionic or electrical charge is surrounded by a counter charge.

A successful charge transport can only occur if the polarization cloud follows the hop of charge, otherwise the charge will hop back. For a mutual movement of charge carrier and surrounding polarization to occur an electrical relaxation time $\tau_0$ is needed. If the frequency is smaller than $1/\tau_0$ then the relaxation is going to be in phase with the external electrical field. In this case the propagation is supported by the applied field and ε* increases with decreasing frequency. In addition, it was observed that for electrolytes ε' increases with decreasing frequency.[321]

## 4.8. Evaluation of ILs for MW application

A value of how efficiently a medium can transform electromagnetic energy into heat at a certain frequency and temperature is given by the following Equation,

$$tan\delta = \frac{\varepsilon''}{\varepsilon'} \qquad [4\text{-}18]$$

where $\varepsilon'$ is the dielectric constant, $\varepsilon''$ the dielectric loss, and tan$\delta$ the dielectric loss tangent (4.3 Dielectric spectroscopy). For MW heating to be economically viable, a high loss tangent is necessary to produce fast heating through efficient absorption of energy. As typically organic solvents are being used, three categories have evolved of high, medium, and low absorbing solvents with, tan$\delta$ > 0.5 for high absorbing mediums, tan$\delta$ = 0.1-0.5 for medium absorption and < 0.1 for low absorbing organic solvents. For example, organic solvents with a high loss tangent are ethylene glycol (1.350), ethanol (0.941), and dimethyl sulfoxide (0.825). Though solvents which do not contain a permanent dipole are essentially MW transparent.[283, 284, 287]

*Table 4-5 Values displayed for tanδ at 100°C, 0.9 GHz and 2.45GHz; exception is [$C_1C_4$Im][$Fe(NO)_2Cl_2$] which could only be measured up to 80°C and the values displayed are at 80°C.*

| Ionic Liquid | tan$\delta$ (0.9 GHz) | tan$\delta$ (2.45 GHz) |
|---|---|---|
| **[$C_1C_4$Im][$FeCl_4$]** | 7.65 | 2.81 |
| **[$C_1C_4$Im][$Fe(NO)_2Cl_2$]** | 0.50 | 0.45 |
| **[$C_1C_4$Im][$InCl_4$]** | 7.95 | 2.81 |
| **[$C_1C_4$Im]$_2$[$CuCl_4$]** | 2.12 | 0.99 |
| **[$C_1C_4$Im]$_2$[$ZnCl_4$]** | 1.21 | 0.61 |
| **[$C_1C_4$Im]$_2$[$NiCl_4$]** | 0.68 | 0.37 |
| **[$C_1C_4$Im]$_2$[$CoCl_4$]** | 0.65 | 0.36 |

Table 4-5 summarizes tan$\delta$ values for all investigated ILs in this work and it can be noted that all ILs show medium to high absorption. Especially at 0.9 GHz the investigated ILs show comparable values for the loss tangent to organic solvents, which make them a good alternative to conventional organic solvents.

## 4.9 Conclusion

This chapter aims to describe the dielectric properties and ionic conductivity for a variety of metal-containing ILs. The dielectric constant and loss were determined for [$C_1C_4$Im][$FeCl_4$], [$C_1C_4$Im][$InCl_4$], [$C_1C_4$Im]$_2$[$CuCl_4$], [$C_1C_4$Im]$_2$[$ZnCl_4$], [$C_1C_4$Im]$_2$[$NiCl_4$], [$C_1C_4$Im]$_2$[$CoCl_4$], and [$C_1C_4$Im][$Fe(NO)_2Cl_2$] using a coaxial slim probe and/or a resonance perturbation cavity. In addition, the conductivity and activation energy were calculated using data obtained with the coaxial slim probe. For validation of the obtained data, impedance spectroscopy was used, and reasonable values were obtained. Moreover, all

ILs show promise for application in MW synthesis as they exhibit significant dielectric constants and loss factors. The observed dielectric constants vary depending on the metal and temperature in a range from ε' = 3.4-13.9, whereas the loss is observed to be in a range of ε'' = 0.5-170. In addition, the loss tangent tan$\delta$ was calculated and medium to high absorption was observed for all investigated ILs making them ideal candidates as solvent and catalyst for MW synthesis.

# Chapter 5

## 5. Thermal properties of cobalt and nickel chloride mixtures with $[C_1C_4Im]Cl$

Halometallate ILs are already used in industrial applications like the Difasol process, where a Nickel coordination complex is used in combination with a chloroaluminate IL as a catalyst for the dimerization of olefins.[86] Chen *et al.* used $[C_1C_4Im]Cl/CoCl_2$ and $[C_1C_4Im]Cl/NiCl_2$, amongst other metals, for the desulfurization of diesel fuel.[333] Another example for the catalytic activity of cobalt and nickel is given by Sasaki *et al.* using immobilized metal containing ILs for the Kharasch addition reaction.[334] Also, Zhong *et al.* used $[C_1C_4Im]_2[NiCl_4]$ as a catalyst for Suzuki cross coupling.[335]

The most commonly occurring halometallate anions $[MCl_4]^{2-}$ in ILs have been characterised for cobalt and nickel halides but even after extensive literature research no phase diagram was found for either of the metal halides.[72, 82, 332, 336, 337] Metal salts, dissolved in ILs can pose difficult anion speciation as they might form multiple complexes. For example reactive dissolution of $AlCl_3$ in an IL can form an equilibrium between $[AlCl_4]^-$ and $[Al_2Cl_7]^-$ at mole fraction $\chi = 0.6$ of $AlCl_3$ (1.4 Halometallate ionic liquids and the challenge of anion speciation; 1.4.1 Phase diagram of chloroaluminate(III) ionic liquids).[26] Therefore, it is important to understand the phase behaviour of ILs especially when working with metal containing ILs.

## 5.1 Experimental techniques used for the preparation of the phase diagram

Explain phase diagram

### 5.1.1 Thermal analysis

**Thermogravimetric analysis**

Thermogravimetric analysis (TGA) measures the mass loss, or increase, under increasing temperature at a certain heating rate. This leads to data where the mass loss can be represented as a function of time or temperature. Another important aspect is a controlled atmosphere, which can be achieved through a purge gas, either an inert or a reactive gas.[338] A TGA instrument consists of a furnace, a balance and sample pans. The primary use of TGA is the investigation of a materials' thermal stability. Mass loss or gain could be due to different factors, including sorption or desorption of volatiles, decomposition, oxidation, and reduction. To observe these processes, a precise measurement of the occurring mass loss is necessary. The balance works with a *null-balance principle*, where at the zero or *null* position, an equal amount of light hits the two photodiodes. When a sample pan is attached to the wire, which is connected to the balance arm, the balance will move away from the *null* position and consequently an unequal amount of light is observed by the photodiodes. To recreate balance, (*i. e.* equal amount of light shines on the two photodiodes) a current is applied which in turn is proportional to the mass loss or gain.[339]

**Differential scanning calorimetry**

DSC, as the name suggests, is a type of calorimetry, which measures heat. In the case of DSC, a controlled temperature program facilitates the measurement of a change in heat flow rate of the sample in comparison to a reference sample. A heat flow DSC achieves this measurement with two individual furnaces, which are kept at a constant temperature according to the set program. With the occurrence of phase transitions, like melting or crystallisation of the sample, more or less energy input is needed to keep the temperature of the furnace constant. This difference in energy input is measured and consequently transformed into a temperature dependent heat flow thermogram.[340]

In the thermogram, the change of heat flow is presented as endothermic or exothermic peaks, and as a step change deviating from the baseline. An exothermic peak means that less energy was needed to keep the sample pan at a constant temperature and accordingly an endothermic peak relates to a phase transition, which required more energy input to be kept at a constant temperature. Phase transitions, which appear as a step, are commonly referred to as glass transitions, because in most cases they relate to an amorphous material melting (*e.g.* glass or polymers).[192]

### 5.1.2 Raman spectroscopy

In Raman spectroscopy, laser radiation is used to produce scattered radiation from the interaction with a sample. Generally, most photons will be scattered elastically (*i.e.* no change of frequency) but a small portion will be scattered

inelastically and their loss of energy is due to the molecule's vibrations. In consequence, the frequencies of these photons correspond to the vibrational frequencies of the molecule. The scattered light observed has several components, namely Rayleigh, Stokes and Anti-Stokes Raman scatter. Rayleigh scatter reflects the wavelength of the incident beam and Stokes and Anti-Stokes Raman appears with a change in wavelength after being scattered from the molecule.[341]

In a typical Raman spectrometer, a microscope connected to a camera is used to focus on the sample, which can be done manually or through a mapping program, where the stage is moved on the z-axis to find the most intense Raman scattering. The laser excitation wavelength is selected according to the sample being investigated. A mechanical shutter is used to only expose the detector to the light in the case of measurement. This avoids the CCD (charge coupled device) detector having to be cleaned continuously and exposure while the detector reads out the collected data. The shutter is followed by a neutral density filter, which can be rotated to adjust the intensity of the laser power. Then, the light is directed on to the sample with a set of mirrors and lenses. The dichroic mirror or beam splitter is used to reflect the wavelength of the laser itself and to ensure only transmission of all other wavelengths. After the light hits the sample, Raman scatter is reflected and the notch filter is used to remove any wavelengths deriving from the laser itself, which have not been previously removed by the dichroic mirror. The light then passes through a confocal aperture, which collects all the light and can be followed by an additional filter removing any residual Rayleigh scattering. A grating is then

used to spread out the light onto the CCD detector, which detects several wavelengths at the same time.[342, 343]

## 5.2 Synthesis and characterisation of $[C_1C_4Im]Cl$/ $CoCl_2$ and $[C_1C_4Im]Cl$/ $NiCl_2$ mixtures

### 5.2.1 Preparation of $[C_1C_4Im]Cl/CoCl_2$ mixtures

The preparation of a range of $[C_1C_4Im]Cl/CoCl_2$ was carried out in a glove box. The mole fraction $\chi CoCl_2$, defined in Equation [5-1], was varied systematically between 0 and 0.95 with increments of approximately 0.05 (see Appendix, 8.1 Phase diagram).

$$xCoCl_2 = \frac{n(CoCl_2)}{n(CoCl_2) + n(C_1C_4ImCl)} \qquad [5\text{-}1]$$

As an example, for the preparation of the mixture $\chi CoCl_2 = 0.33$, $[C_1C_4Im]Cl$ was mixed with 0.5 mol equivalents of anhydrous $CoCl_2$ overnight at 80°C under inert atmosphere and the product was obtained as a viscous liquid, changing from light blue (pure $CoCl_2$) to deep blue. The IL was first obtained as a supercooled liquid but fully crystallised over time, after heating and cooling it for a second time. For other values of $\chi CoCl_2$, stirring for 24 hrs at 80°C led to similar deep blue viscous liquids up to $0.5 \geq \chi CoCl_2$, and for $0.5 \leq \chi CoCl_2$ to dark blue crystalline solids.

### 5.2.2 Preparation of $[C_1C_4Im]Cl/NiCl_2$ mixtures

The $[C_1C_4ImCl]/[NiCl_2]$ mixtures were prepared in the same manner as their cobalt analogues and values were calculated using Equation [5-1] (see Appendix, 8.1 Phase diagram). Similarly to cobalt, deep blue, viscous liquids

were obtained for $0.5 \geq \chi NiCl_2$ and light blue crystalline solids for $0.5 \leq \chi NiCl_2$, in comparison to the yellow $NiCl_2$.

## 5.3 Phase diagram for $[C_1C_4Im]Cl/CoCl_2]$

### 5.3.1 Thermal analysis

**Thermogravimetric analysis**

Firstly, all mixtures of $[C_1C_4Im]Cl/CoCl_2]$ were analysed by TGA which gives indication of the thermal stability of the compound. The thermograms of all mixtures are collated in the Appendix (8.1 Phase diagram). Here, the focus will be on the known species[332] $[C_1C_4Im]_2[CoCl_4]$ ($\chi CoCl_2 = 0.33$) and the influence that a small variation of $\chi CoCl_2$ can have. Therefore, $\chi CoCl_2 = 0.3$ and $\chi CoCl_2 = 0.35$ are of special interest. Furthermore, a crystal was obtained for $[C_1C_4Im]_2[CoCl_4]$ and the crystal structure was determined to have a space group *Cc*, which has been previously reported by Iwasawa *et al.* (8.2 Crystal structure).[332, 344]

All measurements were carried out under $N_2$ flow with a heating rate of 10°C/min. The decomposition onset temperature was determined with a double tangent approach and their crossing point is reported as the onset decomposition temperature. An initial isothermal of 10 minutes at 100°C was used to remove any adsorbed atmospheric water and this initial mass loss was disregarded when determining the decomposition temperature. In all samples the loss of water was less than 5 wt%, except for $\chi CoCl_2 \leq 0.15$ and $\chi CoCl_2 \geq 0.85$ where the mass loss observed at 100°C increased to up to 20 wt%.

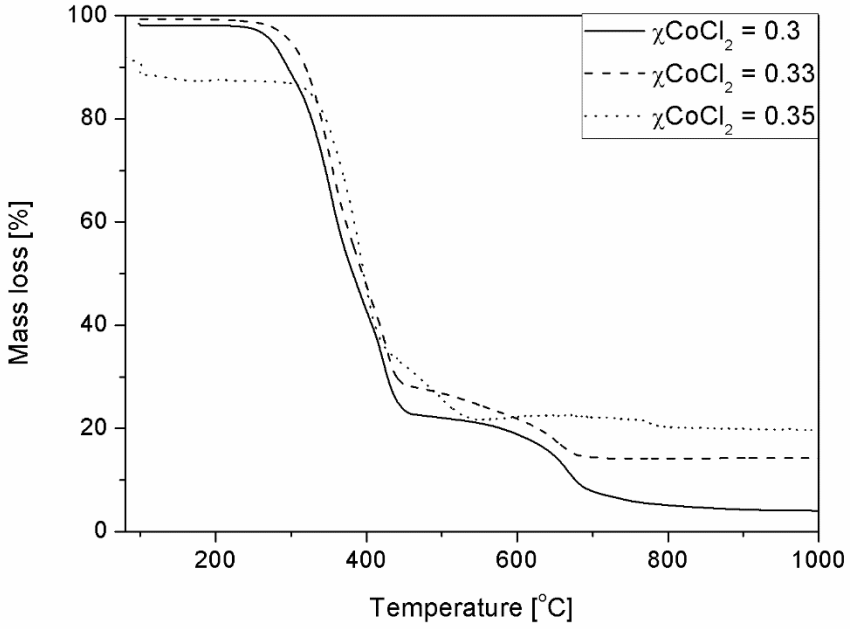



*Figure 5-1 Thermogram from TGA for mole fraction $\chi CoCl_2$ = 0.3, 0.33 and 0.35.*

Figure 5-1 shows the thermograms for the $[C_1C_4Im]Cl/[CoCl_2]$ mixture with mole fraction $\chi CoCl_2$ = 0.3, 0.33 and 0.35 a two-step decomposition is observed, except for $\chi CoCl_2$ = 0.35. For $\chi CoCl_2$ = 0.3 Initial decomposition occurs at an onset temperature of 280°C and a final mass loss is observed at 625°C. $[C_1C_4Im]Cl$ and $CoCl_2$ as pure compounds, individually show decomposition at 260°C and 726°C respectively.[345, 346] A residual of 4 wt% (0.239 mg) was observed at 1000°C, possibly due to formation of a cobalt species such as cobalt oxide which possesses a much higher melting point. It is likely to have formed during the decomposition process due to the presence of adsorbed water molecules. Indeed an initial loss of water was observed at 100°C (2 wt%), which could have initiated the formation of new cobalt oxide species.[347, 348]

The thermogram for $\chi CoCl_2$ = 0.33 (Figure 5-1) presents an initial mass loss of 7 wt% due to loss of water (isothermal at 100°C for 10 minutes). Onset of the

first decomposition step occurs at 330°C, being slightly higher than the decomposition temperature of 270°C reported by Zhang *et al*.[66] A residue of 13 wt% (0.225 mg) is observed at 1000°C, likely corresponding to cobalt oxide.

The thermogram for $\chi CoCl_2$ = 0.35 shows a one-step decomposition at 354°C with an initial mass loss at 100°C, which occurs due to the loss of adsorbed atmospheric water (7 wt%). The residue observed at the end of the heating ramp is 20 wt%, which is considerably higher than for the other samples. A small increase is detectable above 600°C indicating a reactive species, possibly cobalt oxide formation.[338]

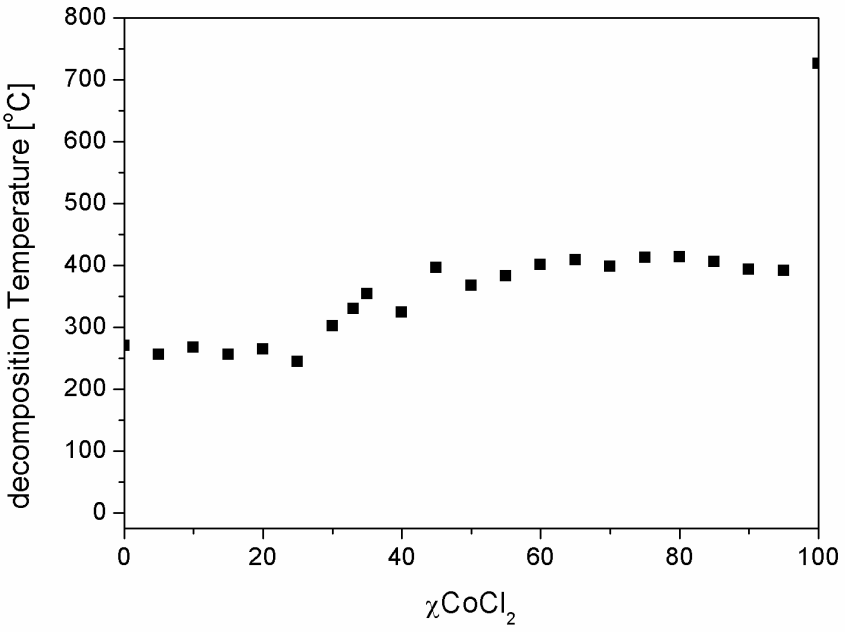



*Figure 5-2 Decomposition temperature for mixtures of $[C_1C_4Im]Cl/[CoCl_2]$ obtained from TGA.*

In Figure 5-2 decomposition temperatures are presented for mixtures of $[C_1C_4Im]Cl/[CoCl_2]$ from mole fraction $\chi CoCl_2$ = 0.05 up to $\chi CoCl_2$ = 0.95 determined by TGA. Values for pure $[C_1C_4Im]Cl$ and $[CoCl_2]$ were taken from the

literature.[346, 349] Initially, the decomposition temperature is comparable to that of $[C_1C_4Im]Cl$ but an increase in stability is notable from $\chi CoCl_2 = 0.35$ onwards. Overall the combination with $[C_1C_4Im]Cl$ significantly lowers the melting point in comparison to pure $CoCl_2$.

**Differential scanning calorimetry**

As discussed in the previous section, the mole fractions of interest lie in the range of 0.3 to 0.35 and are therefore analysed in detail in the following section. The thermograms were measured at a heating rate of 10°C/min with three consecutive cycles recorded for all $[C_1C_4Im]Cl/[CoCl_2]$ mixtures (Appendix, 8.1.1 Differential scanning calorimetry). Only the first two cycles will be displayed for clarity. Crystallisation $T_c$, melting $T_m$ and glass transition temperatures $T_g$ are given as the extrapolated onset temperature determined with an auxiliary line drawn on the curve.

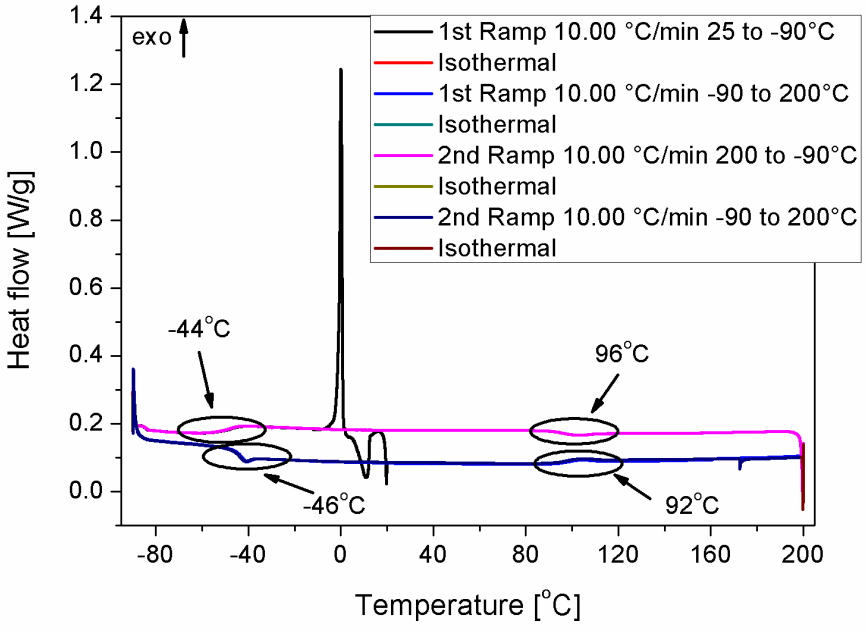


*Figure 5-3 DSC thermogram for mole fraction $\chi CoCl_2 = 0.3$.*

Upon cooling a broad endothermic peak ($T_m$ = 13°C) is observed (Figure 5-3) which corresponds to the sample melting with an enthalpy of ΔH = 5.7 J/g. The endothermic peak transitions into a narrow exothermic peak ($T_c$ = 0.8°C) with an enthalpy of ΔH = 10.6 J/g. However upon heating, no corresponding melting peak to a crystallisation peak can be observed, which means that the sample solidified in a glassy amorphous state.[192] The exothermic peak is followed by a glass transition $T_g$ = -44°C. Glass transitions occur upon on heating and cooling at around -45 and 93°C and are observed for all cycles in the same temperature range (Table 5-1).

*Table 5-1 Crystallisation $T_c$, melting $T_m$ and glass transition temperatures $T_g$ for $\chi CoCl_2 = 0.3$.*

| | **$T_c$ [°C]** | **$\Delta H(T_c)$ [J/g]** | **$T_m$ [°C]** | **$\Delta H(T_m)$ [J/g]** | **$T_g$ [°C]** |
|---|---|---|---|---|---|
| **1st cooling ramp** | 1 | 11 | 13 | 6 | -44 |
| **1st heating ramp** | | | | | -46<br>92 |
| **2nd cooling ramp** | | | | | -43<br>96 |
| **2nd heating ramp** | | | | | -47<br>91 |

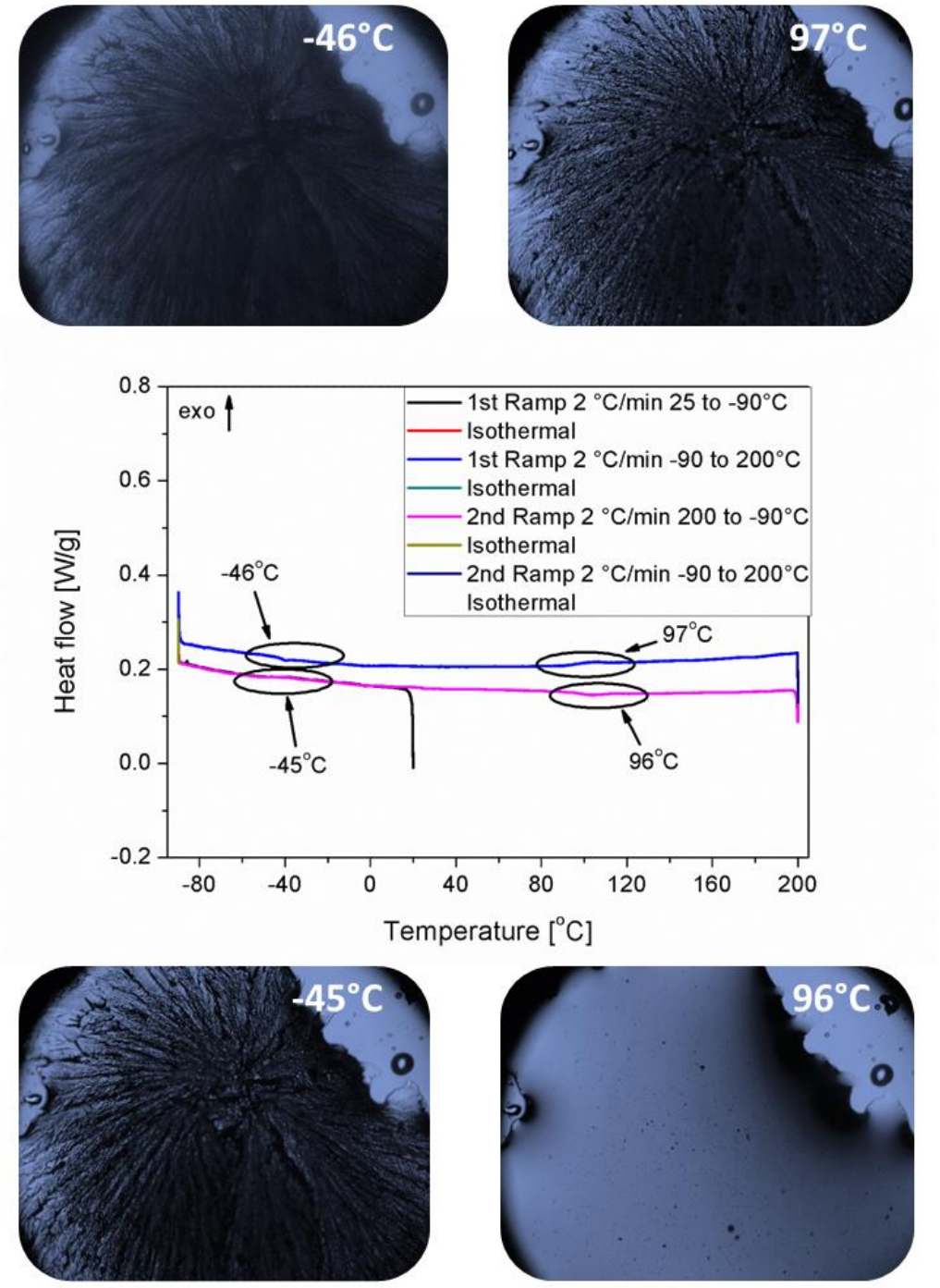



*Figure 5-4 DSC thermogram for mole fraction $\chi CoCl_2$ = 0.33 and pictures taken with a microscope at the phase transitions. Microscope lens magnification used was 10x.*

In Figure 5-4 the thermogram for $\chi CoCl_2$ = 0.33 obtained from DSC is shown together with pictures, taken with a microscope (lens magnification 10x), corresponding to the observed phase transition. The heating rate for the DSC

measurement was reduced to 2°C/min as no cold crystallisation was observed at higher heating rate. Despite this lower heating rate, still no crystallisation was observed, consistent with supercooling of the sample. Upon cooling a solid-solid glass transition is observable through the microscope, which is also visible during heating. At higher temperature, a second glass transition with a solid-solid phase transition is present and is followed by a corresponding glass transition upon cooling, where the sample melts without the presence of an endothermic peak.

*Table 5-2 Crystallisation $T_c$, melting $T_m$ and glass transition temperatures $T_g$ for $\chi CoCl_2 = 0.33$.*

| | $T_c$ [°C] | $\Delta H(T_c)$ [J/g] | $T_m$ [°C] | $\Delta H(T_m)$ [J/g] | $T_g$ [°C] |
|---|---|---|---|---|---|
| **1st cooling ramp** | | | | | -46 |
| **1st heating ramp** | | | | | -45<br>96 |
| **2nd cooling ramp** | | | | | 97<br>-47 |
| **2nd heating ramp** | | | | | -47<br>98 |

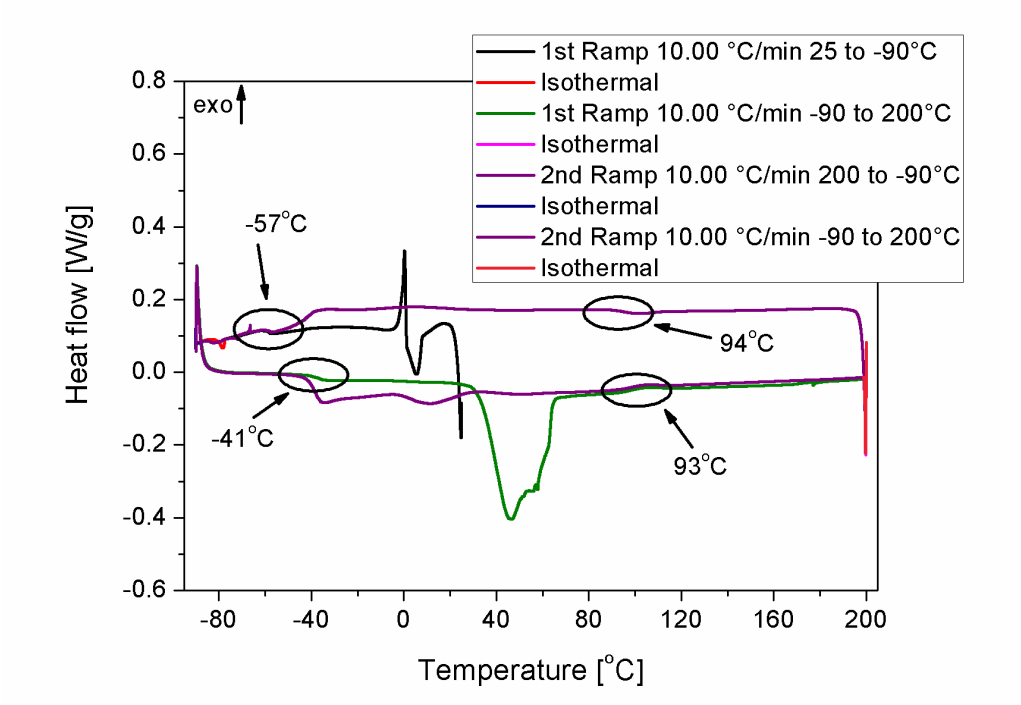



*Figure 5-5 DSC thermogram for mole fraction $\chi CoCl_2 = 0.35$.*

The thermogram obtained for mole fraction $\chi CoCl_2 = 0.35$ is shown in Figure 5-5 and all phase transitions are listed in Table 5-3. Initially upon cooling, an endothermic melting peak is observed at $T_m = 8°C$ ($\Delta H = 4$ J/g), which transitions into an exothermic cold crystallisation peak at $T_c = 1°C$ ($\Delta H = 3$ J/g). Upon heating a glass transition is present at -41°C and followed by a broad endothermic melting peak with an onset temperature of $T_m = 33°C$ ($\Delta H = 45$ J/g). The peak shows a shoulder towards higher temperatures, which suggests the presence of more than one species. Both the cooling and heating ramp display glass transitions at around 94°C. The second heating ramp reveals a glass transition with a superimposed endothermic peak at -42°C, indicating a melt forming a glassy amorphous state. This is directly followed by a broad endothermic peak $T_m = -1°C$ ($\Delta H = 2.9$ J/g), which does not overlap with the previous melting peak suggesting a change in phase upon cooling and heating.

*Table 5-3 Crystallisation $T_c$, melting $T_m$ and glass transition temperatures $T_g$ for $\chi CoCl_2 = 0.35$.*

| | $T_c$ [°C] | $\Delta H(T_c)$ [J/g] | $T_m$ [°C] | $\Delta H(T_m)$ [J/g] | $T_g$ [°C] |
|---|---|---|---|---|---|
| **1st cooling ramp** | 1 | 3 | 8 | 4 | -57 |
| **1st heating ramp** | | | 33 | 45 | -41<br>93 |
| **2nd cooling ramp** | | | | | -38<br>94 |
| **2nd heating ramp** | | | -1 | 3 | -42<br>93 |

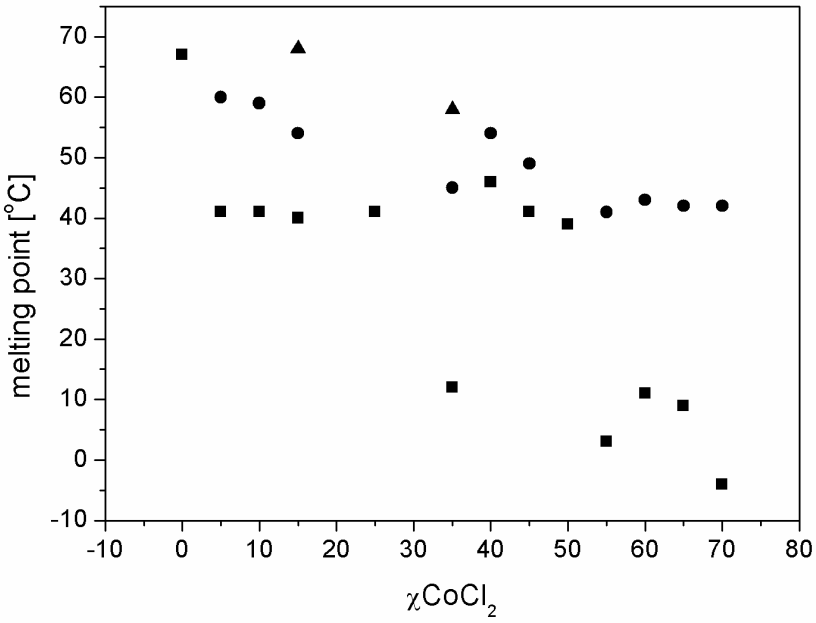



*Figure 5-6 Phase Diagram for mixtures of $[C_1C_4Im]Cl/[CoCl_2]$ with the melting point taken from DSC.*

Figure 5-6 describes the phase diagram for mixtures of $[C_1C_4Im]Cl/[CoCl_2]$ with melting points taken from DSC thermograms, where no point is represented in the phase diagram no melting point was observed.

### 5.3.2 Raman spectra for mixtures of $[C_1C_4Im]Cl/CoCl_2$

Raman spectroscopy can be a powerful tool to further understand the nature of the mixtures of $[C_1C_4Im]Cl/[CoCl_2]$ and to identify any new species that have been formed. Raman spectra were recorded at room temperature using a laser excitation wavelength of 785 nm. Unfortunately for $\chi CoCl_2 = 0.7$ and above no spectra were obtained due to fluorescence from the sample, even though a laser excitation in the near infrared region was selected to avoid fluorescence.

A competing process with Raman scattering is fluorescence emission, as they have similar origins. Fluorescence emission arises from an absorption process, where a photon is emitted from the lowest vibrational level of an excited electronic state. This is directly followed by the absorption of the photon and quickly accompanied by the relaxation to the lowest vibrational level of the electronic state. Depending on the excitation wavelength of the laser used and the sample itself, fluorescence emission can become so strong that it will make it impossible to obtain any valuable information from the Raman scattering.[350] Figure 5-7 shows the Raman spectrum for $\chi CoCl_2 = 0.1$ in a range from 200 to 3500 $cm^{-1}$ with a clear example for fluorescence appearing in the spectrum between 1200 and 2000 $cm^{-1}$.

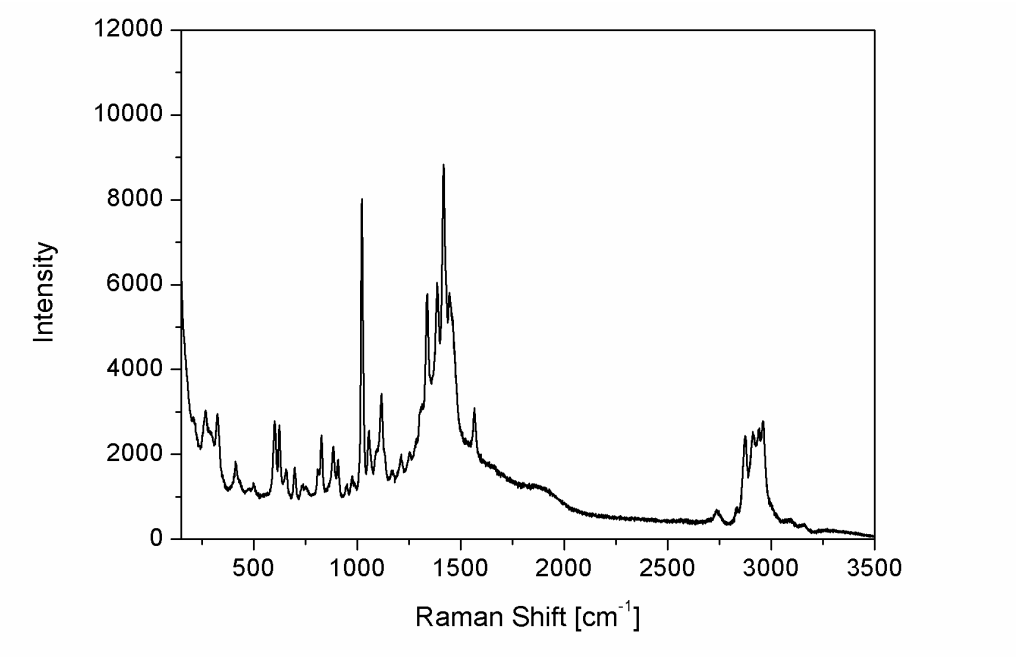



*Figure 5-7 Raman spectrum for $\chi CoCl_2$ = 0.1 measured with excitation wavelength 785 nm at room temperature, showing broad fluorescence around 1500 $cm^{-1}$.*

Figure 5-8 shows Raman spectra for pure $[C_1C_4Im]Cl$ and $[CoCl_2]$, as well as mixtures of $[C_1C_4Im]Cl/[CoCl_2]$ in the range of interest from 200 to 1000 $cm^{-1}$. An elevated baseline can be seen due to contribution of fluorescence from these dark blue mixtures. The pure crystalline $CoCl_2$ does not exhibit any fluorescence and thus does not have an elevated baseline. For pure $[C_1C_4Im]Cl$ an increase in the baseline can be attributed to the borosilicate glass slide holding the sample. Since $[C_1C_4Im]Cl$ is a white crystalline solid a contribution from the glass slide is more pronounced in comparison to the other dark blue samples. The tetrahedral $CoCl_4$ species, present in a $CsCoCl_4$ crystal, exhibits Co-Cl stretching vibrations at $\upsilon$ = 287 and 315 $cm^{-1}$.[351] These stretching vibrations are also present in the sample mixtures, highlighted with a purple box in Figure 5-8.

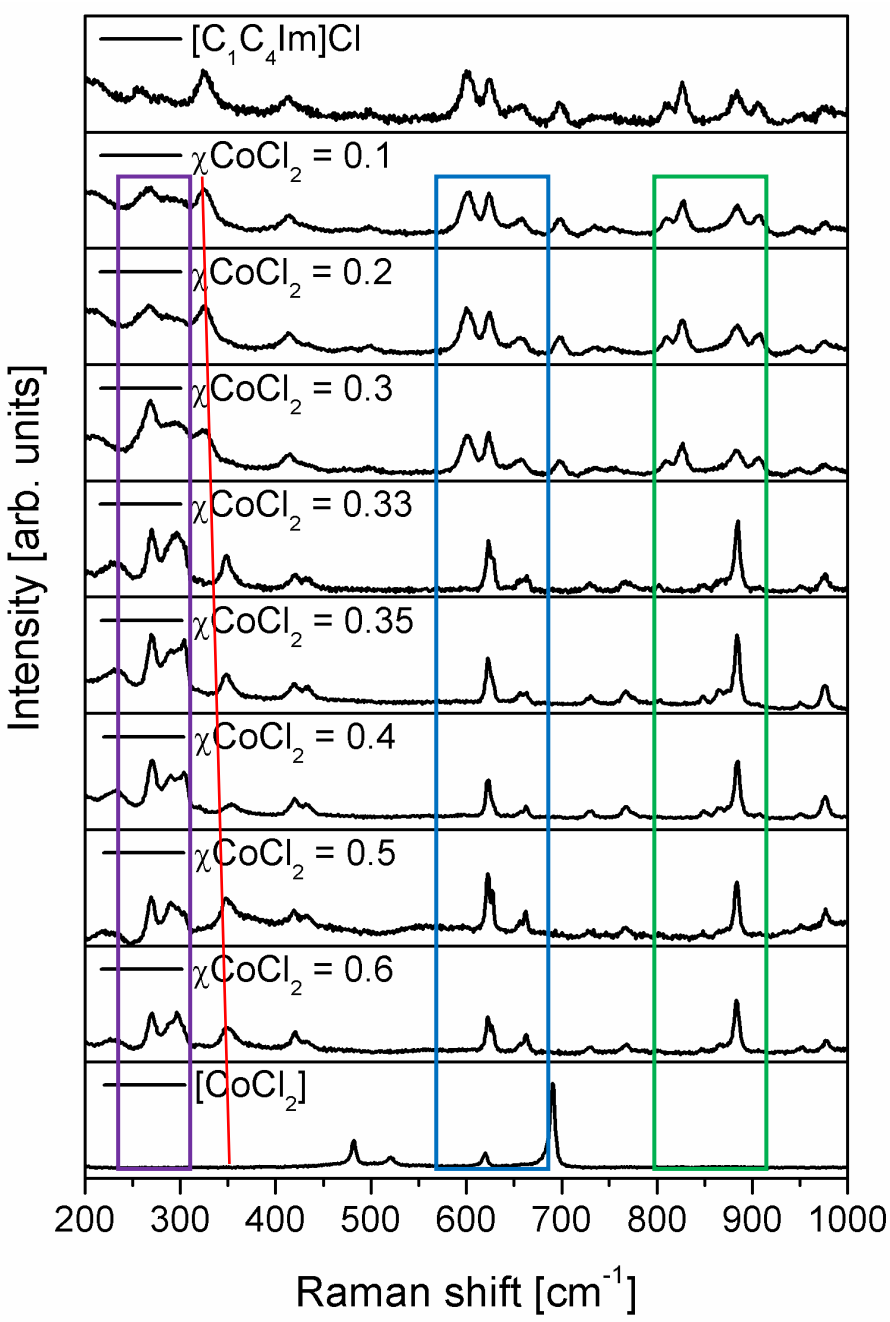



*Figure 5-8 Raman spectra for mixtures of $[C_1C_4Im]Cl/[CoCl_2]$ at room temperature and laser excitation wavelength of 785 nm showing normalized intensity.*

A clear change is visible, when following the peaks from top to bottom, i.e. from $\chi CoCl_2 = 0.1$ to $\chi CoCl_2 = 0.6$. Especially the vibration at 315 $cm^{-1}$ is only a clear peak from $\chi CoCl_2 = 0.33$ onwards. This confirms the formation and presence of the tetrahedral $[CoCl_4]^{2-}$ anion in all mixtures.

The peak at 325 $cm^{-1}$ can be attributed to the $CH_2$-N bend from the alkyl chain of the [$C_1C_4$Im] moiety.[43] A shift towards higher wavenumbers can be followed along the red line, likely indicating the change in coordination due to the formation of a new anion. Hamaguchi *et al.* investigated the differences in the Raman spectrum of [$C_1C_4$Im]Cl depending on the different crystalline forms and the liquid phase. They observed that the vibration between 600 and 900 $cm^{-1}$ (Figure 5-8, blue and green box) changed depending on the physical state of the IL. Indeed, when the physical state of the sample's changes from a liquid to a crystalline solid at room temperature, one peak ($\chi CoCl_2$ = 0.33 to $\chi CoCl_2$ = 0.6) is observed instead of two peaks ([$C_1C_4$Im]Cl; $\chi CoCl_2$ = 0.1 to $\chi CoCl_2$ = 0.3).

Figure 5-9 presents Raman spectra measured at room temperature and laser excitation wavelength 785 nm for $\chi CoCl_2$ = 0.1 to $\chi CoCl_2$ = 0.6 and [$C_1C_4$Im]Cl in the range of 250 to 380 nm. This range highlights the changes around the dominant peaks observed for a $[CoCl_4]^{2-}$ anion, which are reported in the literature at υ = 287 and 315 $cm^{-1}$.[351] A peak growing in intensity (from $\chi CoCl_2$ = 0.1 to $\chi CoCl_2$ = 0.6) can be noted in the range of υ = 260-270 nm and is shifted to higher wavelength with increasing $CoCl_2$ mole fraction (blue line). Interestingly, Lockwood *et al.* reported similar wavelengths for a complex of the type $CsCoCl_3$ and $RbCoCl_3$.[352] A broad second peak can be observed at $\chi CoCl_2$ = 0.33 to 0.6, which could be two peaks overlapping corresponding to the two peaks generally observed for the tetrahedral cobalt halide. A peak around 330 nm (red box) observed also in the Raman spectra for [$C_1C_4$Im]Cl is present until $\chi CoCl_2$ = 0.3, but then is no longer visible and a peak around 350 nm is observed starting at $\chi CoCl_2$ = 0.33 (purple box). This likely indicates the

absence of a free chloride due to the formation of the tetrahedral anion. This would lead to the postulation, that in $\chi CoCl_2 = 0.33$ to 0.6 the species $[CoCl_4]^{2-}$ is present.

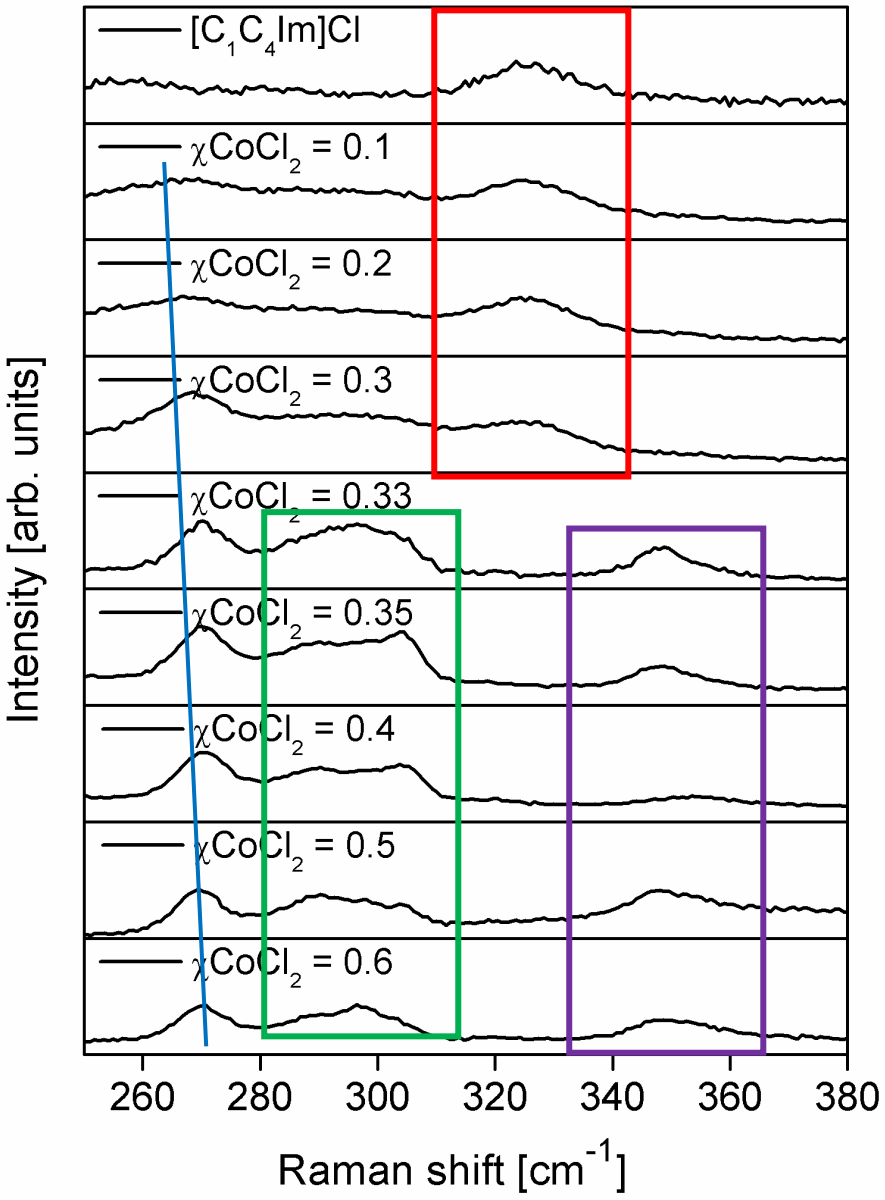



*Figure 5-9 Raman spectra for mixtures of $[C_1C_4Im]Cl/[CoCl_2]$ at room temperature and laser excitation wavelength of 785 nm showing normalized intensity.*

## 5.4 Phase Diagram for $[C_1C_4Im]Cl/[NiCl_2]$

### 5.4.1 Thermal analysis

**Thermogravimetric Analysis**

Firstly, all mixtures of $[C_1C_4Im]Cl/[NiCl_2]$ were analysed by TGA which gives an indication of the thermal stability of the compound. The thermograms of all mixtures are collated in the Appendix (8.1 Phase diagram). Here, the focus will be on the known species[335, 336] $[C_1C_4Im]_2[NiCl_4]$ ($\chi NiCl_2 = 0.33$) and the influence that a small variation of $\chi NiCl_2$ can have. Therefore, $\chi NiCl_2 = 0.3$ and $\chi NiCl_2 = 0.35$ are of special interest.

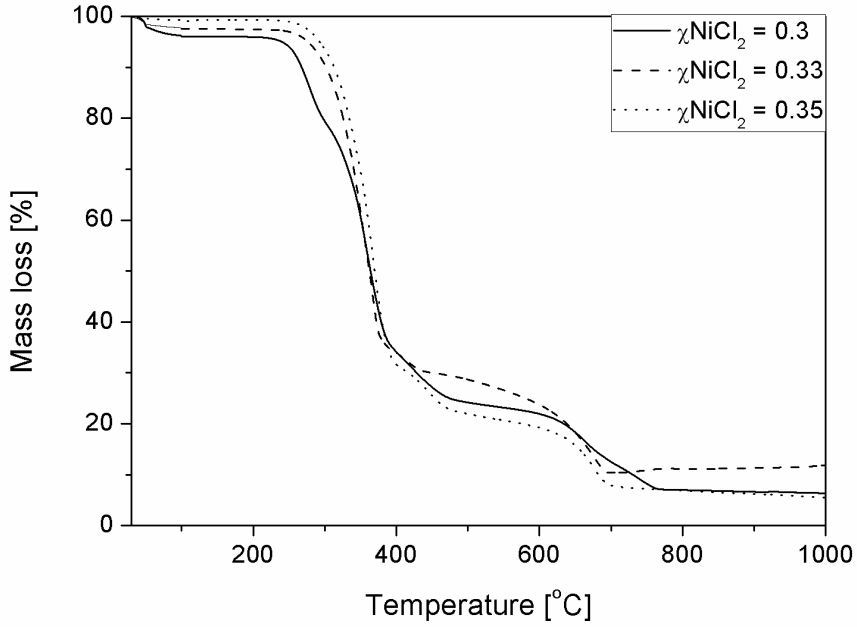



*Figure 5-10 TGA thermogram for mole fraction χNiCl2 = 0.3, 0.33 and 0.35.*

Figure 5-10 shows the thermal decomposition thermograms for $\chi NiCl_2 = 0.3$, 0.33 and 0.35 presenting a two-step decomposition. The initial decomposition onset for $\chi NiCl_2 = 0.3$ occurs at 253°C, followed by a second step at 625°C.

Initially the loss of atmospheric water is observed at an isothermal for 10 minutes at 100°C (4 wt%).

The thermogram for $\chi NiCl_2$ = 0.33 (Figure 5-10) presents an initial mass loss of 3 wt% due to loss of water (isothermal at 100°C for 10 minutes). Onset of the first decomposition step occurs at 315°C, being slightly lower than the decomposition temperature of 332°C reported by Zhang *et al*.[66] The second decomposition step is observed at 615°C and a residue of 12 wt% at 1000°C, likely corresponding to nickel oxide. A slight mass increase can be observed after the final decomposition step, indicating the formation of a reactive species.[338] The thermogram for $\chi NiCl_2$ = 0.35 (Figure 5-10) presents a first decomposition step at 311°C and a residue of 5 wt% is observed at 1000°C, likely corresponding to nickel oxide.

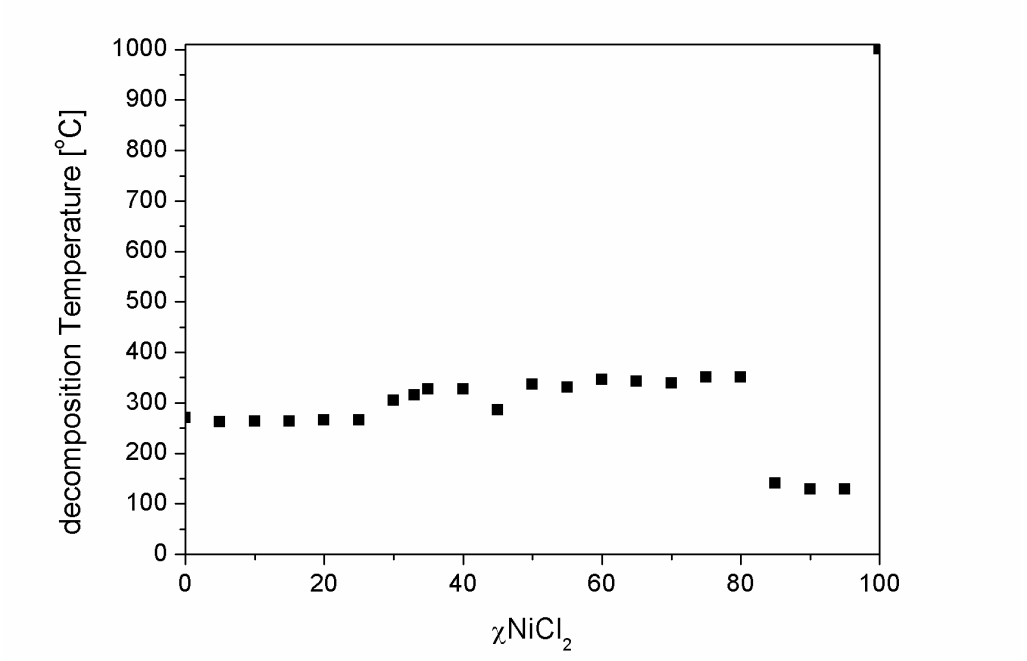



*Figure 5-11 Decomposition temperature for mixtures of $[C_1C_4Im]Cl/[NiCl_2]$ taken from TGA.*

In Figure 5-11, decomposition temperatures are presented for mixtures of $[C_1C_4Im]Cl/[NiCl_2]$ from mole fraction $\chi NiCl_2$ = 0.05 up to $\chi NiCl_2$ = 0.95 determined by TGA. Values for pure $[C_1C_4Im]Cl$ and $NiCl_2$ were taken from the literature.[349, 353] Initially, the decomposition temperature is comparable to $[C_1C_4Im]Cl$ until an increased stability is noted from $\chi NiCl_2$ = 0.3 onwards up to $\chi NiCl_2$ = 0.8. However, there is an exception for $\chi NiCl_2$ = 0.45, where a small drop in decomposition temperature is observed. For $\chi NiCl_2$ = 0.85 to $\chi NiCl_2$ = 0.95 stability decreases drastically.

**Differential scanning calorimetry**

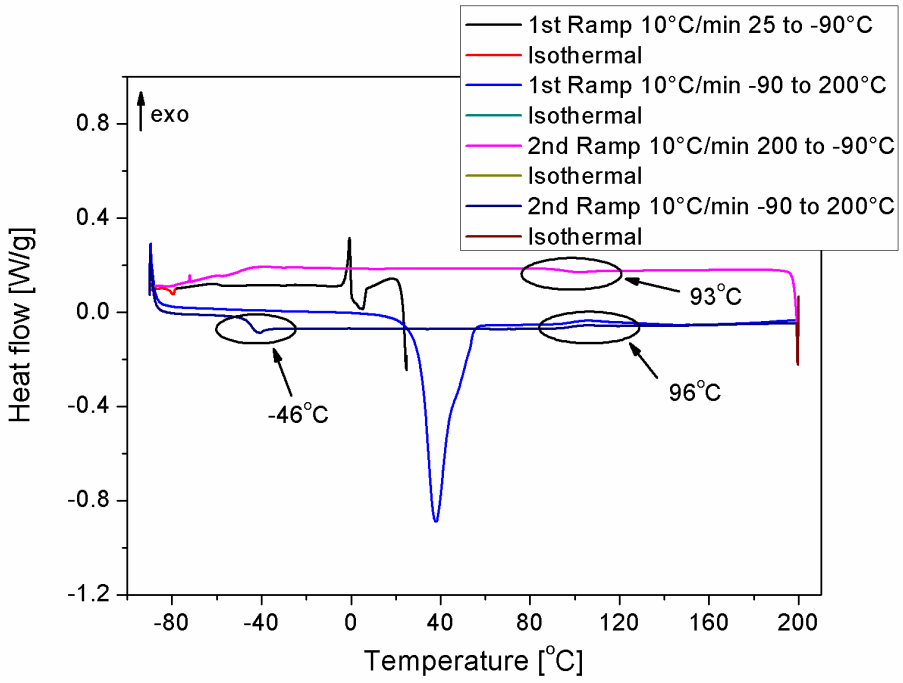



*Figure 5-12 DSC thermogram for mole fraction $\chi NiCl_2$ = 0.3.*

Figure 5-12 shows the thermogram for $\chi NiCl_2$ = 0.3 and all phase transitions are listed in Table 5-4. The cooling ramp is started at room temperature and an exothermic crystallisation peak is observed at approximately 0°C ($\Delta H(T_c)$ = 4

J/g). Upon heating, a corresponding broad endothermic peak is visible at 31°C ($\Delta H(T_m)$ = 68 J/g), which suggests the presence of more than one species melting at this point or a mixture of a crystalline and an amorphous material. Glass transitions are detected upon cooling and heating at around 95°C and show reversible phase transitions. The second heating ramp only presents a glass transition with a superpositioned endothermic peak ($T_g$ = -46°C) indicating that the sample solidified as an amorphous glass.

*Table 5-4 Crystallisation $T_c$, melting $T_m$ and glass transition temperatures $T_g$ for $\chi NiCl_2$ = 0.3.*

| | **$T_c$ [°C]** | **$\Delta H(T_c)$ [J/g]** | **$T_m$ [°C]** | **$\Delta H(T_m)$ [J/g]** | **$T_g$ [°C]** |
|---|---|---|---|---|---|
| **1st cooling ramp** | 0 | 4 | | | |
| **1st heating ramp** | | | 31 | 68 | 96 |
| **2nd cooling ramp** | | | | | 93 |
| **2nd heating ramp** | | | | | -46<br>96 |

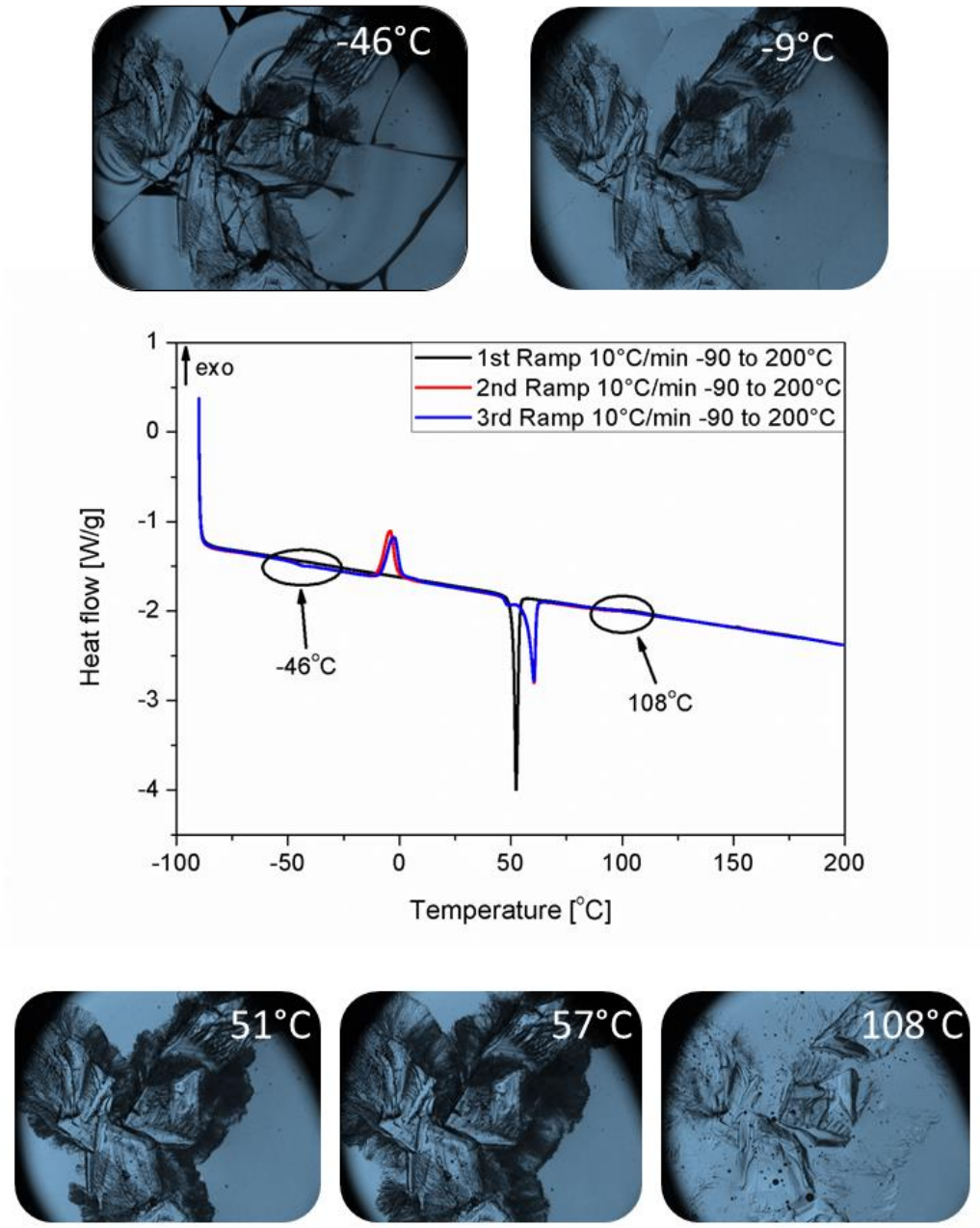



*Figure 5-13 DSC thermogram for mole fraction $\chi NiCl_2$ = 0.33 and microscope images showing phase transitions. A microscope lens with a magnification of 10x was used.*

For clarity, Figure 5-13 only shows the three heating ramps measured for $\chi NiCl_2$ = 0.33, the full thermogram can be found in the Appendix (8.1.1 Differential scanning calorimetry, Figure 8-26). A microscope was used to observe phase

transitions during heating and cooling cycles. An exothermic crystallisation peak is observed at 8°C ($\Delta H(T_c)$ = 4 [J/g]) and a corresponding melting peak ($T_m$ = 51°C; $\Delta H(T_m)$ = 57 [J/g]) is noticeable upon heating. The pictures taken through the microscope confirm the observation. In the second and third ramp, crystallisation and melting is detected at the same temperature during heating (see Table 5-5). A glass transition also occurs before transitioning into a melting peak. The glass transition at -46°C indicates birefringence when investigated under the microscope, possibly showing liquid crystalline behaviour. Unfortunately, it was not possible to observe the same behaviour when a polarizable optical microscope was used.

*Table 5-5 Crystallisation $T_c$, melting $T_m$ and glass transition temperatures $T_g$ for $\chi NiCl_2$ = 0.33.*

| | **$T_c$ [°C]** | **$\Delta H(T_c)$ [J/g]** | **$T_m$ [°C]** | **$\Delta H(T_m)$ [J/g]** | **$T_g$ [°C]** |
|---|---|---|---|---|---|
| **1st cooling ramp** | 8 | 4 | | | |
| **1st heating ramp** | | | 51 | 57 | |
| **2nd cooling ramp** | | | | | |
| **2nd heating ramp** | -9 | 37 | 57 | 24 | -46<br>47<br>108 |
| **3rd cooling ramp** | | | | | |
| **3rd heating ramp** | -9 | 37 | 57 | 24 | -46<br>47<br>108 |

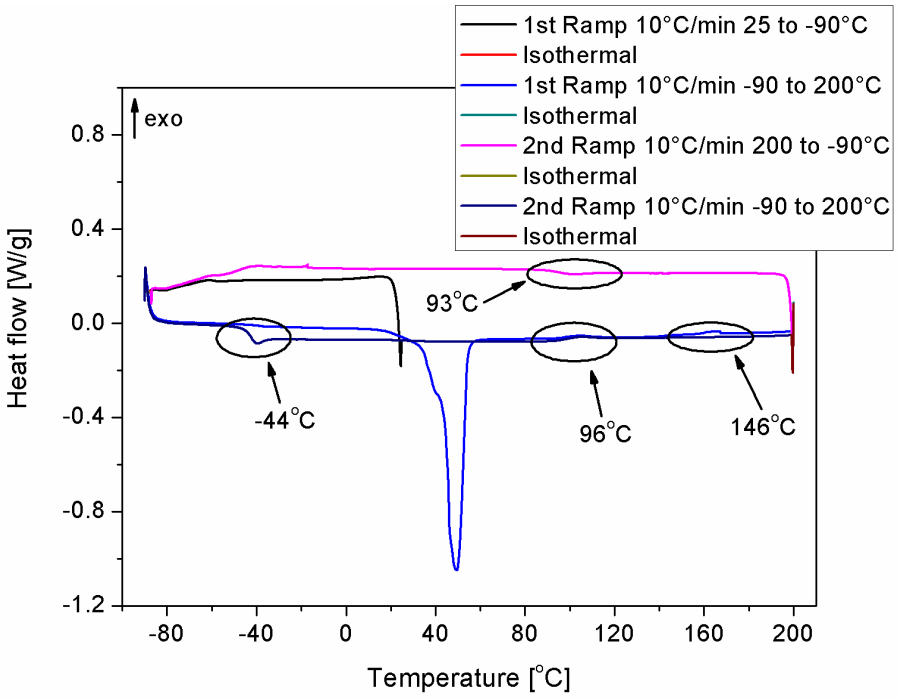



*Figure 5-14 DSC thermogram for mole fraction $\chi NiCl_2$ = 0.35 mole fraction.*

The thermogram obtained for mole fraction $\chi NiCl_2$ = 0.35 is shown in Figure 5-14 and all phase transitions are listed in Table 5-6. Upon heating, an endothermic melting peak is observed at $T_m$ = 44°C (ΔH = 63 J/g), which shows a shoulder towards lower temperatures, which suggests the presence of more than one species. This is followed by a glass transition at 96 and 146°C, which is present in both subsequent heating and cooling ramps at 93°C. In addition, the second heating ramp reveals a glass transition with a superimposed endothermic peak at -44°C, indicating a melt forming a glassy amorphous state.[192]

*Table 5-6 Crystallisation $T_c$, melting $T_m$ and glass transition temperatures $T_g$ for $\chi NiCl_2$ = 0.35.*

| | $T_c$ [°C] | ΔH($T_c$) [J/g] | $T_m$ [°C] | ΔH($T_m$) [J/g] | $T_g$ [°C] |
|---|---|---|---|---|---|
| **1st cooling ramp** | | | | | |

| | | | |
|---|---|---|---|
| **1st heating ramp** | 44 | 63 | 96<br>146 |
| **2nd cooling ramp** | | | 93 |
| **2nd heating ramp** | | | -44<br>93 |

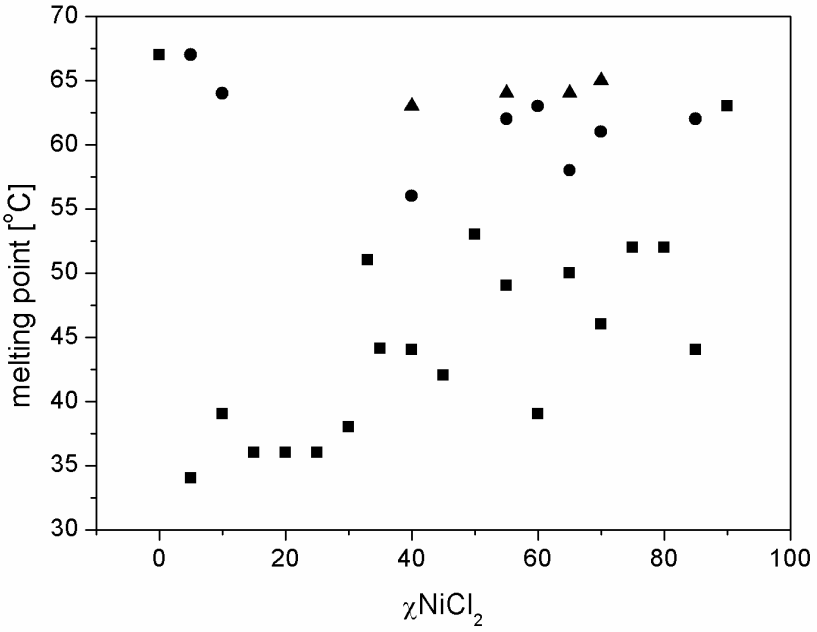



*Figure 5-15 Phase diagram for mixtures of [$C_1C_4$Im]Cl/[$NiCl_2$] with melting points taken from DSC.*

Figure 5-15 shows the phase diagram obtained from DSC for mixtures of [$C_1C_4$Im]Cl and [$NiCl_2$]. Thermograms were analysed for endothermic melting peaks and the peak temperature is presented in the phase diagram. As expected from the multiple phase transitions observed previously, a complex phase diagram is obtained with no clear eutectic. Generally, low melting temperatures are noted for $\chi NiCl_2$ = 0.1 to $\chi NiCl_2$ = 0.3 and increasing melting points with increasing concentration of $NiCl_2$.

### 5.4.2 X-ray photoelectron spectroscopy

X-ray photoelectron spectroscopy was used to analyse the oxidation state of nickel in the obtained $NiCl_2$/IL mixtures. It was found impossible to obtain Raman spectra from the samples, as the only response observed was noise. Possibly occurring from multiple phase changes within the sample due to laser excitation. The multiple phase transitions observed with DSC (5.4.1 Thermal analysis) also made it challenging to record XP spectra, therefore the data presented here is preliminary but will need more work in the future.

All spectra were charge corrected to the $C_{aliphatic}$ 1s = 285 eV, except for pure metal samples where adventitious carbon was used.[354] Only homogeneous samples were used i.e. $\chi NiCl_2$ = 0.1 to $\chi NiCl_2$ = 0.6. Some samples presented O 1s and Si 2p peaks, originating from the precursor $NiCl_2$. $Ar^+$ bombardment to etch the sample surface was not carried out as previous experiments showed damage to the sample.[72] Figure 5-16 shows normalized high resolution XP spectra for the Ni 2p peak for $\chi NiCl_2$ = 0.1 to $\chi NiCl_2$ = 0.6 and pure $NiCl_2$. Binding energies of the main photoelectron peaks are given in Table 5-7.

The Ni 2p photoelectron peak presents multiplet splitting into Ni $2p_{1/2}$ and Ni $2p_{3/2}$, as well as satellite peaks. A red line is added to highlight the shift to higher binding energies with increasing $NiCl_2$ amount. The spectrum obtained for $\chi NiCl_2$ = 0.33 shows the expected peak pattern reported in the literature, suggesting the presence of $[NiCl_4]^{2-}$.[72]

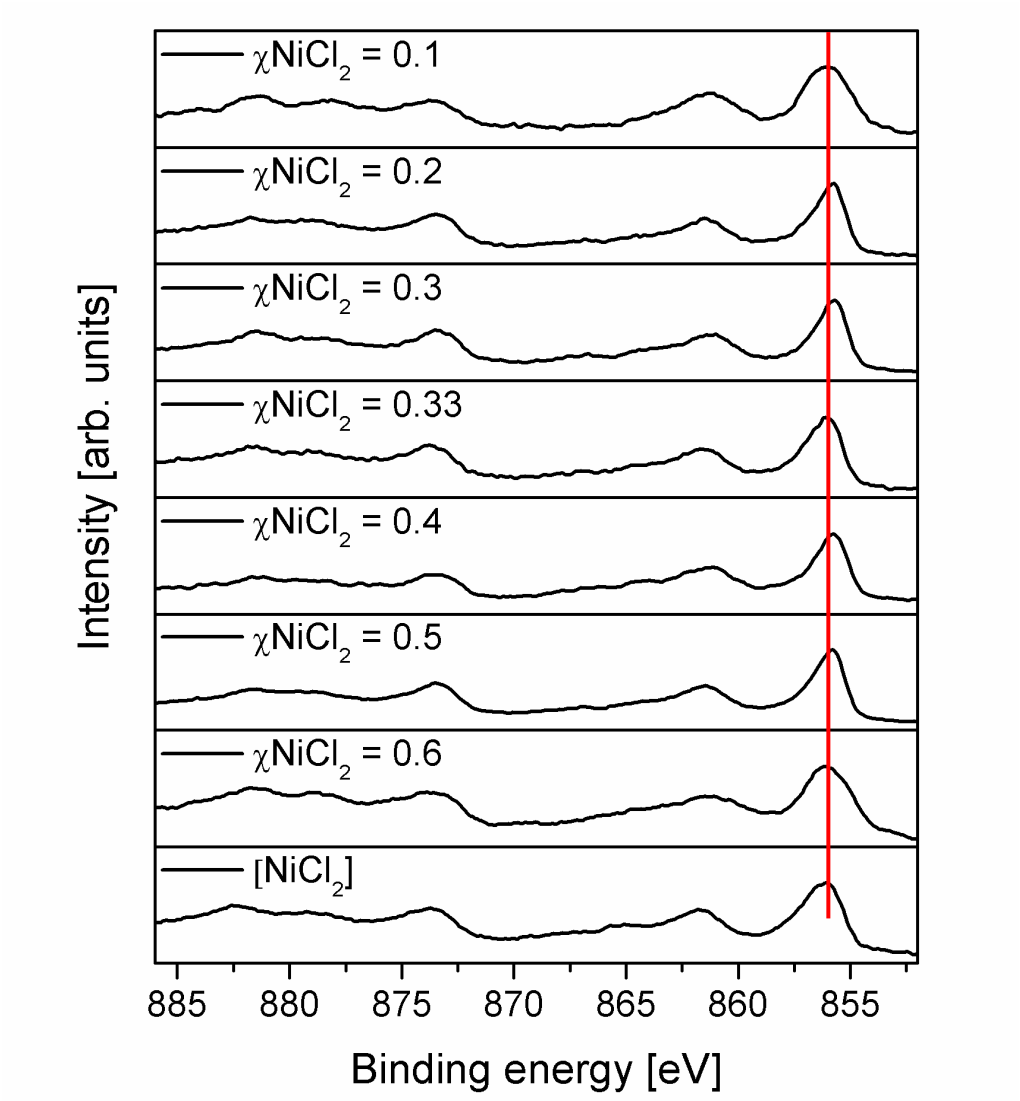



*Figure 5-16 High resolution XP spectra for Ni 2p for the mixtures of [$C_1C_4$Im]Cl/[$NiCl_2$]. All spectra are charge corrected to $C_{aliphatic}$ 1s = 285.0 eV. The red line is a guide for the eyes.*

In Figure 5-17 normalized high resolution XP spectra for Cl 2p are displayed with increasing $NiCl_2$ concentration and [$C_1C_4$Im]Cl and [$NiCl_2$] as a comparison. A significant shift towards higher binding energies can be observed (red line). In addition, a third peak appeared for $\chi NiCl_2$ = 0.2 to $\chi NiCl_2$ = 0.4 towards lower binding energies, indicating more than one discrete electronic environment. Indeed, a similar occurrence was reported by Terrade *et al.* for tin chloride/IL mixtures.[115] The molar fraction $\chi NiCl_2$ = 0.33 displays a discrete spin-orbit coupled doublet with an energy separation of 1.6 eV. However, the doublet

presents a shoulder towards lower binding energy, suggesting a surplus of $[C_1C_4Im]Cl$ precursor.

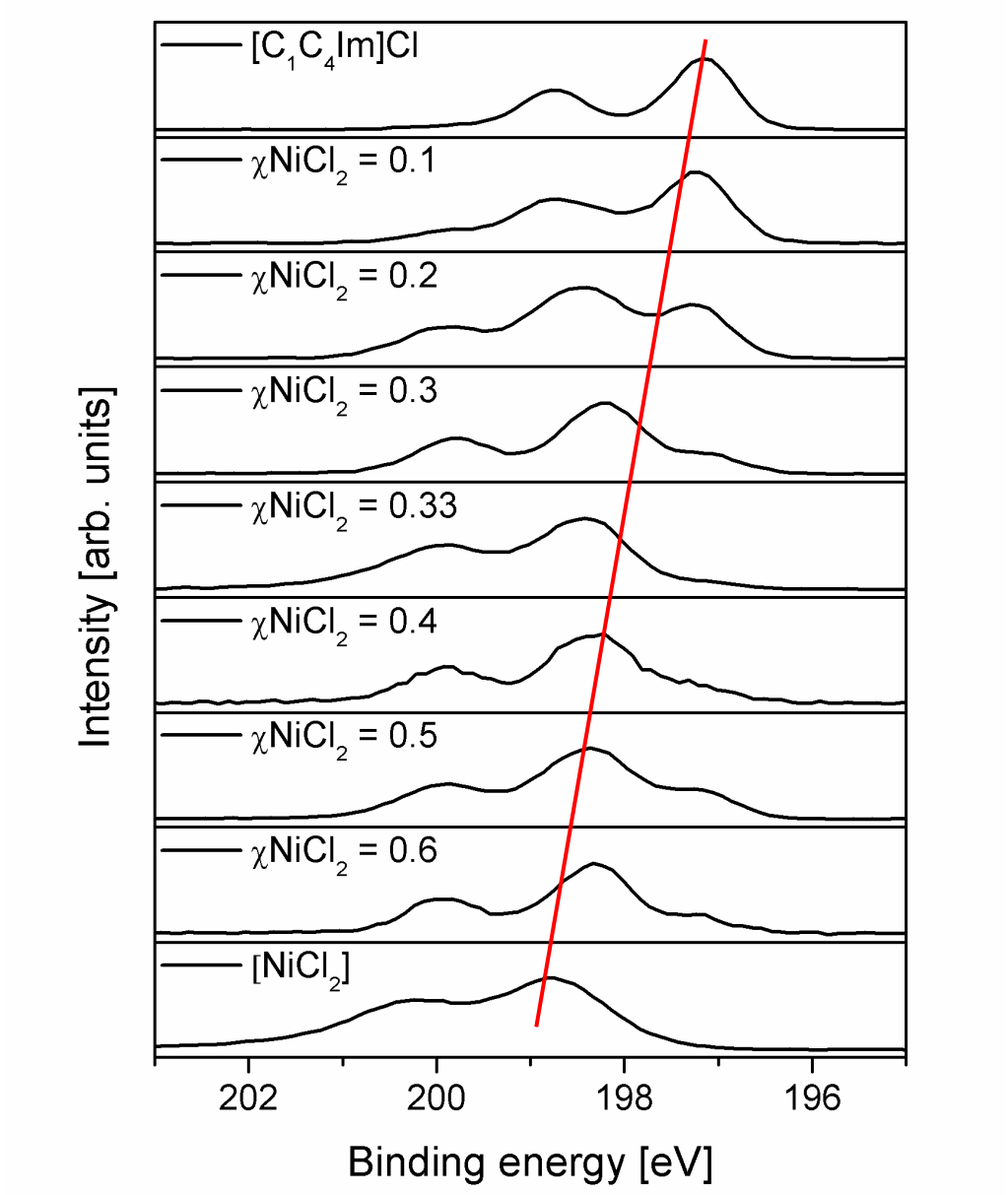



*Figure 5-17 High resolution XP spectra for Cl 2p for the mixtures of $[C_1C_4Im]Cl/[NiCl_2]$. All spectra are charge corrected to $C_{aliphatic}$ 1s = 285.0 eV. The red line is a guide for the eyes.*

*Table 5-7 Binding energies in electron Volts for pure [$C_1C_4$Im]Cl and [$NiCl_2$], as well as mixtures of the two. All spectra are charge corrected to Caliphatic 1s = 285.0 eV.*

| | | Binding energy [eV] | | | | |
|---|---|---|---|---|---|---|
| **Compound** | $\chi_{NiCl2}$ | C 1s | N 1s | Ni $2p_{3/2}$ | Cl $2p_{3/2}$ | Ni Auger |
| **[$C_1C_4$Im]Cl** | 0 | 285.0 | 401.8 | | 197.2 | |
| **[$C_1C_4$Im]Cl/$NiCl_2$** | 0.1 | 285.0 | 401.9 | 856.1 | 197.2 | 642.3 |
| **[$C_1C_4$Im]Cl/$NiCl_2$** | 0.2 | 285.0 | 401.7 | 855.7 | 198.5 | 641.6 |
| **[$C_1C_4$Im]Cl/$NiCl_2$** | 0.3 | 285.0 | 401.7 | 855.8 | 198.2 | 643.3 |
| **[$C_1C_4$Im]Cl/$NiCl_2$** | 0.33 | 285.0 | 401.8 | 856.0 | 198.4 | 642.8 |
| **[$C_1C_4$Im]Cl/$NiCl_2$** | 0.4 | 285.0 | 401.7 | 855.8 | 198.2 | 641.7 |
| **[$C_1C_4$Im]Cl/$NiCl_2$** | 0.5 | 285.0 | 401.7 | 855.7 | 198.1 | 640.4 |
| **[$C_1C_4$Im]Cl/$NiCl_2$** | 0.6 | 285.0 | 401.7 | 855.7 | 198.1 | 642.8 |
| **$NiCl_2$** | 1 | 285.0 | | 856.3 | 198.8 | 642.8 |

## 5.5 Conclusion

In this part of the work mixtures of $CoCl_2$ and $NiCl_2$ with [$C_1C_4$Im]Cl were systematically prepared and analysed with thermal and spectroscopic methods. Discrete anion formation, in the form $[MCl_4]^{2-}$, was observed for both nickel and cobalt. As expected, a small difference in mole fraction led to a change in speciation. Interestingly, no other anion formation was observed within this work, such as a dimeric species. In both cases only the presence of $[MCl_4]^{2-}$ was confirmed and the free [$C_1C_4$Im]Cl species. It can be concluded that for mole fractions other than $\chi MCl_2 = 0.33$, a mixture of $[C_1C_4Im]_2[MCl_4]$, $MCl_2$ and [$C_1C_4$Im]Cl is present. For mole fraction $\chi MCl_2 = 0.1$ to $\chi MCl_2 = 0.6$ it is most

likely $MCl_2$ and $[C_1C_4Im]Cl$ dissolved in $[C_1C_4Im]_2[MCl_4]$. For mole fraction $\chi MCl_2 \geq 0.65$ a non-homogeneous mixture was observed, where $MCl_2$ precipitated from the mixture. Finally, utmost care must be taken when preparing these halometallate ILs, because as demonstrated the smallest deviation from the ideal mixture can lead to an unwanted change in speciation.

# General conclusion

## 6. Conclusion and future work

### 6.1 Conclusion

In this work a variety of halometallate ILs were synthesised and characterised regarding their dielectric properties. Different anions were investigated, including Co(II), Ni(II), Cu(II), Zn(II), In(III), and Fe(III) halides. Firstly, a phase diagram for Co(II) chloride and Ni(II) chloride with $[C_1C_4Im]Cl$ was prepared. A discrete anion formation was observed at $\chi MCl_2$ = 0.33 in both instances. However, the formation of one or more species, other than $[MCl_4]^{2-}$, could not be confirmed, even though DSC indicates the formation of more than one species. The phase diagram for $[C_1C_4Im]Cl/CoCl_2$ shows a peritectic point at $\chi CoCl_2$ = 0.33, corresponding to the pure $[C_1C_4Im]_2[CoCl_4]$ and a eutectic at $\chi CoCl_2$ = 0.25. Raman spectroscopy confirmed the presence of $[CoCl_4]^{2-}$ in the mixtures $\chi CoCl_2$ = 0.1 to 0.6 with varying intensity. Mixtures of $[C_1C_4Im]Cl/NiCl_2$ displayed complex phase behaviour and consequently an intricate phase diagram was obtained. XPS suggests the presence of $[C_1C_4Im]_2[NiCl_4]$ at $\chi NiCl_2$ = 0.33, as previously reported in the literature.[72]

Dielectric properties and conductivity were successfully examined using dielectric spectroscopy and impedance spectroscopy. As expected, all halometallate ILs showed dielectric constants and loss viable for an application in MW reactions. Therefore, making them excellent candidates as solvent or solvent dopant to improve MW heating in otherwise MW transparent

materials. The observed dielectric constants vary depending on the metal and temperature in a range from ε' = 3.4-13.9, whereas the loss is observed to be in a range of ε'' = 0.5-170. Furthermore, two techniques showed comparable results regarding the dielectric properties of the halometallate ILs investigated, namely the coaxial slim probe and the resonant perturbation cavity.

Finally, the IL $[C_1C_4Im][Fe(NO)_2Cl_2]$ was employed as Lewis acid catalyst for the conversion of $CO_2$ to form cyclic carbonates from epoxides. The reaction was successfully carried out at moderate temperature and pressure (40°C, 2 bar). In addition, through mechanistic and kinetic studies the catalytically active species was revealed to be $[C_1C_4Im]Cl$ and $[Fe(NO)_2Cl]$. Furthermore, a wide range of substrates demonstrated versatility of the catalyst, yielding moderate to good conversion for all substrates employed.

All in all, this work has shown the advantages, current challenges, and future possibilities of halometallate ILs. As Lewis acid catalysts they can improve reaction performance, when simultaneously acting as a solvent and show capacity for inductive heating. As such they achieve multiple operations even when present in small quantity.

## 6.2 Future work

This work has shown several promising results, yet the field of halometallate ILs still poses some unanswered questions, which were outside of the scope of this thesis. For example, an in-depth XPS and EXAFS study could be used to investigate the challenging phase transitions observed, in particular for the Ni(II) mixtures.

Moreover, the use of Lewis acidic halometallate IL catalysts in inductive heating processes show great promise, as has been shown in this work. There is not only potential in the use of halometallate ILs as solvents/solvent dopant but also as catalysts. Therefore, the next step would be, their application in MW synthesis or another inductive heating technique, such as magneto-thermal heating.

Dielectric properties could be further investigated using different techniques like OKE spectroscopy or terahertz dielectric spectroscopy to detect relaxation mechanisms which have been so far undetected. Furthermore, a theoretical model could be developed to help understanding of the complex behaviour.

# 7. Methods and materials

## 7.1 Analytical methods

### 7.1.1 Dielectric spectroscopy

Dielectric spectroscopy was carried out using a coaxial slim probe with a HP8510C vector network analyser and a resonance perturbation cavity with a copper cavity using 912 and 2470 MHz close to the allocated ISM band frequencies. It is connected to a furnace with a temperature control unit, a Hewlett Packard 8753C vector network analyser (VNA), and a vertical sample actuator to move the sample between the furnace and the cavity. All experiments were repeated three times per temperature after a 10 minute calibration time.

### 7.1.2 Impedance spectroscopy

An Autolab PGSTAT302 (EcoChemie, the Netherlands) was used to carry out galvanostatic impedance spectroscopy in a frequency range of 0.1 to $10^4$ Hz. A two electrode system with two platinum electrodes was used. Three repeat measurements were carried out per temperature.

### 7.1.3 Nuclear magnetic resonance (NMR)

$^{1}H$ and $^{13}C$ NMR spectra were recorded on a Bruker DPX400 400 MHz and a DPX500 500 MHz nuclear magnetic resonance spectrometer. ILs were measured solvent free using an inlet tube, where the IL is in a small tube inside the NMR tube with deuterated solvent.

### 7.1.4 Gas chromatography (GC)

Analyses (determination of enantiomeric excess) of the reaction mixtures were performed on a Thermo Scientific Trace 1310 Gas Chromatograph with a Lipodex A (hexakis-(2,3,6-tri-O-pentyl)-α-cyclodextrin) 25m column.

### 7.1.5 Thermogravimetric analysis (TGA)

Thermogravimetric measurements were carried out on a TA instruments Discovery at a heating rate of 10°C/min and in a temperature range from 20 to 1000°C under $N_2$ in a platinum crucible.

### 7.1.6 Differential scanning calorimetry (DSC)

DSC was carried out using a TA instrument Discovery typically at a heating rate of 10°C/min and in a temperature range of -90°C to 200°C with three cycles. Samples were prepared in the glovebox using hermetically sealed platinum crucibles.

### 7.1.7 Inductively coupled plasma optical emission spectrometry (ICP-OES)

The iron and chloride content determination were performed through analysis of the samples by ICP-OES on a Perkin Elmer Optima 2000 DV ICP-OES. The samples were prepared by diluting 25 mL of IL with approximated iron concentration of 150 mg/L (ppm) (and, when chloride is present, the chloride concentration is between 100-150 mg/L (ppm) in $HNO_3$ with a concentration of 2% (v/V). Calibration curves were prepared using standard solutions of concentrations between 0 to 250 ppm for iron and 0 to 800 ppm for chloride prepared by dilution of the standard solution. The iron Standard for ICP TraceCERT® (10'000 mg/L Fe in nitric acid) was supplied by Sigma Aldrich.

### 7.1.8 Electrospray ionization mass spectrometry (ESI-MS)

ESI-MS analyses were carried out on a Bruker ESI-TOF MicroTOF II.

### 7.1.9 Fourier transform infrared spectroscopy (ATR FT-IR)

ATR FT-IR measurements were performed on a Bruker Alpha Series FT-IR spectrometer equipped with an attenuated total reflectance (ATR) module. The ATR FT-IR spectra were recorded by collecting 16 scans of a compound in the ATR module.

### 7.1.10 Raman spectroscopy

Raman spectroscopy was carried out on a Horiba LabRAM HR at room temperature.

### 7.1.11 Electron paramagnetic resonance (EPR)

EPR analyses were performed on a Bruker EMX with Bruker ER041XG MW bridge (X-band) at room temperature (r.t.) and at 77 K in a quartz Dewar.

### 7.1.12 X-ray photoelectron spectroscopy (XPS)

XPS measurements were carried out using a Kratos AXIS Ultra DLD instrument. The chamber pressure during the measurements was $5 \times 10^{-9}$ Torr. Wide energy range survey scans were collected at a pass energy of 80 eV in hybrid slot lens mode and a step size of 0.5 eV. High-resolution data on the C 1s, Cl 2p, N 1s and Fe 2p photoelectron peaks was collected at pass energy 20 eV over energy ranges suitable for each peak, and collection times of 5 min, step sizes of 0.1 eV. The charge neutraliser filament was used to prevent the sample charging over the irradiated area. The X-ray source was a monochromated Al Kα emission, run at 10 mA and 12 kV (120 W). The energy range for each 'pass energy' (resolution) was calibrated using the Kratos Cu $2p_{3/2}$, Ag $3d_{5/2}$ and Au

$4f_{7/2}$ three-point calibration method. The transmission function was calibrated using a clean gold sample method for all lens modes and the Kratos transmission generator software within Vision II. The data were processed with CASAXPS (Version 2.3.17). Peaks were fitted using GL(30) line shapes (70% Gaussian and 30% Lorentzian). The wide scan and high resolution spectra were calibrated to the alkyl chain at 285.0 eV.[72]

### 7.1.13 Magnetization measurements

DC magnetic susceptibility measurement was performed using Quantum Design PPMS magnetometer whilst heating from 2 to 300 K under an applied magnetic field of strength 1 kOe. Magnetization as a function of field (H) was measured using the same magnetometer in the $-80 \leq H/kOe \leq 80$ at 2 K after cooling the sample in zero field.

# 8. Appendix

## 8.1 Phase diagram

*Table 8-1 Mole fraction calculation for $C_1C_4ImCl/CoCl_2$ mixtures.*

| **%$CoCl_2$** | **n$C_1C_4ImCl$ (mol)** | **n$CoCl_2$ (mol)** | **m$C_1C_4ImCl$ (mg)** | **m$CoCl_2$ (mg)** | **Total (mg)** |
|---|---|---|---|---|---|
| **5%** | 5.51 | 0.29 | 962.35 | 37.65 | 1000 |
| **10%** | 5.29 | 0.59 | 923.71 | 76.29 | 1000 |
| **15%** | 5.06 | 0.89 | 884.03 | 115.97 | 1000 |
| **20%** | 4.83 | 1.21 | 843.29 | 156.71 | 1000 |
| **25%** | 4.59 | 1.53 | 801.42 | 198.58 | 1000 |
| **30%** | 4.34 | 1.86 | 758.39 | 241.61 | 1000 |
| **35%** | 4.09 | 2.20 | 714.15 | 285.85 | 1000 |
| **40%** | 3.83 | 2.55 | 668.64 | 331.36 | 1000 |
| **45%** | 3.56 | 2.91 | 621.82 | 378.18 | 1000 |
| **50%** | 3.28 | 3.28 | 573.61 | 426.39 | 1000 |
| **55%** | 3.00 | 3.67 | 523.96 | 476.04 | 1000 |
| **60%** | 2.71 | 4.06 | 472.81 | 527.19 | 1000 |
| **65%** | 2.40 | 4.47 | 420.08 | 579.92 | 1000 |
| **70%** | 2.09 | 4.89 | 365.70 | 634.30 | 1000 |
| **75%** | 1.77 | 5.32 | 309.59 | 690.41 | 1000 |
| **80%** | 1.44 | 5.76 | 251.67 | 748.33 | 1000 |
| **85%** | 1.10 | 6.22 | 191.85 | 808.15 | 1000 |

| | | | | | |
|---|---|---|---|---|---|
| **90%** | 0.74 | 6.70 | 130.04 | 869.96 | 1000 |
| **95%** | 0.38 | 7.19 | 66.12 | 933.88 | 1000 |

*Table 8-2 Mole fraction calculation for $C_1C_4ImCl/NiCl_2$ mixtures.*

| **%$NiCl_2$** | **n$C_1C_4ImCl$ (mol)** | **n$NiCl_2$ (mol)** | **m$C_1C_4ImCl$ (mg)** | **m$NiCl_2$ (mg)** | **Total (mg)** |
|---|---|---|---|---|---|
| **5%** | 5.51 | 0.29 | 962.42 | 37.58 | 1000 |
| **10%** | 5.29 | 0.59 | 923.84 | 76.16 | 1000 |
| **15%** | 5.06 | 0.89 | 884.22 | 115.78 | 1000 |
| **20%** | 4.83 | 1.21 | 843.53 | 156.47 | 1000 |
| **25%** | 4.59 | 1.53 | 801.72 | 198.28 | 1000 |
| **30%** | 4.34 | 1.86 | 758.73 | 241.27 | 1000 |
| **35%** | 4.09 | 2.20 | 714.53 | 285.47 | 1000 |
| **40%** | 3.83 | 2.55 | 669.05 | 330.95 | 1000 |
| **45%** | 3.56 | 2.91 | 622.25 | 377.75 | 1000 |
| **50%** | 3.29 | 3.29 | 574.06 | 425.94 | 1000 |
| **55%** | 3.00 | 3.67 | 524.42 | 475.58 | 1000 |
| **60%** | 2.71 | 4.06 | 473.27 | 526.73 | 1000 |
| **65%** | 2.41 | 4.47 | 420.53 | 579.47 | 1000 |
| **70%** | 2.10 | 4.89 | 366.13 | 633.87 | 1000 |
| **75%** | 1.77 | 5.32 | 309.99 | 690.01 | 1000 |
| **80%** | 1.44 | 5.77 | 252.02 | 747.98 | 1000 |
| **85%** | 1.10 | 6.23 | 192.14 | 807.86 | 1000 |

| | | | | | |
|---|---|---|---|---|---|
| **90%** | 0.75 | 6.71 | 130.25 | 869.75 | 1000 |
| **95%** | 0.38 | 7.20 | 66.24 | 933.76 | 1000 |

### 8.1.1 Differential scanning calorimetry

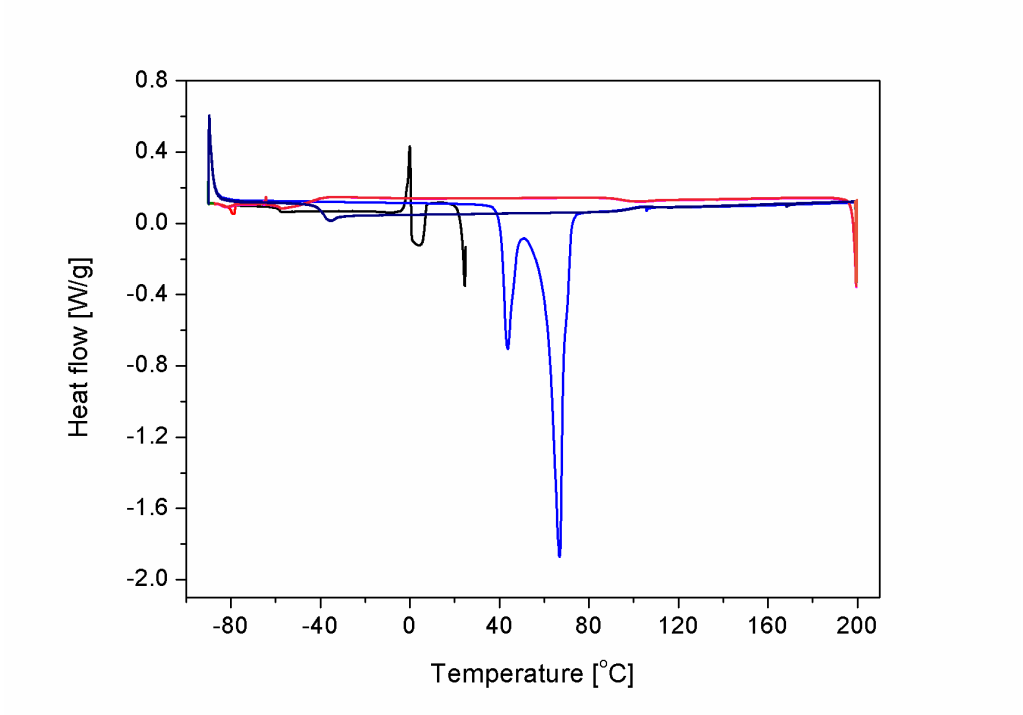



*Figure 8-1 DSC thermogram for mole fraction $\chi CoCl_2 = 0.05$.*

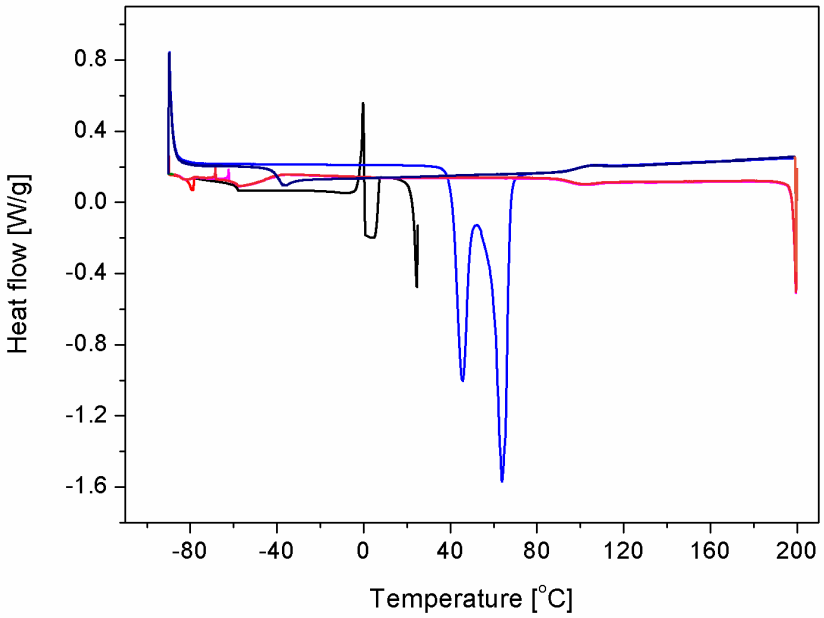



*Figure 8-2 DSC thermogram for mole fraction $\chi CoCl_2 = 0.1$.*

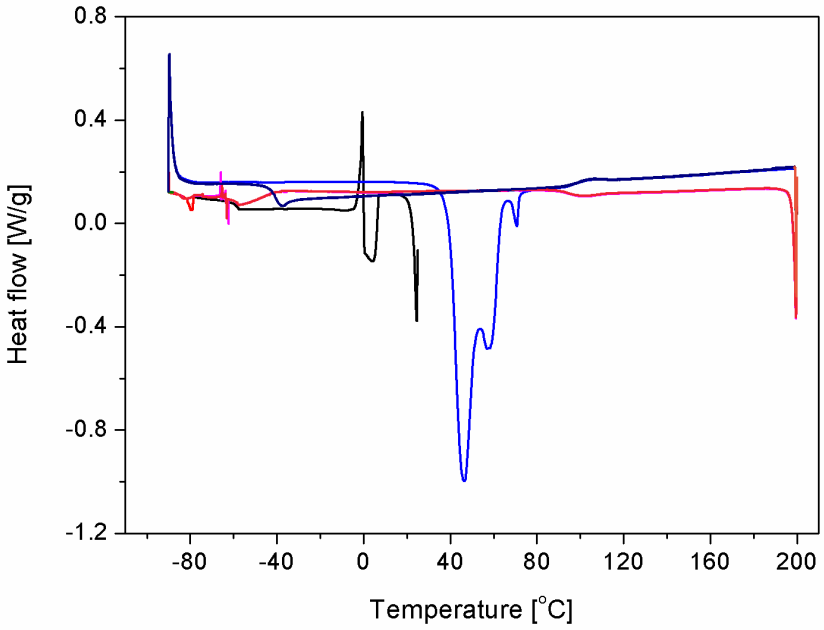



*Figure 8-3 DSC thermogram for mole fraction $\chi CoCl_2 = 0.15$.*

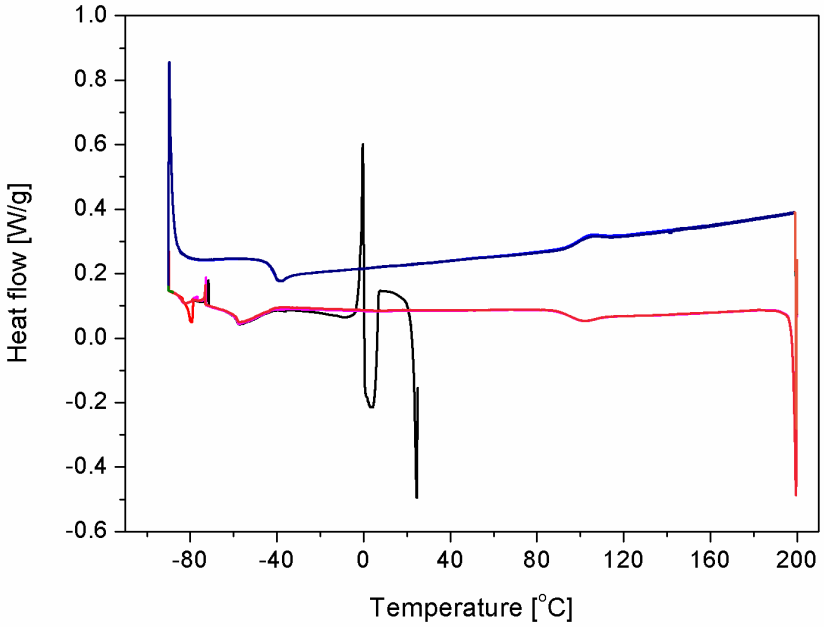



*Figure 8-4 DSC thermogram for mole fraction $\chi CoCl_2 = 0.2$.*

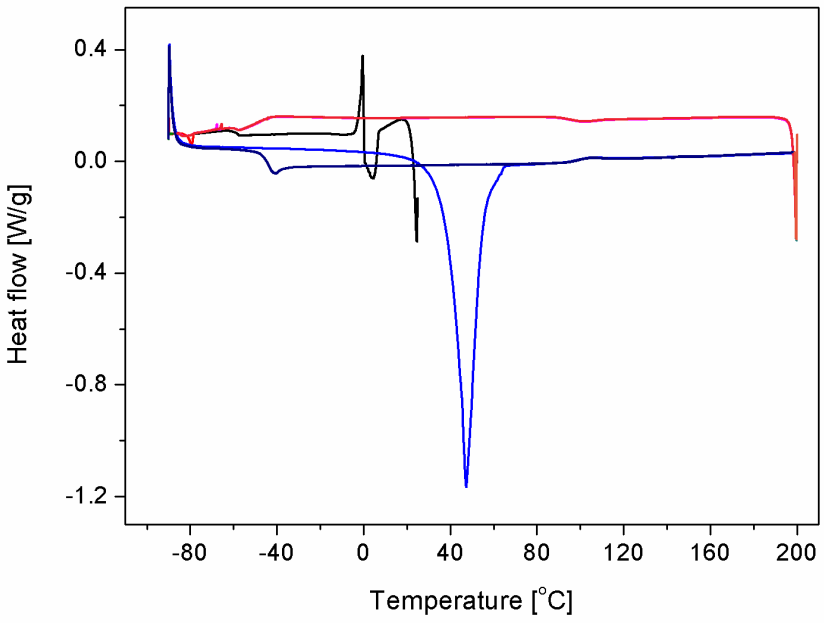



*Figure 8-5 DSC thermogram for mole fraction $\chi CoCl_2 = 0.25$.*

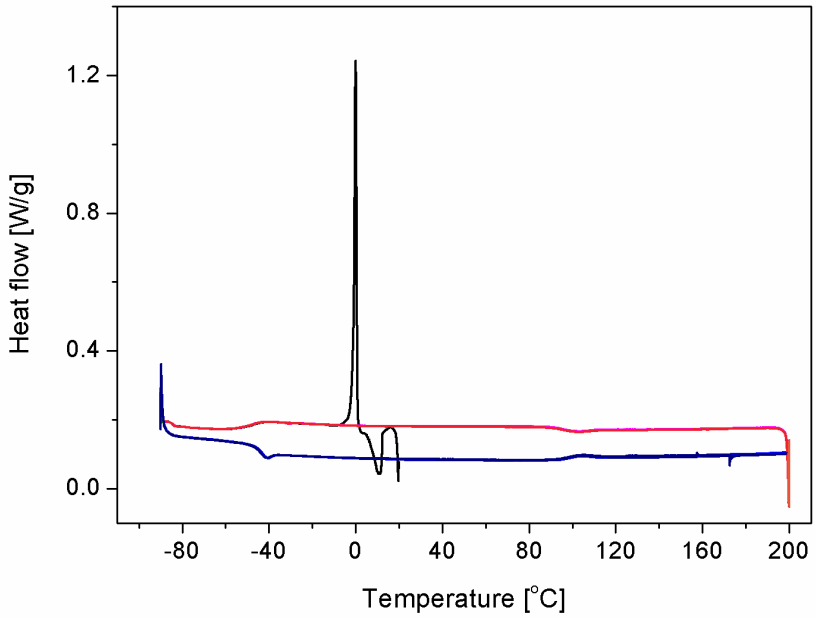



*Figure 8-6 DSC thermogram for mole fraction $\chi CoCl_2 = 0.3$.*

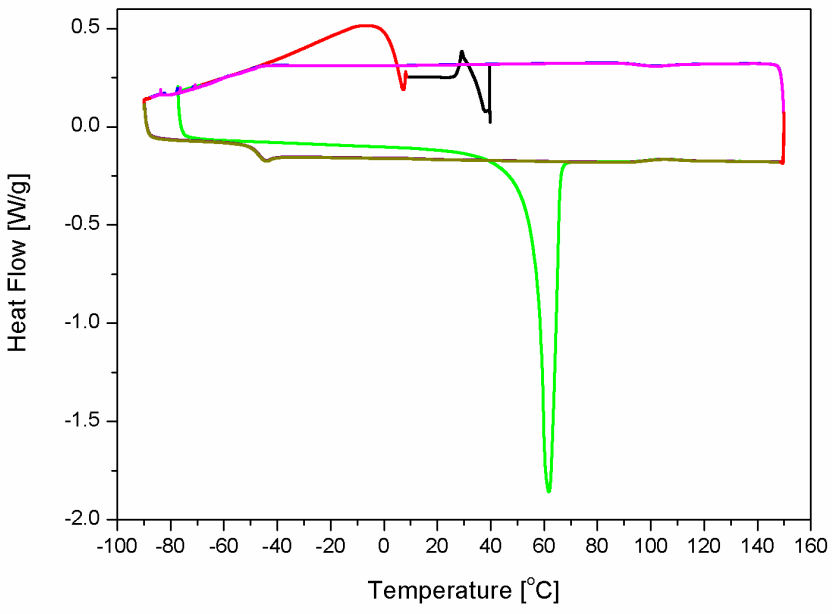



*Figure 8-7 DSC thermogram for mole fraction $\chi CoCl_2 = 0.33$.*

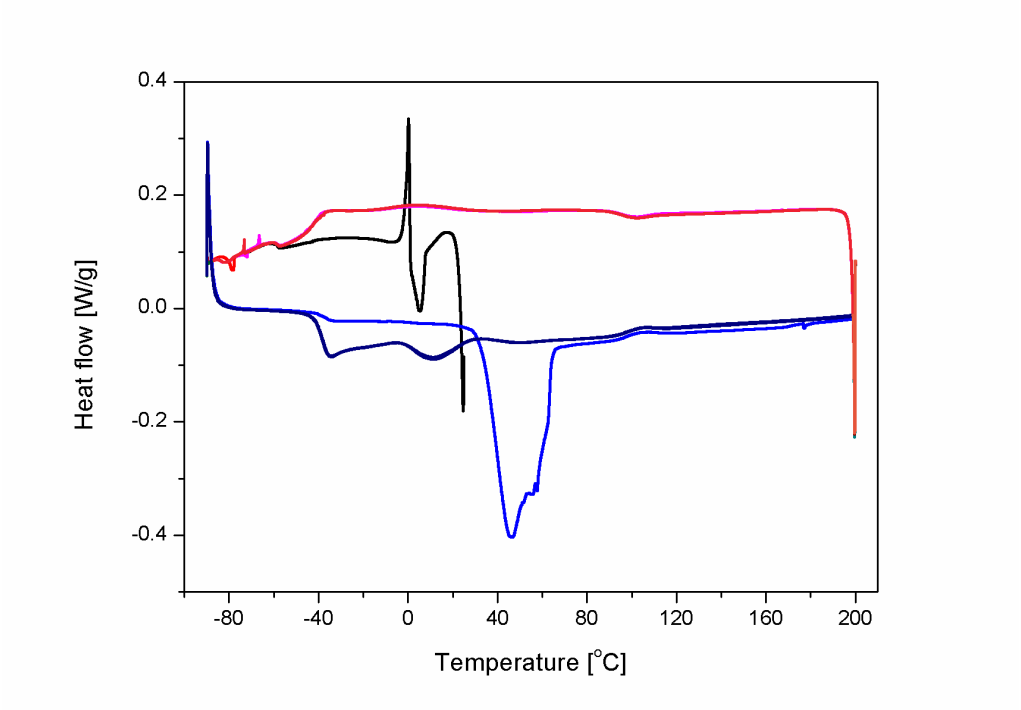



*Figure 8-8 DSC thermogram for mole fraction $\chi CoCl_2 = 0.35$.*

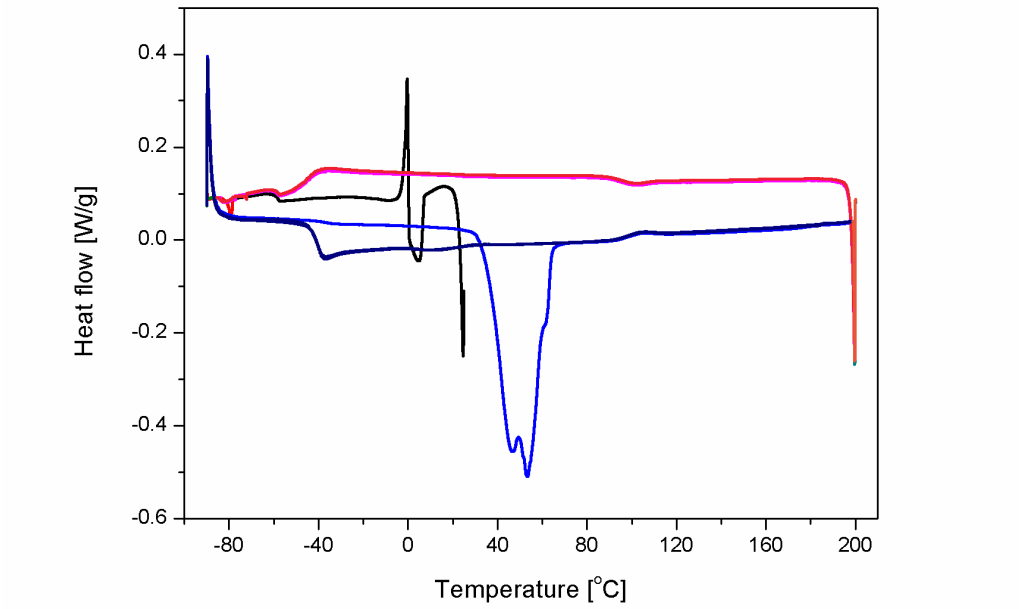



*Figure 8-9 DSC thermogram for mole fraction $\chi CoCl_2 = 0.4$.*

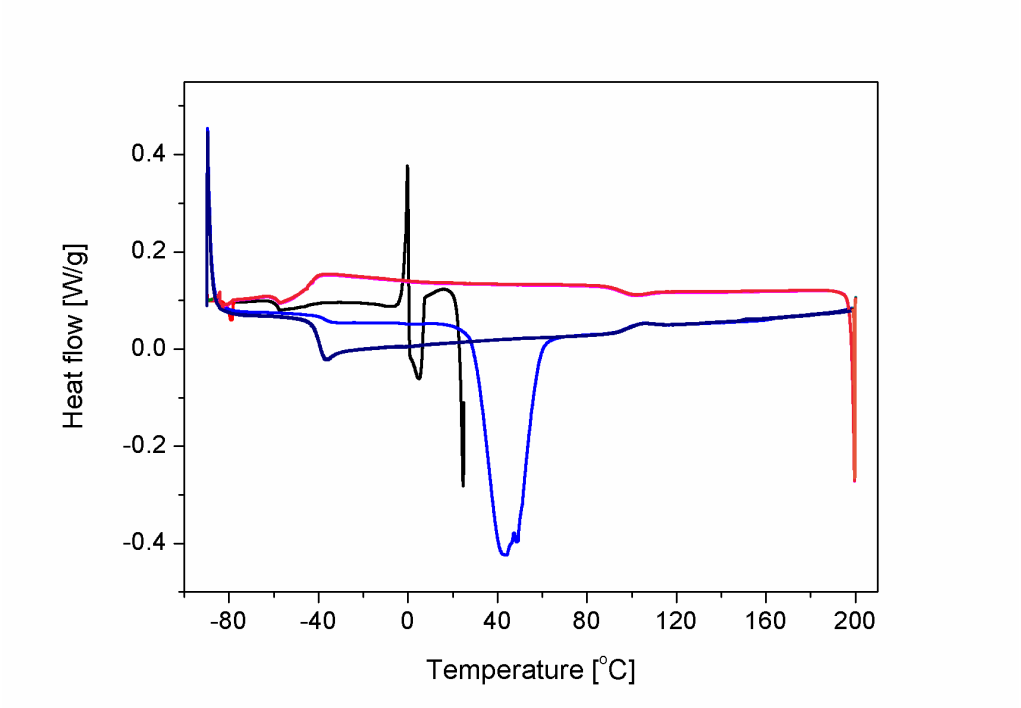



*Figure 8-10 DSC thermogram for mole fraction $\chi CoCl_2 = 0.45$.*

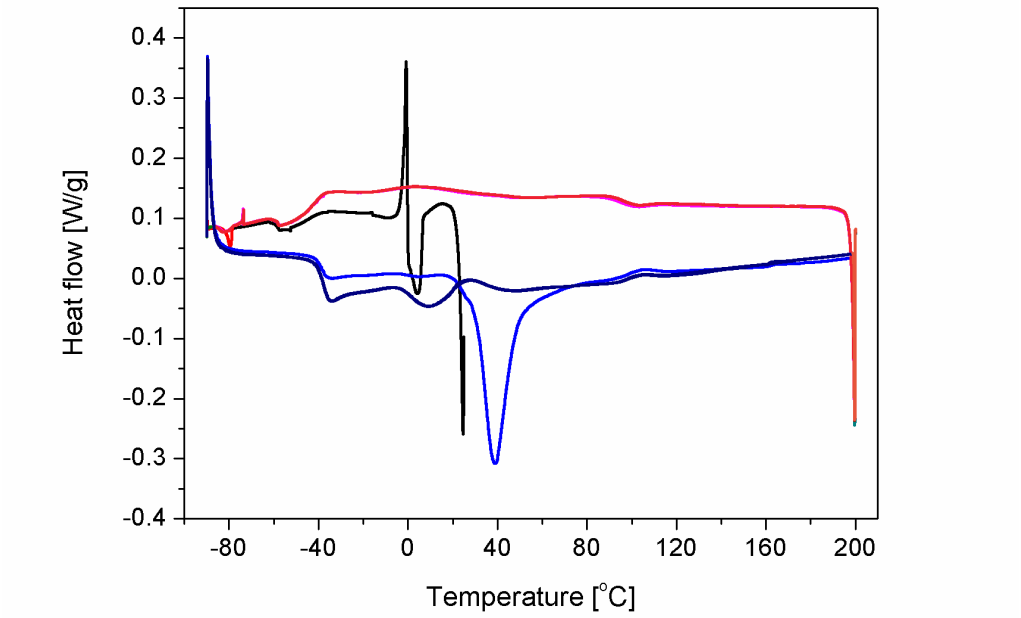



*Figure 8-11 DSC thermogram for mole fraction $\chi CoCl_2 = 0.5$.*

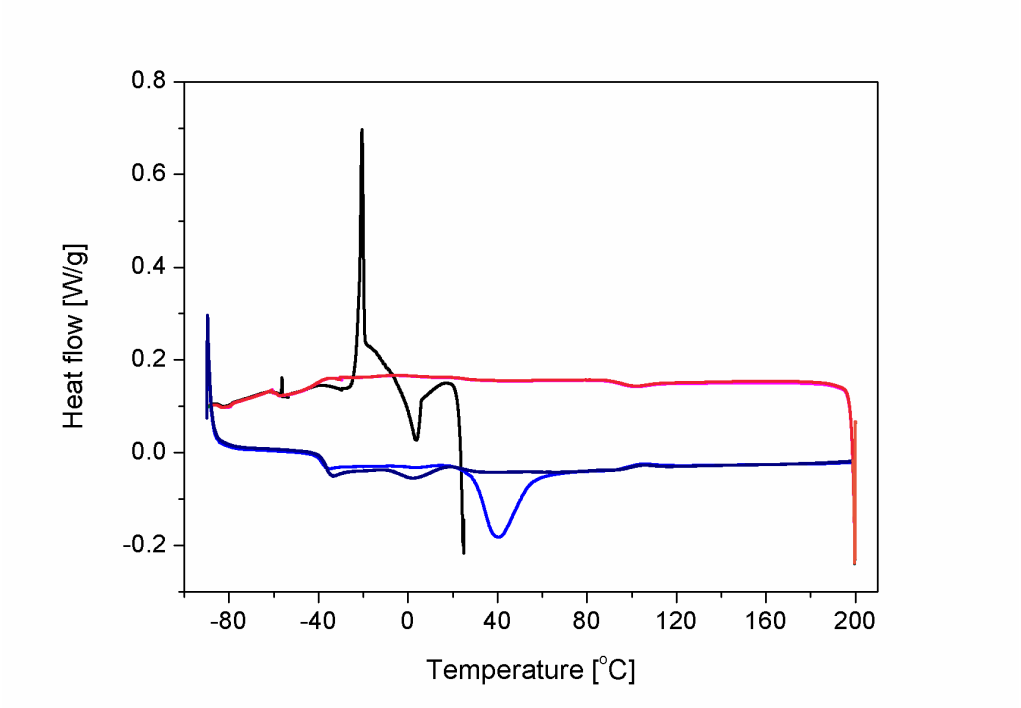



*Figure 8-12 DSC thermogram for mole fraction $\chi CoCl_2 = 0.55$.*

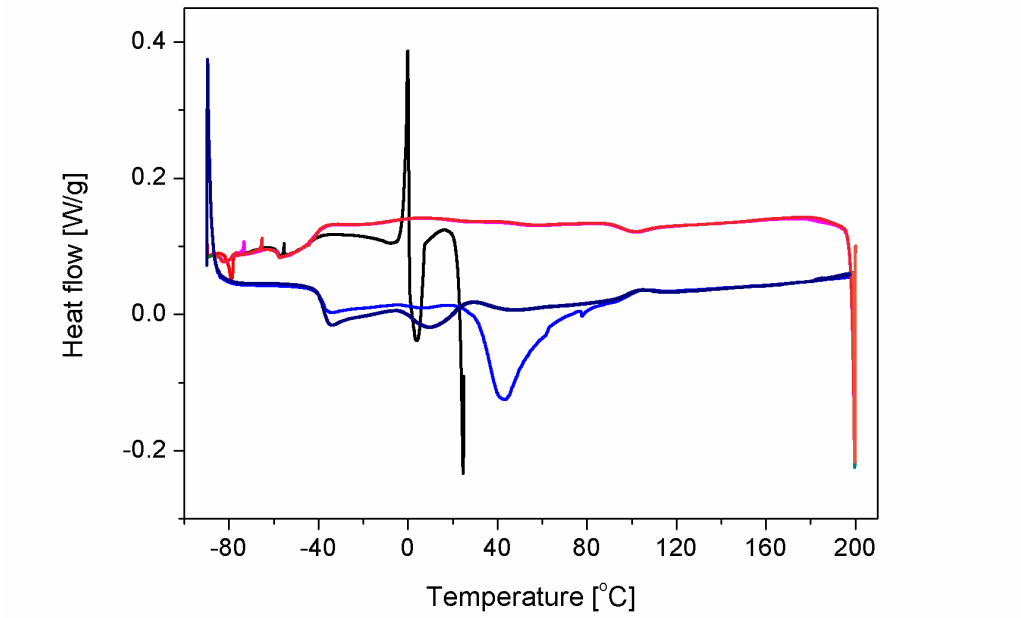



*Figure 8-13 DSC thermogram for mole fraction $\chi CoCl_2 = 0.6$.*

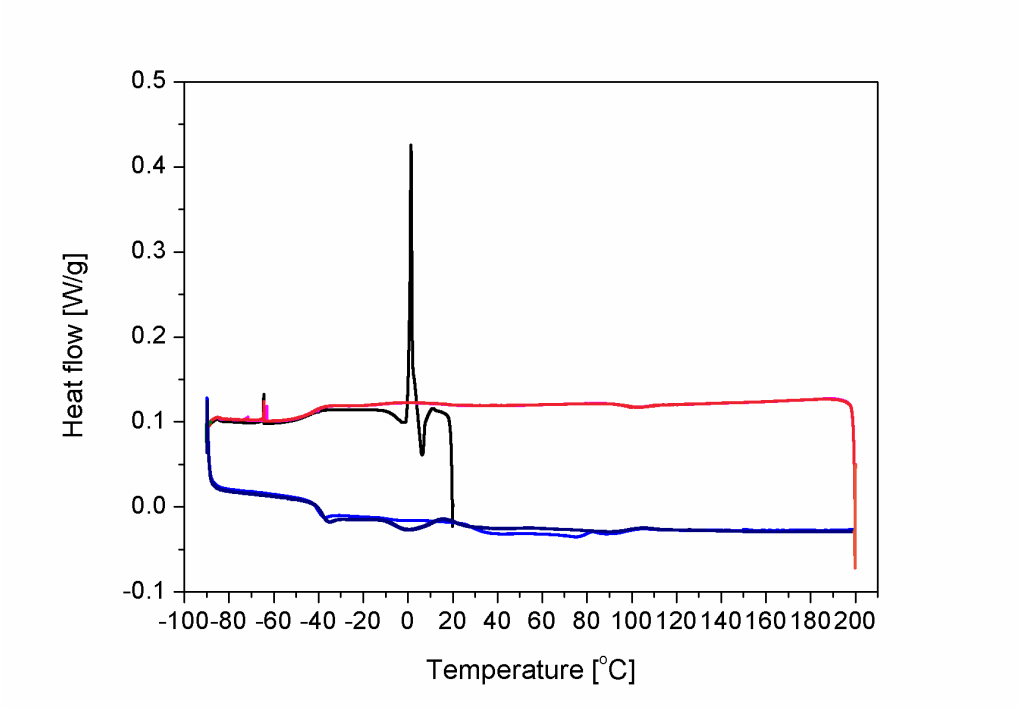



*Figure 8-14 DSC thermogram for mole fraction $\chi CoCl_2 = 0.65$.*

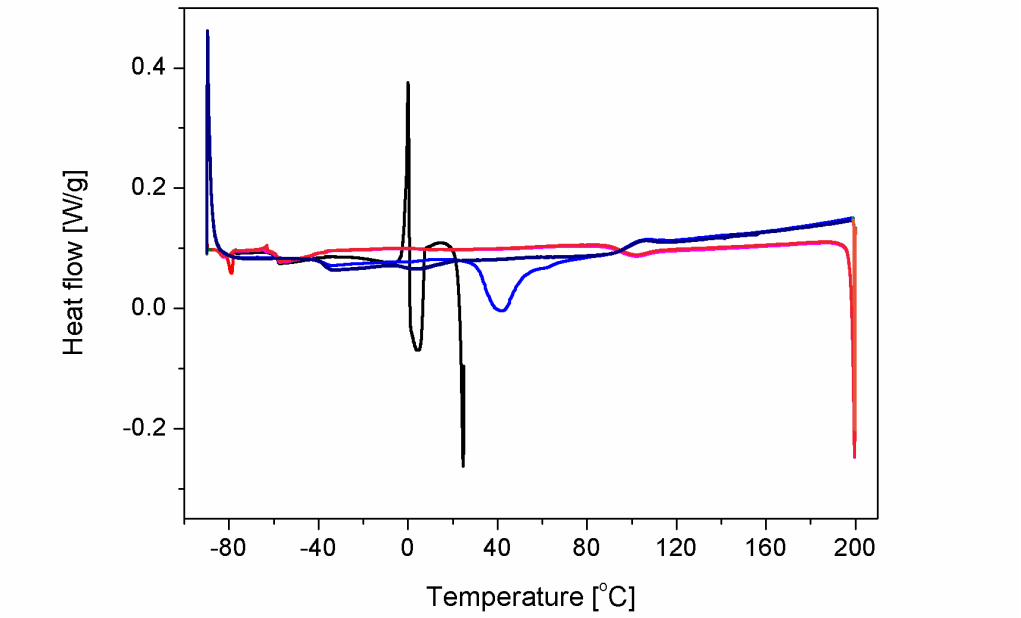



*Figure 8-15 DSC thermogram for mole fraction $\chi CoCl_2 = 0.7$.*

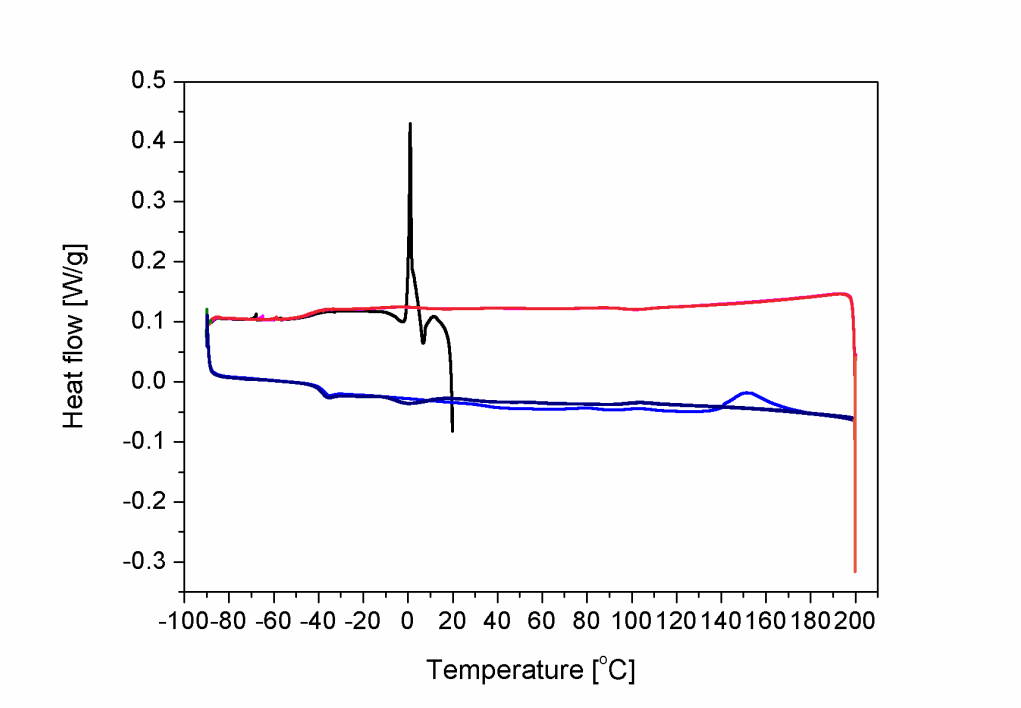



*Figure 8-16 DSC thermogram for mole fraction $\chi CoCl_2 = 0.75$.*

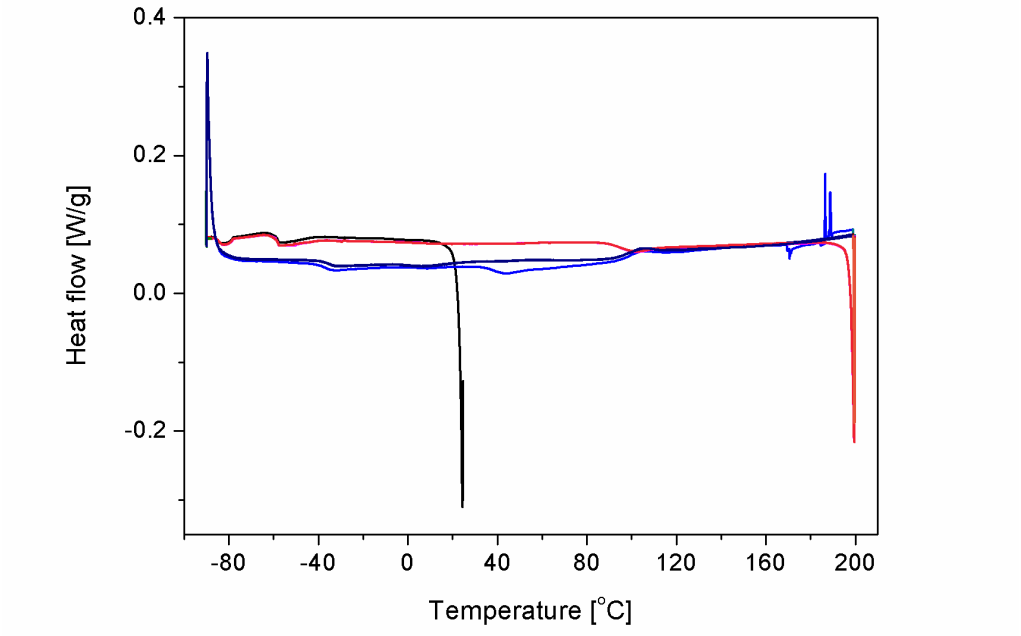



*Figure 8-17 DSC thermogram for mole fraction $\chi CoCl_2 = 0.8$.*

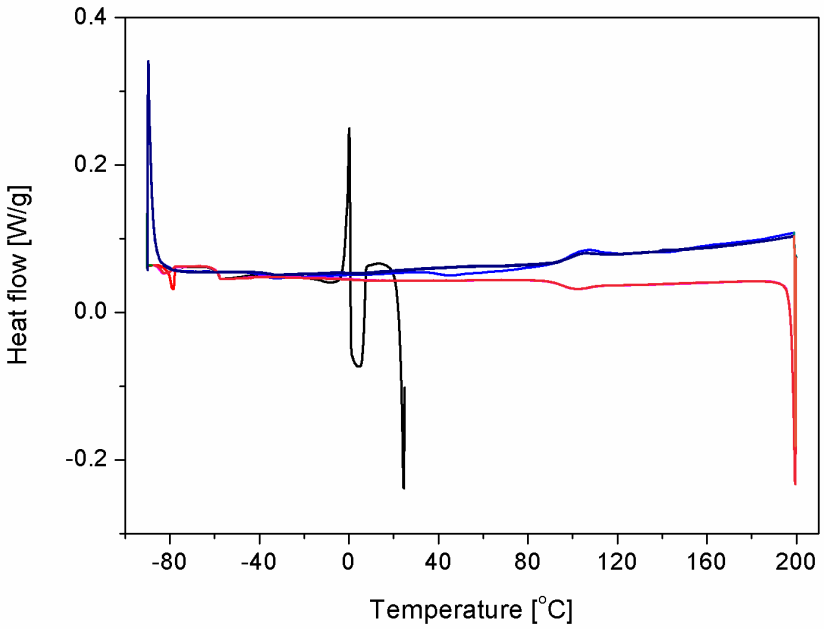



*Figure 8-18 DSC thermogram for mole fraction $\chi CoCl_2 = 0.85$.*

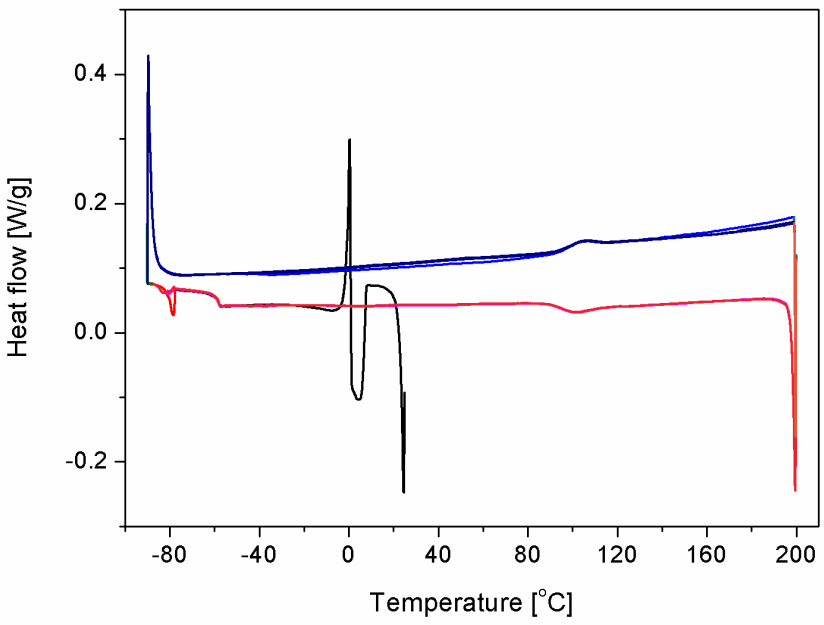



*Figure 8-19 DSC thermogram for mole fraction $\chi CoCl_2 = 0.9$.*

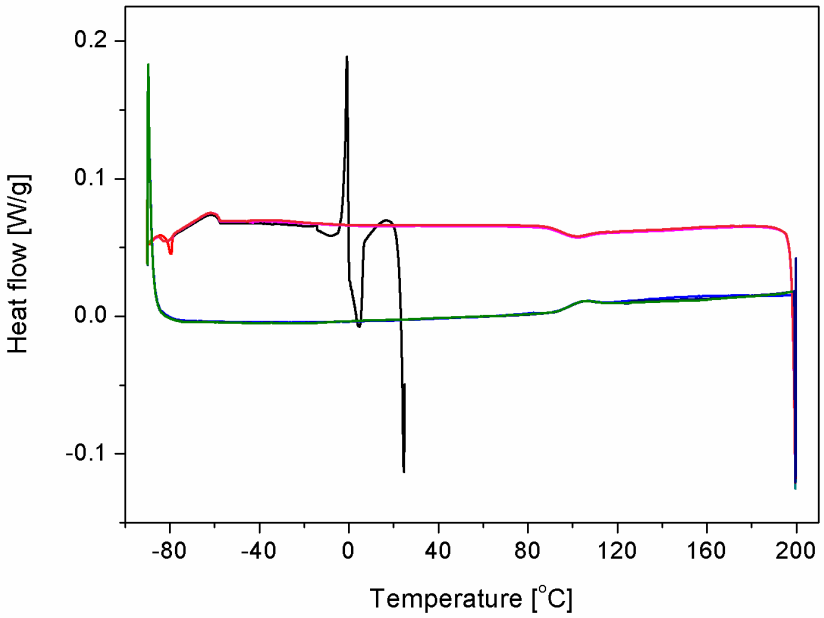



*Figure 8-20 DSC thermogram for mole fraction $\chi CoCl_2 = 0.95$.*

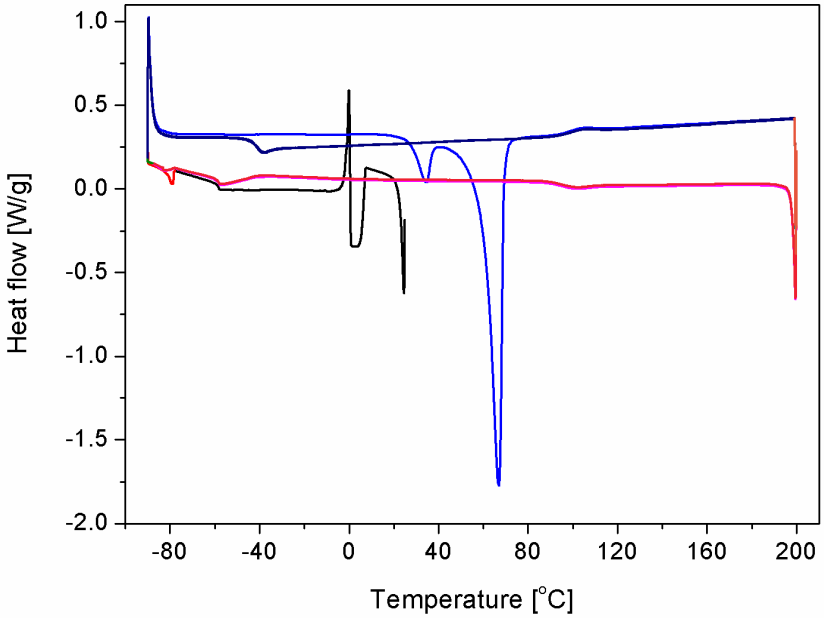



*Figure 8-21 DSC thermogram for mole fraction $\chi NiCl_2 = 0.05$.*

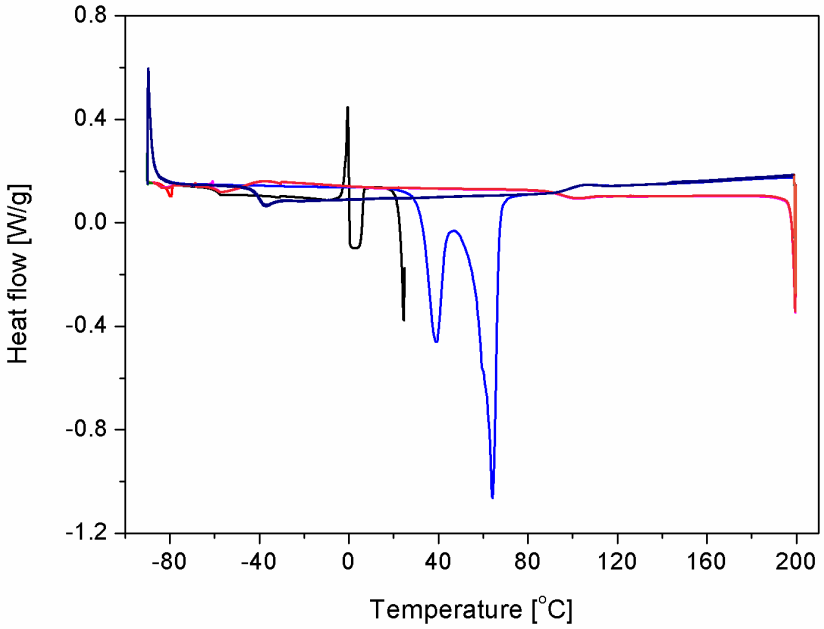



*Figure 8-22 DSC thermogram for mole fraction χ $NiCl_2$ = 0.1.*

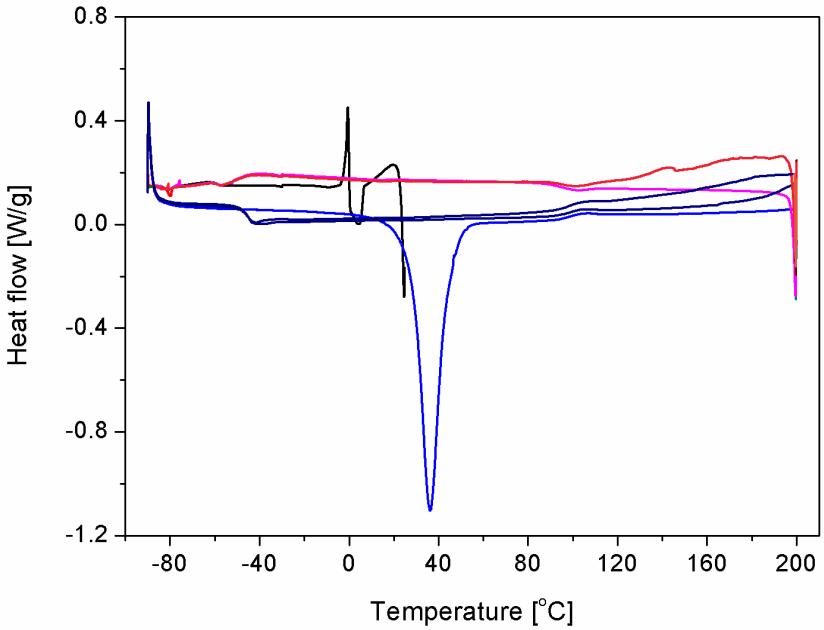



*Figure 8-23 DSC thermogram for mole fraction χ $NiCl_2$ = 0.15.*

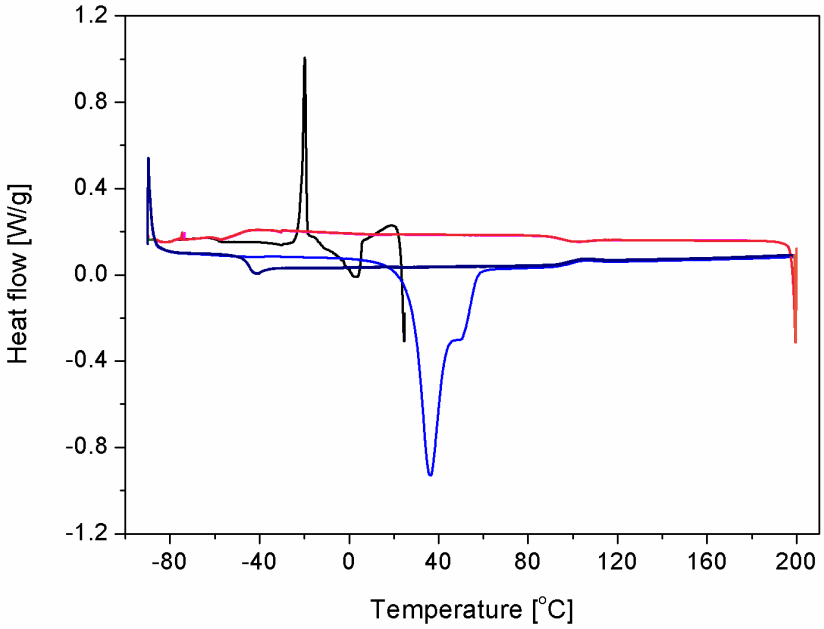



*Figure 8-24 DSC thermogram for mole fraction χ $NiCl_2$ = 0.2.*

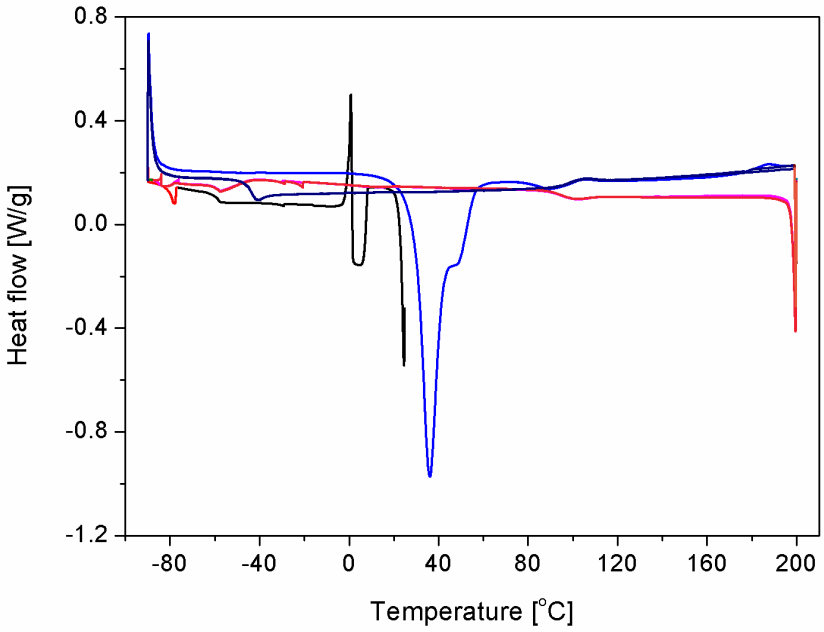



*Figure 8-25 DSC thermogram for mole fraction χ $NiCl_2$ = 0.25.*

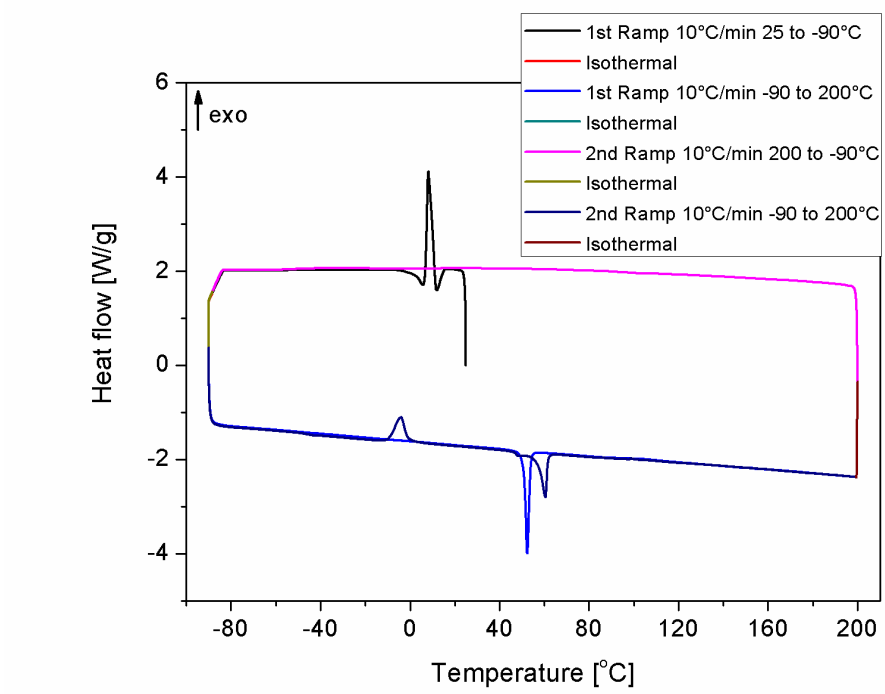



*Figure 8-26 DSC thermogram for mole fraction χ $NiCl_2$ = 0.33.*

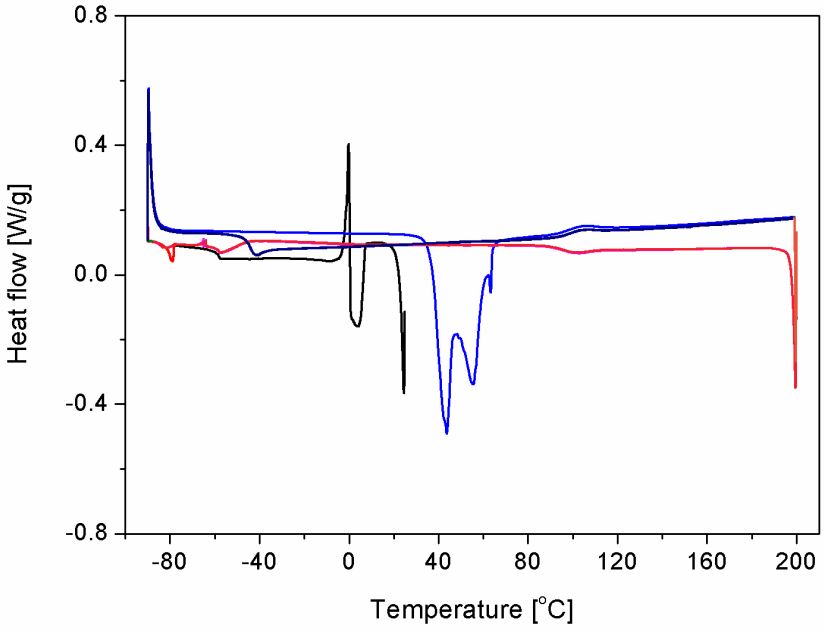



*Figure 8-27 DSC thermogram for mole fraction χ $NiCl_2$ = 0.4.*

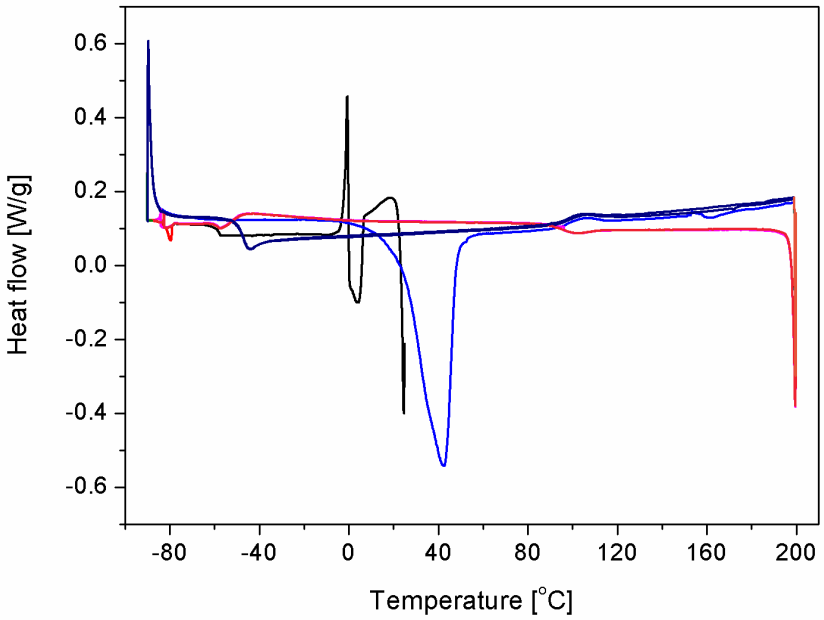



*Figure 8-28 DSC thermogram for mole fraction χ $NiCl_2$ = 0.45.*

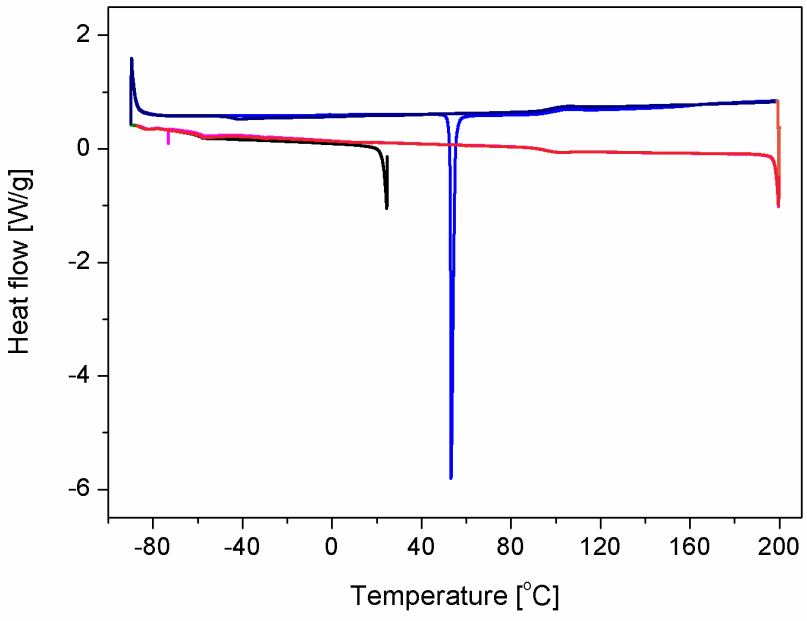



*Figure 8-29 DSC thermogram for mole fraction χ $NiCl_2$ = 0.5.*

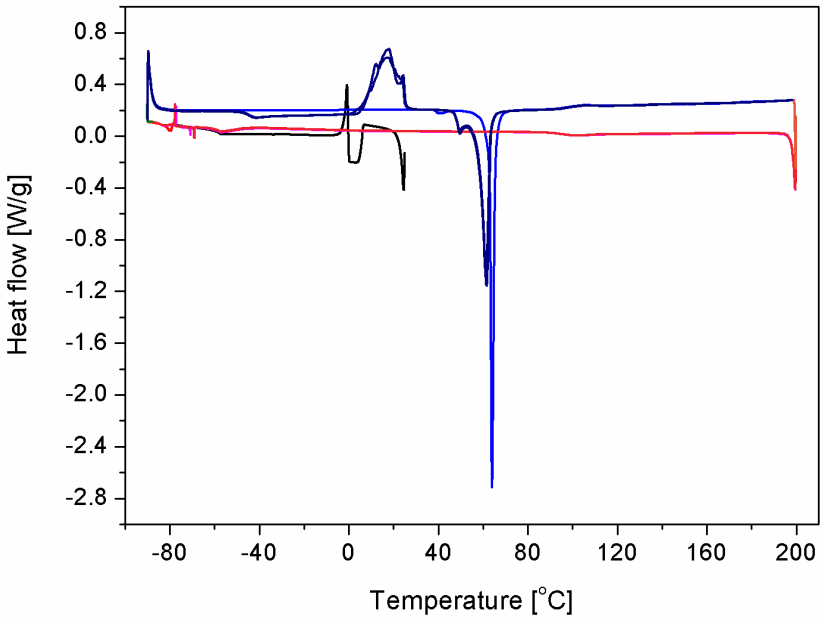



*Figure 8-30 DSC thermogram for mole fraction χ $NiCl_2$ = 0.55.*

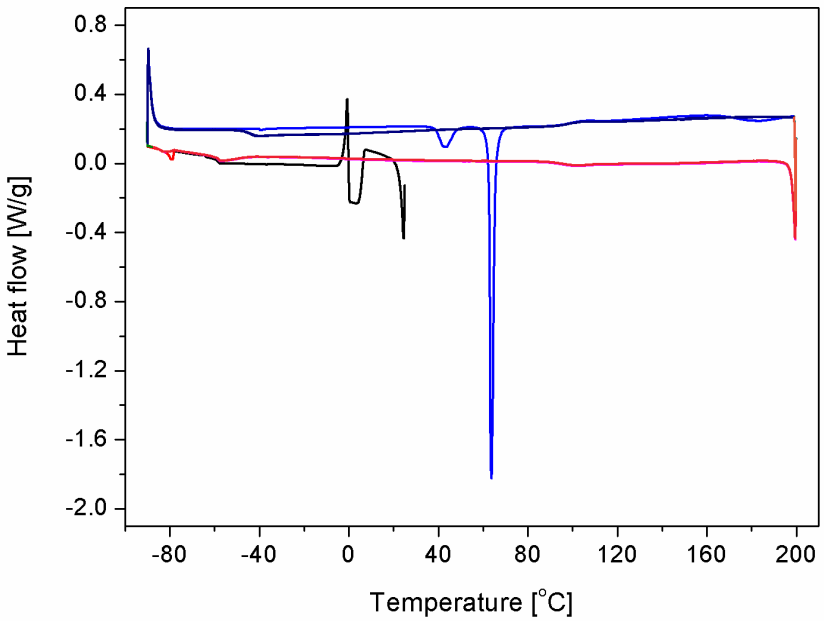



*Figure 8-31 DSC thermogram for mole fraction χ $NiCl_2$ = 0.6.*

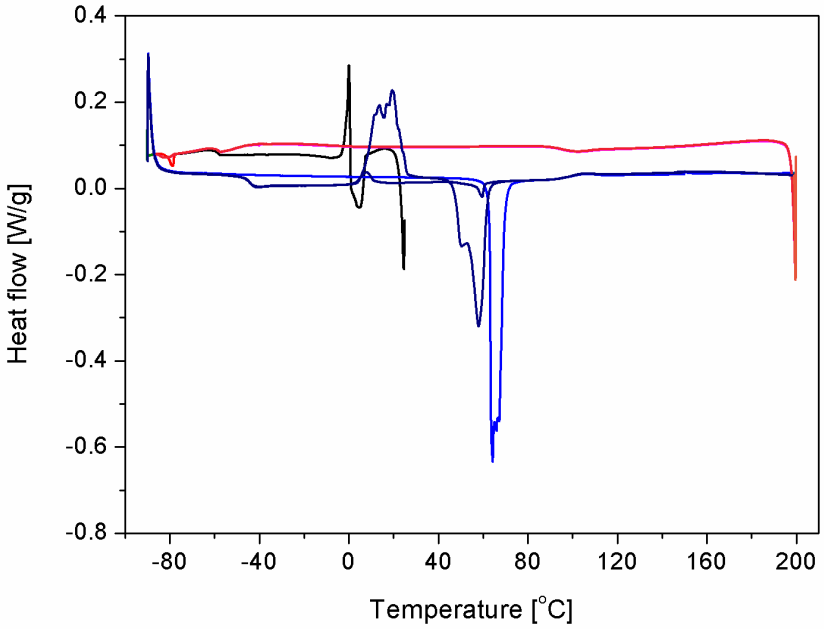



*Figure 8-32 DSC thermogram for mole fraction χ $NiCl_2$ = 0.65.*

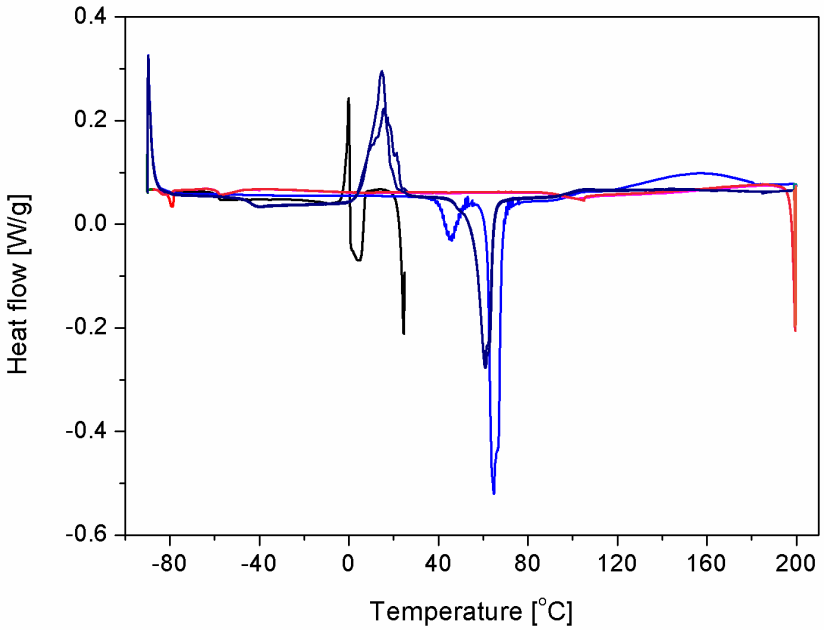



*Figure 8-33 DSC thermogram for mole fraction χ $NiCl_2$ = 0.7.*

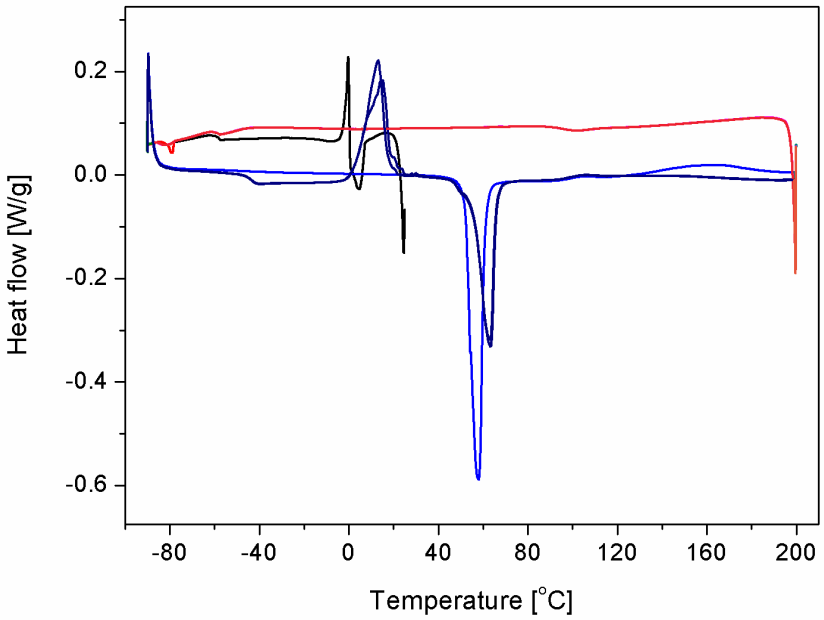



*Figure 8-34 DSC thermogram for mole fraction χ $NiCl_2$ = 0.75.*

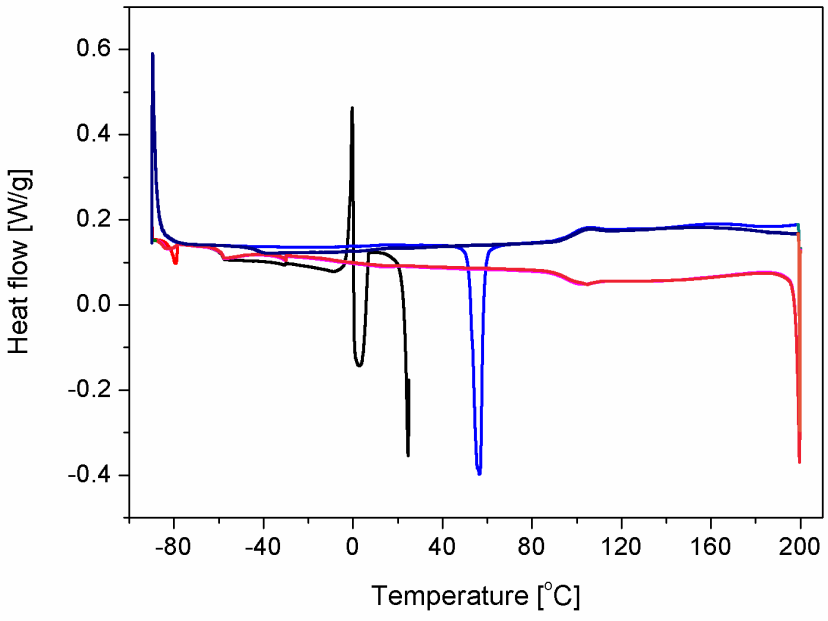



*Figure 8-35 DSC thermogram for mole fraction χ $NiCl_2$ = 0.8.*

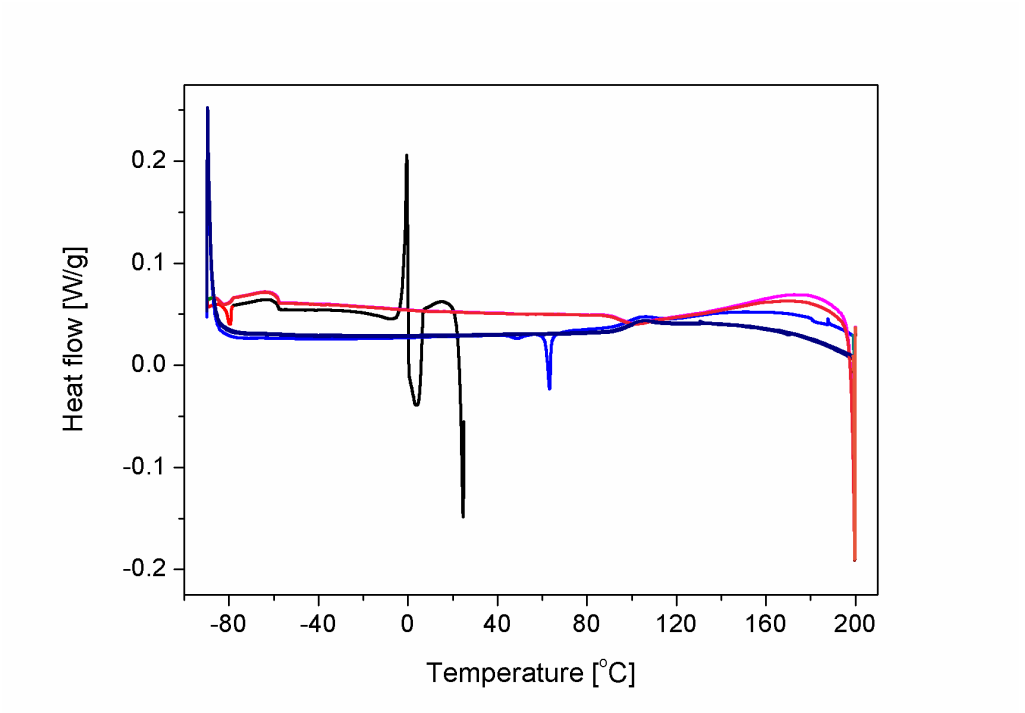



*Figure 8-36 DSC thermogram for mole fraction χ $NiCl_2$ = 0.85.*

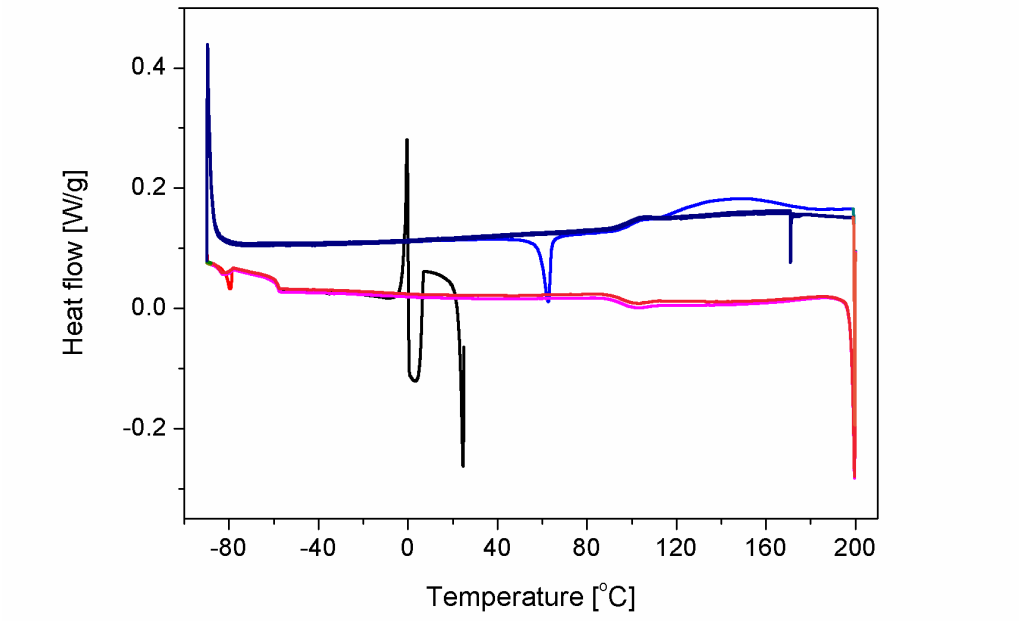



*Figure 8-37 DSC thermogram for mole fraction χ $NiCl_2$ = 0.9.*

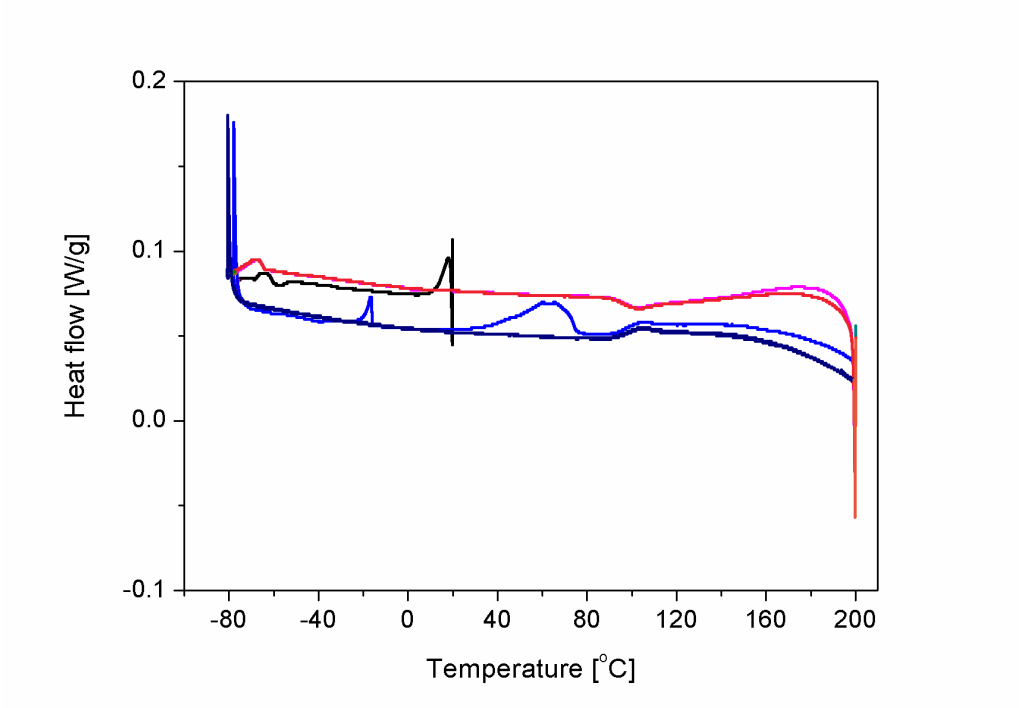



*Figure 8-38 DSC thermogram for mole fraction χ $NiCl_2$ = 0.95.*

## 8.1.2 Thermogravimetric analysis

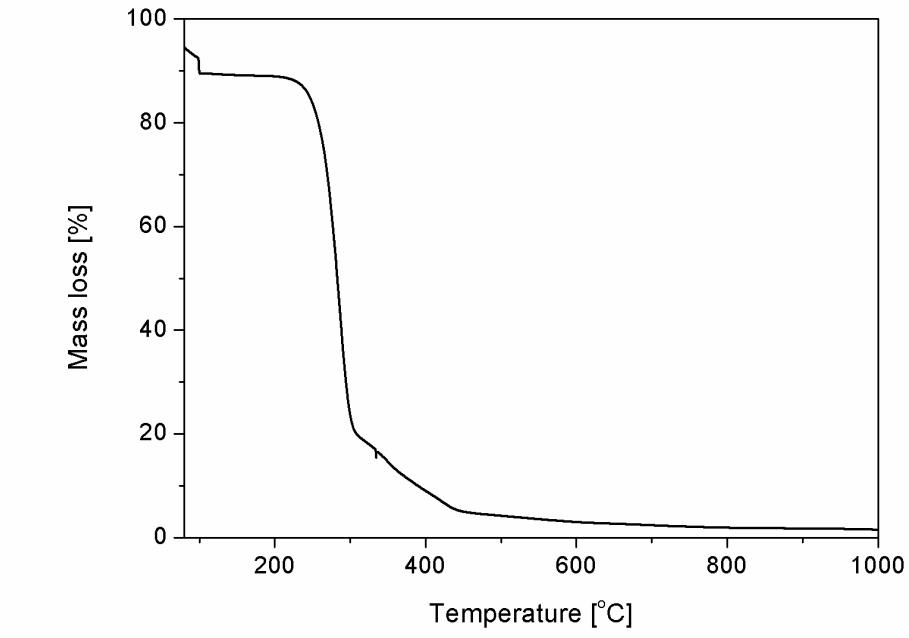



*Figure 8-39 TGA thermogram for mole fraction χ$CoCl_2$ = 0.05.*

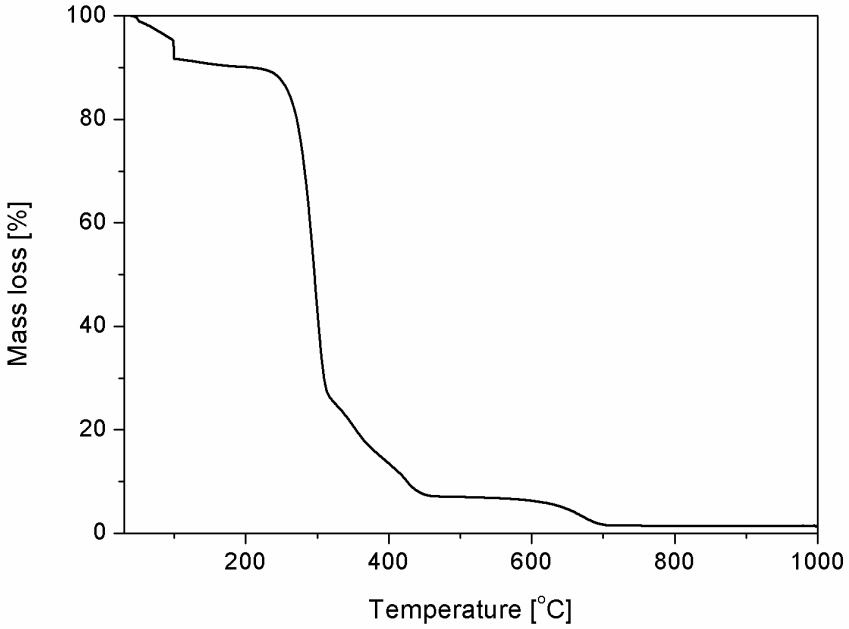



*Figure 8-40 TGA thermogram for mole fraction $\chi CoCl_2 = 0.1$.*

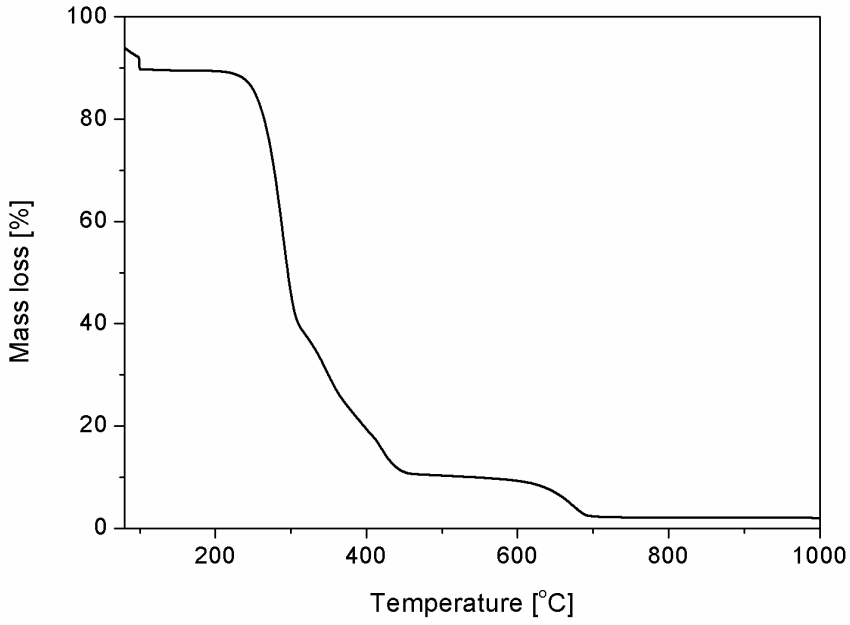



*Figure 8-41 TGA thermogram for mole fraction $\chi CoCl_2 = 0.15$.*

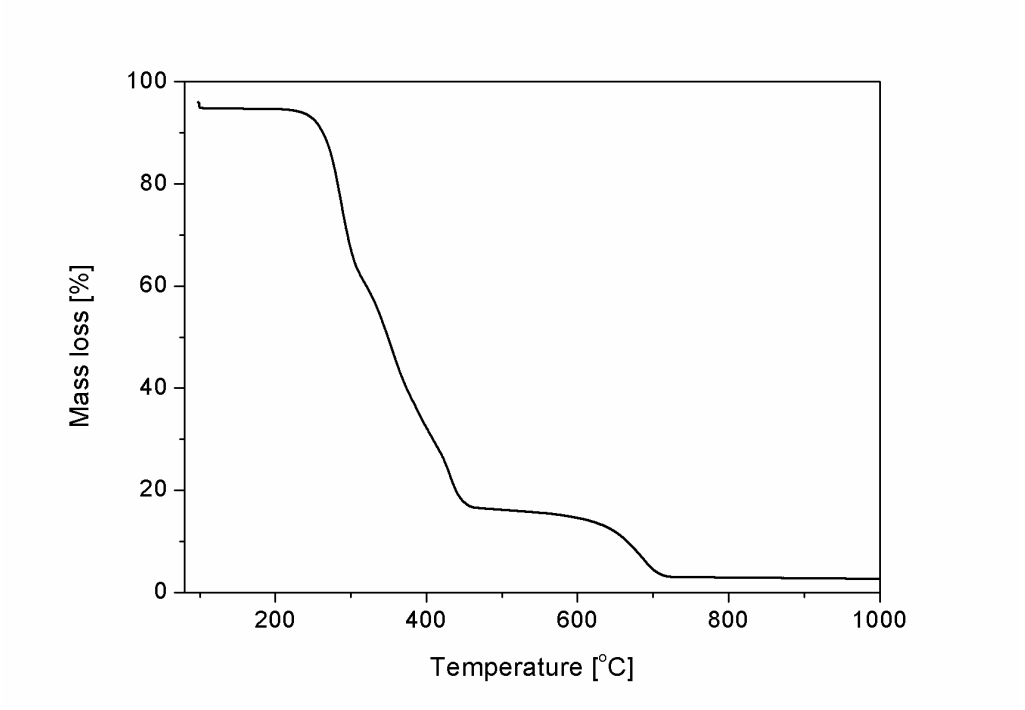



*Figure 8-42 TGA thermogram for mole fraction $\chi CoCl_2 = 0.2$.*

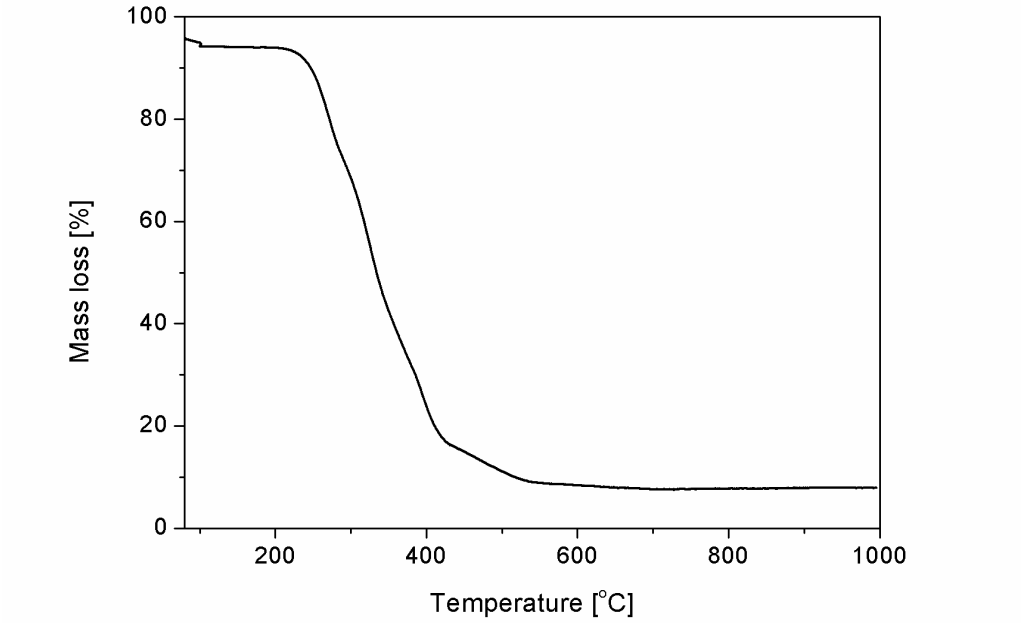



*Figure 8-43 TGA thermogram for mole fraction $\chi CoCl_2 = 0.25$.*

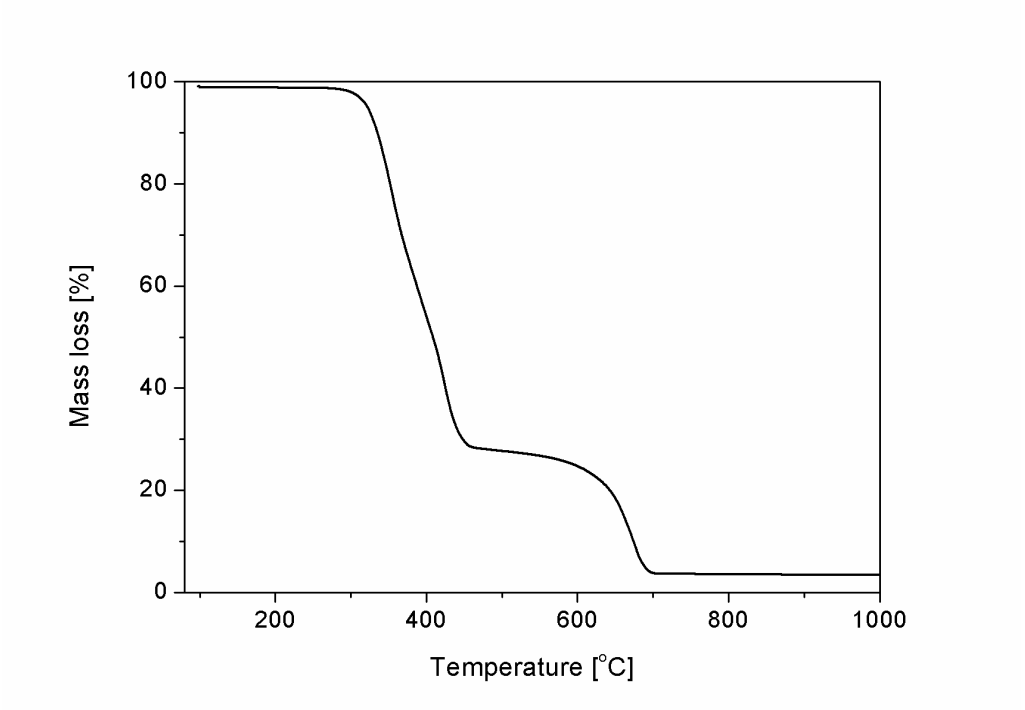



*Figure 8-44 TGA thermogram for mole fraction $\chi CoCl_2 = 0.4$.*

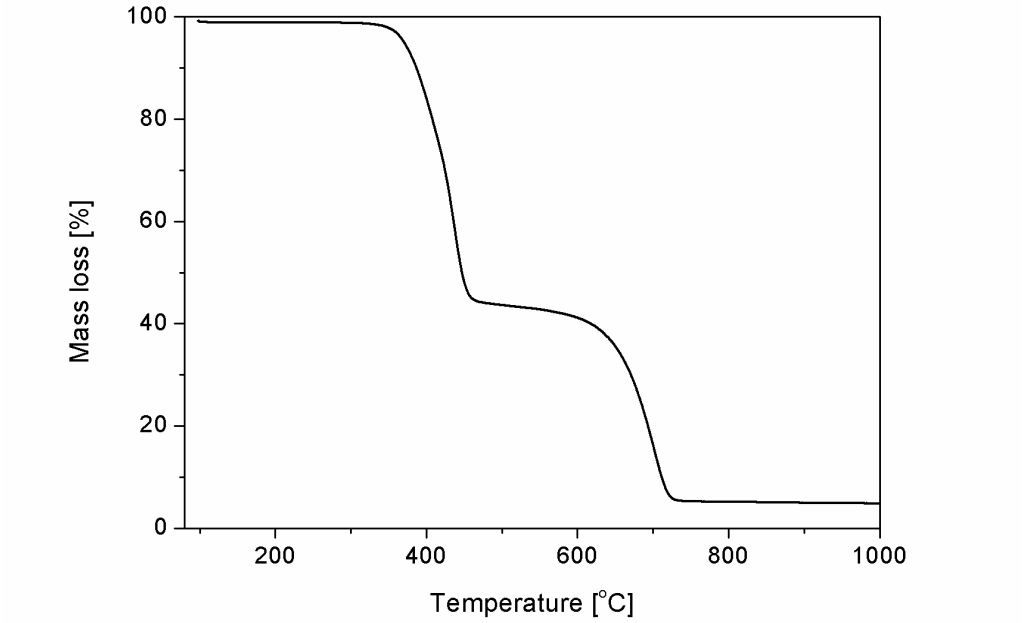



*Figure 8-45 TGA thermogram for mole fraction $\chi CoCl_2 = 0.45$.*

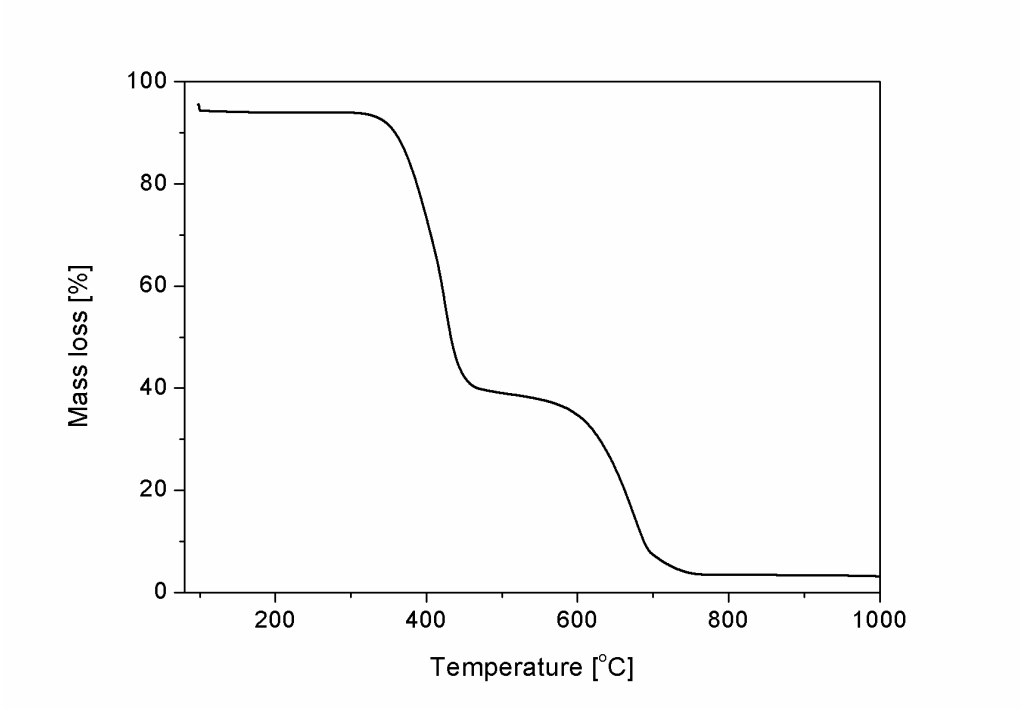



*Figure 8-46 TGA thermogram for mole fraction $\chi CoCl_2 = 0.5$.*

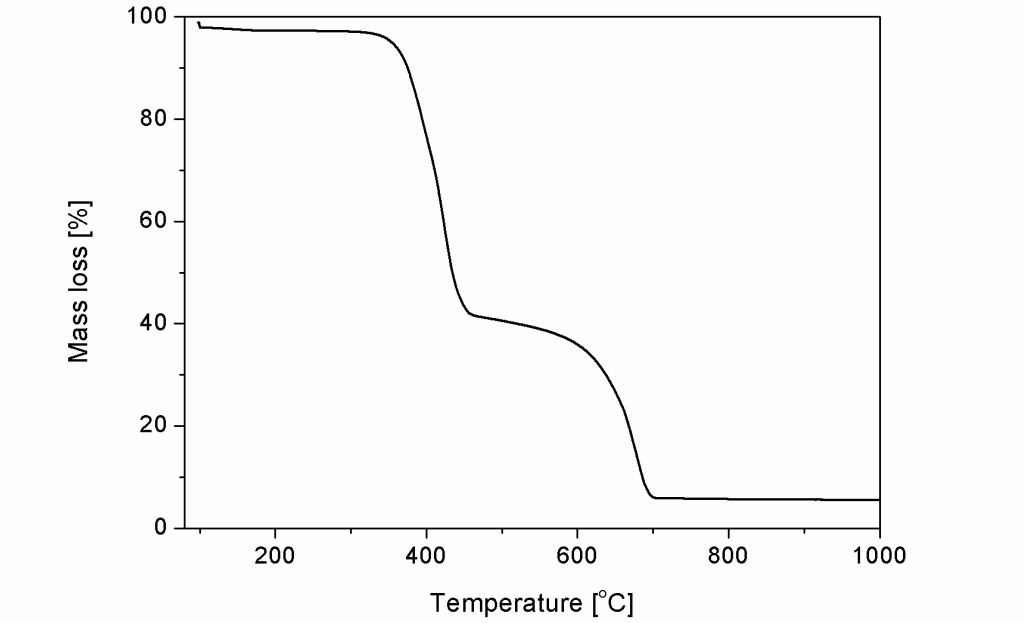



*Figure 8-47 TGA thermogram for mole fraction $\chi CoCl_2 = 0.55$.*

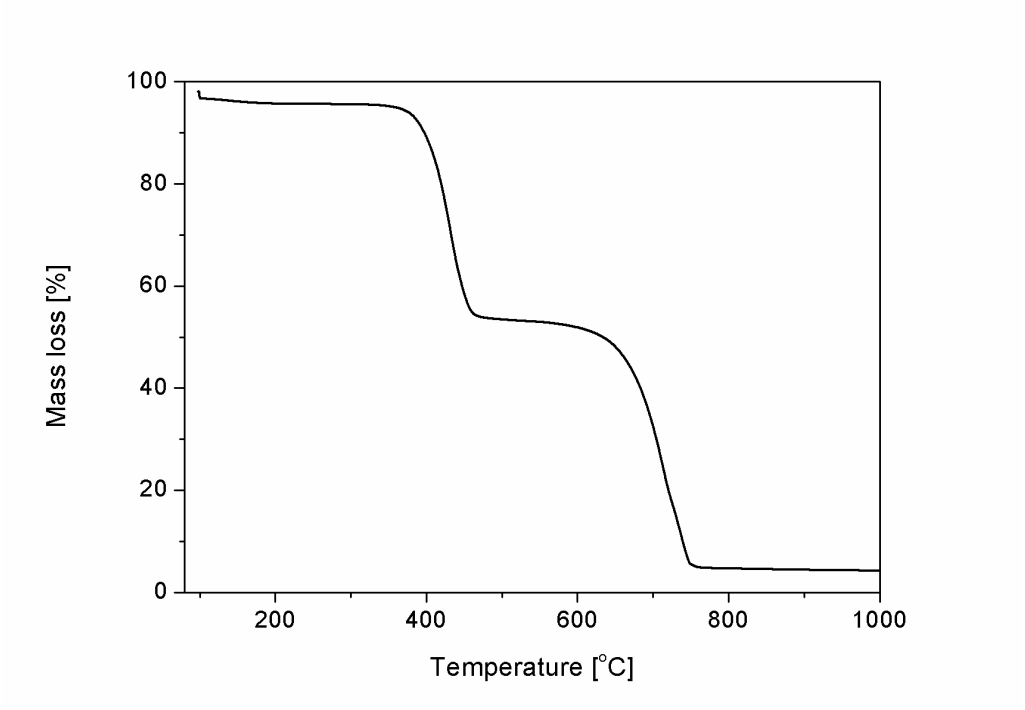



*Figure 8-48 TGA thermogram for mole fraction $\chi CoCl_2 = 0.6$*

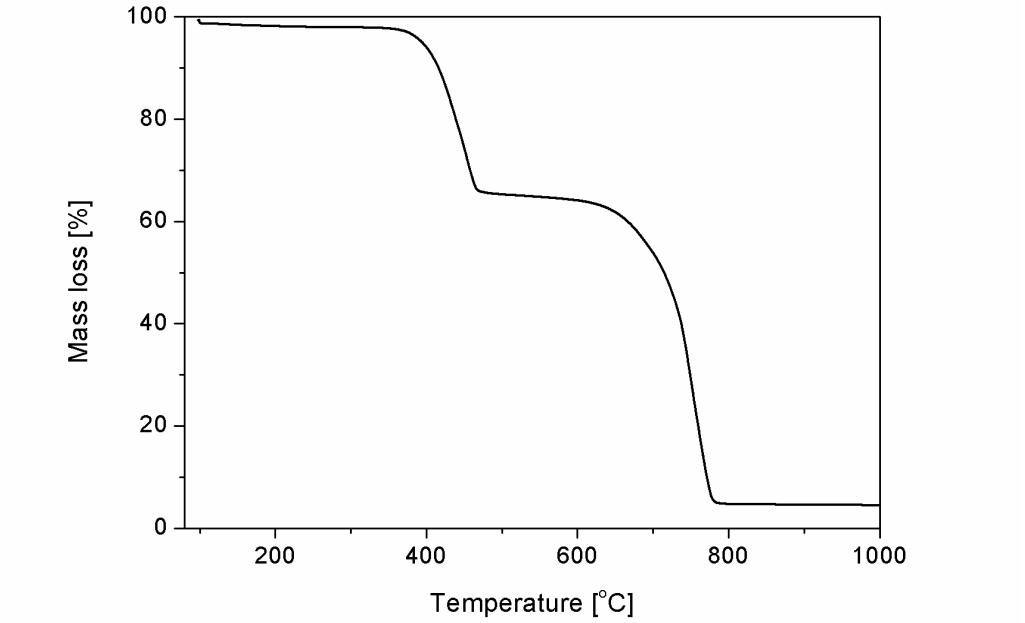



*Figure 8-49 TGA thermogram for mole fraction $\chi CoCl_2 = 0.65$.*

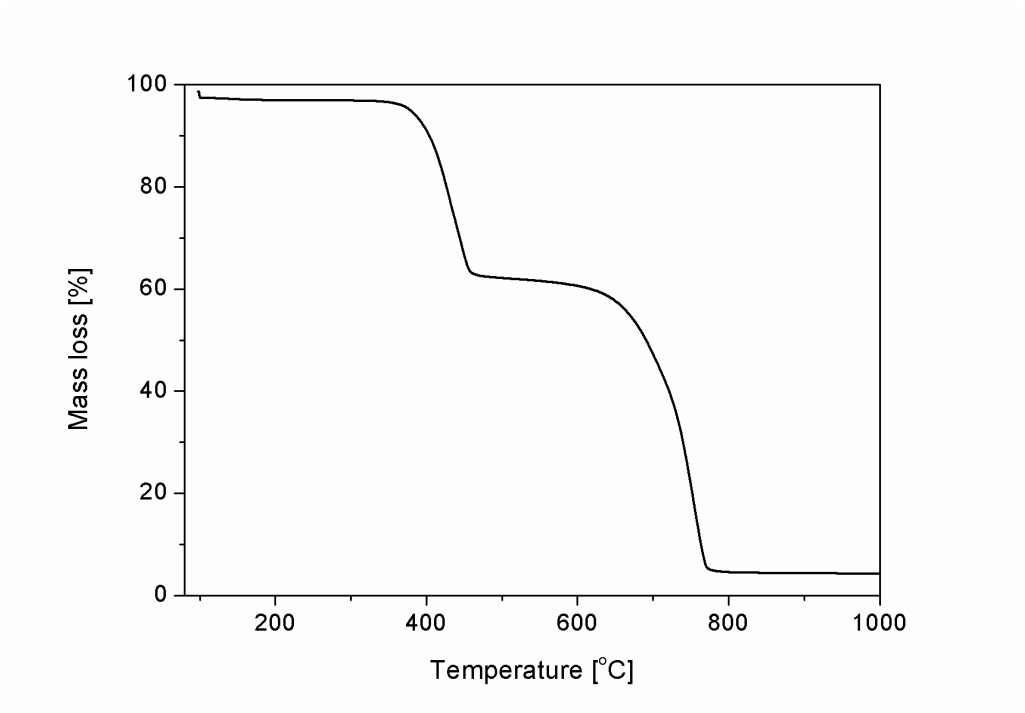



*Figure 8-50 TGA thermogram for mole fraction χ$CoCl_2$ = 0.7.*

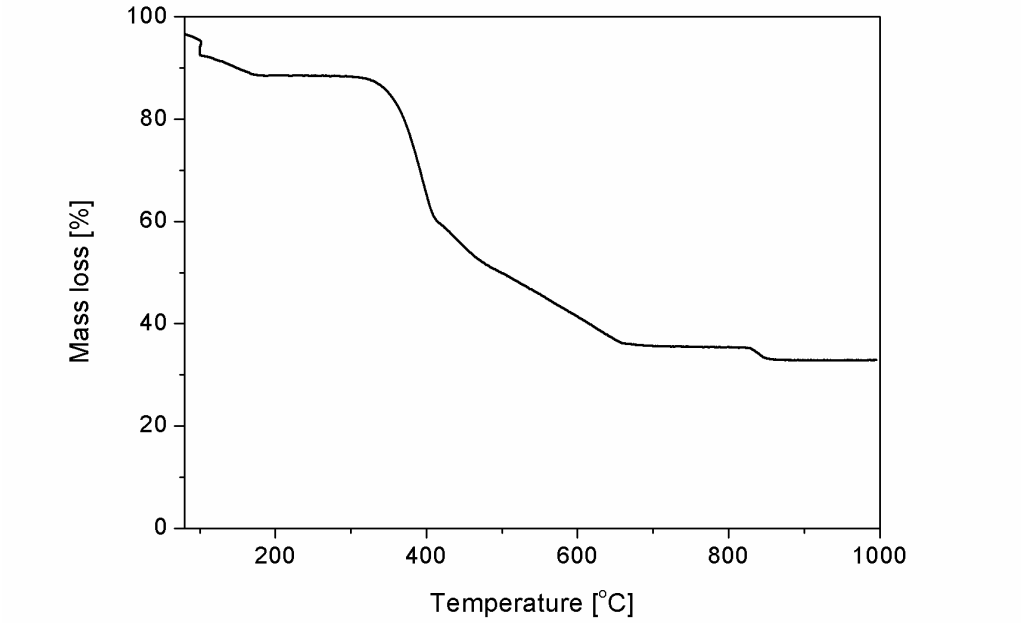



*Figure 8-51 TGA thermogram for mole fraction χCoCl2 = 0.75.*

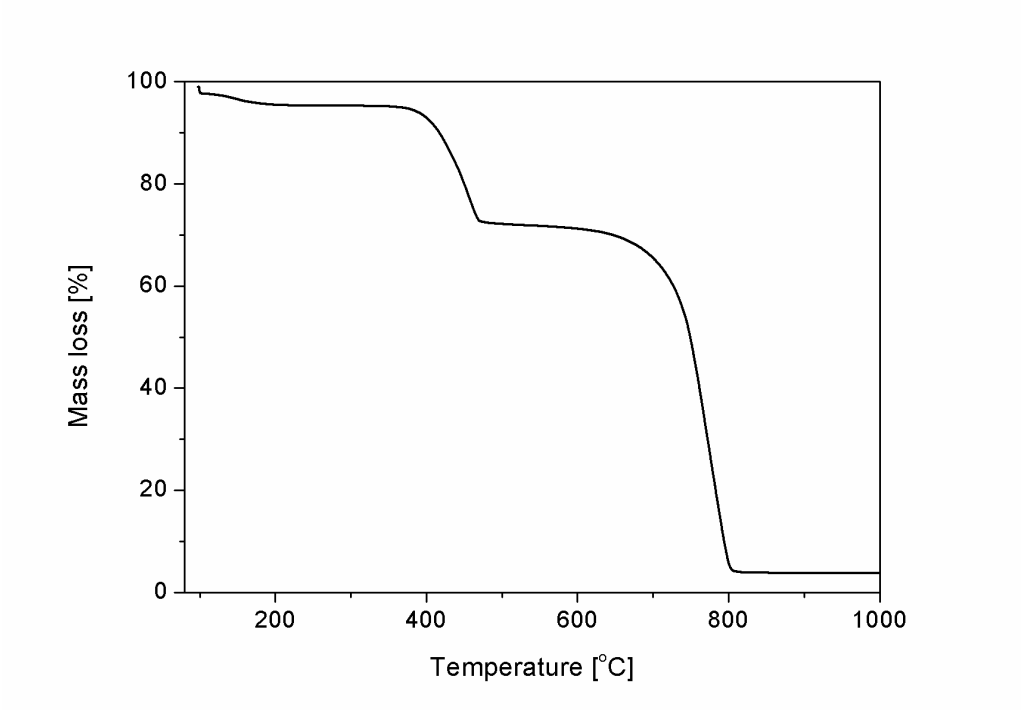



*Figure 8-52 TGA thermogram for mole fraction $\chi CoCl_2 = 0.8$.*

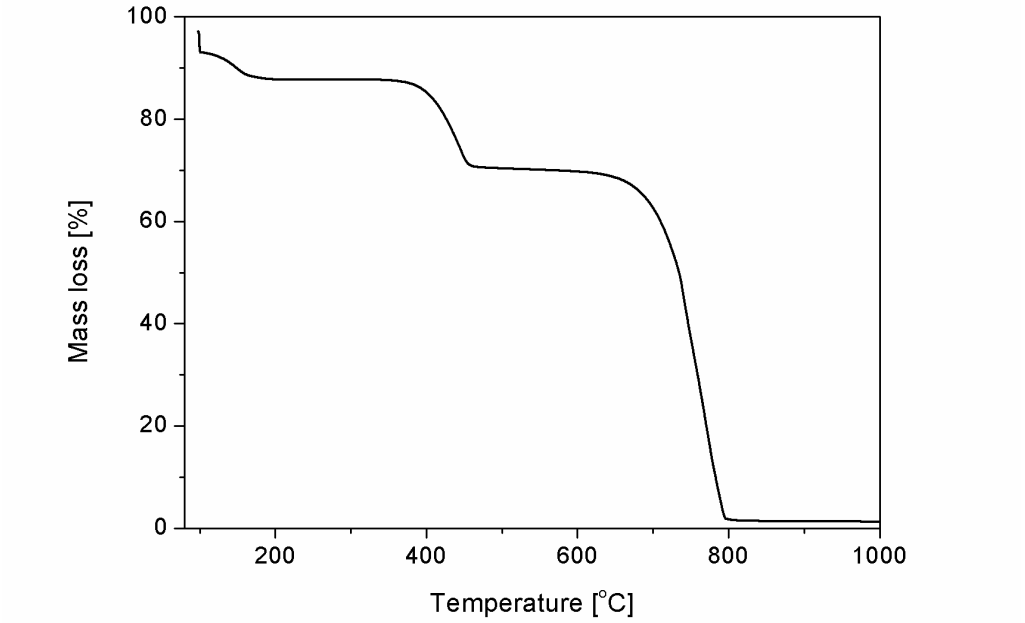



*Figure 8-53 TGA thermogram for mole fraction $\chi CoCl_2 = 0.85$.*

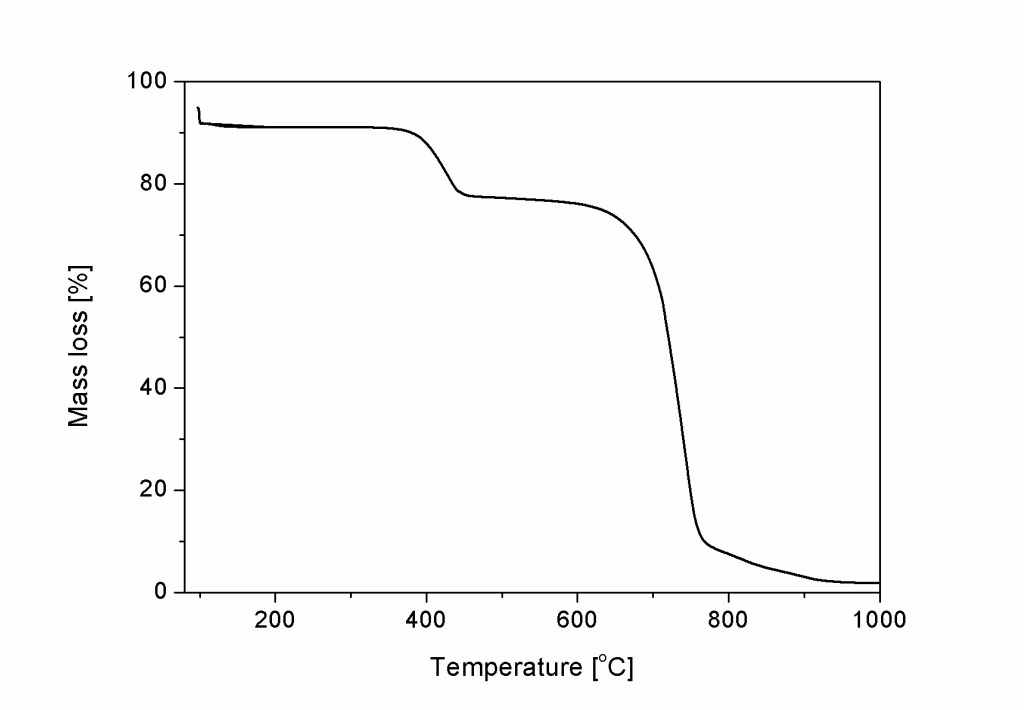



*Figure 8-54 TGA thermogram for mole fraction $\chi CoCl_2 = 0.9$.*

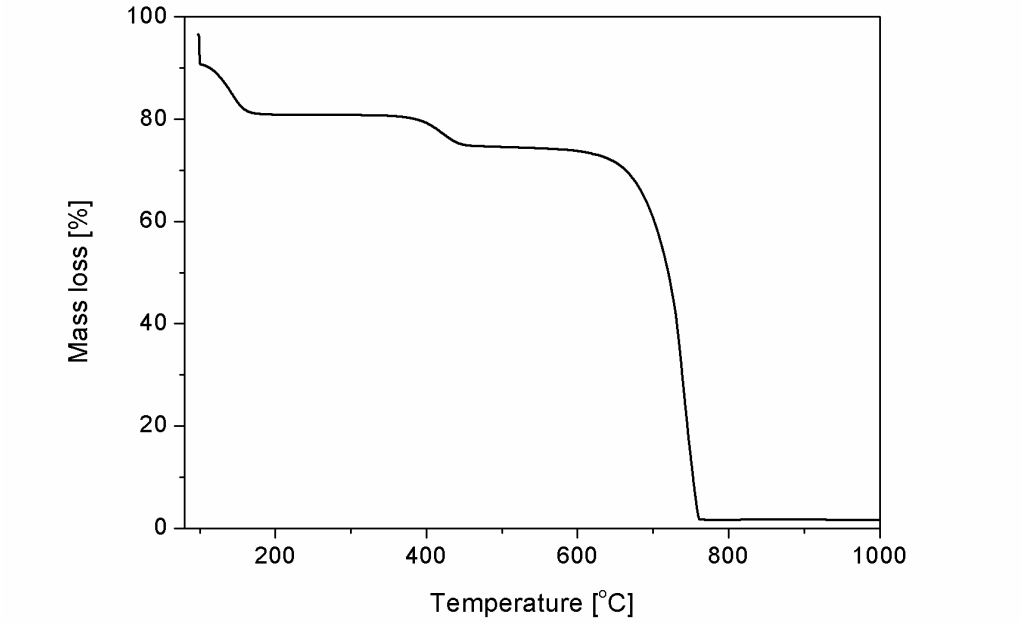



*Figure 8-55 TGA thermogram for mole fraction $\chi CoCl_2 = 0.95$.*

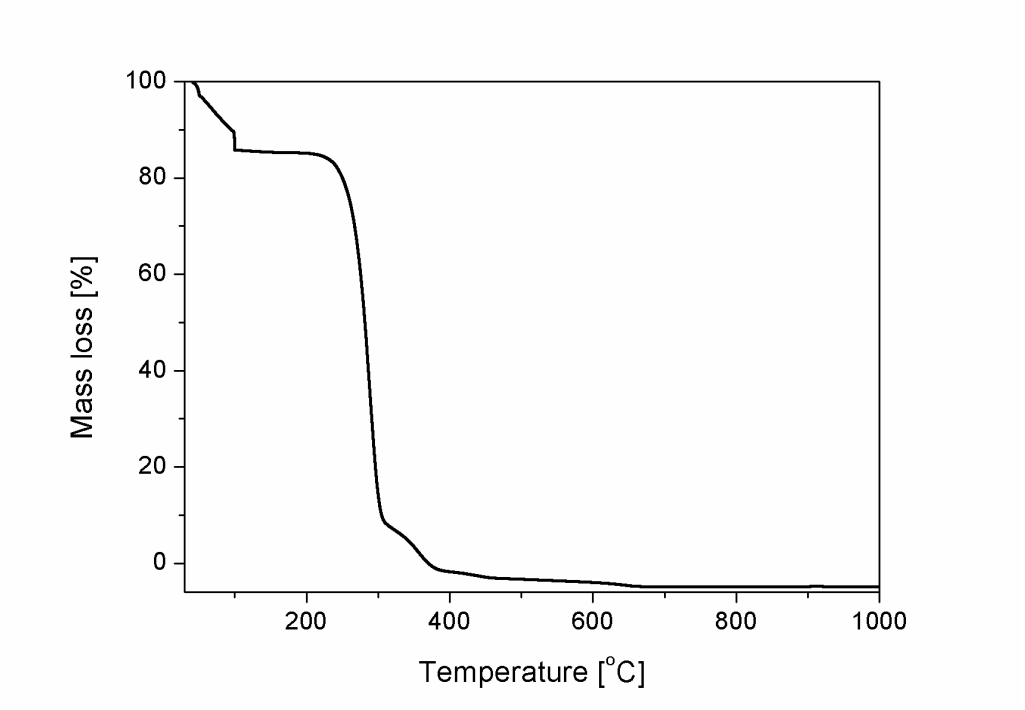



*Figure 8-56 TGA thermogram for mole fraction $\chi NiCl_2 = 0.05$.*

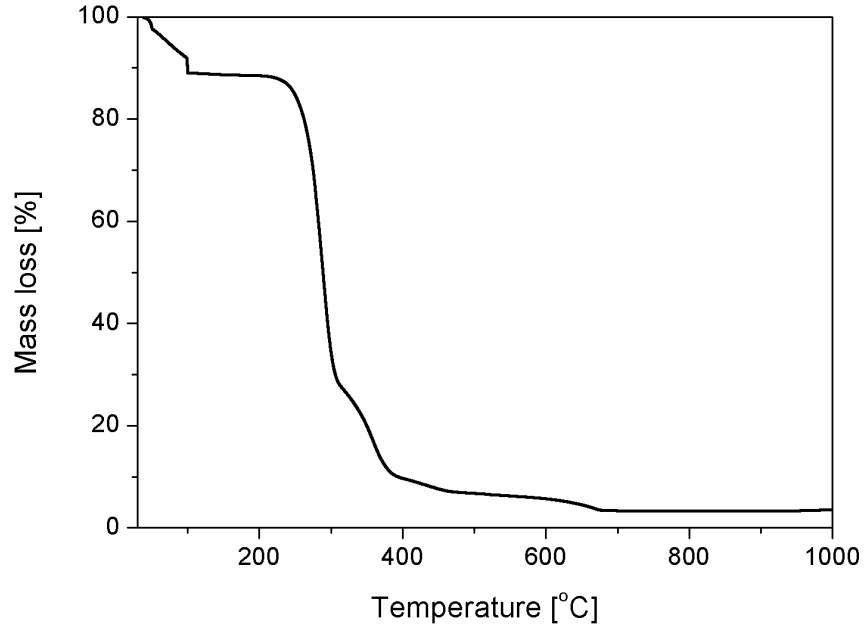



*Figure 8-57 TGA thermogram for mole fraction $\chi NiCl_2 = 0.1$.*

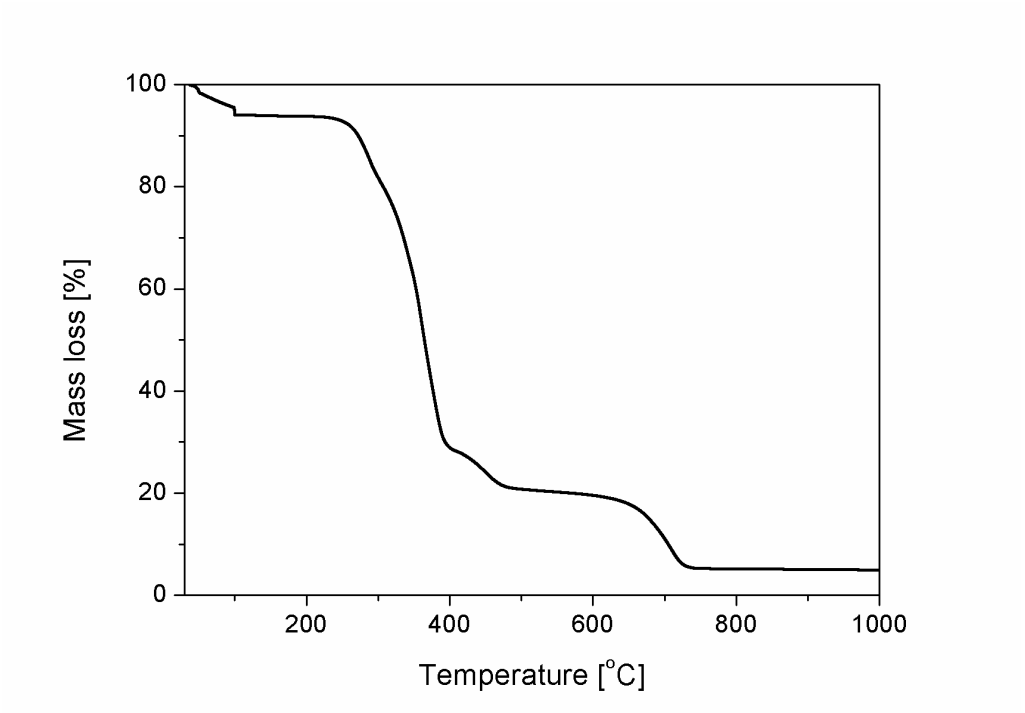



*Figure 8-58 TGA thermogram for mole fraction $\chi NiCl_2 = 0.15$.*

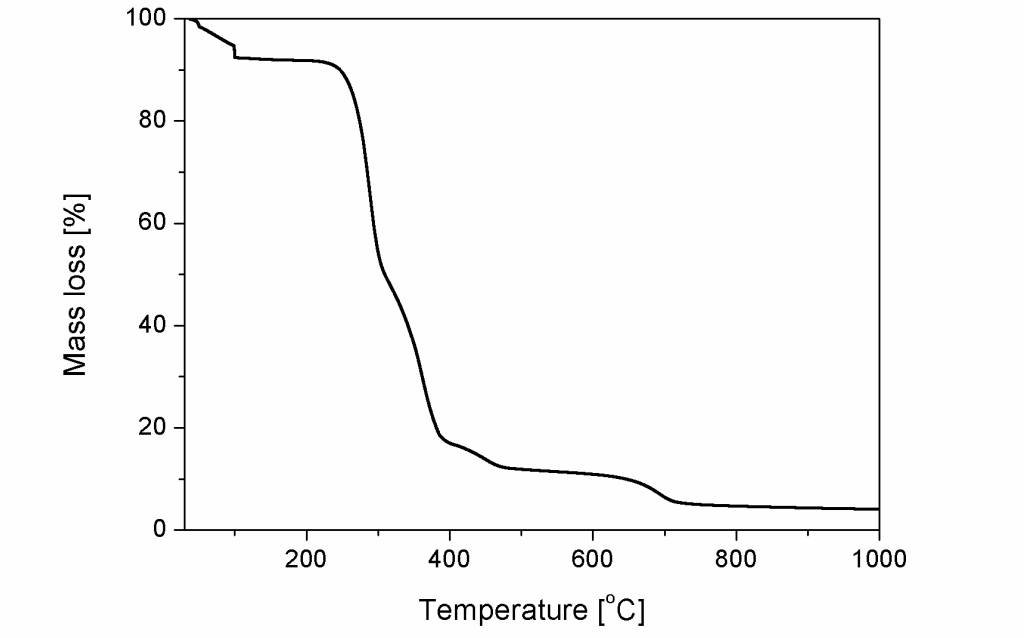



*Figure 8-59 TGA thermogram for mole fraction $\chi NiCl_2 = 0.2$.*

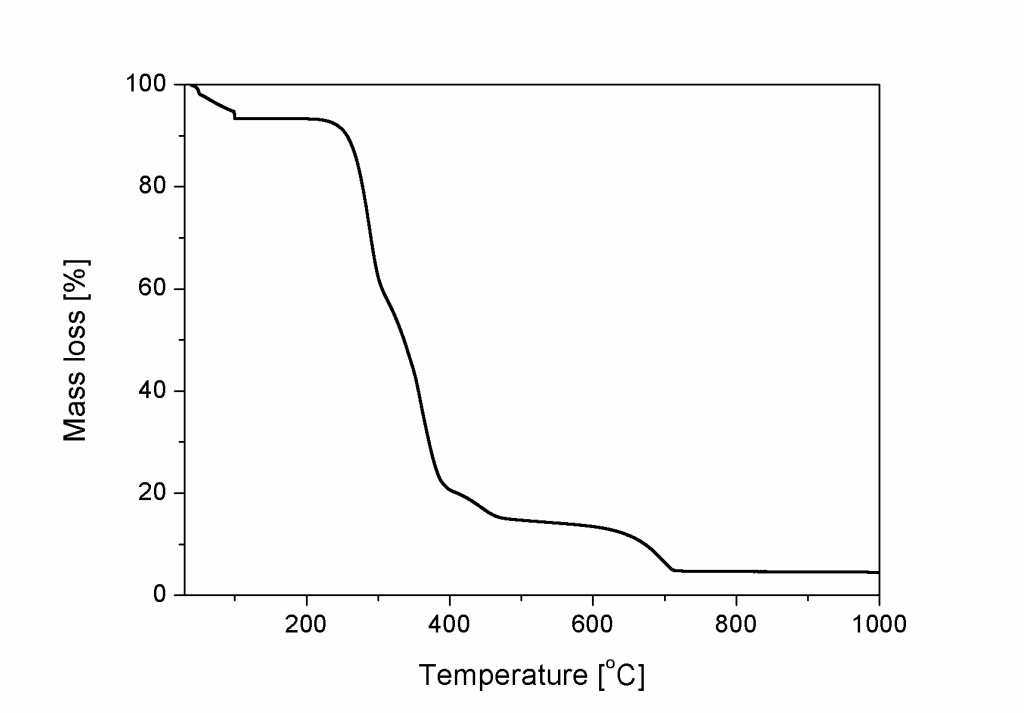



*Figure 8-60 TGA thermogram for mole fraction $\chi NiCl_2 = 0.25$.*

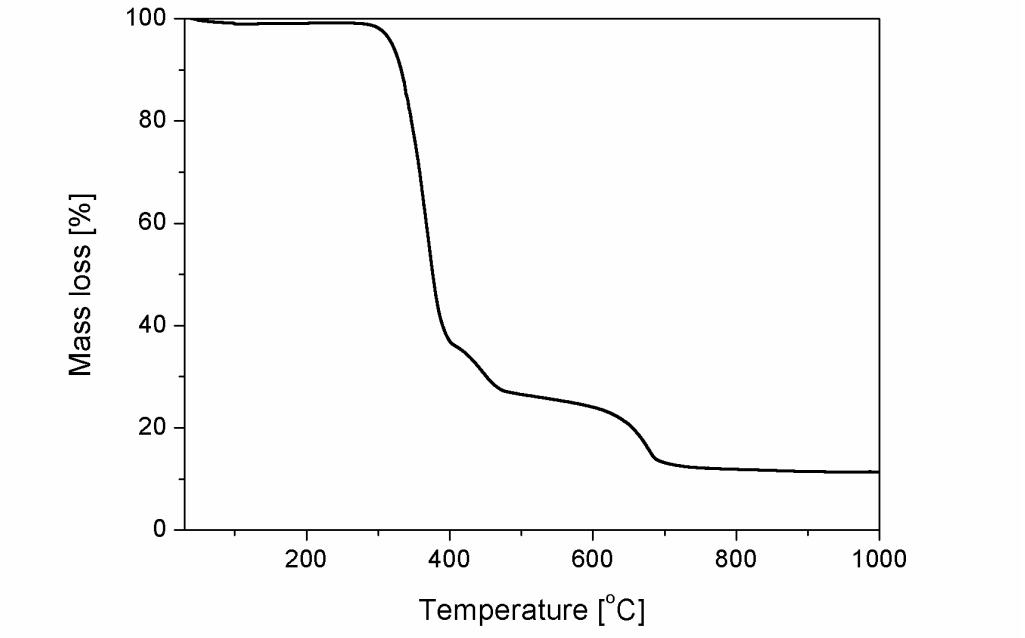



*Figure 8-61 TGA thermogram for mole fraction $\chi NiCl_2 = 0.4$.*

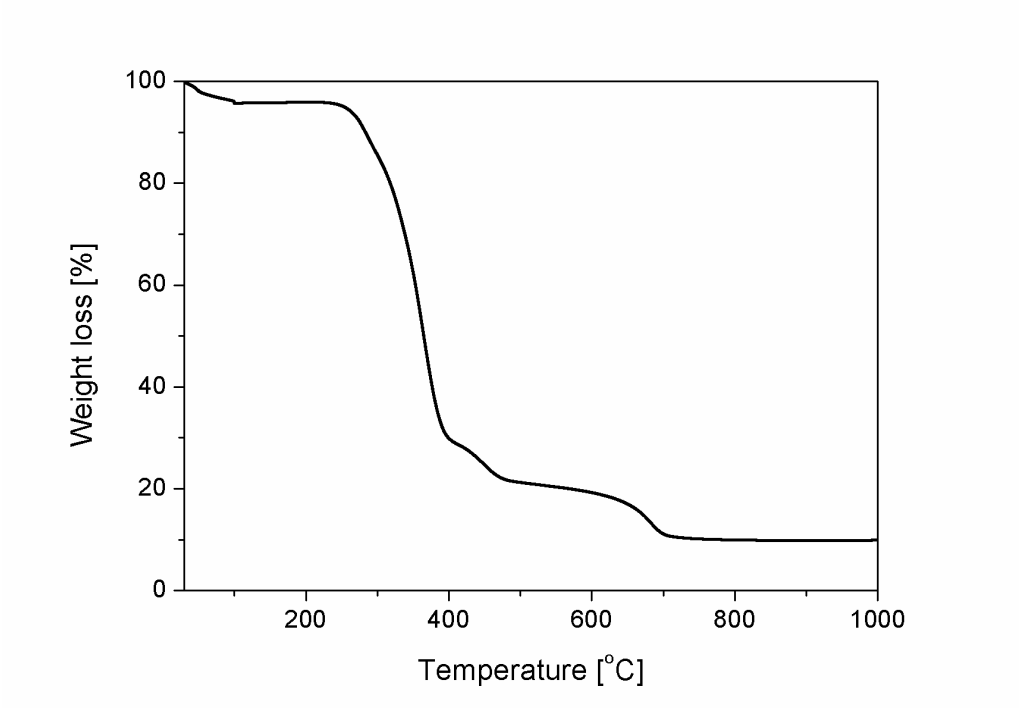



*Figure 8-62 TGA thermogram for mole fraction $\chi NiCl_2 = 0.45$.*

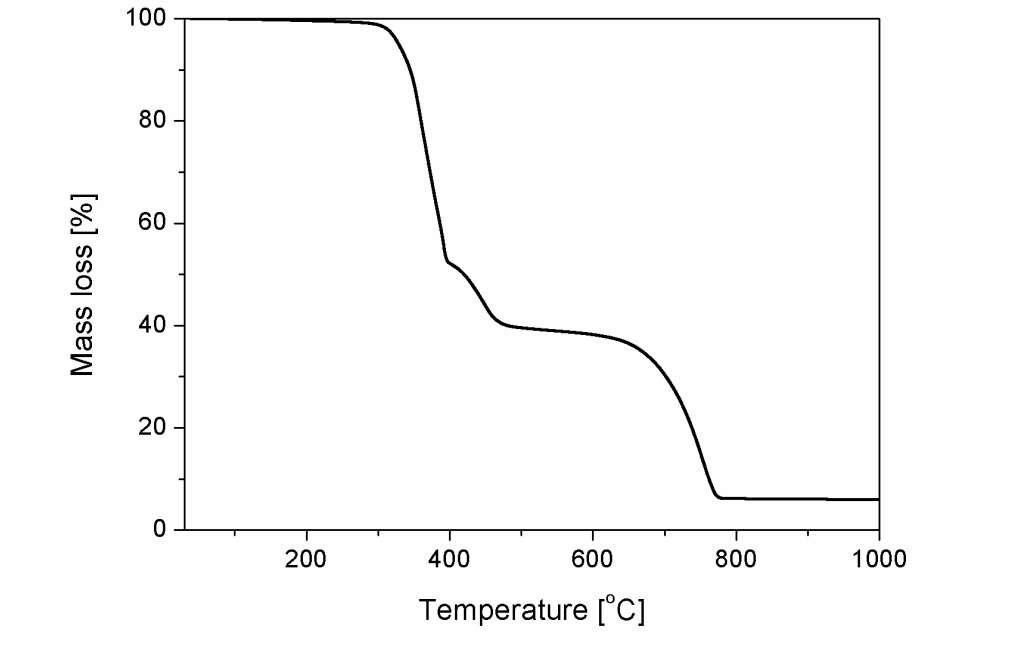



*Figure 8-63 TGA thermogram for mole fraction $\chi NiCl_2 = 0.5$.*

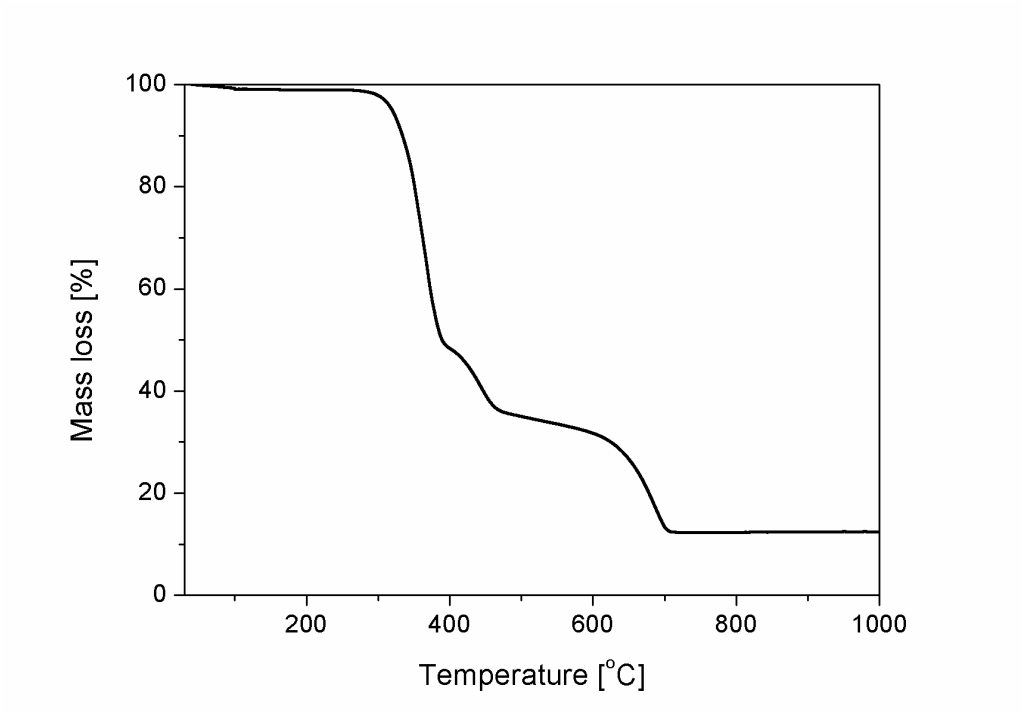



*Figure 8-64 TGA thermogram for mole fraction χ$NiCl_2$ = 0.55.*

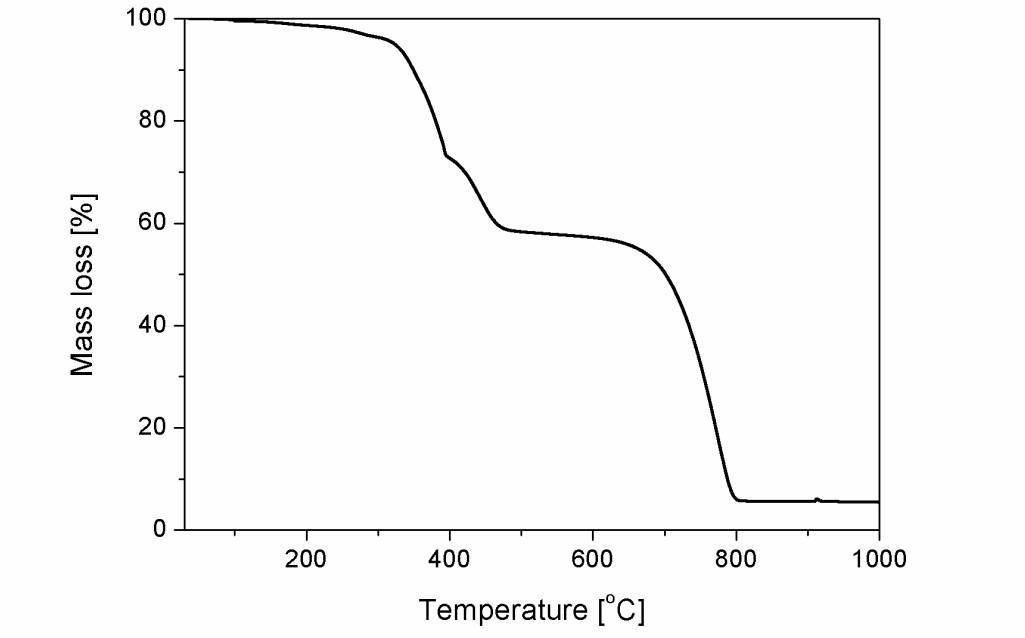



*Figure 8-65 TGA thermogram for mole fraction χ$NiCl_2$ = 0.6.*

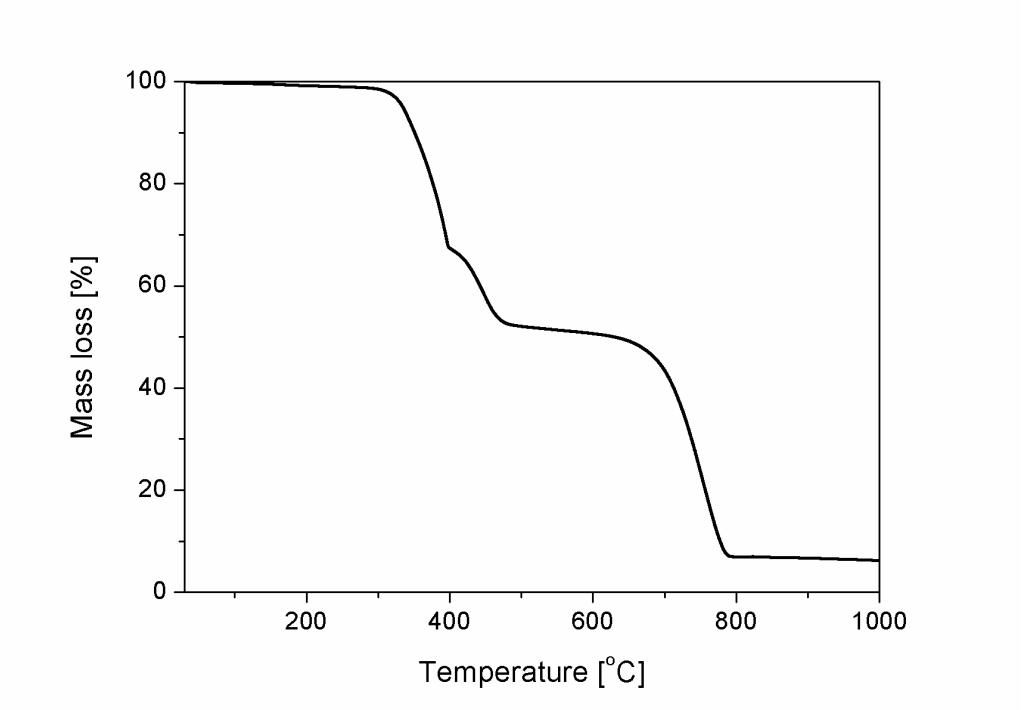



*Figure 8-66 TGA thermogram for mole fraction $\chi NiCl_2 = 0.65$.*

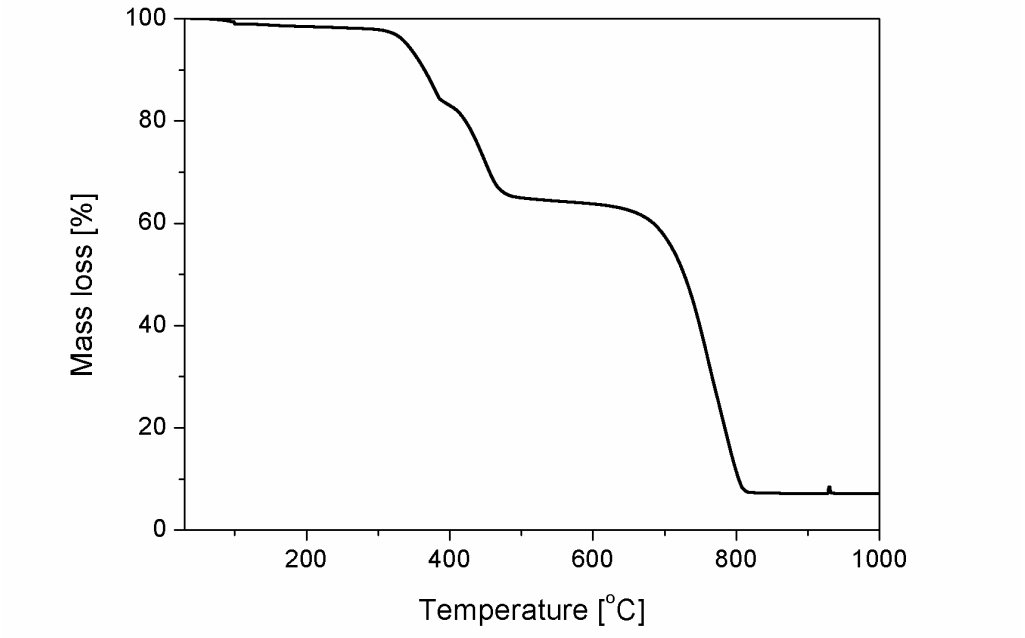



*Figure 8-67 TGA thermogram for mole fraction $\chi NiCl_2 = 0.7$.*

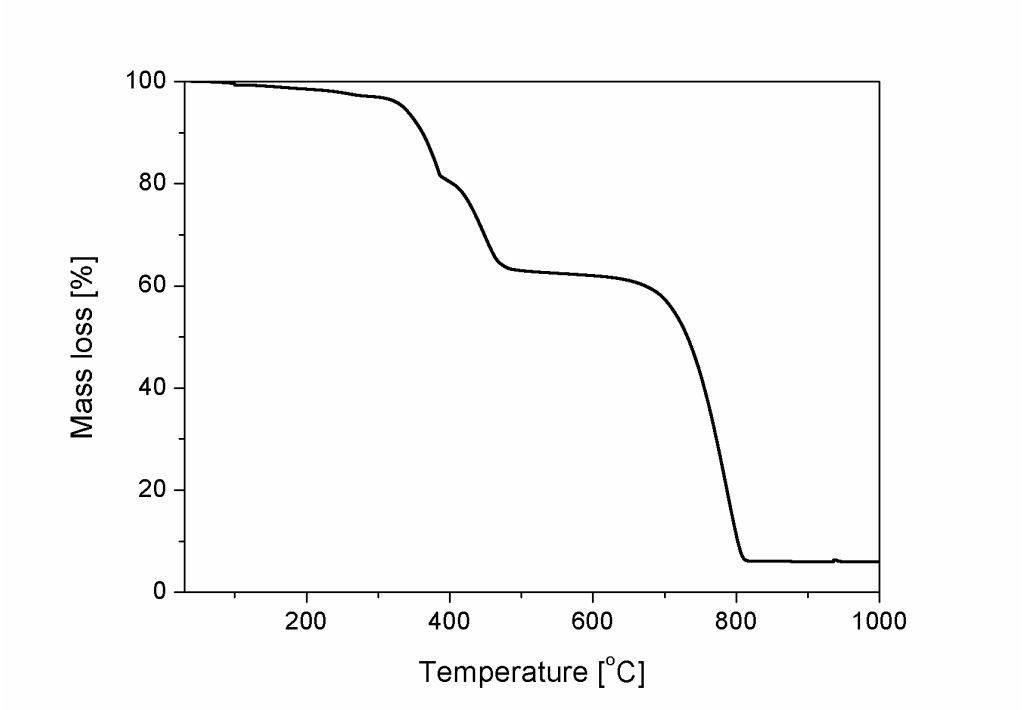



*Figure 8-68 TGA thermogram for mole fraction $\chi NiCl_2 = 0.75$.*

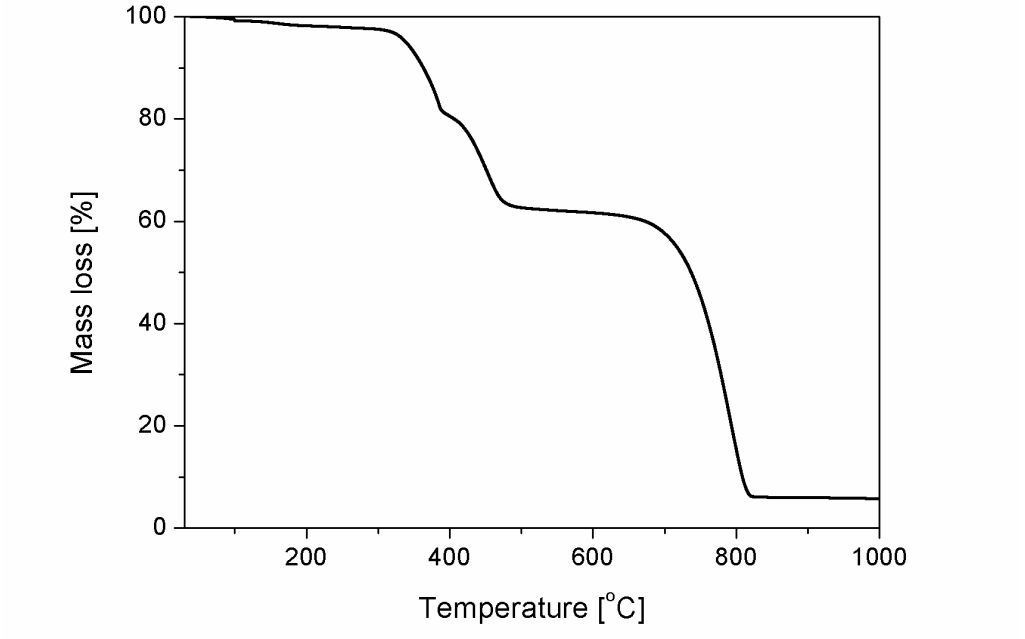



*Figure 8-69 TGA thermogram for mole fraction $\chi NiCl_2 = 0.8$.*

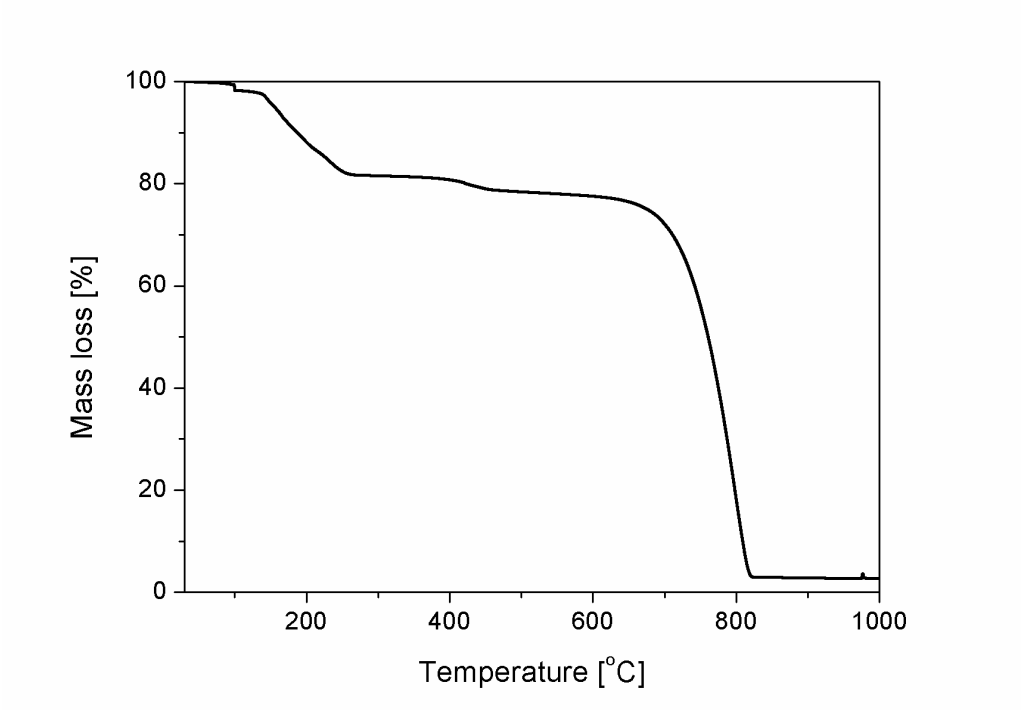



*Figure 8-70 TGA thermogram for mole fraction $\chi NiCl_2 = 0.85$.*

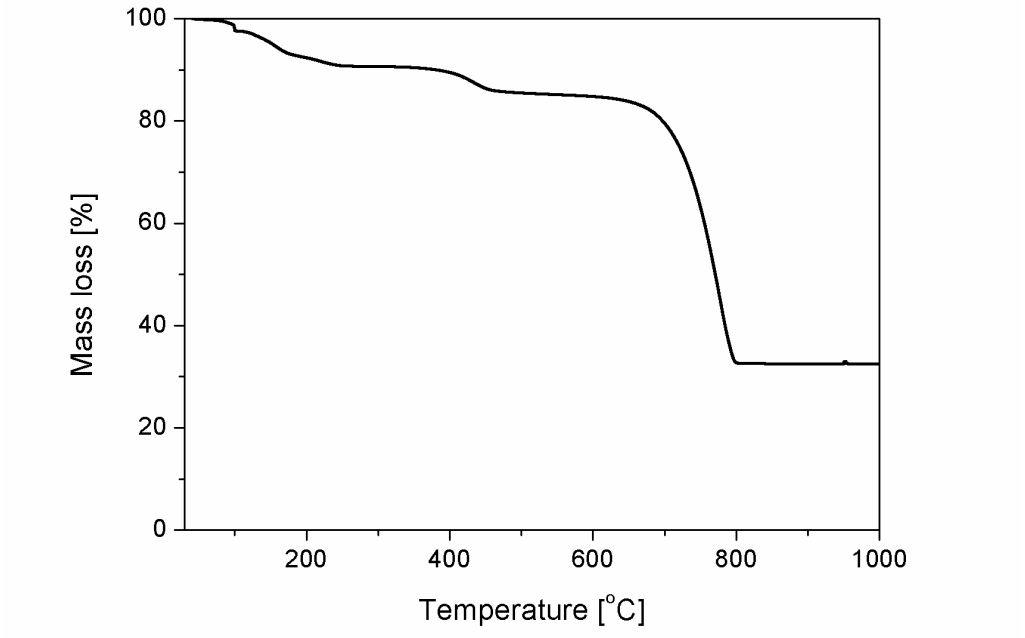



*Figure 8-71 TGA thermogram for mole fraction $\chi NiCl_2 = 0.9$.*

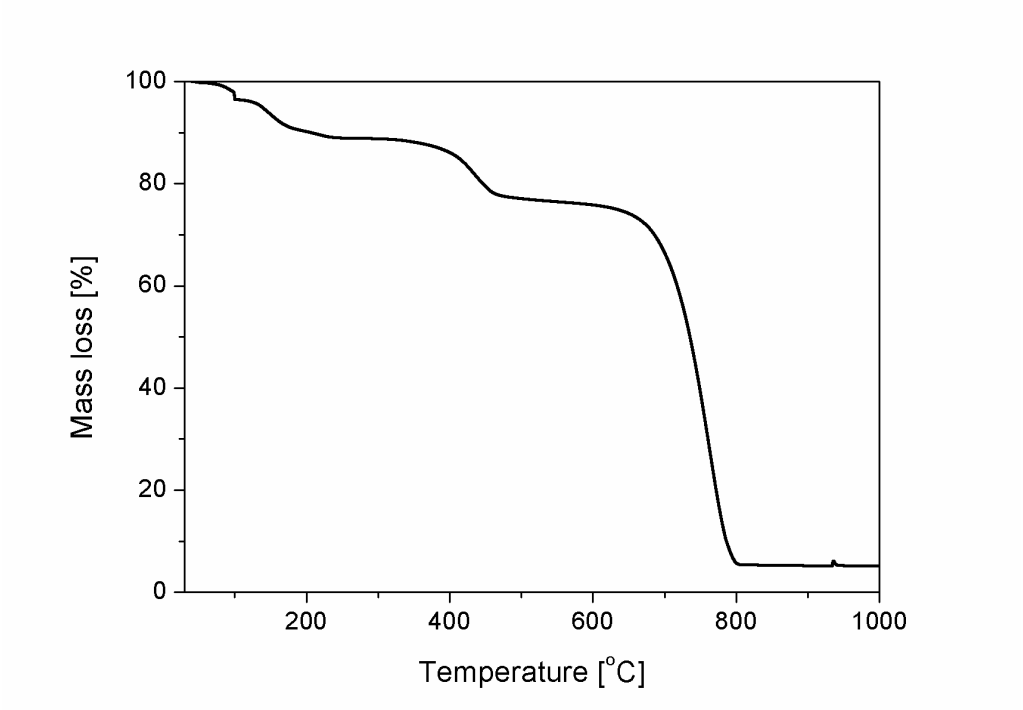



*Figure 8-72 TGA thermogram for mole fraction $\chi NiCl_2 = 0.95$.*

## 8.2 Crystal structure

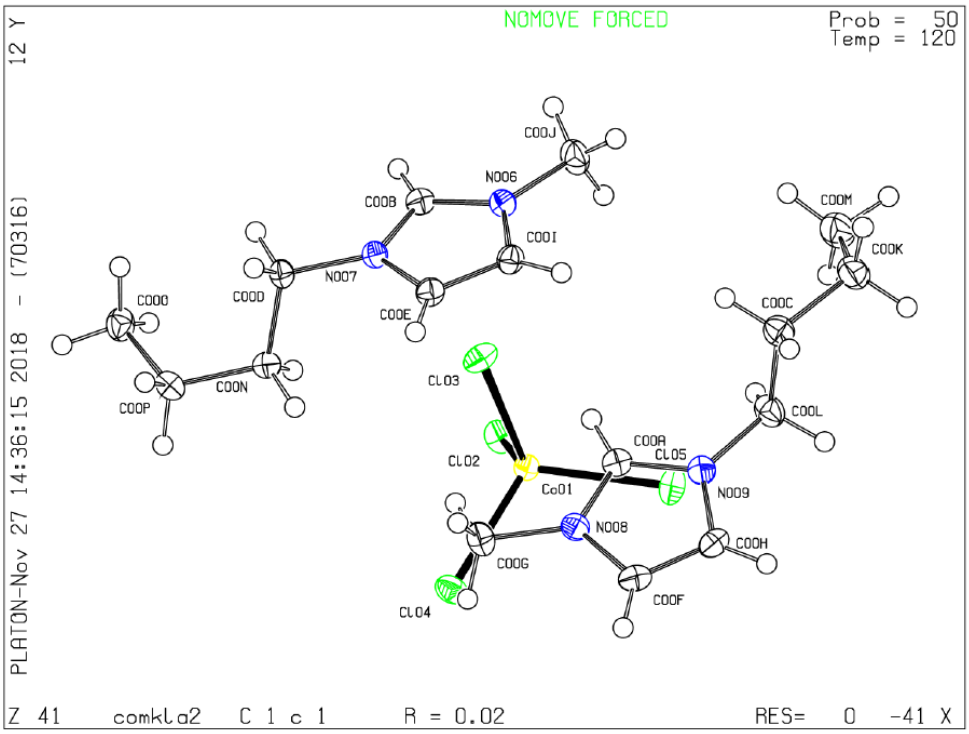
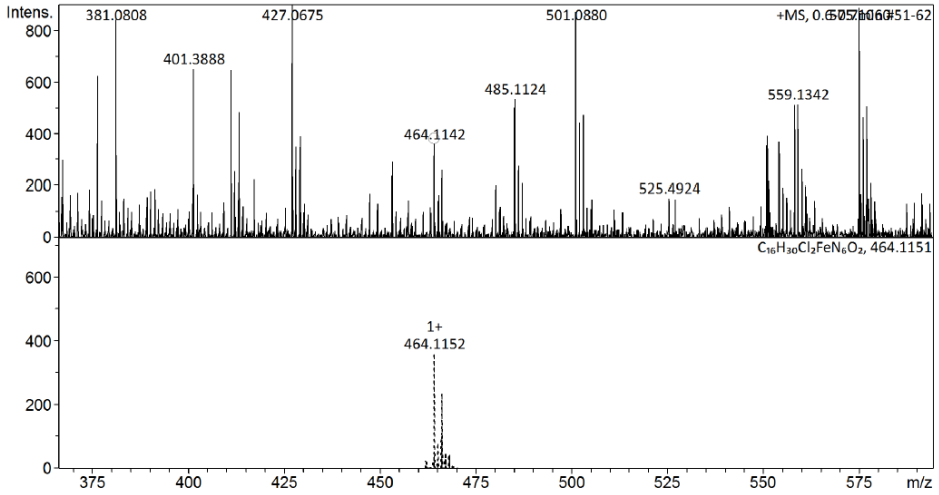



*Figure 8-73 Crystal structure obtained for $[C_1C_4Im]_2[CoCl_4]$. Cell a=14.3690 (2), b=9.7041 (1), c=16.8425 (2), alpha=90, beta=107.662 (1), gamma=90, Temperature: 120 K.*

*Table 8-3 Crystal structure refinement data.*

| | **Calculated** | **Reported** |
|---|---|---|
| **Volume** | 2237.79 (5) | 2237.79 (5) |
| **Space group** | C c | C1 C1 |
| **Hall group** | C -2yc | C -2yc |
| **Moiety formula** | 2(C8 H15 N2), Cl4 Co | 2(C8 H15 N2), Cl4 Co |
| **Sum formula** | C16 H30 Cl4 Co N4 | C16 H30 Cl4 Co N4 |
| **Mr** | 479.17 | 479.17 |
| **Dx, g cm$^{-3}$** | 1.422 | 1.422 |
| **Z** | 4 | 4 |
| **Mu (mm$^{-1}$)** | 1.252 | 1.252 |
| **F000** | 996.0 | 996.0 |
| **F000'** | 999.92 | |
| **h, k, l max** | 19, 13, 22 | 18, 13, 22 |
| **$N_{ref}$** | 5880 (2943) | 5620 |
| **$T_{min}$, $T_{max}$** | 0.602, 0.779 | 0.402, 1.000 |
| **$T_{min'}$** | 0.573 | |

## 8.3 ESI-MS spectroscopy




| Meas. m/z | # | Ion Formula | Score | m/z | err [mDa] | err [ppm] | mSigma |
|---|---|---|---|---|---|---|---|
| 139.123247 | 1 | C8H15N2 | 100.00 | 139.122975 | -0.3 | -2.0 | 0.3 |
| 313.215118 | 1 | C16H30ClN4 | 100.00 | 313.215351 | 0.2 | 0.7 | 2.5 |
| | 2 | C14H31ClN4Na | 26.75 | 313.212945 | -2.2 | -6.9 | 10.1 |
| | 3 | C11H30ClN6O2 | 4.32 | 313.211328 | -3.8 | -12.1 | 22.9 |
| 464.114225 | 1 | C16H30Cl2FeN6O2 | 100.00 | 464.115119 | 1.0 | 2.1 | 91.2 |

*Figure 8-74 ESI-MS spectrum of $[C_1C_4Im][Fe(NO)_2Cl_2]$ in the positive mode.*

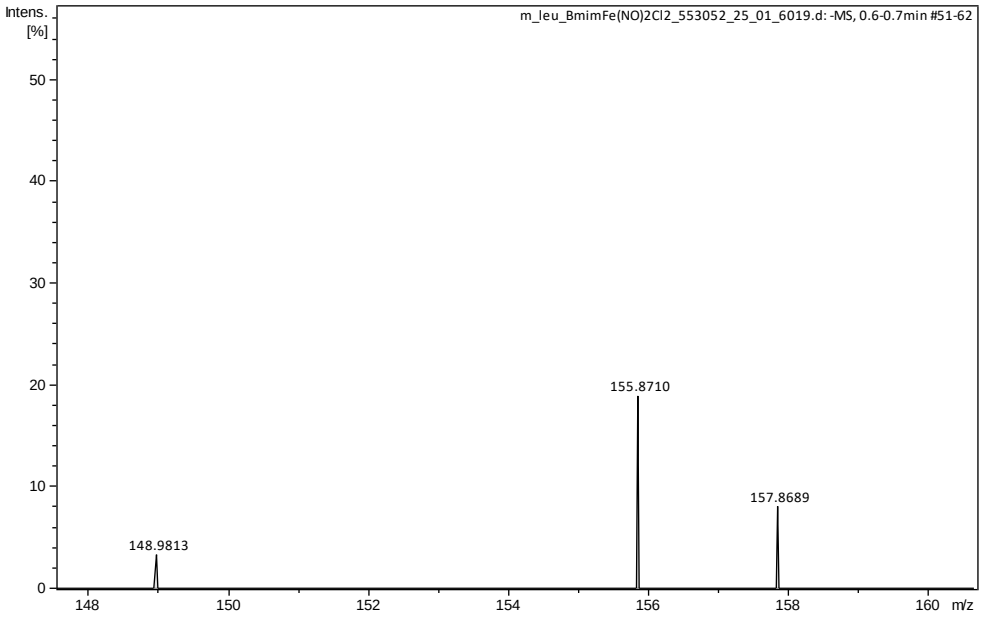



*Figure 8-75 ESI-MS negative mode for $[C_1C_4Im][Fe(NO)_2Cl_2]$. m/z = 155.8710 and 157.8689 belong to the fragment $[Fe(NO)Cl_2]$.*

## 8.4 Nuclear magnetic resonance spectroscopy

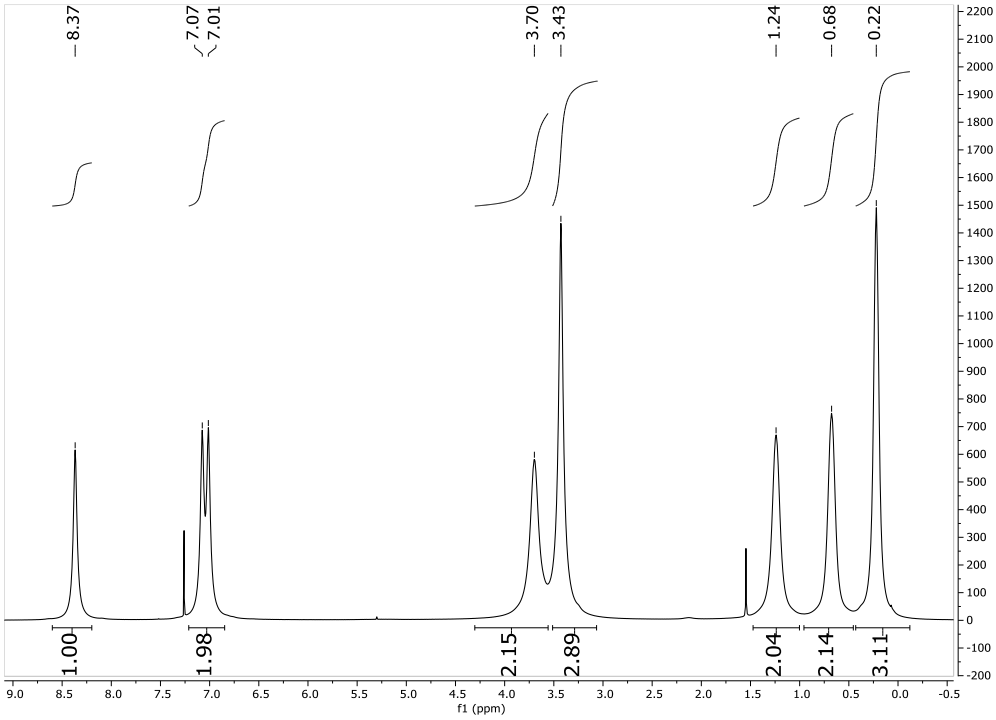



*Figure 8-76 $^{1}$H-NMR of $[C_1C_4Im]_2[ZnCl_4]$ measured at 400 MHz with an inlet tube under solvent free conditions.*

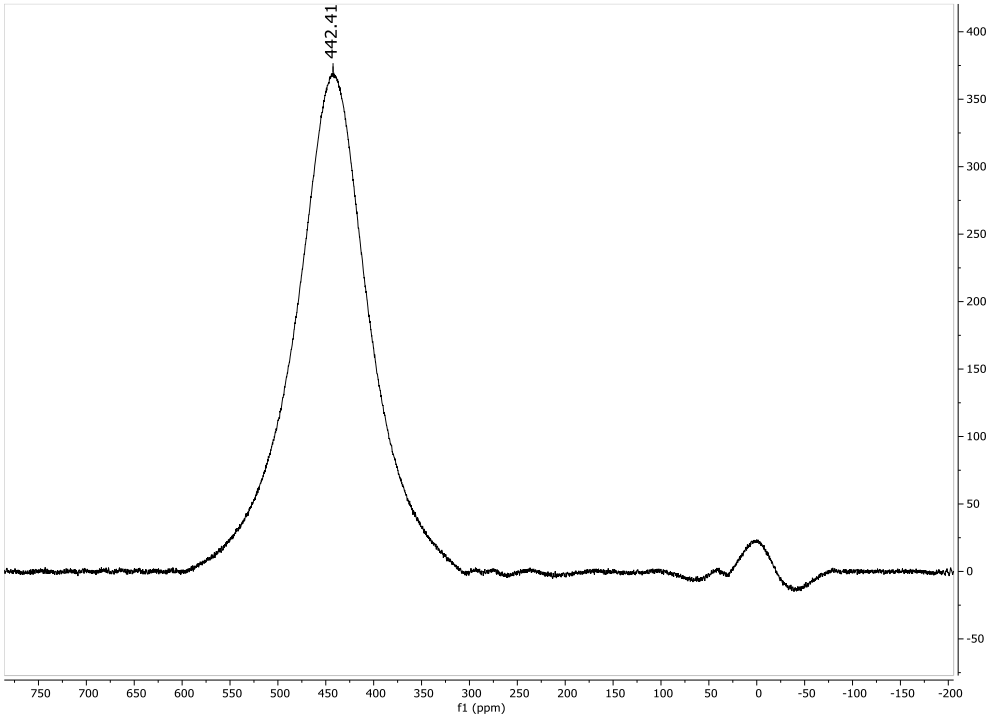



*Figure 8-77 $^{115}$Indium NMR measured at 400 MHz with an inlet tube under solvent free conditions for $[C_1C_4Im][InCl_4]$.*

## 8.5 Dielectric spectroscopy

### 8.5.1 Arrhenius fit – conductivity versus inverse temperature

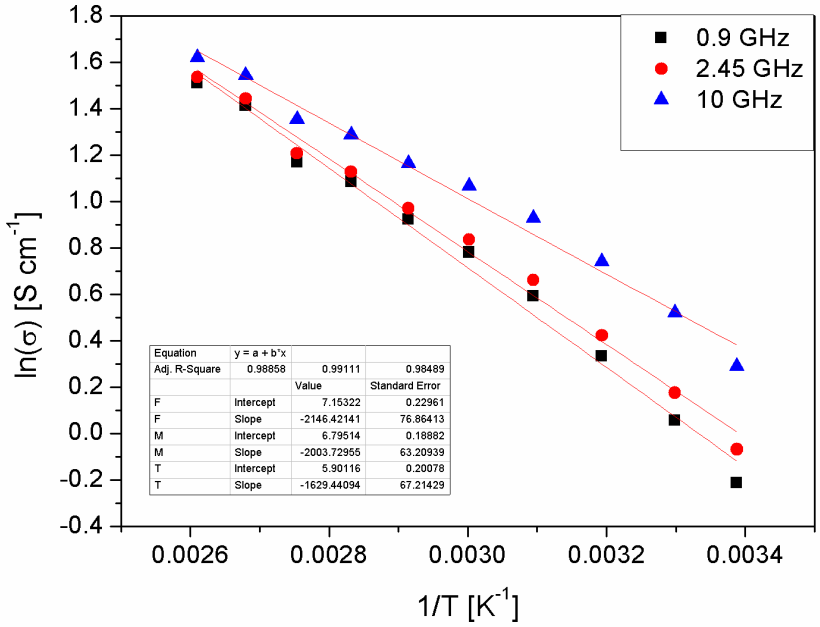



*Figure 8-78 Ionic conductivity plotted versus the inverse temperature for $[C_1C_4Im][FeCl_4]$. The solid line represents an Arrhenius fit.*

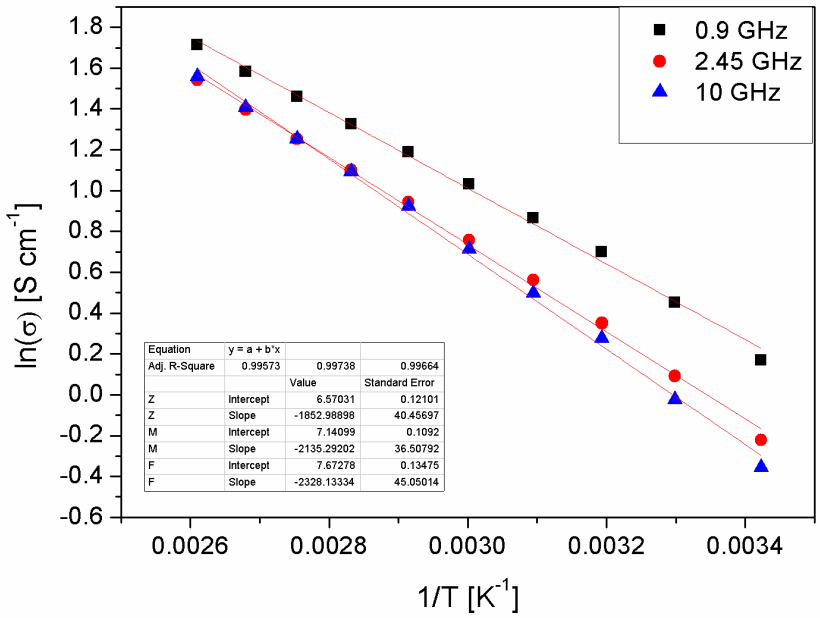



*Figure 8-79 Ionic conductivity plotted versus the inverse temperature for $[C_1C_4Im][InCl_4]$. The solid line represents an Arrhenius fit.*

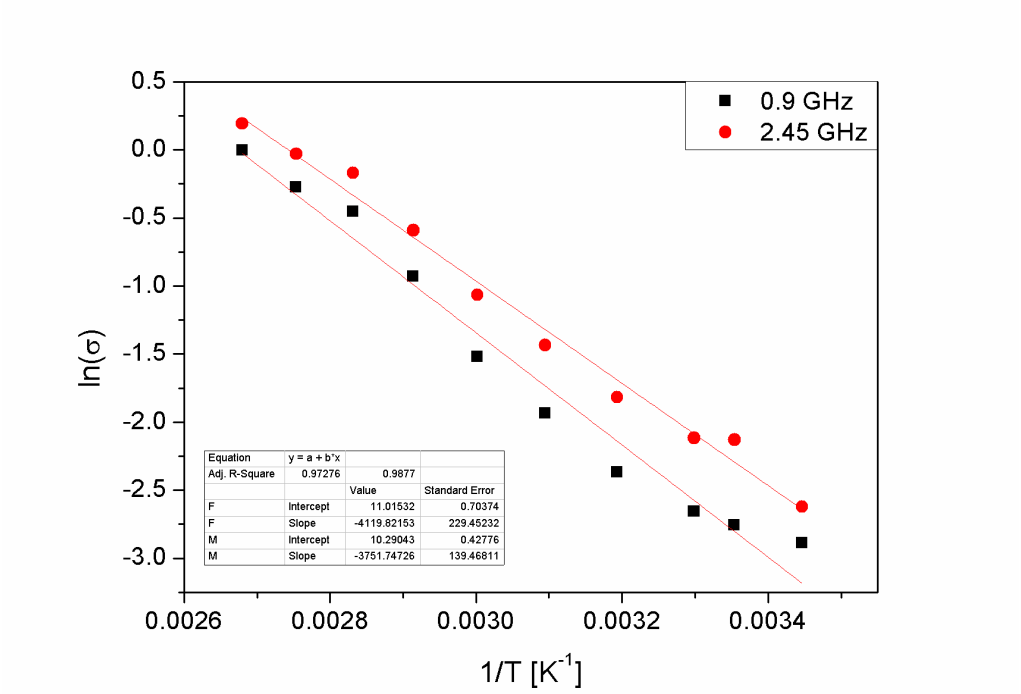



*Figure 8-80 Ionic conductivity plotted versus the inverse temperature for $[C_1C_4Im]_2[CuCl_4]$. The solid line represents an Arrhenius fit.*

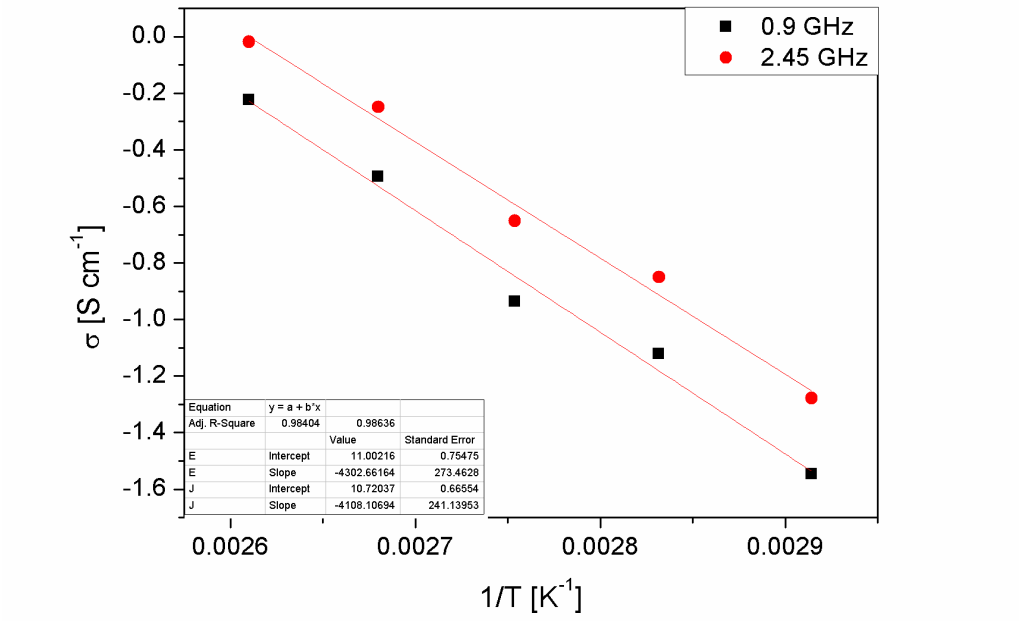



*Figure 8-81 Ionic conductivity plotted versus the inverse temperature for $[C_1C_4Im]_2[ZnCl_4]$. The solid line represents an Arrhenius fit.*

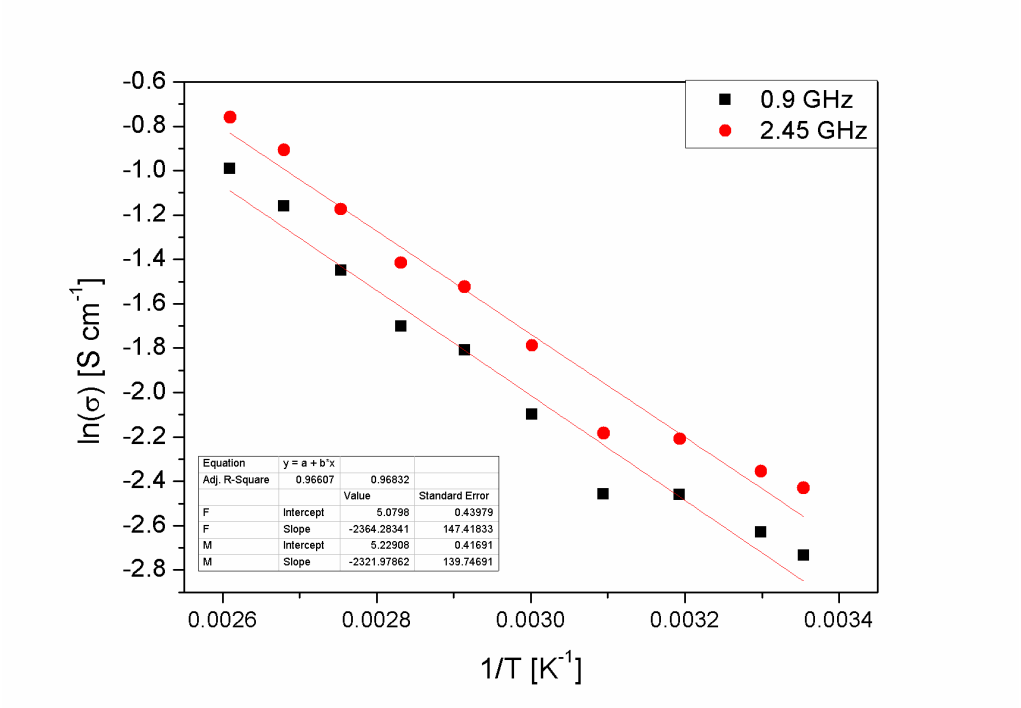



*Figure 8-82 Ionic conductivity plotted versus the inverse temperature for $[C_1C_4Im]_2[NiCl_4]$. The solid line represents an Arrhenius fit.*

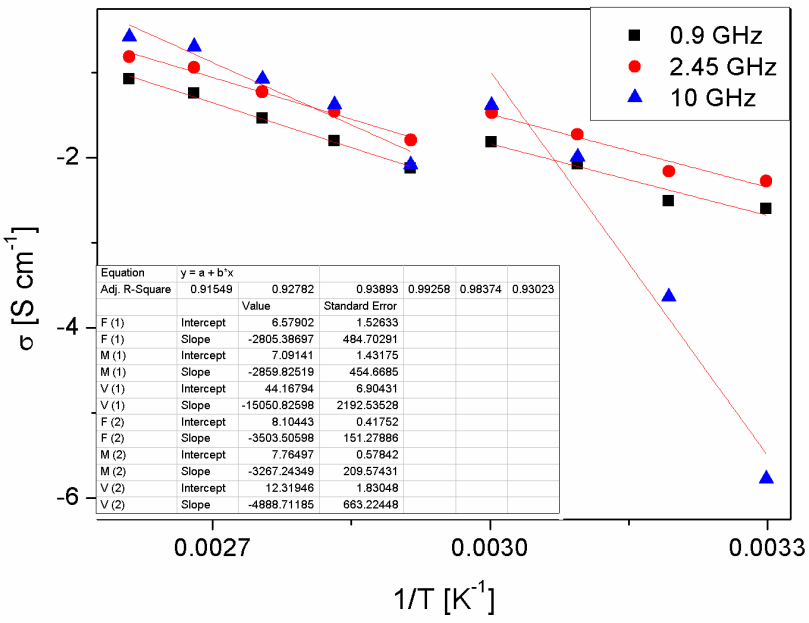



*Figure 8-83 Ionic conductivity plotted versus the inverse temperature for $[C_1C_4Im]_2[CoCl_4]$. The solid line represents an Arrhenius fit.*

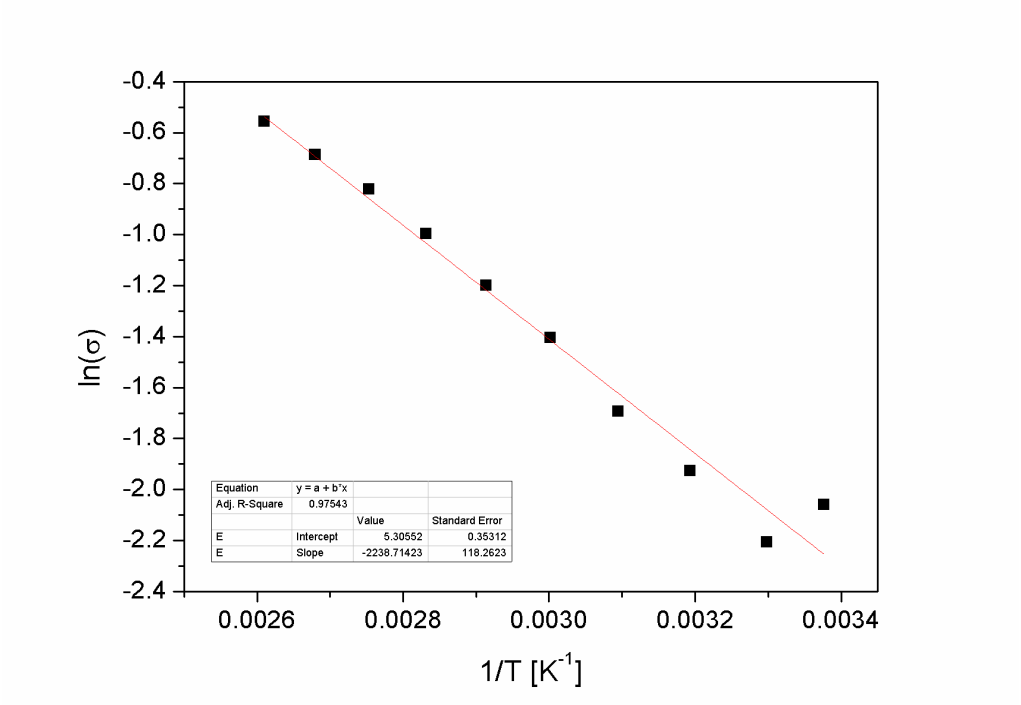



*Figure 8-84 Ionic conductivity plotted versus the inverse temperature for $[C_1C_4Im][FeCl_4]$ from Impedance Spectroscopy. The solid line represents an Arrhenius fit.*

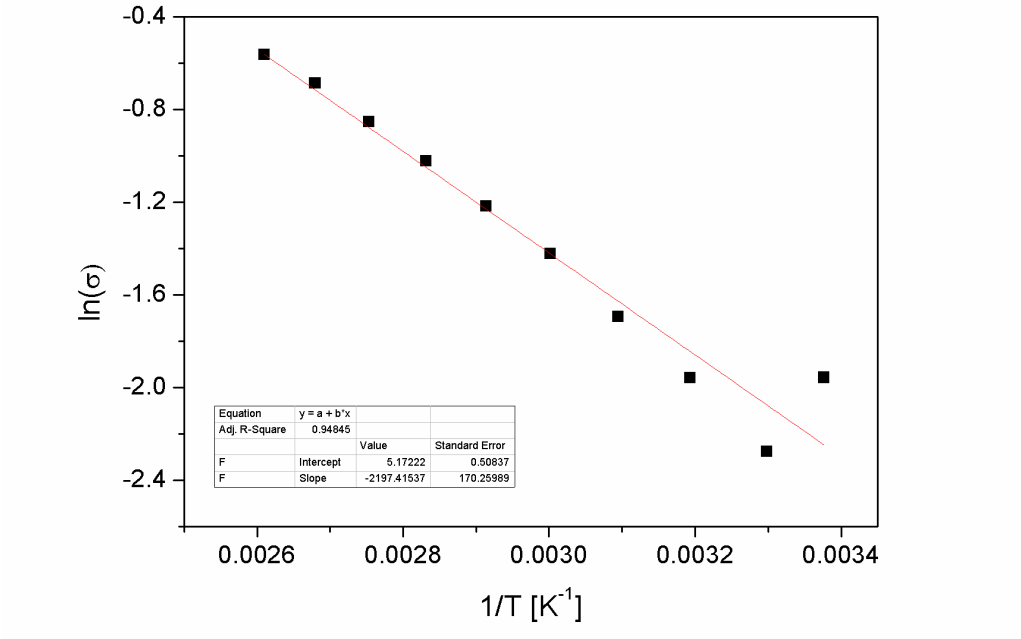



*Figure 8-85 Ionic conductivity plotted versus the inverse temperature for $[C_1C_4Im][InCl_4]$ from Impedance Spectroscopy. The solid line represents an Arrhenius fit.*

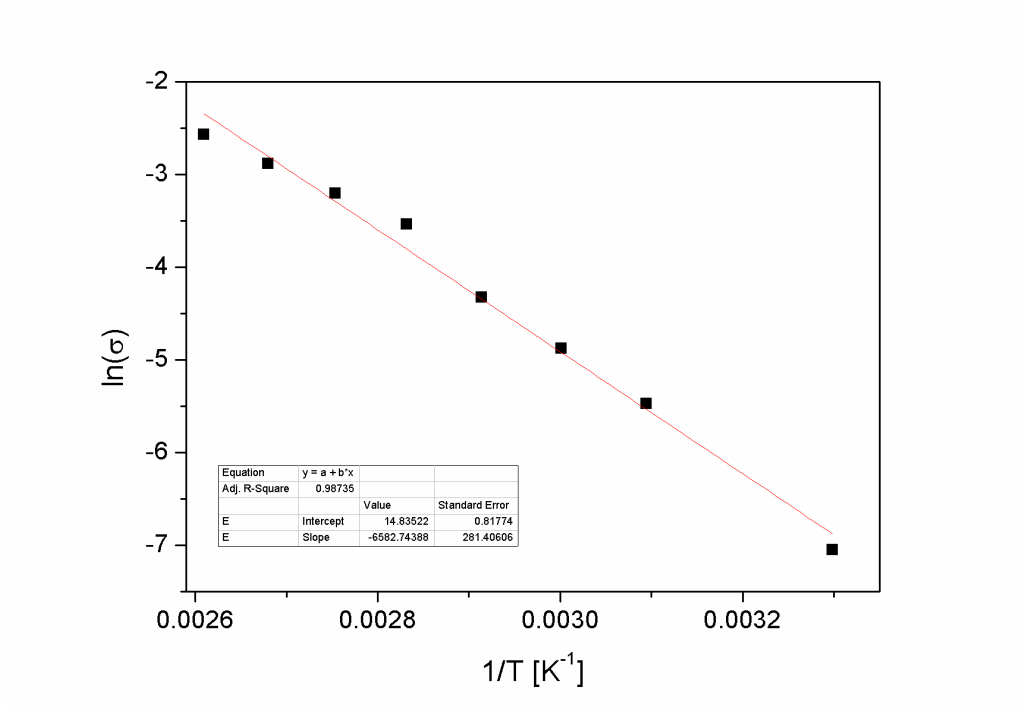



*Figure 8-86 Ionic conductivity plotted versus the inverse temperature for $[C_1C_4Im]_2[ZnCl_4]$ from Impedance Spectroscopy. The solid line represents an Arrhenius fit.*

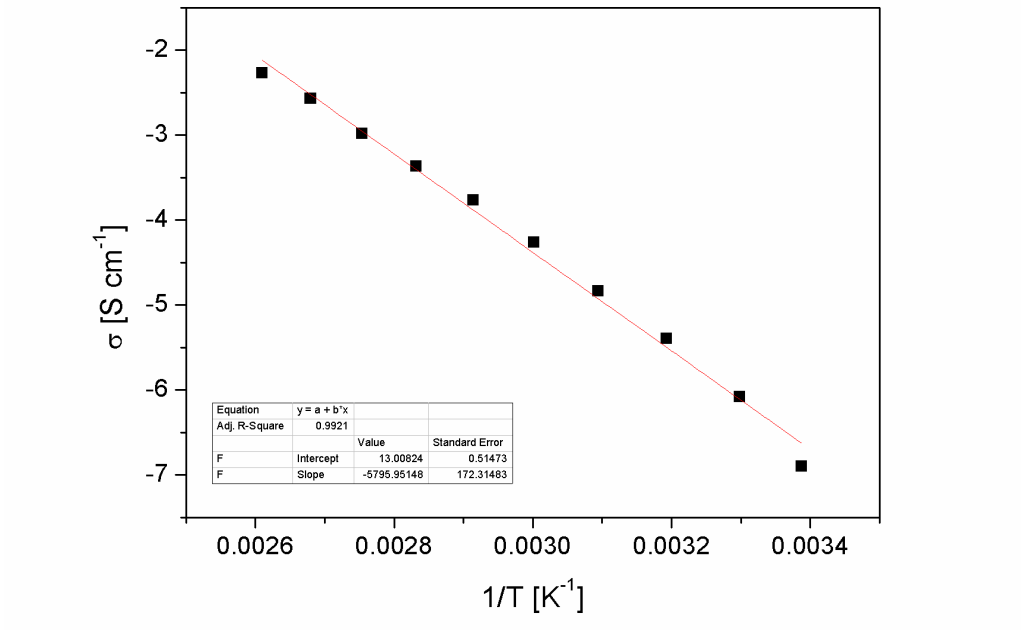



*Figure 8-87 Ionic conductivity plotted versus the inverse temperature for $[C_1C_4Im]_2[CuCl_4]$ from Impedance Spectroscopy. The solid line represents an Arrhenius fit.*

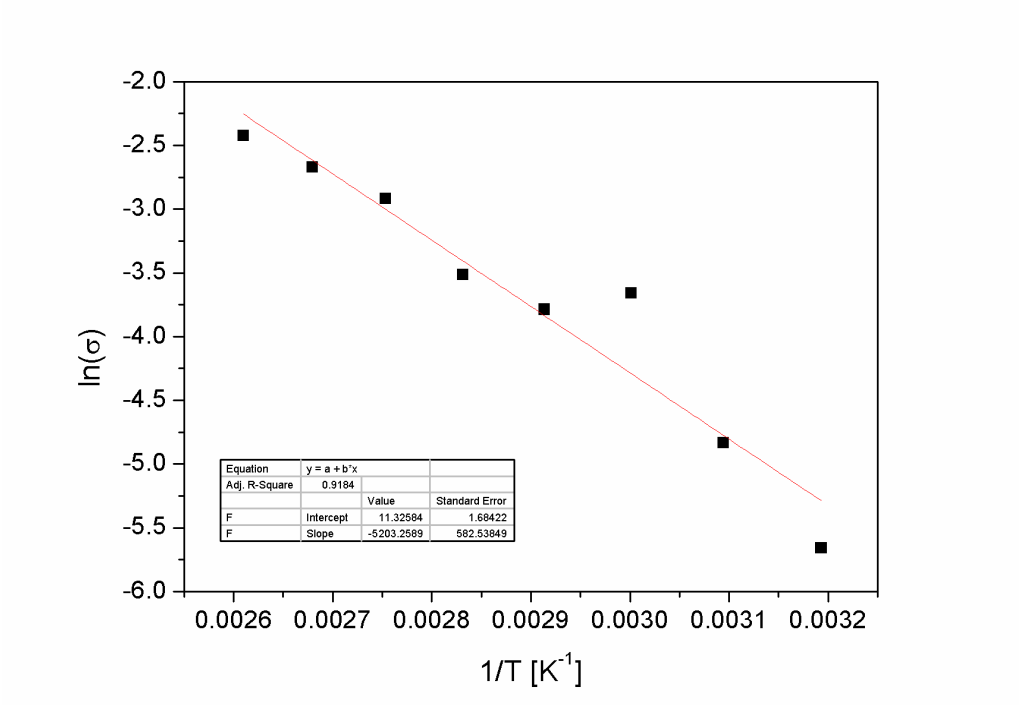



*Figure 8-88 Ionic conductivity plotted versus the inverse temperature for $[C_1C_4Im]_2[NiCl_4]$ from Impedance Spectroscopy. The solid line represents an Arrhenius fit.*

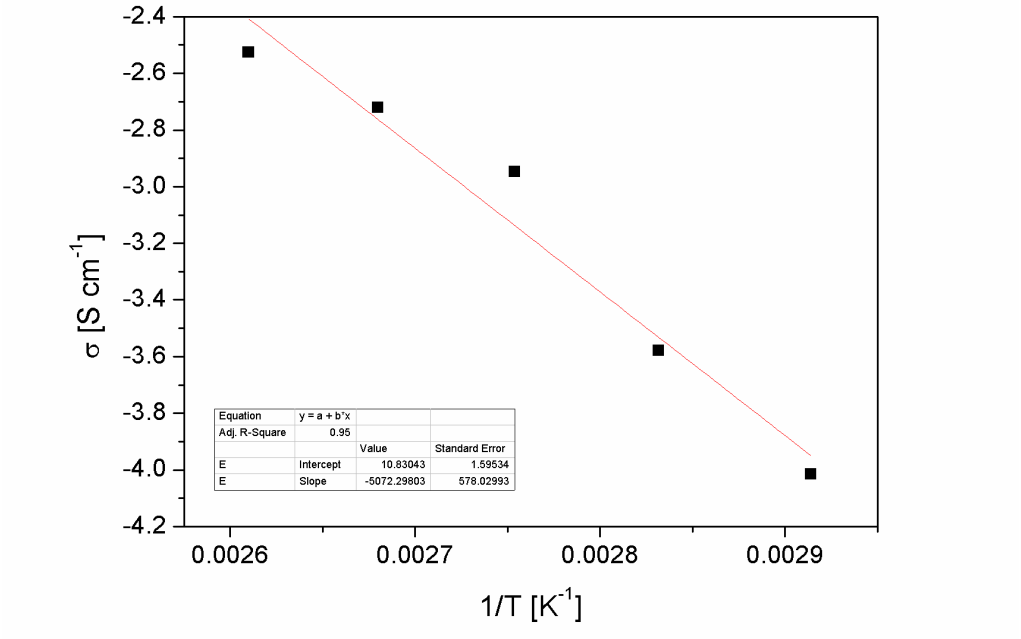



*Figure 8-89 Ionic conductivity plotted versus the inverse temperature for $[C_1C_4Im]_2[CoCl_4]$ from Impedance Spectroscopy. The solid line represents an Arrhenius fit.*

## 8.6 Impedance spectroscopy

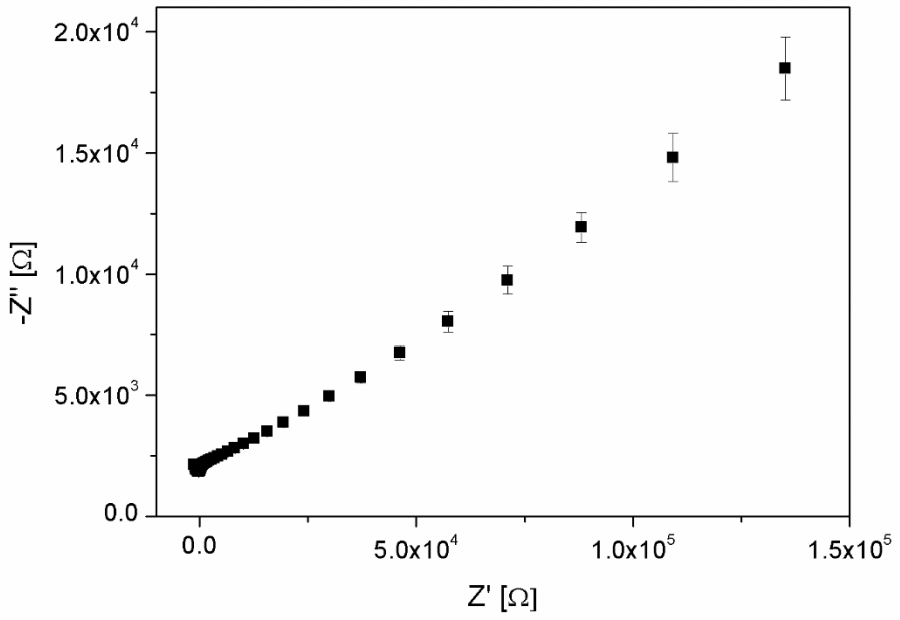



*Figure 8-90 Impedance spectroscopy of $[C_1C_4Im][InCl_4]$ at 24°C. Average of three measurements shown and standard deviation.*

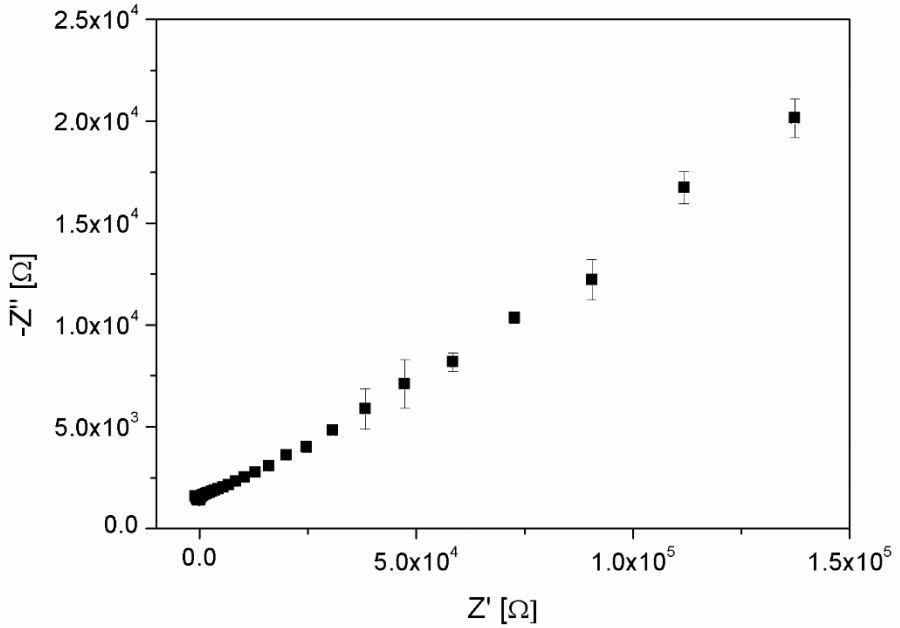



*Figure 8-91 Impedance spectroscopy of $[C_1C_4Im][InCl_4]$ at 30°C. Average of three measurements shown and standard deviation.*

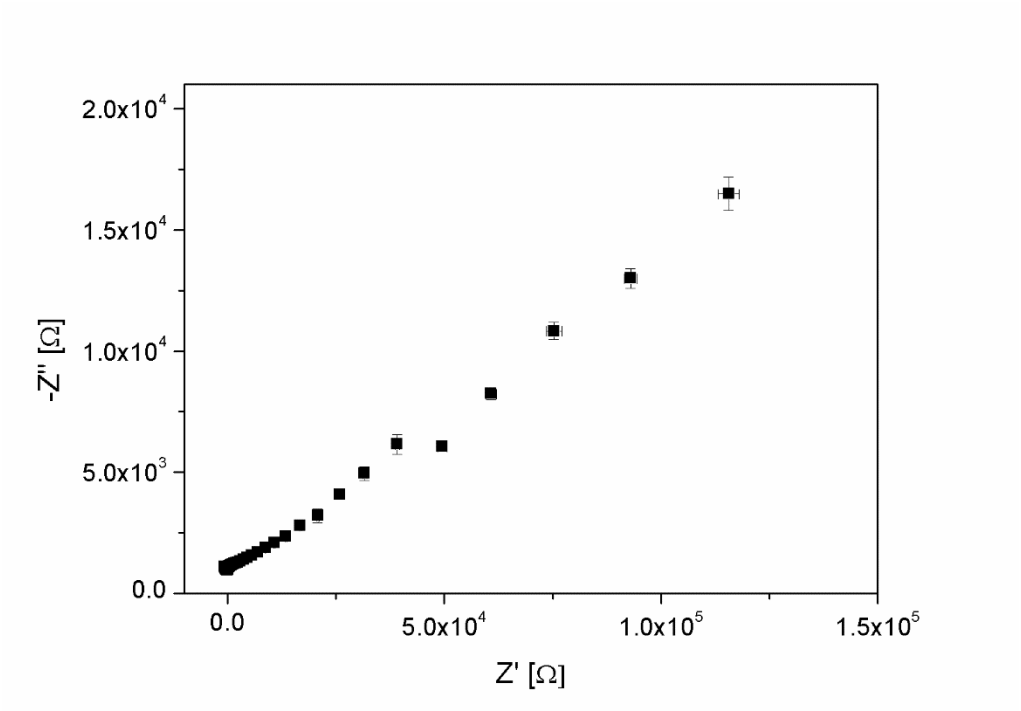



*Figure 8-92 Impedance spectroscopy of $[C_1C_4Im][InCl_4]$ at 40°C. Average of three measurements shown and standard deviation.*

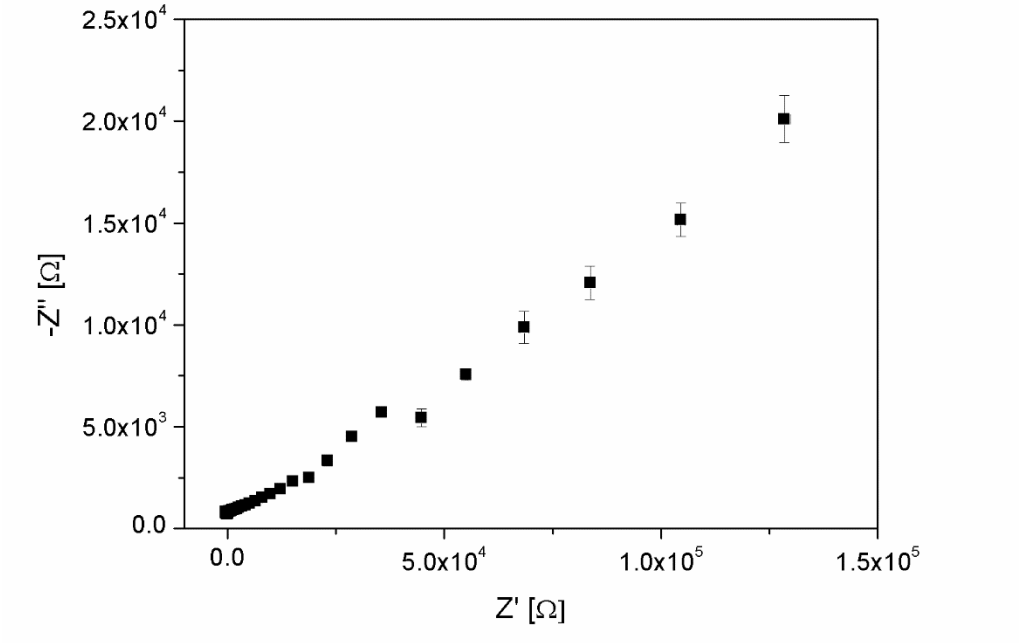



*Figure 8-93 Impedance spectroscopy of $[C_1C_4Im][InCl_4]$ at 50°C. Average of three measurements shown and standard deviation.*

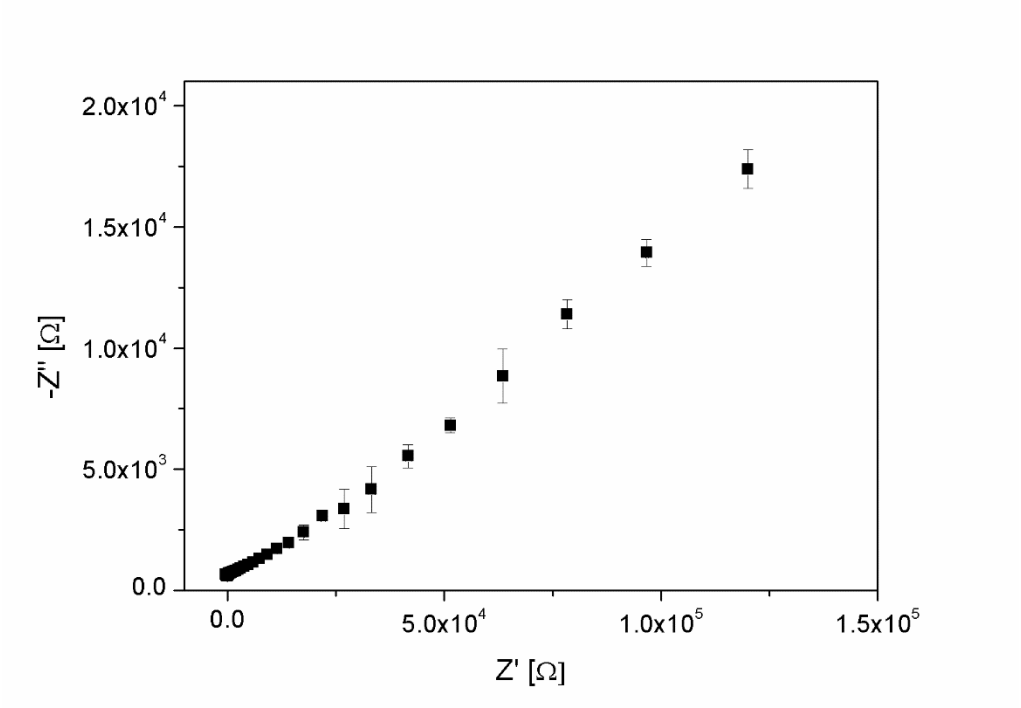



*Figure 8-94 Impedance spectroscopy of $[C_1C_4Im][InCl_4]$ at 60°C. Average of three measurements shown and standard deviation.*

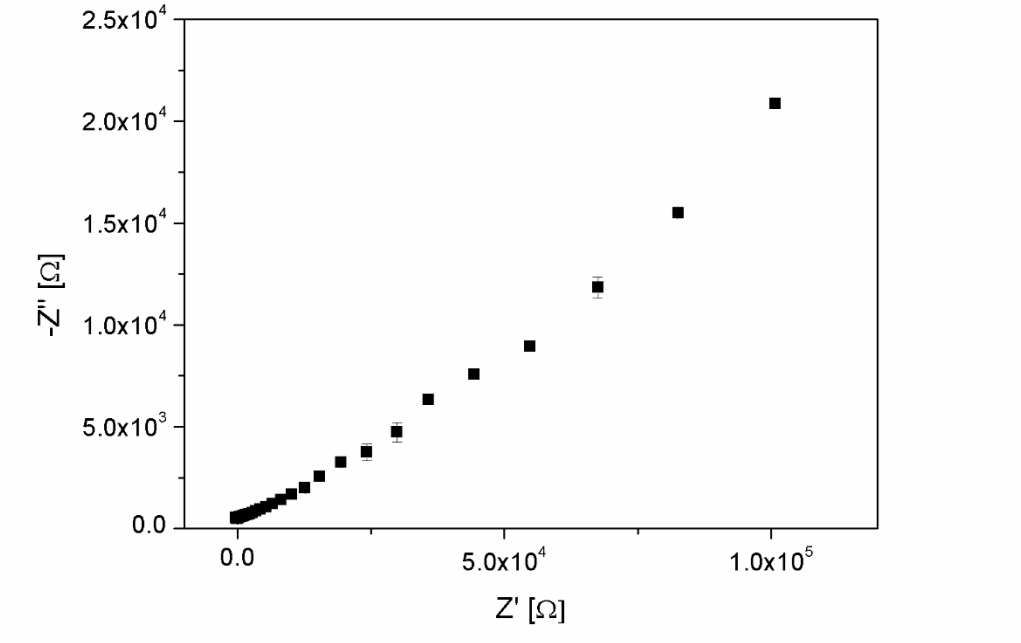



*Figure 8-95 Impedance spectroscopy of $[C_1C_4Im][InCl_4]$ at 70°C. Average of three measurements shown and standard deviation.*

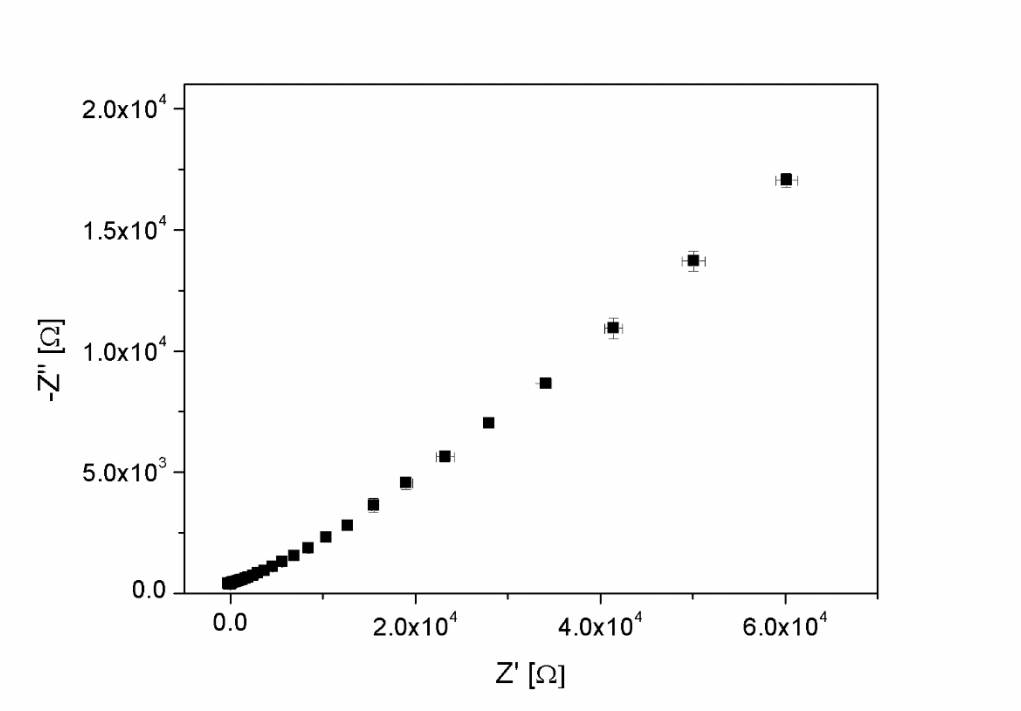



*Figure 8-96 Impedance spectroscopy of $[C_1C_4Im][InCl_4]$ at 80°C. Average of three measurements shown and standard deviation.*

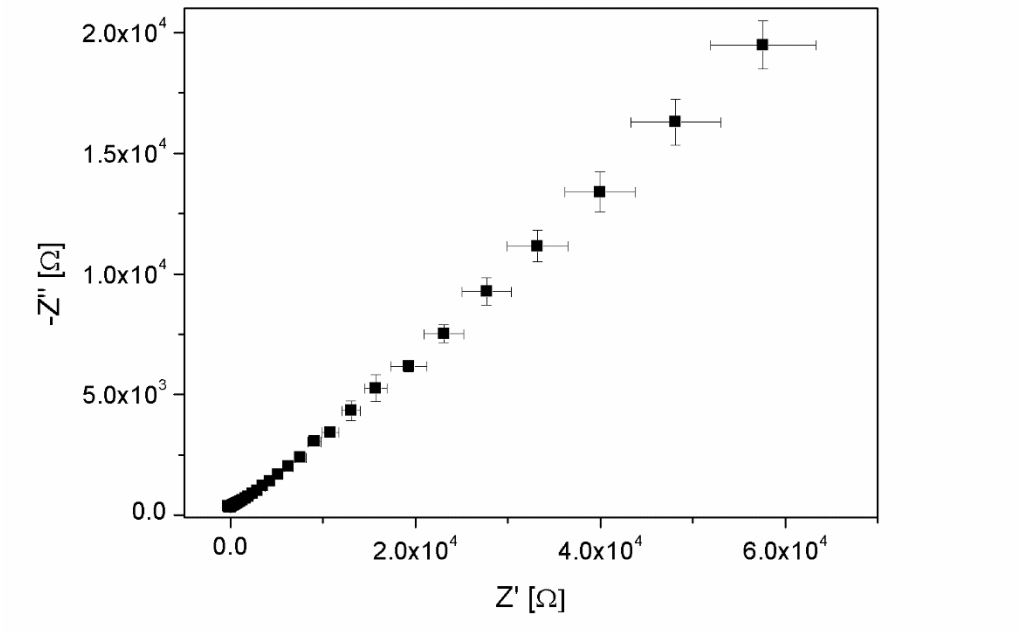



*Figure 8-97 Impedance spectroscopy of $[C_1C_4Im][InCl_4]$ at 90°C. Average of three measurements shown and standard deviation.*

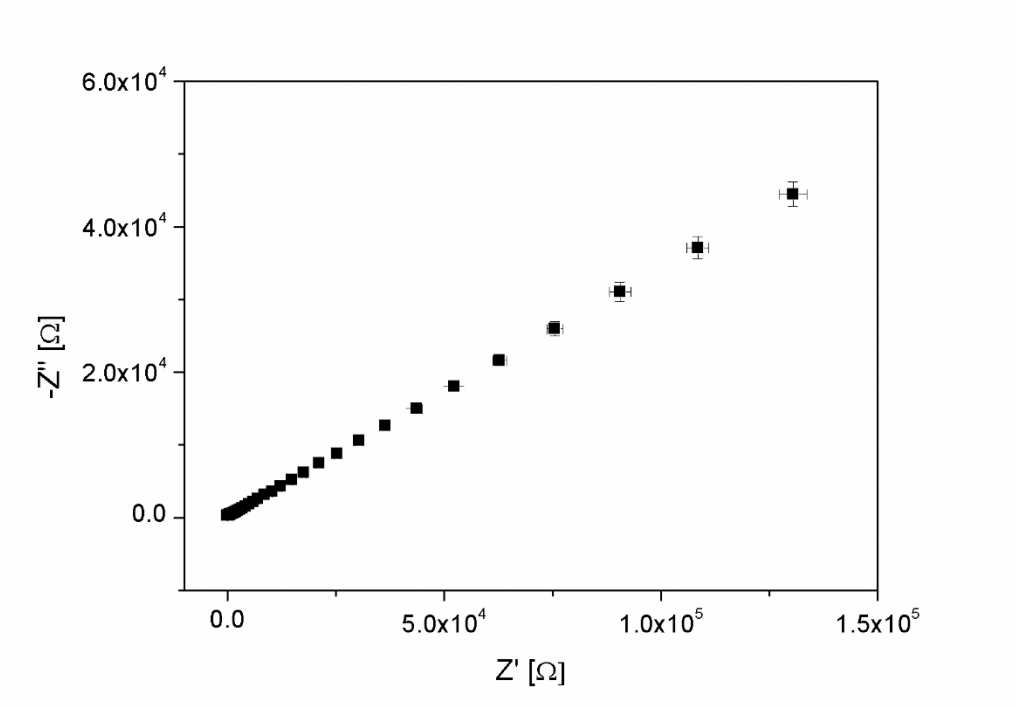



*Figure 8-98 Impedance spectroscopy of $[C_1C_4Im][InCl_4]$ at 100°C. Average of three measurements shown and standard deviation.*

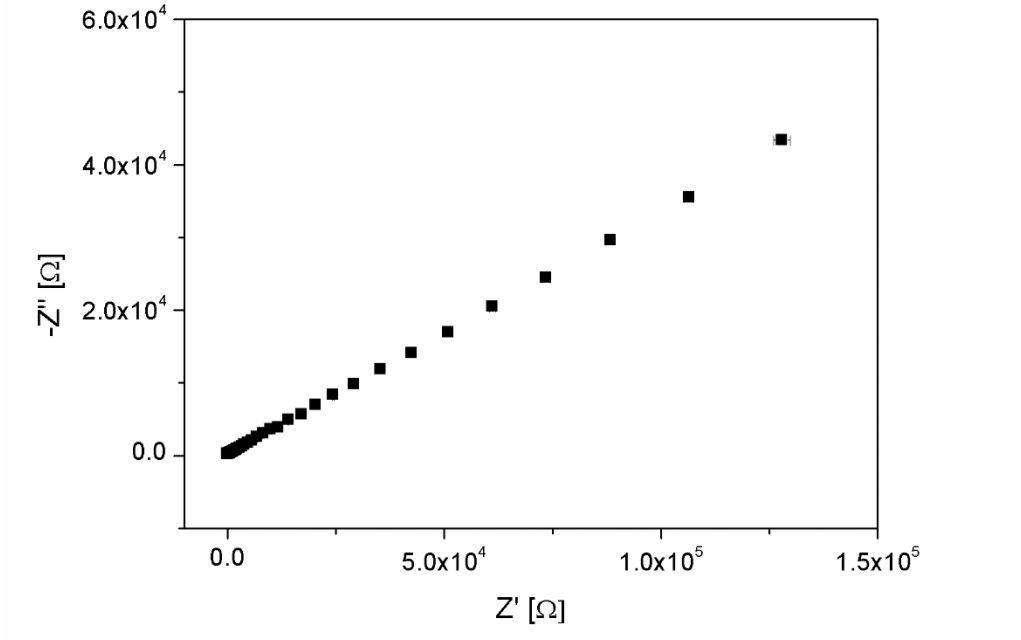



*Figure 8-99 Impedance spectroscopy of $[C_1C_4Im][InCl_4]$ at 110°C. Average of three measurements shown and standard deviation.*

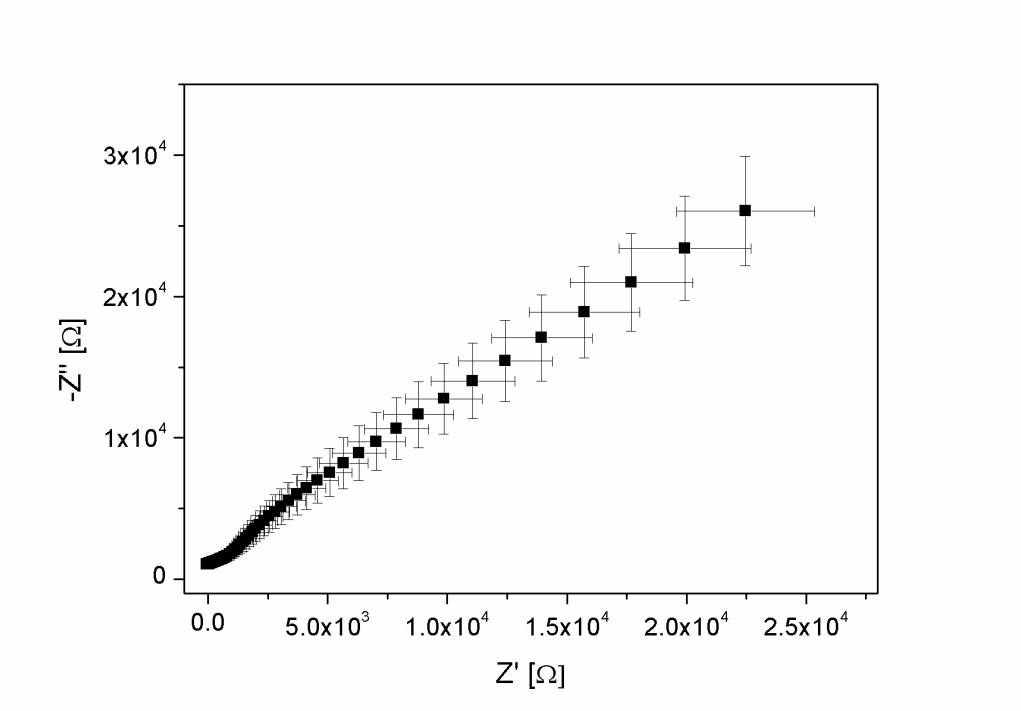



*Figure 8-100 Impedance spectroscopy of [$C_1C_4$Im][$FeCl_4$] at 23°C. Average of three measurements shown and standard deviation.*

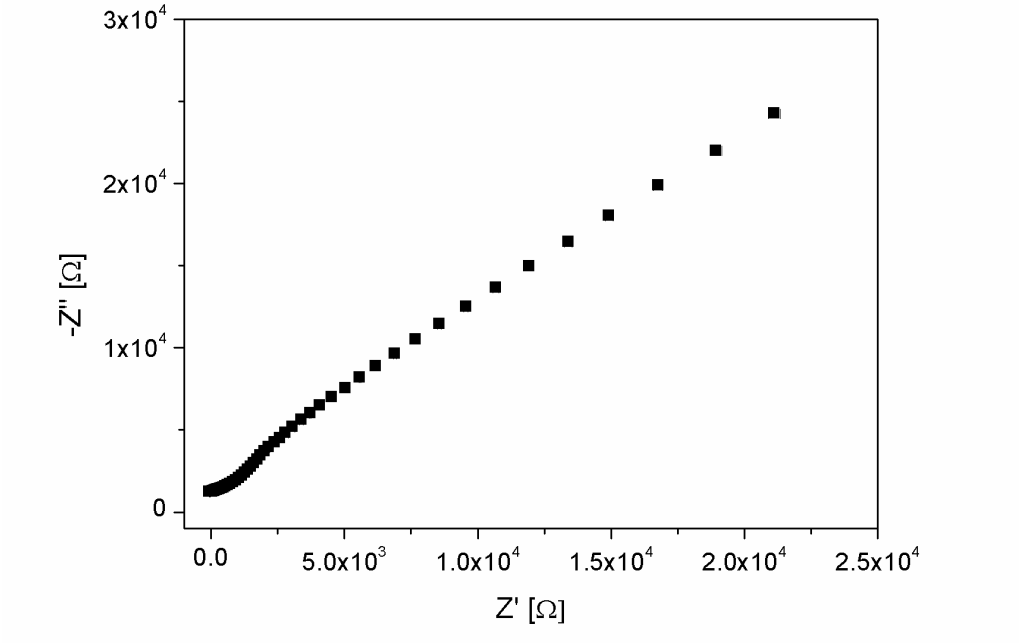



*Figure 8-101 Impedance spectroscopy of [$C_1C_4$Im][$FeCl_4$] at 30°C. Average of three measurements shown and standard deviation.*

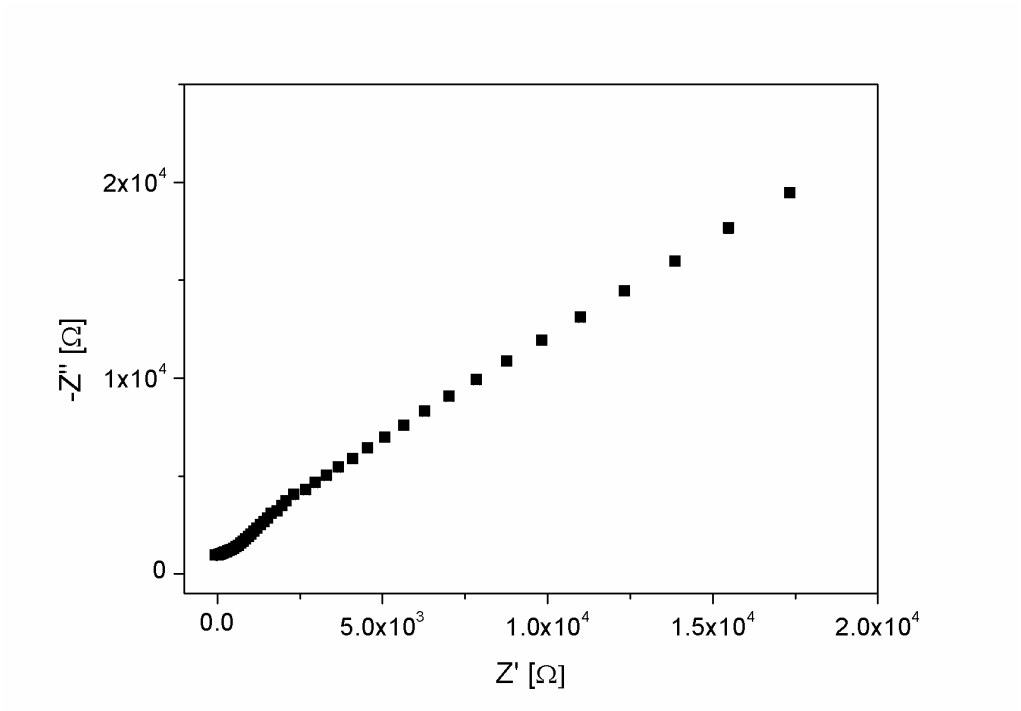



*Figure 8-102 Impedance spectroscopy of [$C_1C_4$Im][$FeCl_4$] at 40°C. Average of three measurements shown and standard deviation.*

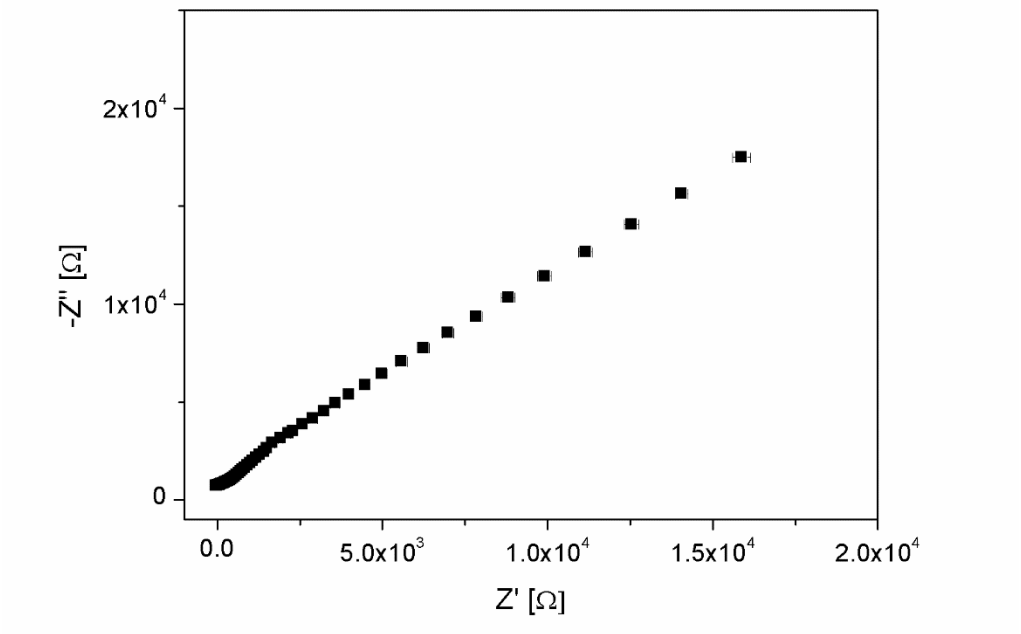



*Figure 8-103 Impedance spectroscopy of [$C_1C_4$Im][$FeCl_4$] at 50°C. Average of three measurements shown and standard deviation.*

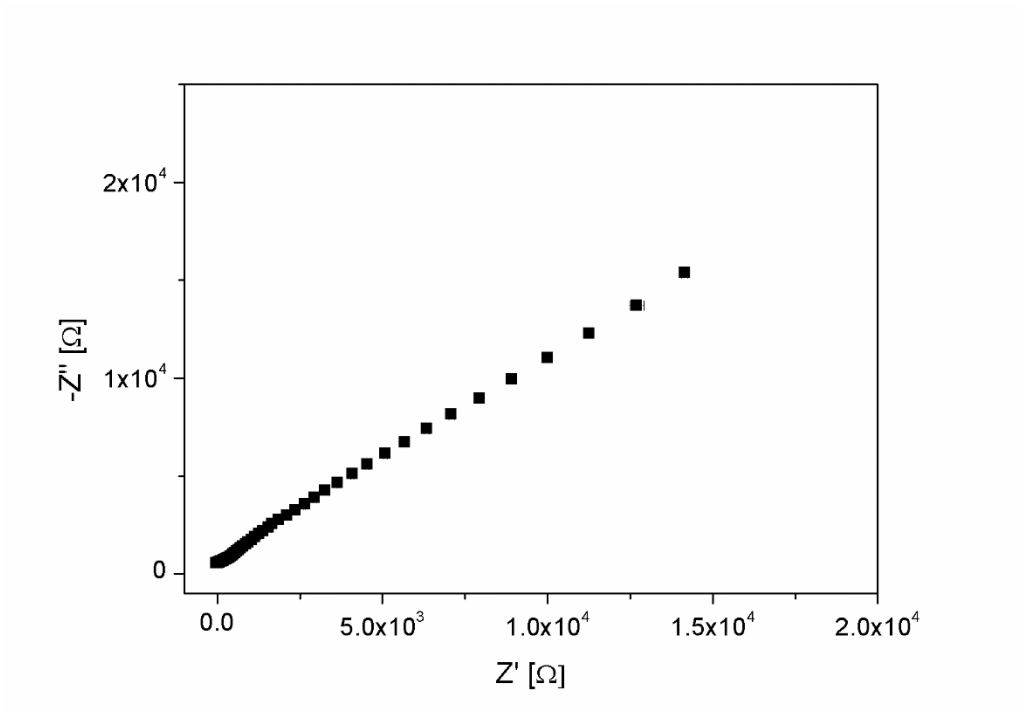



*Figure 8-104 Impedance spectroscopy of [$C_1C_4$Im][$FeCl_4$] at 60°C. Average of three measurements shown and standard deviation.*

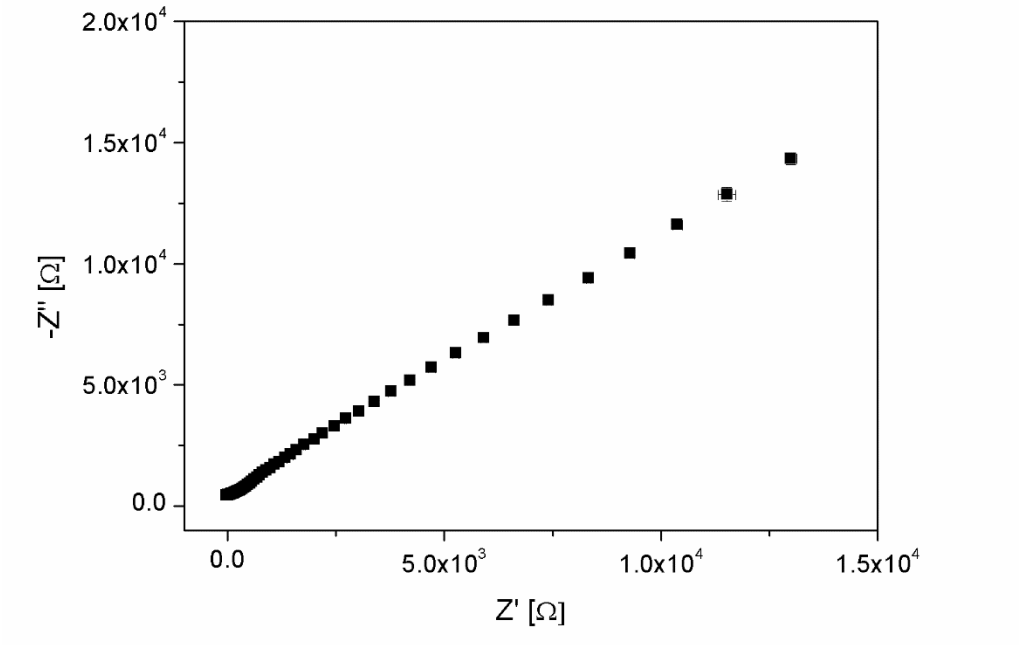



*Figure 8-105 Impedance spectroscopy of [$C_1C_4$Im][$FeCl_4$] at 70°C. Average of three measurements shown and standard deviation.*

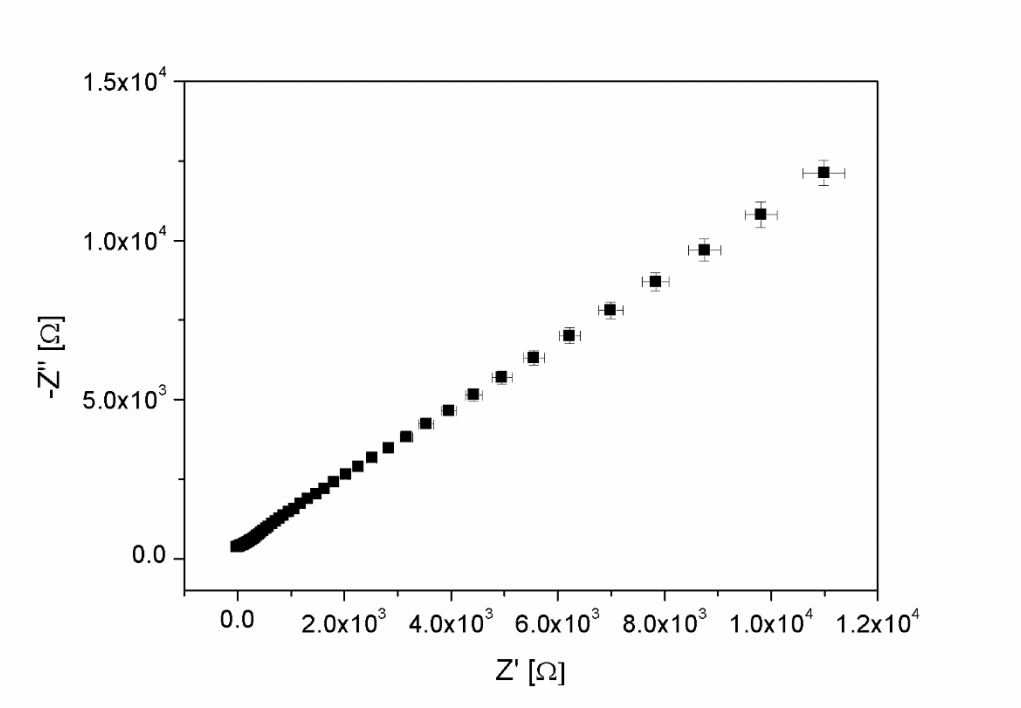



*Figure 8-106 Impedance spectroscopy of [$C_1C_4$Im][$FeCl_4$] at 80°C. Average of three measurements shown and standard deviation.*

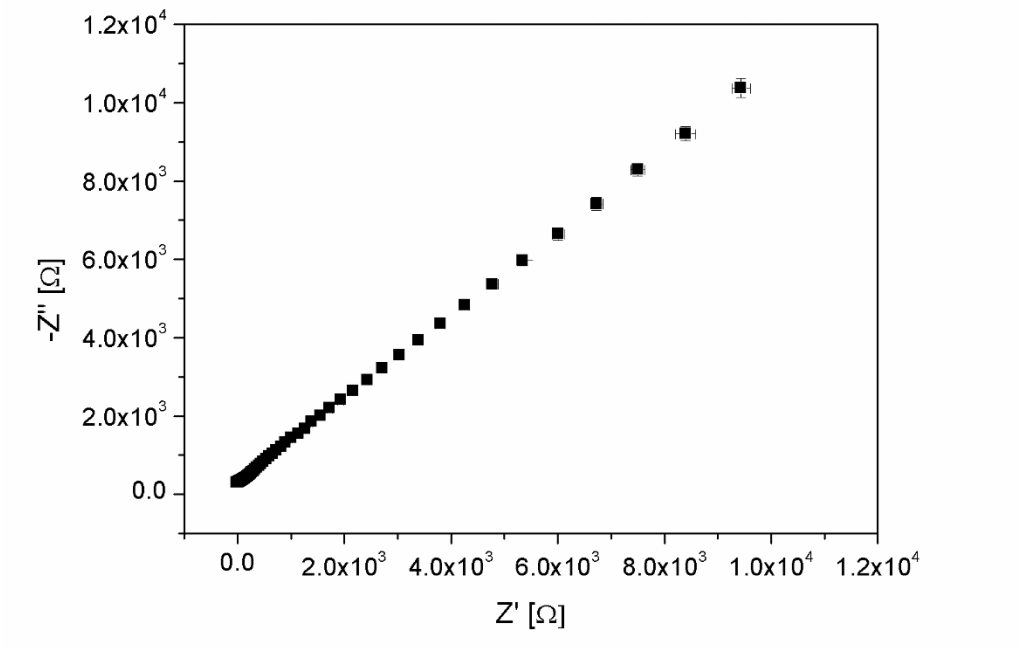



*Figure 8-107 Impedance spectroscopy of [$C_1C_4$Im][$FeCl_4$] at 90°C. Average of three measurements shown and standard deviation.*

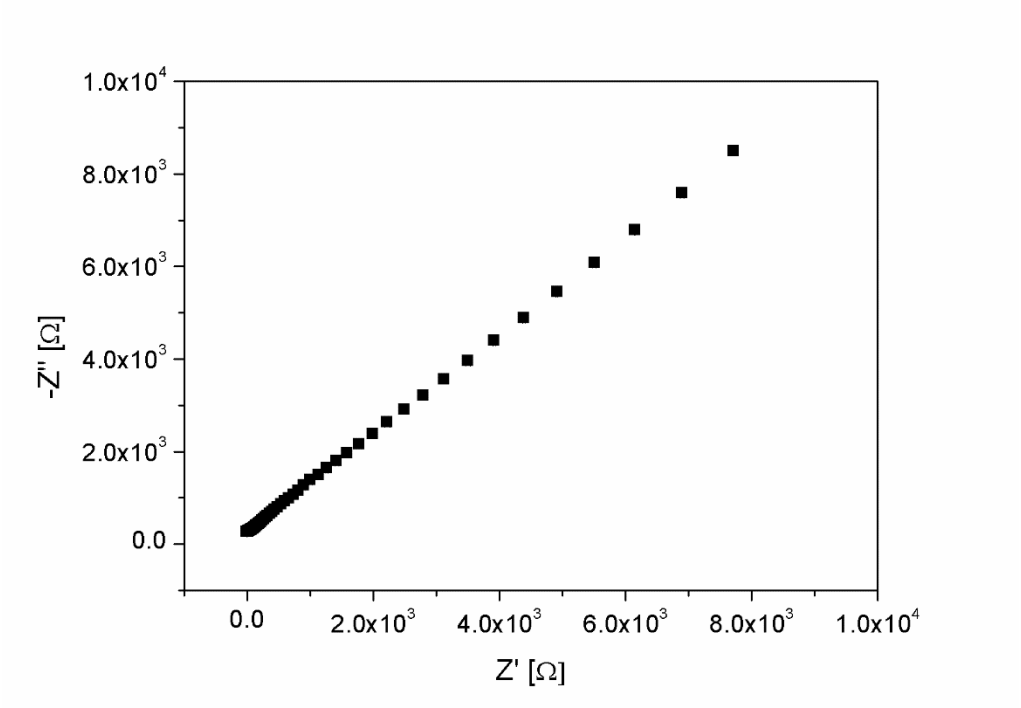



*Figure 8-108 Impedance spectroscopy of $[C_1C_4Im][FeCl_4]$ at 100°C. Average of three measurements shown and standard deviation.*

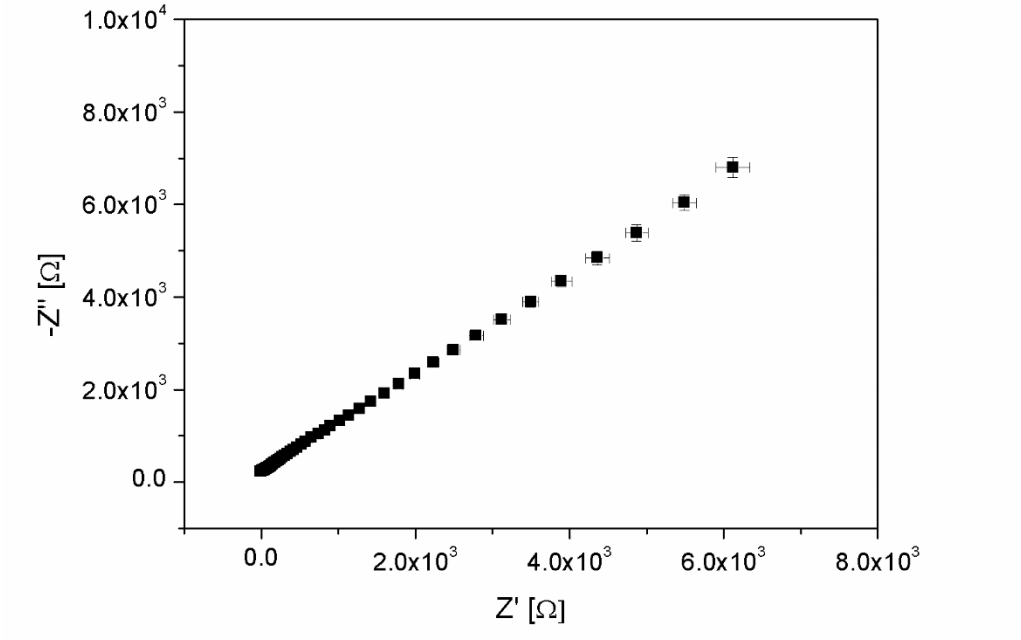



*Figure 8-109 Impedance spectroscopy of $[C_1C_4Im][FeCl_4]$ at 110°C. Average of three measurements shown and standard deviation.*

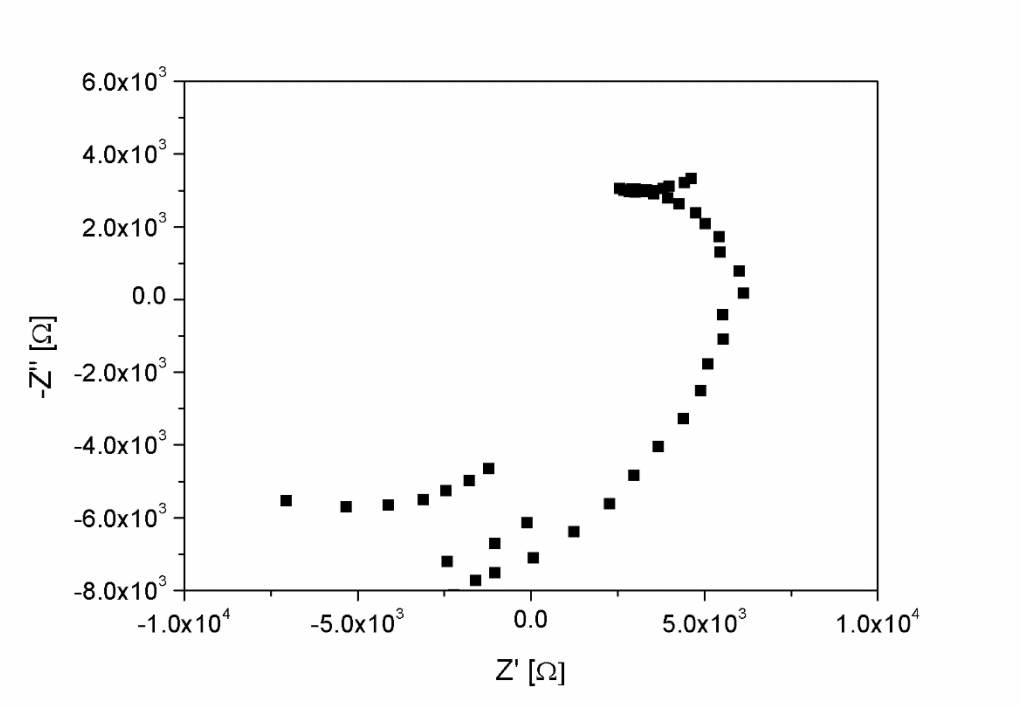



*Figure 8-110 Impedance spectroscopy of $[C_1C_4Im]_2[CuCl_4]$ at 22°C. Average of three measurements shown and standard deviation.*

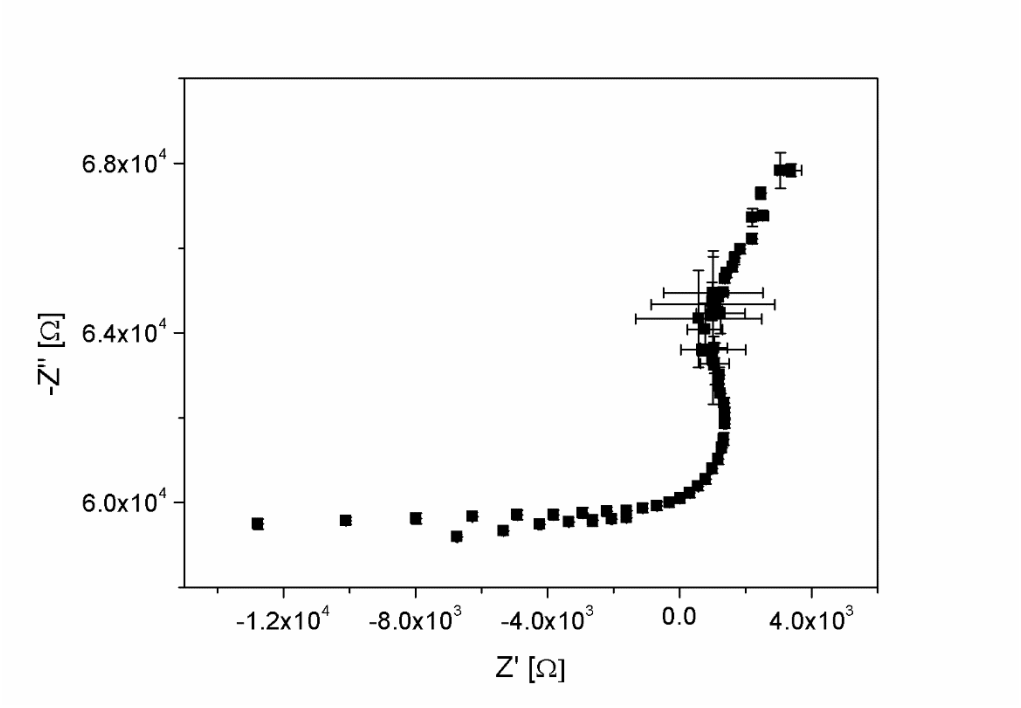



*Figure 8-111 Impedance spectroscopy of $[C_1C_4Im]_2[CuCl_4]$ at 30°C. Average of three measurements shown and standard deviation.*

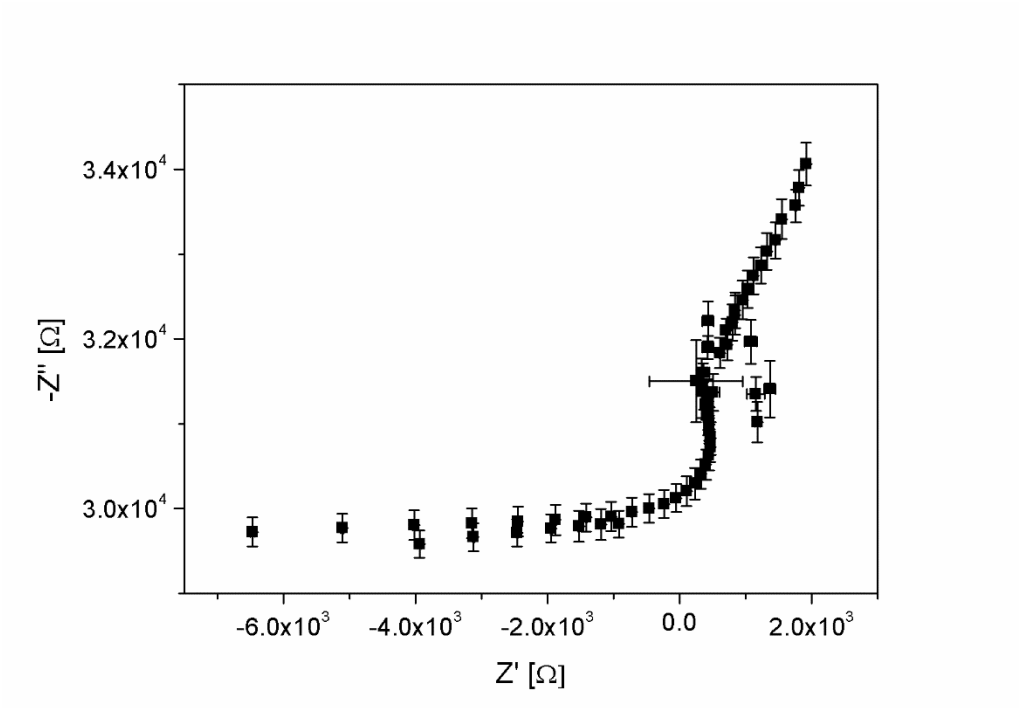



*Figure 8-112 Impedance spectroscopy of $[C_1C_4Im]_2[CuCl_4]$ at 40°C. Average of three measurements shown and standard deviation.*

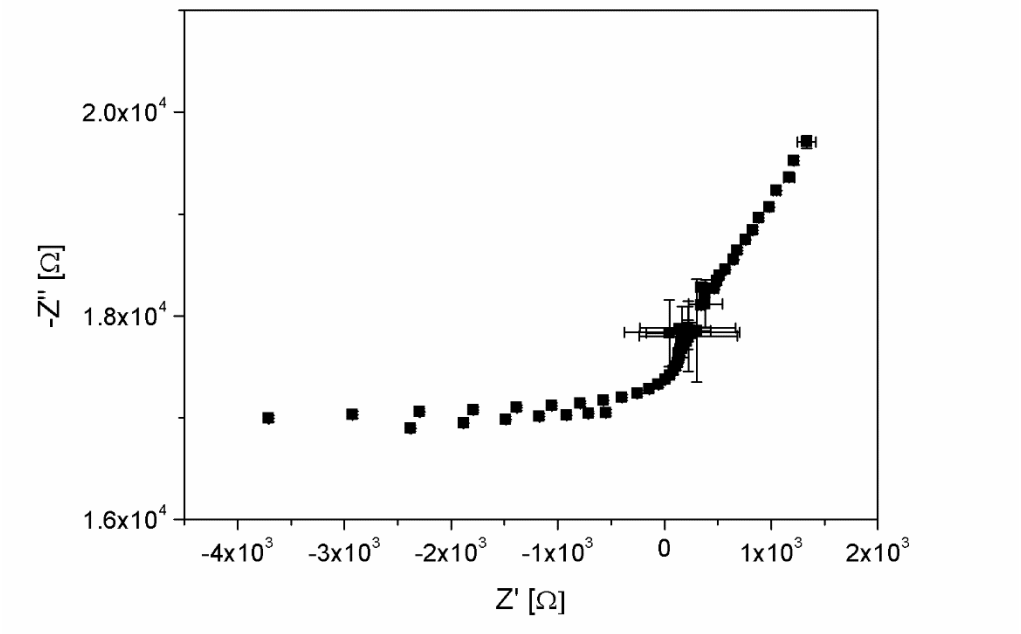



*Figure 8-113 Impedance spectroscopy of $[C_1C_4Im]_2[CuCl_4]$ at 50°C. Average of three measurements shown and standard deviation.*

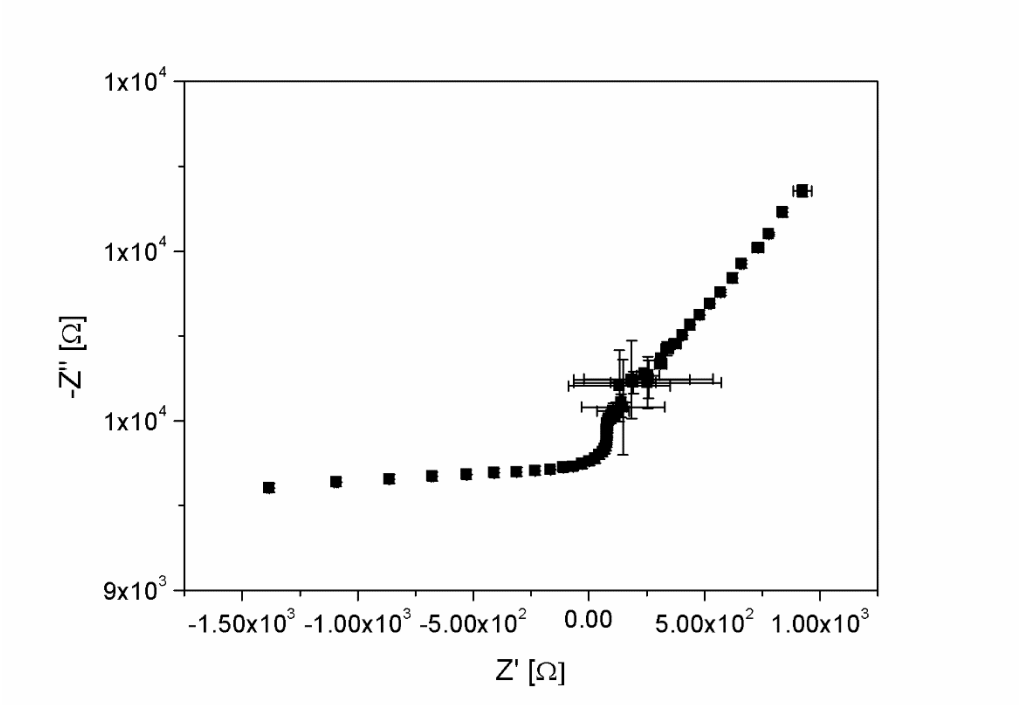



*Figure 8-114 Impedance spectroscopy of $[C_1C_4Im]_2[CuCl_4]$ at 60°C. Average of three measurements shown and standard deviation.*

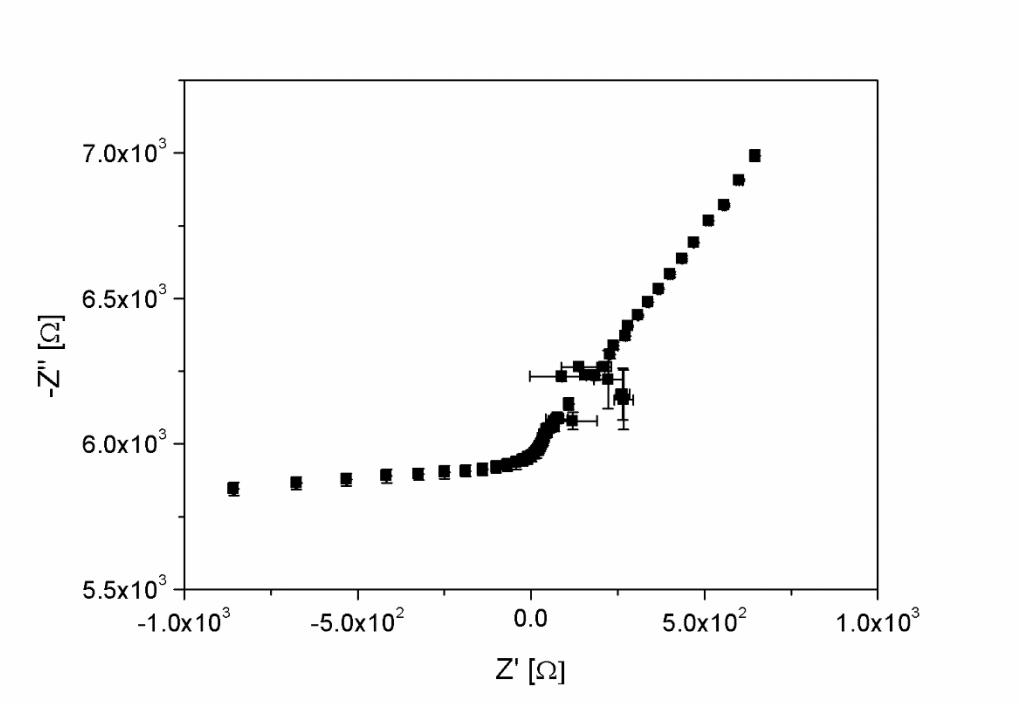



*Figure 8-115 Impedance spectroscopy of $[C_1C_4Im]_2[CuCl_4]$ at 70°C. Average of three measurements shown and standard deviation.*

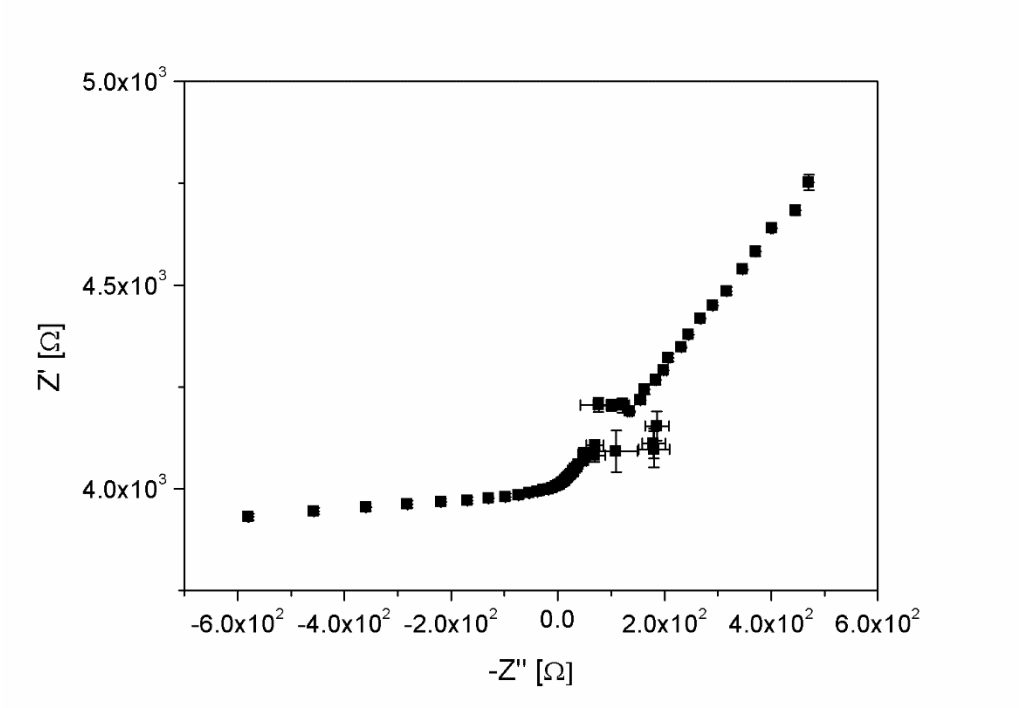



*Figure 8-116 Impedance spectroscopy of $[C_1C_4Im]_2[CuCl_4]$ at 80°C. Average of three measurements shown and standard deviation.*

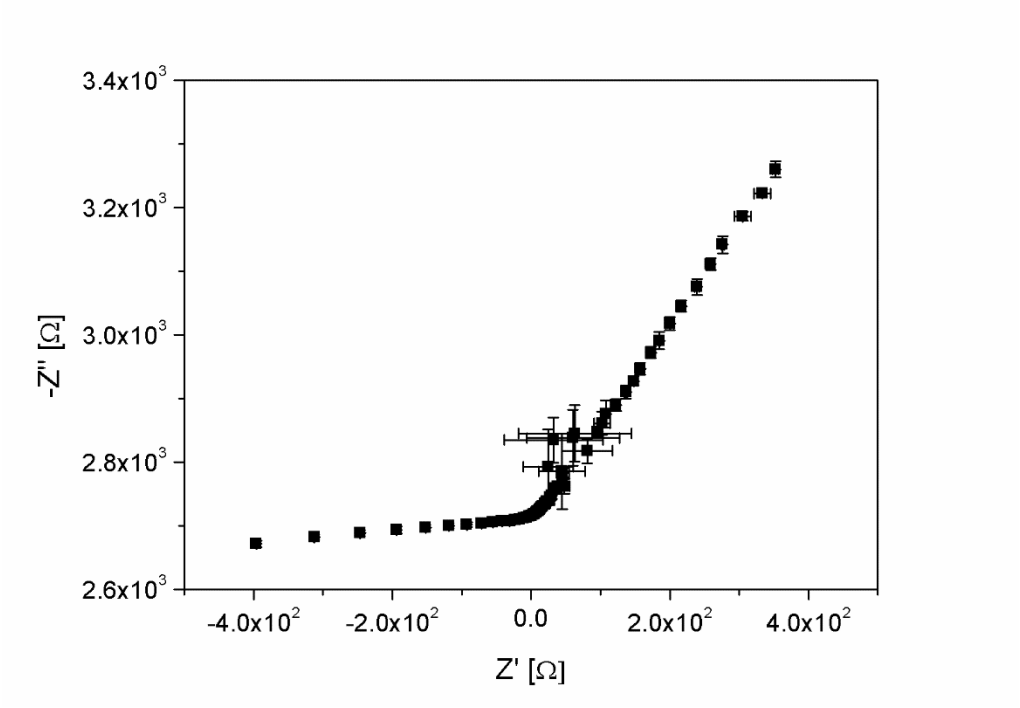



*Figure 8-117 Impedance spectroscopy of $[C_1C_4Im]_2[CuCl_4]$ at 90°C. Average of three measurements shown and standard deviation.*

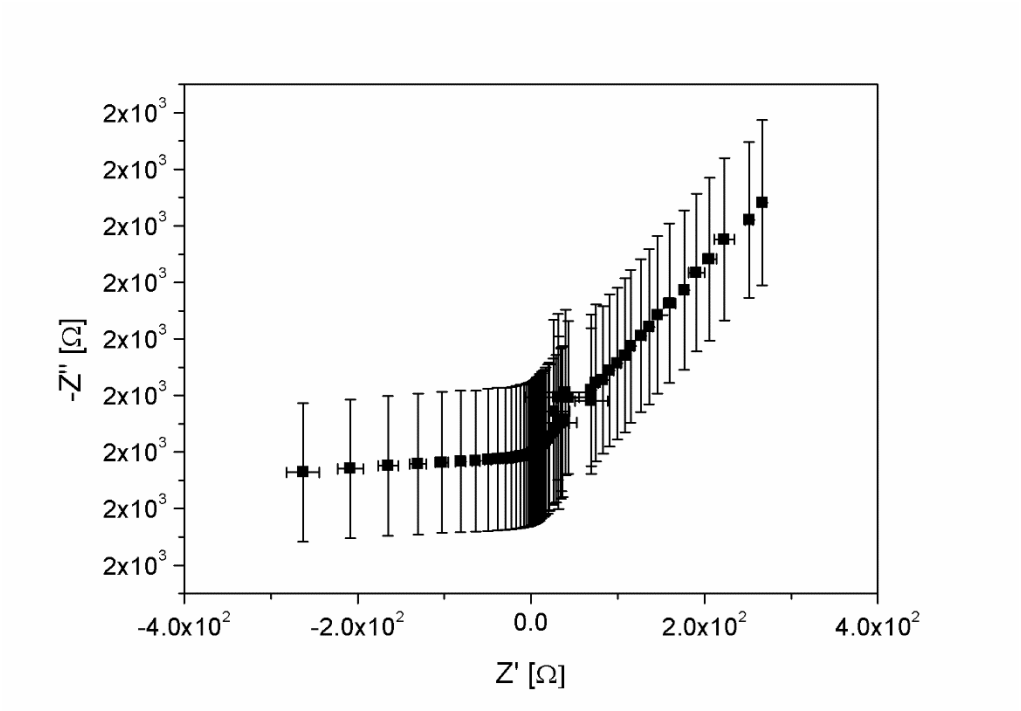



*Figure 8-118 Impedance spectroscopy of $[C_1C_4Im]_2[CuCl_4]$ at 100°C. Average of three measurements shown and standard deviation.*

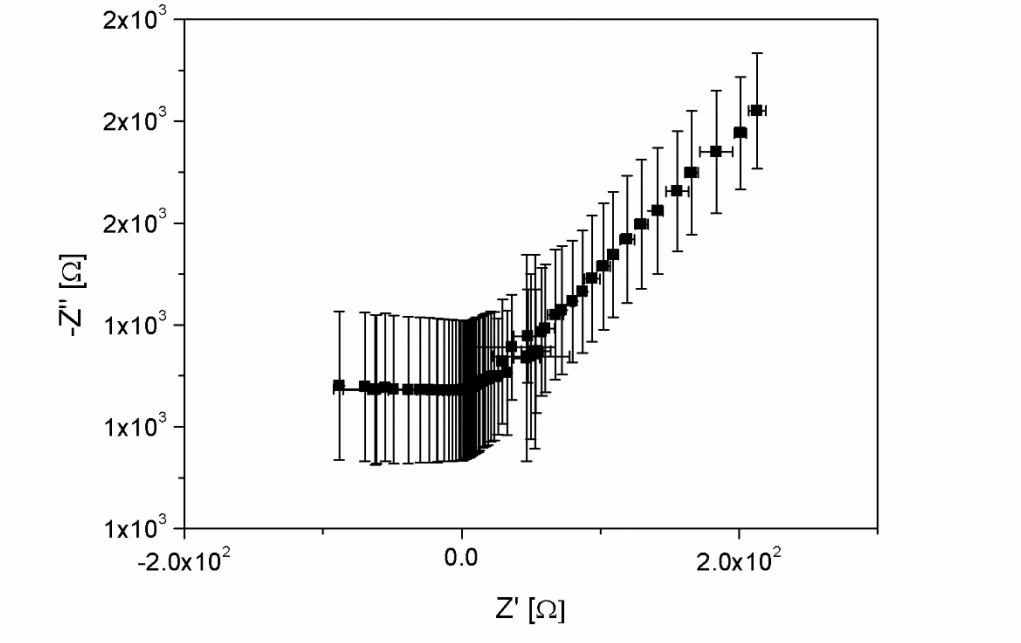



*Figure 8-119 Impedance spectroscopy of $[C_1C_4Im]_2[CuCl_4]$ at 110°C. Average of three measurements shown and standard deviation.*

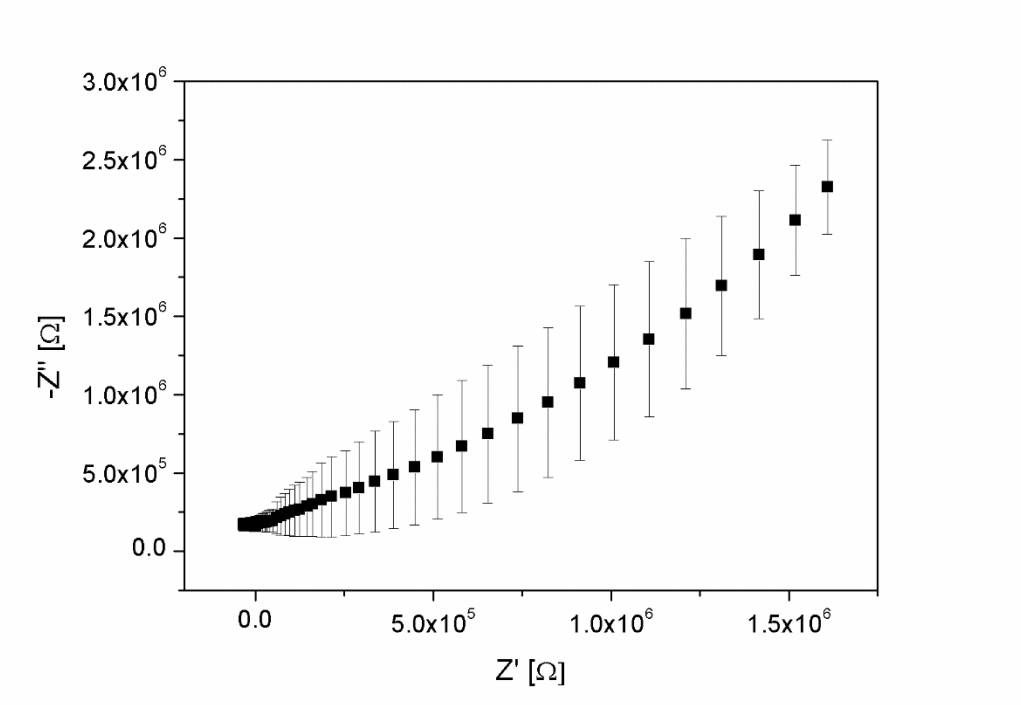



*Figure 8-120 Impedance spectroscopy of $[C_1C_4Im]_2[ZnCl_4]$ at 30°C. Average of three measurements shown and standard deviation.*

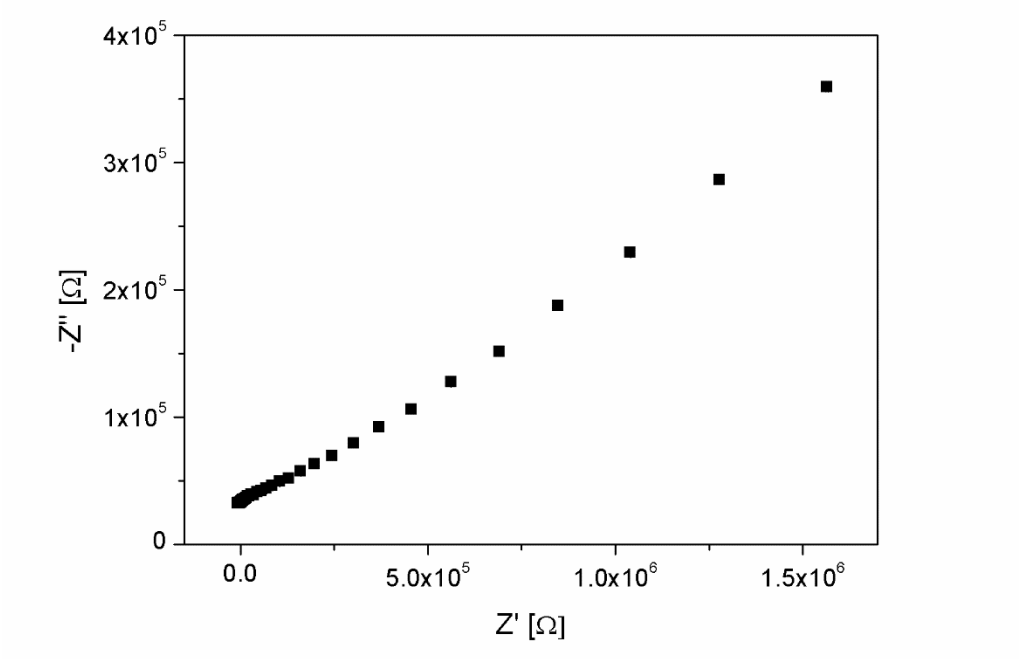



*Figure 8-121 Impedance spectroscopy of $[C_1C_4Im]_2[ZnCl_4]$ at 50°C. Average of three measurements shown and standard deviation.*

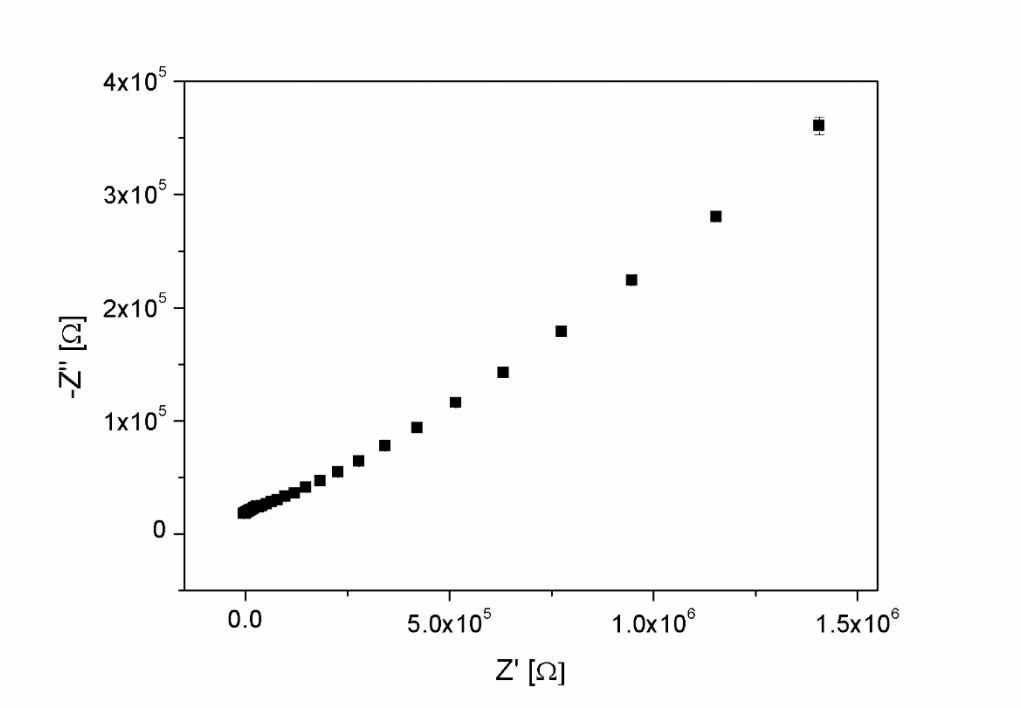



*Figure 8-122 Impedance spectroscopy of $[C_1C_4Im]_2[ZnCl_4]$ at 60°C. Average of three measurements shown and standard deviation.*

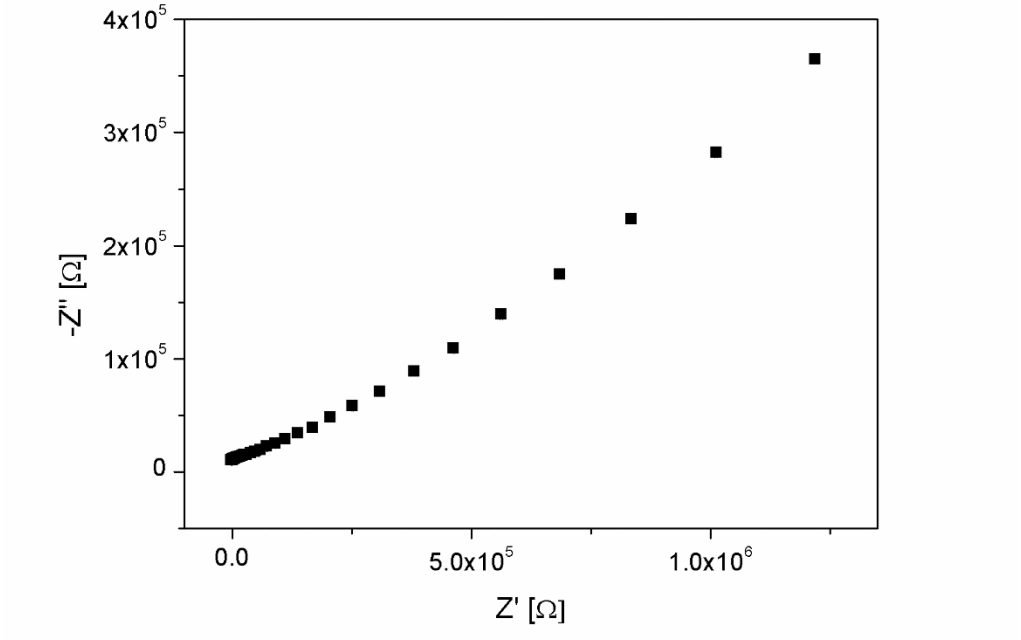



*Figure 8-123 Impedance spectroscopy of $[C_1C_4Im]_2[ZnCl_4]$ at 70°C. Average of three measurements shown and standard deviation.*

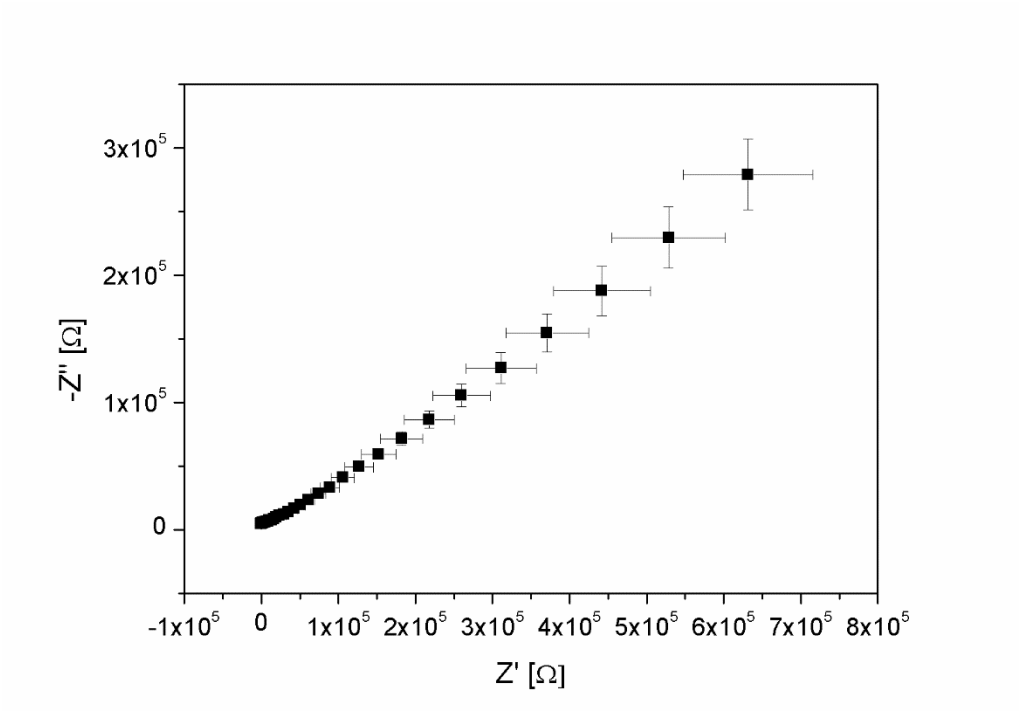



*Figure 8-124 Impedance spectroscopy of $[C_1C_4Im]_2[ZnCl_4]$ at 80°C. Average of three measurements shown and standard deviation.*

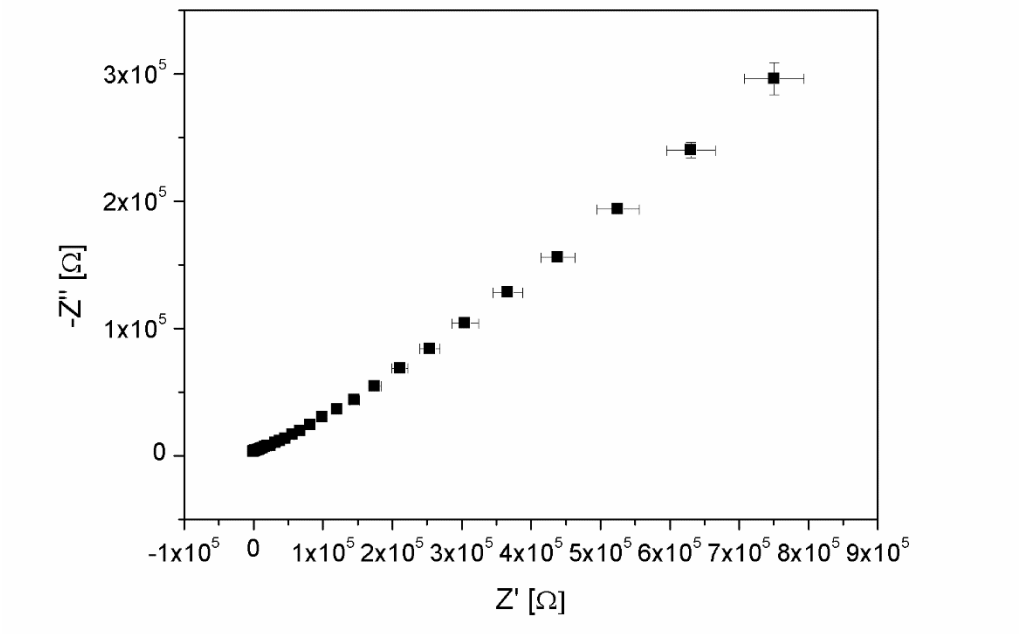



*Figure 8-125 Impedance spectroscopy of $[C_1C_4Im]_2[ZnCl_4]$ at 90°C. Average of three measurements shown and standard deviation.*

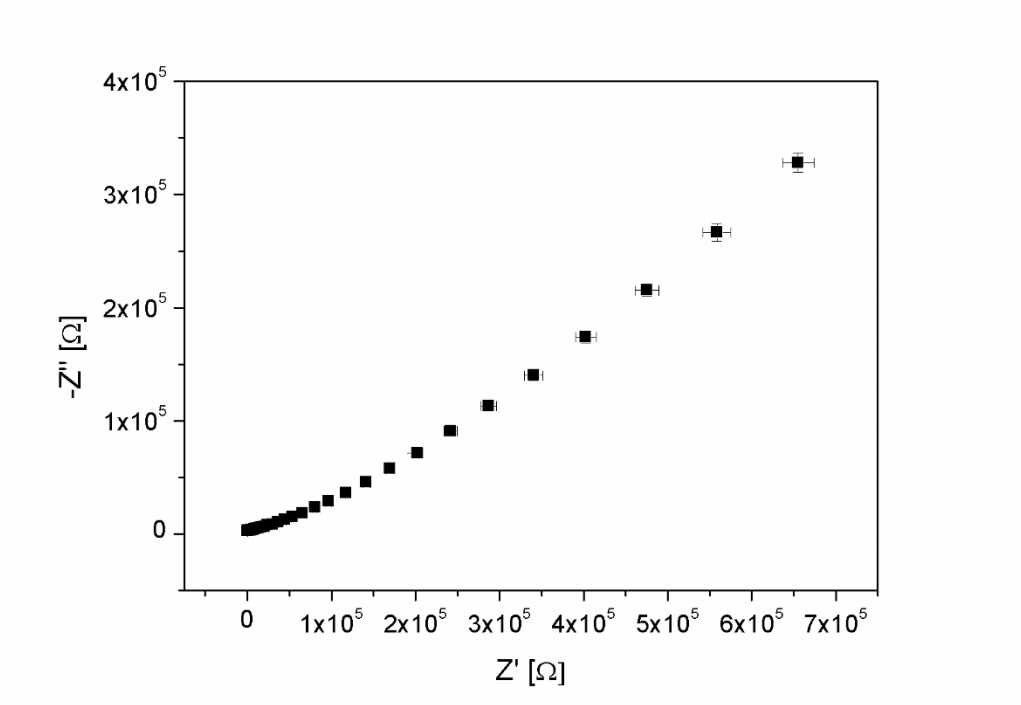



*Figure 8-126 Impedance spectroscopy of $[C_1C_4Im]_2[ZnCl_4]$ at 100°C. Average of three measurements shown and standard deviation.*

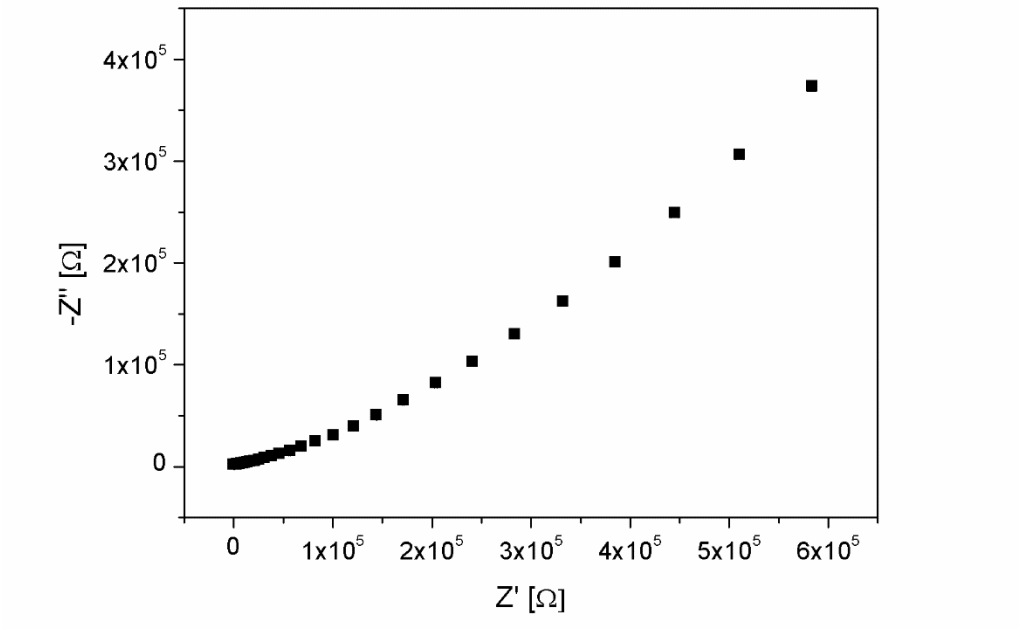



*Figure 8-127 Impedance spectroscopy of $[C_1C_4Im]_2[ZnCl_4]$ at 110°C. Average of three measurements shown and standard deviation.*

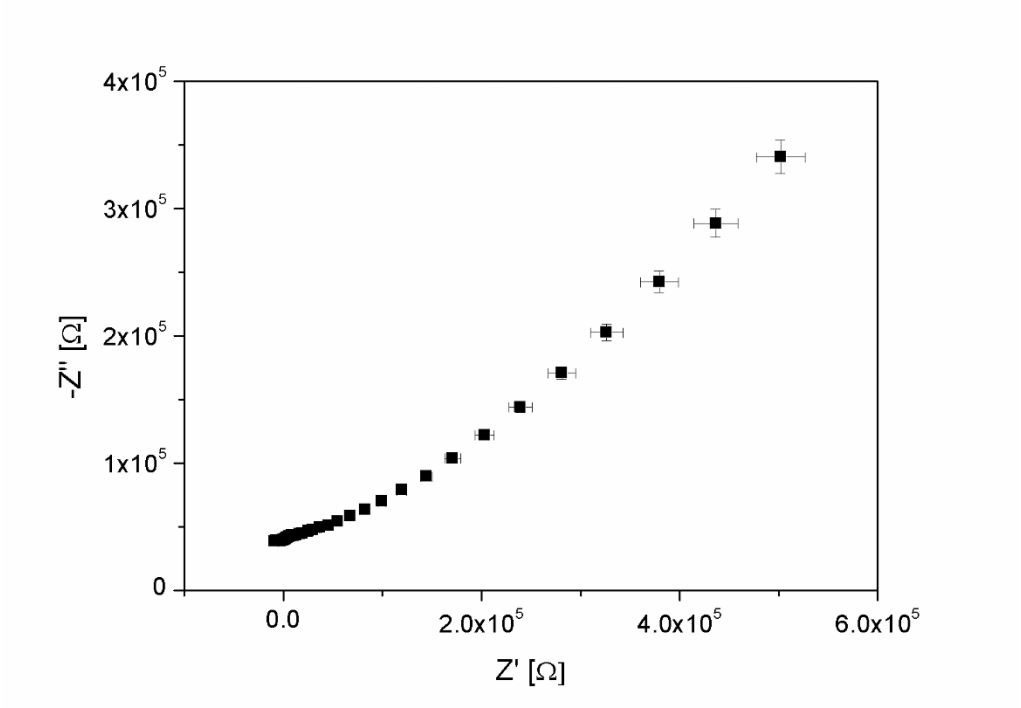



*Figure 8-128 Impedance spectroscopy of $[C_1C_4Im]_2[NiCl_4]$ at 40°C. Average of three measurements shown and standard deviation.*

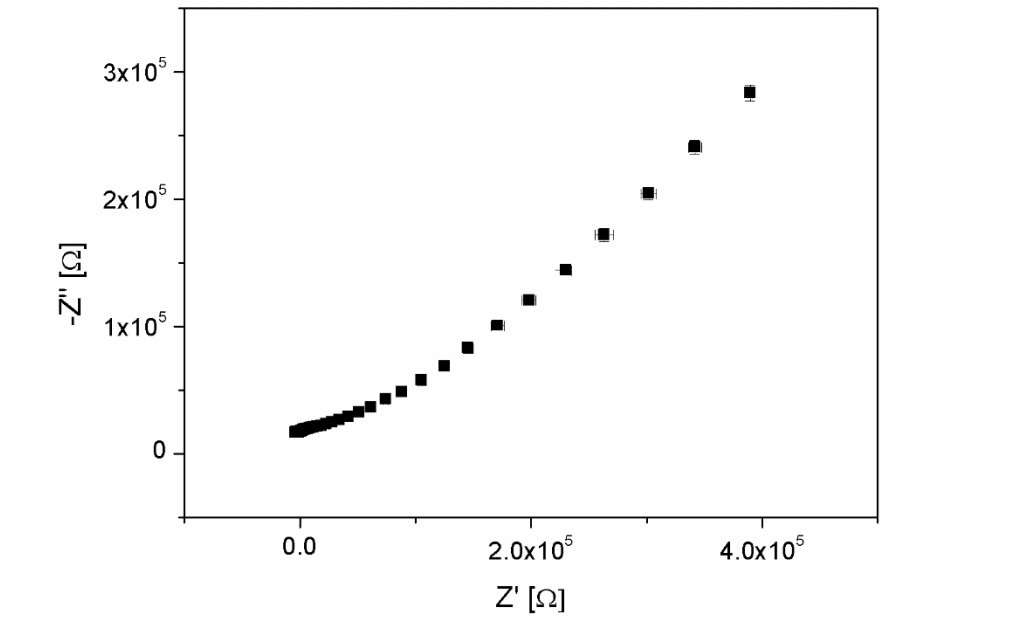



*Figure 8-129 Impedance spectroscopy of $[C_1C_4Im]_2[NiCl_4]$ at 50°C. Average of three measurements shown and standard deviation.*

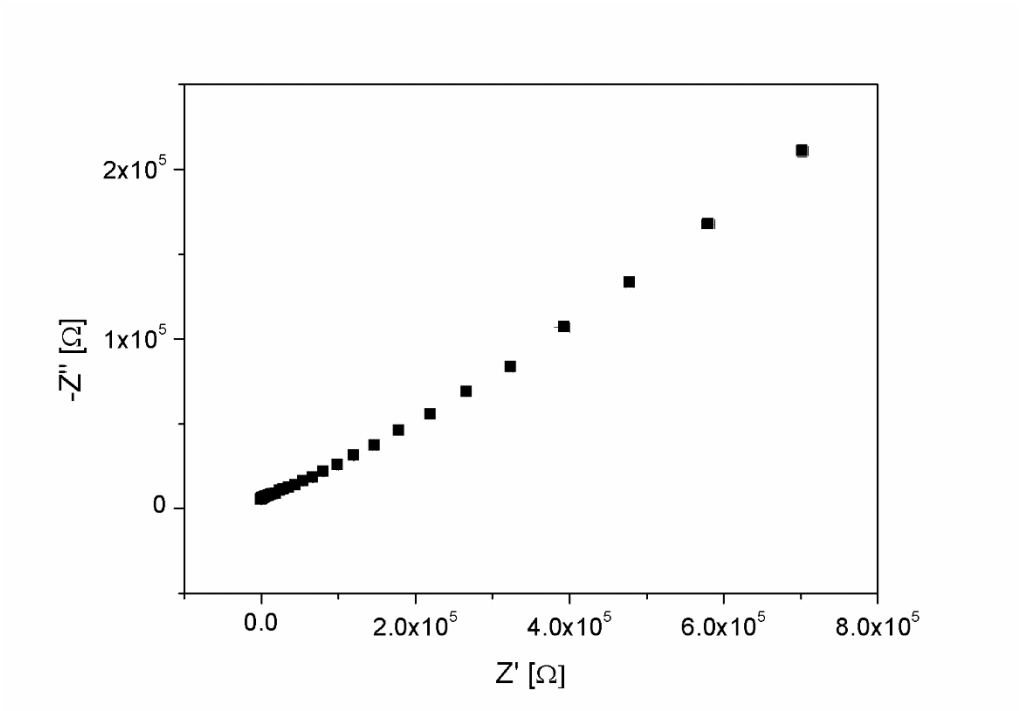



*Figure 8-130 Impedance spectroscopy of $[C_1C_4Im]_2[NiCl_4]$ at 60°C. Average of three measurements shown and standard deviation.*

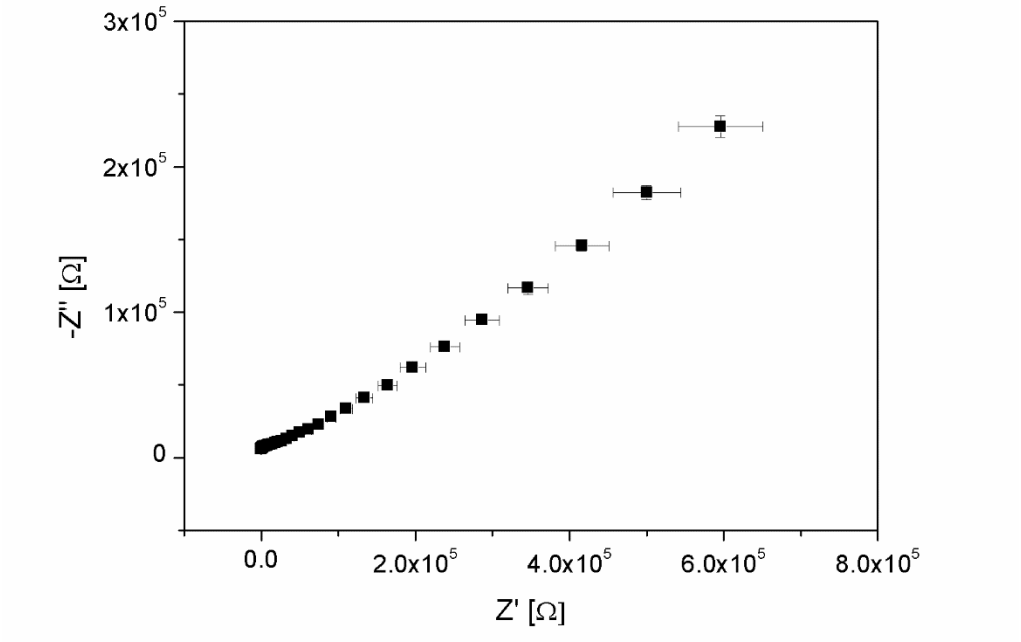



*Figure 8-131 Impedance spectroscopy of $[C_1C_4Im]_2[NiCl_4]$ at 70°C. Average of three measurements shown and standard deviation.*

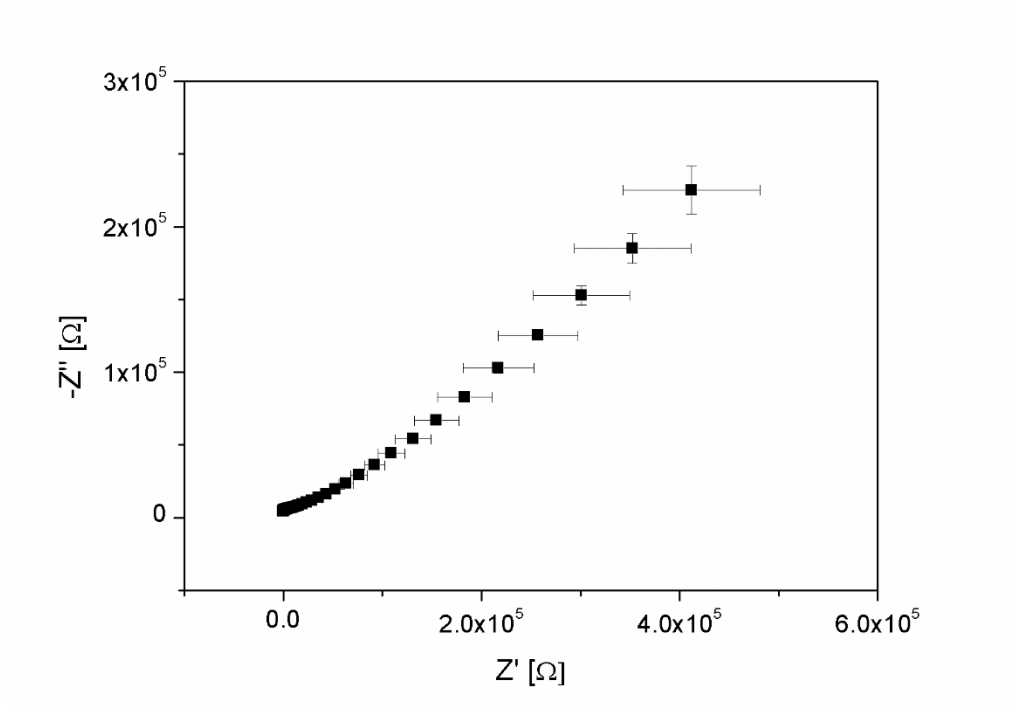



*Figure 8-132 Impedance spectroscopy of $[C_1C_4Im]_2[NiCl_4]$ at 80°C. Average of three measurements shown and standard deviation.*

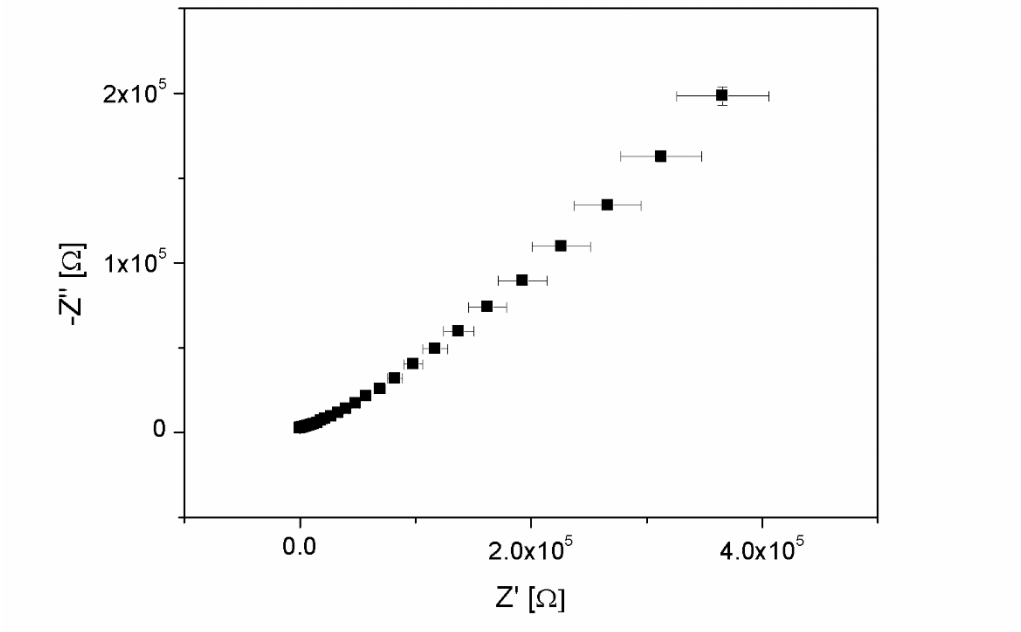



*Figure 8-133 Impedance spectroscopy of $[C_1C_4Im]_2[NiCl_4]$ at 90°C. Average of three measurements shown and standard deviation.*

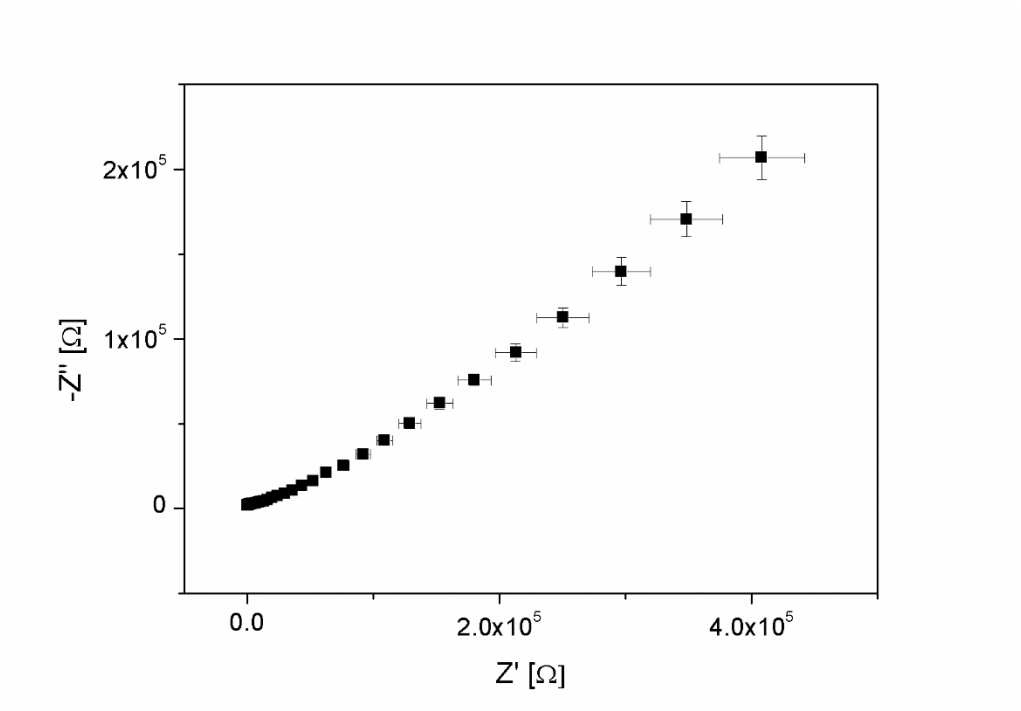



*Figure 8-134 Impedance spectroscopy of $[C_1C_4Im]_2[NiCl_4]$ at 100°C. Average of three measurements shown and standard deviation.*

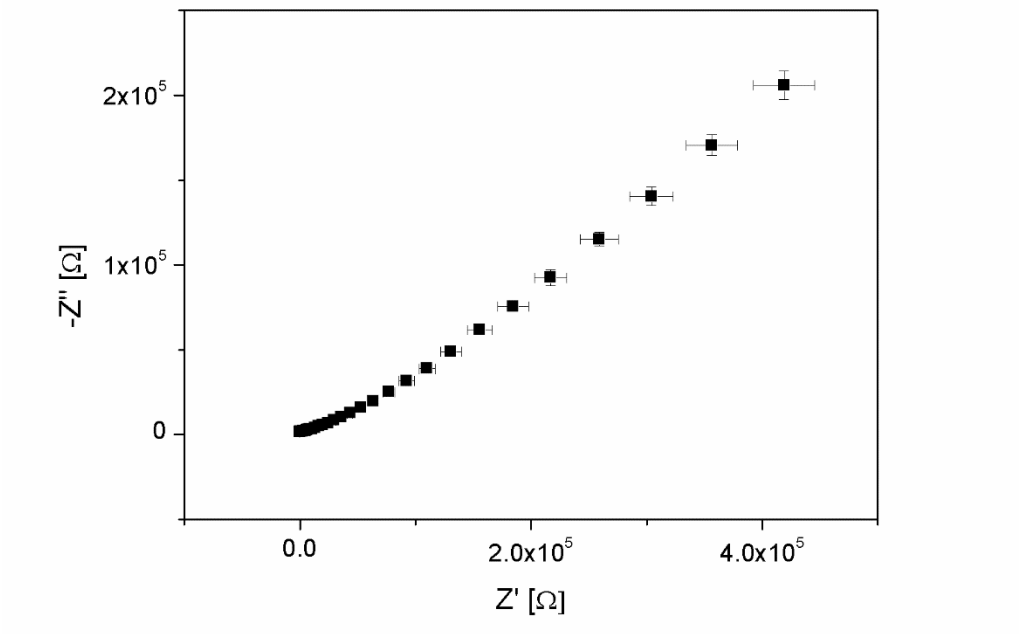



*Figure 8-135 Impedance spectroscopy of $[C_1C_4Im]_2[NiCl_4]$ at 110°C. Average of three measurements shown and standard deviation.*

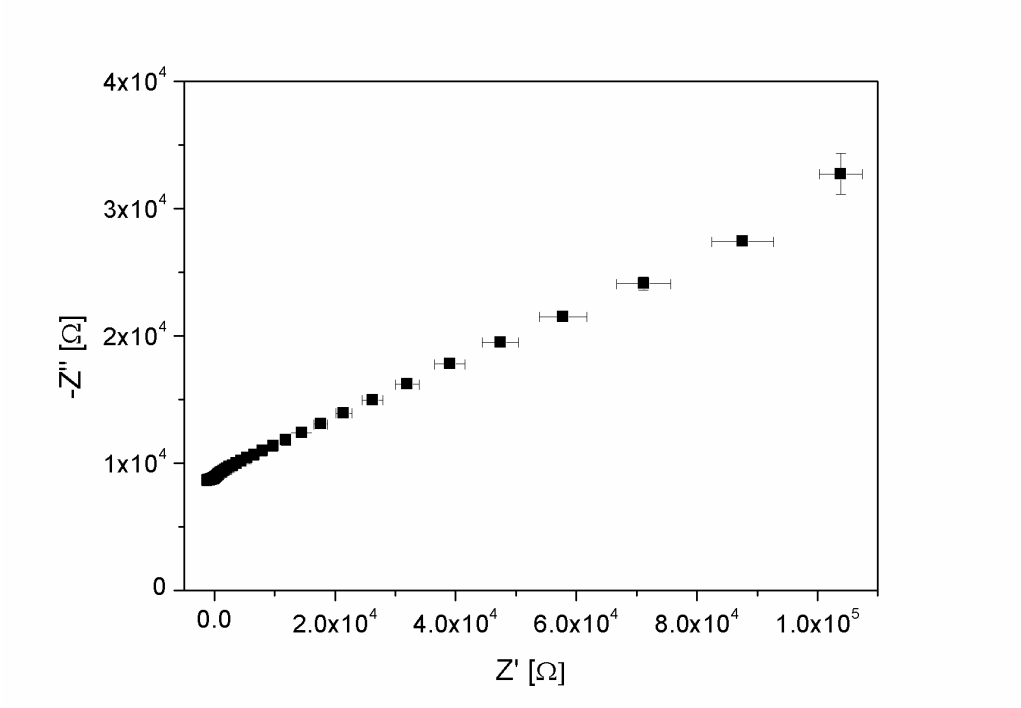



*Figure 8-136 Impedance spectroscopy of $[C_1C_4Im]_2[CoCl_4]$ at 70°C. Average of three measurements shown and standard deviation.*

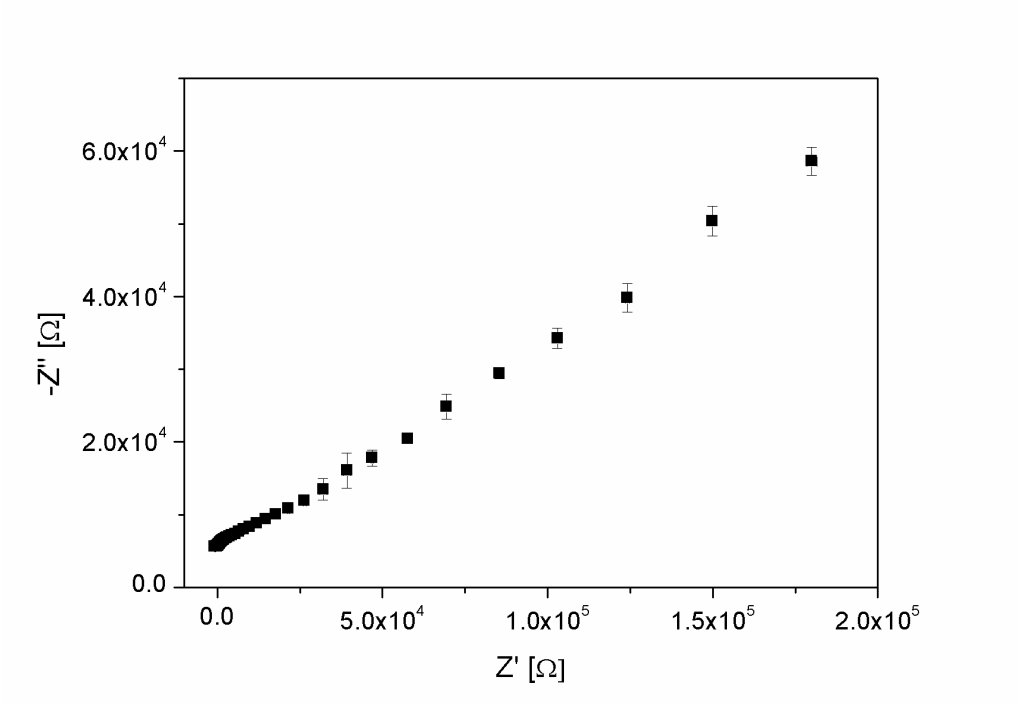



*Figure 8-137 Impedance spectroscopy of $[C_1C_4Im]_2[CoCl_4]$ at 80°C. Average of three measurements shown and standard deviation.*

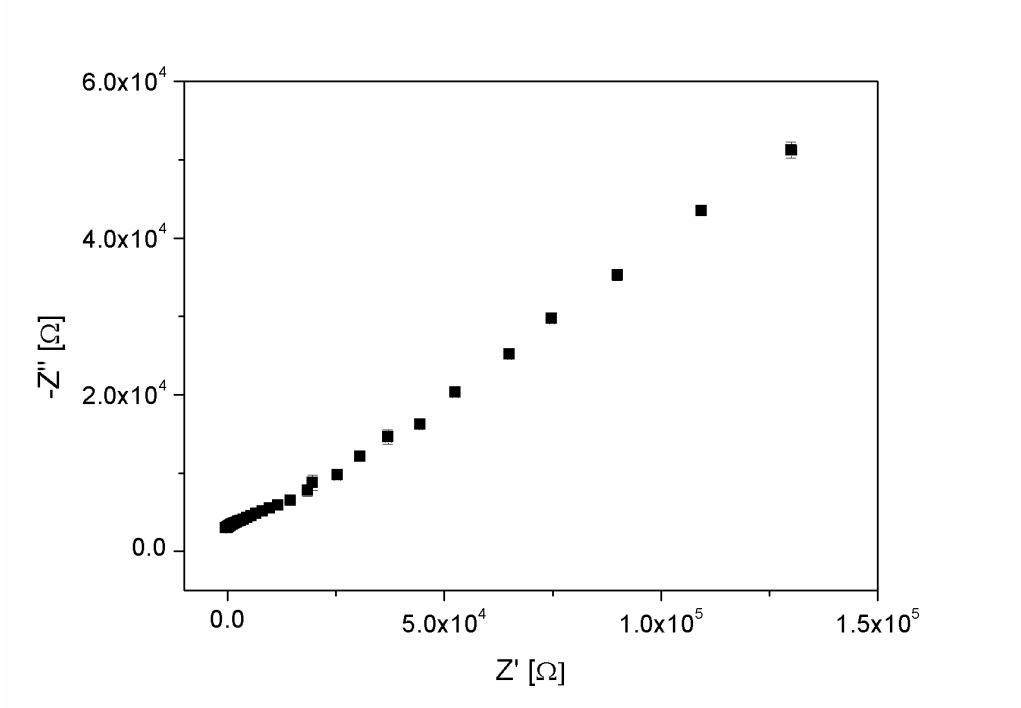



*Figure 8-138 Impedance spectroscopy of $[C_1C_4Im]_2[CoCl_4]$ at 90°C. Average of three measurements shown and standard deviation.*

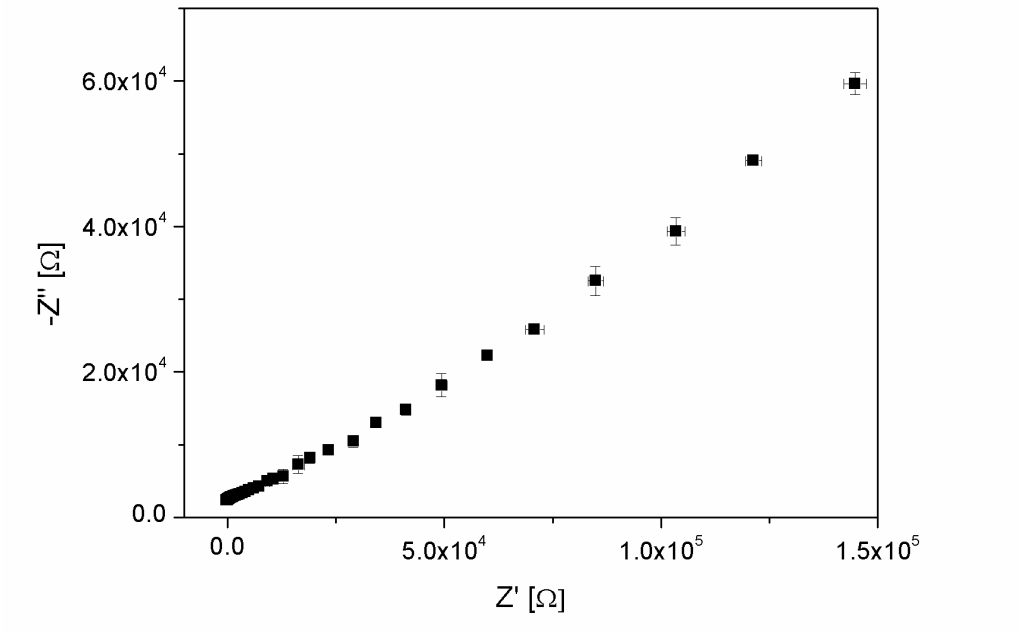



*Figure 8-139 Impedance spectroscopy of $[C_1C_4Im]_2[CoCl_4]$ at 100°C. Average of three measurements shown and standard deviation.*

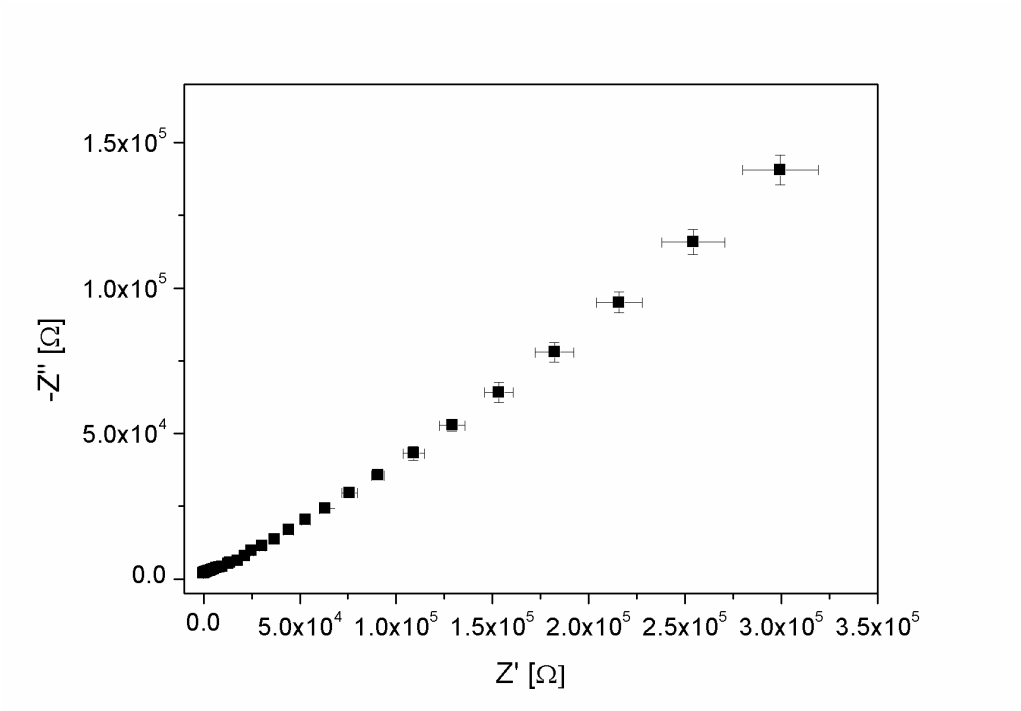



*Figure 8-140 Impedance spectroscopy of $[C_1C_4Im]_2[CoCl_4]$ at 110°C. Average of three measurements shown and standard deviation.*

## 8.7 Magnetization measurements

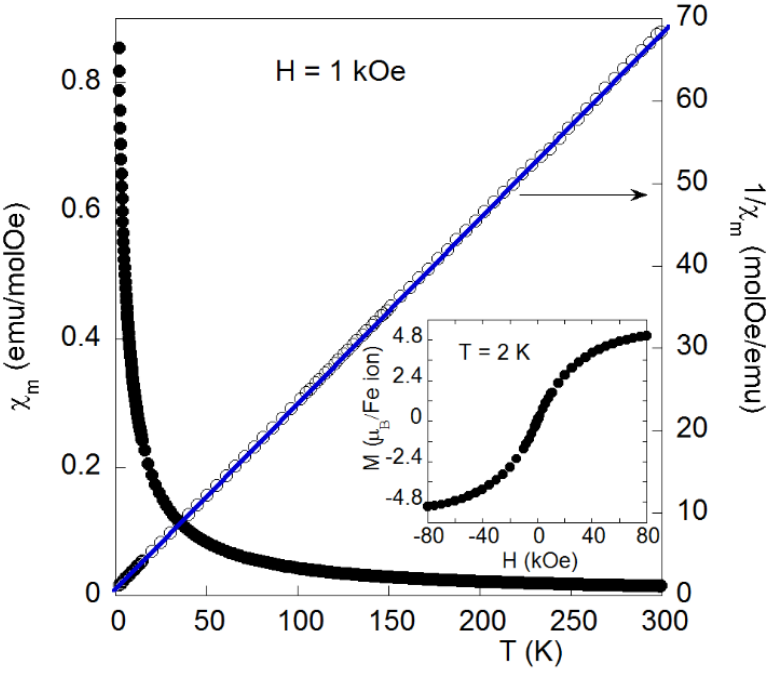
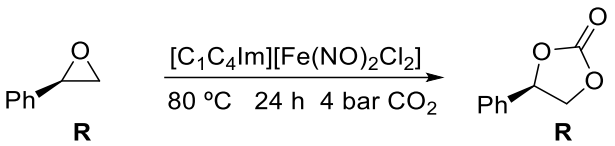


*Figure 8-141 Temperature dependence of molar magnetic susceptibilities, χm, and reciprocal, χm−1. The blue solid line is the fit according to Curie−Weiss law. (Bottom) magnetic hysteresis loops, M(H), collected at 2 K.*

The molar magnetic susceptibility of the Fe-based IL (Figure 8-141) is in good agreement with that found in other metal ILs based on [$FeCl_4^-$] ion.[34, 35, 40] The effective magnetic moment ($\mu_{eff}$), obtained by fitting of the inverse of molar magnetic susceptibility using the Curie–Weiss law (Figure 8-141, blue) has a value of 5.95 ($\mu_B$/molecule), which agrees with the expected value of 5.92 $\mu_B$ for $Fe^{3+}$ ion.[40] Moreover, the magnetization data (see inset in Figure 8-141) tends to saturate above 50 kOe with a value of 5.11 $m_B$/Fe ion at 80 kOe, which is near from the expected fully saturated value of 5 $m_B$/Fe for a $Fe^{3+}$ ion. Both data are a fingerprint indicating that $Fe^{3+}$ is the main oxidation state of iron in the metal-based IL.[40]

## 8.8 GC chromatograms



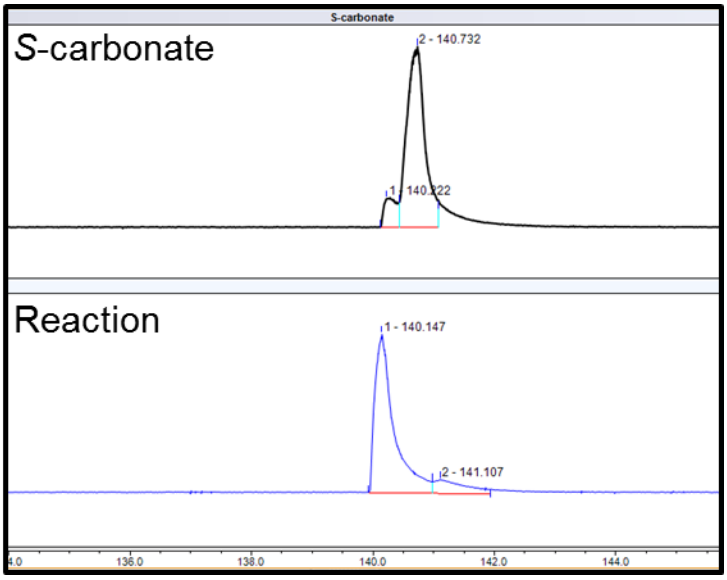
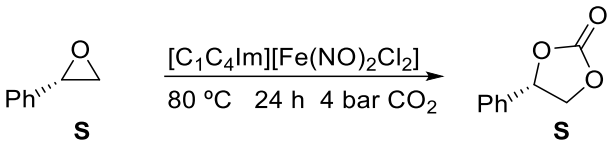



*Figure 8-142 GC Chromatogram for the formation of R-4-phenyl-1,3-dioxolan-2-one by cycloaddition of $CO_2$ with R-styrene oxide catalysed by $[C_1C_4Im][Fe(NO)_2Cl_2]$ Reagents: $[C_1C_4Im][Fe(NO)_2Cl_2]$, 0.1665 mmol; styrene oxide, 1.665 mmol.*[258]



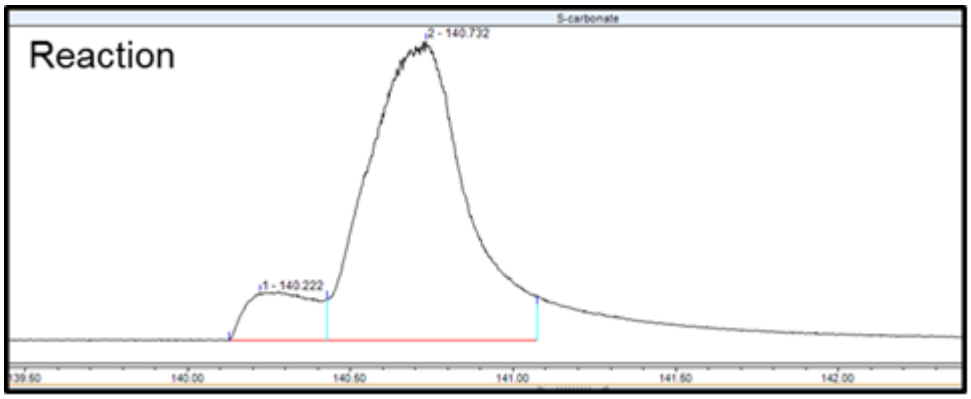
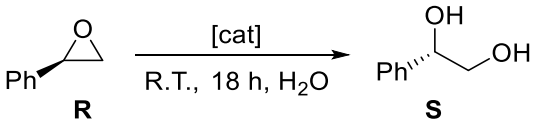




*Figure 8-143 GC Chromatogram for the formation of S-4-phenyl-1,3-dioxolan-2-one by cycloaddition of CO2 with S-styrene oxide catalysed by $[C_1C_4Im][Fe(NO)_2Cl_2]$. Reagents: $[C_1C_4Im][Fe(NO)_2Cl_2]$, 0.1665 mmol; styrene oxide, 1.665 mmol.*



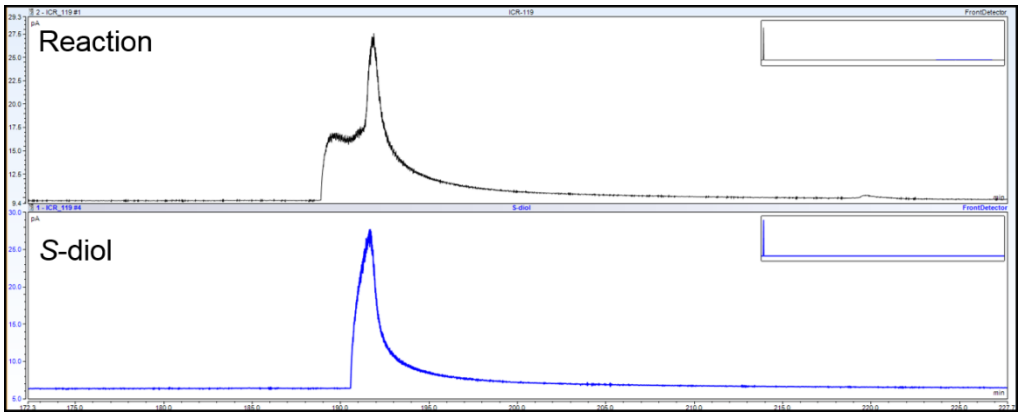
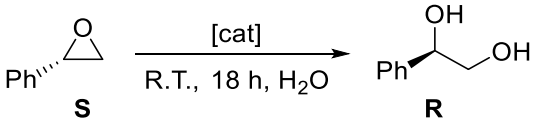




*Figure 8-144 GC Chromatogram for the formation of S-1-phenyl-1,2-ethanediol by reaction of R-styrene oxide with $H_2O$ catalysed by $[C_1C_4Im][Fe(NO)_2Cl_2]$. Reagents and conditions: $[C_1C_4Im][Fe(NO)_2Cl_2]$, 0.1665 mmol; R-styrene oxide, 1.665 mmol; $H_2O$, 1 mL.*



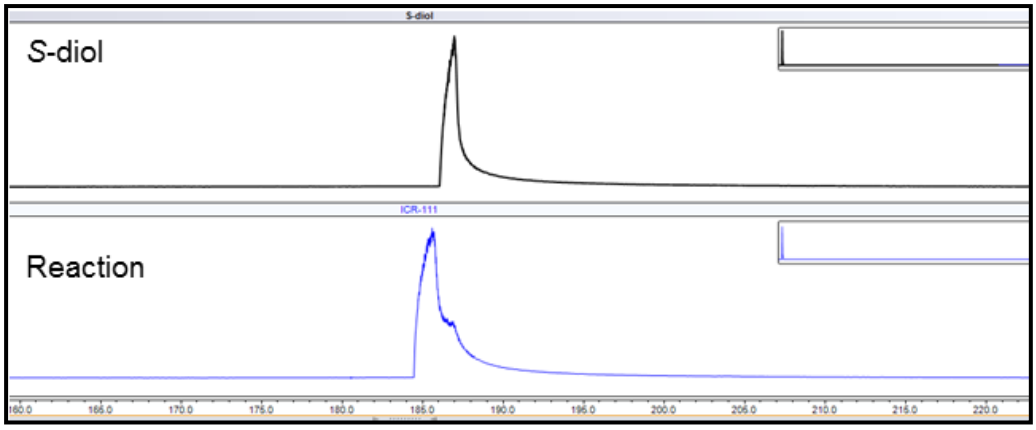



*Figure 8-145 GC Chromatogram for the formation of R-1-phenyl-1,2-ethanediol by reaction of S-styrene oxide with $H_2O$ catalysed by $[C_1C_4Im][Fe(NO)_2Cl_2]$. Reagents and conditions: $[C_1C_4Im][Fe(NO)_2Cl_2]$, 0.1665 mmol; S-styrene oxide, 1.665 mmol; $H_2O$, 1 mL.*

## 8.9 Kinetic experiments

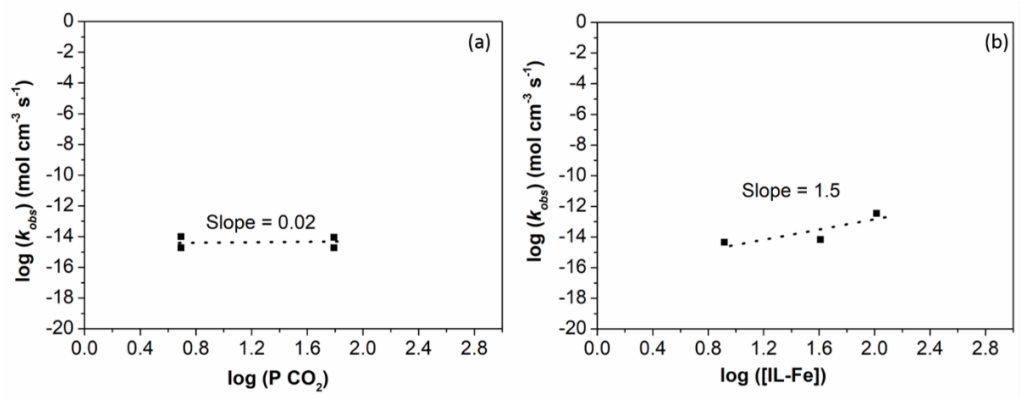


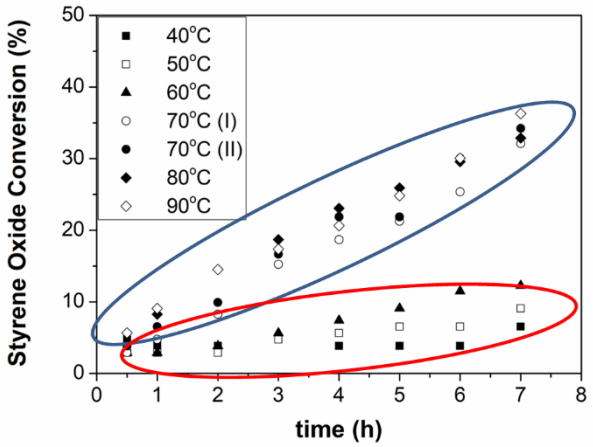

*Figure 8-146 Double logarithmic plot to determine the order respect to (a) $CO_2$ and (b) $[C_1C_4Im][Fe(NO)_2Cl_2]$.*

$k_{obs} = k\,[CO_2]^b\,[[C_1C_4Im][Fe(NO)_2Cl_2]]^c$, thus

$\log(k_{obs}) = b\cdot\log[CO_2] + c\cdot\log[[C_1C_4Im][Fe(NO)_2Cl_2]] + \log(k)$

Then, plot of $\log(k_{obs})$ against $\log[CO_2]$ will have slope equal to b, whereas a plot of $\log(k_{obs})$ against $\log[[C_1C_4Im][Fe(NO)_2Cl_2]]$ will have slope equal to c.

| T (ºC) | $k_{obs}$ (mol · cm$^{-3}$ · s$^{-1}$) |
|---|---|
| 40 | $8.28 \cdot 10^{-7}$ |
| 50 | $3.46 \cdot 10^{-6}$ |
| 60 | $7.01 \cdot 10^{-6}$ |
| 70 (I) | $1.16 \cdot 10^{-5}$ |
| 70 (II) | $1.23 \cdot 10^{-5}$ |
| 80 | $1.30 \cdot 10^{-5}$ |
| 90 | $1.38 \cdot 10^{-5}$ |



# 9. References


1. H.-P. Steinrück and P. Wasserscheid, *Catal. Lett.*, 2014, **145**, 380-397.
2. R. Hayes, G. G. Warr and R. Atkin, *Chem. Rev.*, 2015, **115**, 6357-6426.
3. C. J. Clarke, W.-C. Tu, O. Levers, A. Bröhl and J. P. Hallett, *Chem. Rev.*, 2018, **118**, 747-800.
4. K. S. Egorova, E. G. Gordeev and V. P. Ananikov, *Chem. Rev.*, 2017, **117**, 7132-7189.
5. A. P. Abbott, K. Ryder, P. Licence and A. W. Taylor, in *Ionic Liquids Completely UnCOILed*, eds. N. V. Plechkova and K. R. Seddon, Wiley, Hoboken, New Jersey, 2015, pp. 1-12.
6. T. Welton, *Chem. Rev.*, 1999, **99**, 2071-2084.
7. N. V. Plechkova and K. R. Seddon, *Chem. Soc. Rev.*, 2008, **37**, 123-150.
8. M. Antonietti, D. Kuang, B. Smarsly and Y. Zhou, *Angew. Chem. Int. Ed.*, 2004, **43**, 4988-4992.
9. A. P. Abbott, G. Frisch and K. S. Ryder, *Annu. Rep. Prog. Chem., Sect. A: Inorg. Chem.*, 2008, **104**, 21-45.
10. X. Han and D. W. Armstrong, *Acc. Chem. Res.*, 2007, **40**, 1079-1086.
11. C. D. Tran, *Anal. Lett.*, 2007, **40**, 2447-2464.
12. V. I. Pârvulescu and C. Hardacre, *Chem. Rev.*, 2007, **107**, 2615-2665.
13. A. A. Kornyshev, *J. Phys. Chem. B*, 2007, **111**, 5545-5557.
14. F. van Rantwijk and R. A. Sheldon, *Chem. Rev.*, 2007, **107**, 2757-2785.
15. W. L. Hough and R. D. Rogers, *Bull. Chem. Soc. Jpn.*, 2007, **80**, 2262-2269.
16. J. Estager, J. D. Holbrey and M. Swadźba-Kwaśny, *Chem. Soc. Rev.*, 2014, **43**, 847-886.
17. Z. Lei, C. Dai and B. Chen, *Chem. Rev.*, 2014, **114**, 1289-1326.
18. R. M. Lynden-Bell, M. G. Del Pópolo, T. G. A. Youngs, J. Kohanoff, C. G. Hanke, J. B. Harper and C. C. Pinilla, *Acc. Chem. Res.*, 2007, **40**, 1138-1145.
19. N. Winterton, *J. Mater. Chem.*, 2006, **16**, 4281-4293.
20. L. Weng, X. Liu, Y. Liang and Q. Xue, *Tribol. Lett.*, 2007, **26**, 11-17.
21. D. M. Blake, L. Moens, D. Rudnicki and H. Pilath, *J. Sol. Energy Eng.*, 2005, **128**, 54-57.
22. Y. Yoshida and G. Saito, *J. Mater. Chem.*, 2006, **16**, 1254-1262.
23. K. Lunstroot, K. Driesen, P. Nockemann, C. Görller-Walrand, K. Binnemans, S. Bellayer, J. Le Bideau and A. Vioux, *Chem. Mater.*, 2006, **18**, 5711-5715.
24. C. B. Jones, R. Haiges, T. Schroer and K. O. Christe, *Angew. Chem. Int. Ed.*, 2006, **45**, 4981-4984.
25. J. S. Wilkes, *Green Chem.*, 2002, **4**, 73-80.
26. R. J. Gale, B. Gilbert and R. A. Osteryoung, *Inorg. Chem.*, 1978, **17**, 2728-2729.
27. J. S. Wilkes, J. A. Levisky, R. A. Wilson and C. L. Hussey, *Inorg. Chem.*, 1982, **21**, 1263-1264.

28. L. C. Brown, J. M. Hogg and M. Swadźba-Kwaśny, *Top Curr Chem (Z)*, 2017, **375**, 78-118.
29. B. Scrosati, J. Hassoun and Y.-K. Sun, *Energy Environ. Sci*, 2011, **4**, 3287-3295.
30. D. R. MacFarlane, N. Tachikawa, M. Forsyth, J. M. Pringle, P. C. Howlett, G. D. Elliott, J. H. Davis, M. Watanabe, P. Simon and C. A. Angell, *Energy Environ. Sci*, 2014, **7**, 232-250.
31. M. Watanabe, M. L. Thomas, S. Zhang, K. Ueno, T. Yasuda and K. Dokko, *Chem. Rev.*, 2017, **117**, 7190-7239.
32. F. Liu, Y. Deng, X. Han, W. Hu and C. Zhong, *J. Alloys Compd.*, 2016, **654**, 163-170.
33. Q. Zhang, Q. Wang, S. Zhang, X. Lu and X. Zhang, *ChemPhysChem*, 2016, **17**, 335-351.
34. A. Garcia-Saiz, I. de Pedro, P. Migowski, O. Vallcorba, J. Junquera, J. A. Blanco, O. Fabelo, D. Sheptyakov, J. C. Waerenborgh, M. T. Fernandez-Diaz, J. Rius, J. Dupont, J. A. Gonzalez and J. R. Fernandez, *Inorg. Chem.*, 2014, **53**, 8384-8396.
35. A. García-Saiz, I. de Pedro, O. Vallcorba, P. Migowski, I. Hernández, L. Fernández Barquin, I. Abrahams, M. Motevalli, J. Dupont, J. A. Gonzalez and J. R. Fernández, *RSC Adv.*, 2015, **5**, 60835-60848.
36. A. Garcia-Saiz, P. Migowski, O. Vallcorba, J. Junquera, J. A. Blanco, J. A. Gonzalez, M. T. Fernandez-Diaz, J. Rius, J. Dupont, J. Rodriguez Fernandez and I. de Pedro, *Chem.: Eur. J.*, 2014, **20**, 72-76.
37. Z.-L. Xie and A. Taubert, *ChemPhysChem*, 2011, **12**, 364-368.
38. X. Yu, X. Yuan, Y. Zhao and L. Ren, *ACS Macro Letters*, 2019, **8**, 1504-1510.
39. S. Hayashi and H.-o. Hamaguchi, *Chem. Lett.*, 2004, **33**, 1590-1591.
40. I. de Pedro, O. Fabelo, A. Garcia-Saiz, O. Vallcorba, J. Junquera, J. A. Blanco, J. C. Waerenborgh, D. Andreica, A. Wildes, M. T. Fernandez-Diaz and J. R. Fernandez, *Phys. Chem. Chem. Phys.*, 2016, **18**, 21881-21892.
41. I. de Pedro, A. García-Saiz, J. González, I. Ruiz de Larramendi, T. Rojo, C. A. M. Afonso, S. P. Simeonov, J. C. Waerenborgh, J. A. Blanco, B. Ramajo and J. R. Fernández, *Phys. Chem. Chem. Phys.*, 2013, **15**, 12724-12733.
42. I. de Pedro, D. P. Rojas, J. Albo, P. Luis, A. Irabien, J. A. Blanco and J. R. Fernandez, *J Phys Condens Matter*, 2010, **22**, 1-4.
43. A. Garcia-Saiz, I. de Pedro, J. A. Blanco, J. Gonzalez and J. Rodriguez Fernandez, *J. Phys. Chem. B*, 2013, **117**, 3198-3206.
44. Z.-L. Xie, A. Jeličić, F.-P. Wang, P. Rabu, A. Friedrich, S. Beuermann and A. Taubert, *J. Mater. Chem.*, 2010, **20**, 9543-9549.
45. J. R. Diniz, T. B. de Lima, R. Galaverna, A. L. de Oliveira, D. A. C. Ferreira, F. C. Gozzo, M. N. Eberlin, J. Dupont and B. A. D. Neto, *Phys. Chem. Chem. Phys.*, 2018, **20**, 24716-24725.
46. P. N. Bartlett, J. Burt, D. A. Cook, C. Y. Cummings, M. W. George, A. L. Hector, M. M. Hasan, J. Ke, W. Levason, D. Pugh, G. Reid, P. W. Richardson, D. C. Smith, J. Spencer, N. Suleiman and W. Zhang, *Chem. - Eur. J.*, 2016, **22**, 302-309.
47. JP5711350B1, 2015.

48. S. Tyrrell, G. Behrendt and P. Nockemann, *Inorg. Chem.*, 2015, **54**, 4495-4503.
49. S. Anvar, I. Mohammadpoor-Baltork, S. Tangestaninejad, M. Moghadam, V. Mirkhani, A. R. Khosropour, A. Landarani Isfahani and R. Kia, *ACS Comb. Sci.*, 2014, **16**, 93-100.
50. D. C. Apperley, C. Hardacre, P. Licence, R. W. Murphy, N. V. Plechkova, K. R. Seddon, G. Srinivasan, M. Swadzba-Kwasny and I. J. Villar-Garcia, *Dalton Trans.*, 2010, **39**, 8679-8687.
51. Y. J. Kim and R. S. Varma, *J. Org. Chem.*, 2005, **70**, 7882-7891.
52. Y. J. Kim and R. S. Varma, *Tetrahedron Lett.*, 2005, **46**, 1467-1469.
53. H. Q. N. Gunaratne, T. J. Lotz and K. R. Seddon, *New J. Chem.*, 2010, **34**, 1821-1824.
54. A. Van den Bossche, W. Vereycken, T. Vander Hoogerstraete, W. Dehaen and K. Binnemans, *ACS Sustainable Chem. Eng.*, 2019, **7**, 14451-14459.
55. Y. Yu, Y. Yue, B. Wang, H. He, Z.-T. Hu, J. Zhao and X. Li, *Catalysts*, 2019, **9**, 504.
56. F. Neve, O. Francescangeli, A. Crispini and J. Charmant, *Chem. Mater.*, 2001, **13**, 2032-2041.
57. E. A. Pidko, V. Degirmenci, R. A. van Santen and E. J. M. Hensen, *Inorg. Chem.*, 2010, **49**, 10081-10091.
58. K. F. Wang, F. F. Jian, R. R. Zhuang and H. L. Xiao, *Cryst. Growth Des.*, 2009, **9**, 3934-3940.
59. T. Brunelet and G. Gelbard, *J. Chem. Res., Synop.*, 1985, 264-265.
60. M. C. Buzzeo, A. H. Iqbal, C. M. Long, D. Millar, S. Patel, M. A. Pellow, S. A. Saddoughi, A. L. Smenton, J. F. C. Turner, J. D. Wadhawan, R. G. Compton, J. A. Golen, A. L. Rheingold and L. H. Doerrer, *Inorg. Chem.*, 2004, **43**, 7709-7725.
61. P. De Vreese, N. R. Brooks, K. Van Hecke, L. Van Meervelt, E. Matthijs, K. Binnemans and R. Van Deun, *Inorg. Chem.*, 2012, **51**, 4972-4981.
62. B. F. Gilmore, G. P. Andrews, G. Borberly, M. J. Earle, M. A. Gilea, S. P. Gorman, A. F. Lowry, M. McLaughlin and K. R. Seddon, *New J. Chem.*, 2013, **37**, 873-876.
63. D. D. Axtell, B. W. Good, W. W. Porterfield and J. T. Yoke, *J. Am. Chem. Soc.*, 1973, **95**, 4555-4559.
64. E. N. Golubeva, A. I. Kokorin, D. I. Kochubei, V. I. Pergushov and V. V. Kriventsov, *Kinet. Catal.*, 2002, **43**, 408-411.
65. K. Thiel, T. Klamroth, P. Strauch and A. Taubert, *Phys. Chem. Chem. Phys.*, 2011, **13**, 13537-13543.
66. Q. Wang, Y. Geng, X. Lu and S. Zhang, *ACS Sustainable Chem. Eng.*, 2015, **3**, 340-348.
67. A. Abouserie, K. Zehbe, P. Metzner, A. Kelling, C. Günter, U. Schilde, P. Strauch, T. Körzdörfer and A. Taubert, *Eur. J. Inorg. Chem.*, 2017, **2017**, 5640-5649.
68. S. Saikia, P. Gogoi, A. K. Dutta, P. Sarma and R. Borah, *J. Mol. Catal. A: Chem.*, 2016, **416**, 63-72.

69. I. Dindarloo Inaloo and S. Majnooni, *ChemistrySelect*, 2019, **4**, 7811-7817.
70. S. Liu, H. Zhou, S. Yu, C. Xie, F. Liu and Z. Song, *Chem. Eng. J.*, 2011, **174**, 396-399.
71. N. Azizi, M. Abdoli-Senejani and F. Abbasi, *Tetrahedron Lett.*, 2016, **57**, 5009-5011.
72. A. W. Taylor, S. Men, C. J. Clarke and P. Licence, *RSC Adv.*, 2013, **3**, 9436-9445.
73. J. Estager, P. Nockemann, K. R. Seddon, M. Swadźba-Kwaśny and S. Tyrrell, *Inorg. Chem.*, 2011, **50**, 5258-5271.
74. K. S. Lovejoy, C. A. Corley, E. K. Cope, M. C. Valentine, J. G. Leid, G. M. Purdy, J. S. Wilkes, A. T. Koppisch and R. E. Del Sesto, *Crystal Growth & Design*, 2012, **12**, 5357-5364.
75. J. Wang and C. Wang, *ACS Sustainable Chem. Eng.*, 2019, **7**, 12457-12463.
76. J. Li, W. Zhu, J. Ji, P. Wang, Y. Lan, N. Gao, X. Yin, H. Wang and G. Li, *ACS Applied Materials & Interfaces*, 2016, **8**, 11008-11017.
77. K. Santra, K. D. Clark, N. Maity, J. W. Petrich and J. L. Anderson, *J. Phys. Chem. B*, 2018, **122**, 7747-7756.
78. E. Santos, J. Albo, A. Rosatella, C. A. M. Afonso and Á. Irabien, *Journal of Chemical Technology & Biotechnology*, 2014, **89**, 866-871.
79. S. Schaltin, P. Nockemann, B. Thijs, K. Binnemans and J. Fransaer, *Electrochem. Solid-State Lett.*, 2007, **10**, D104-D107.
80. S. Wellens, B. Thijs and K. Binnemans, *Green Chem.*, 2012, **14**, 1657-1665.
81. M. B. Meredith, C. H. McMillen, J. T. Goodman and T. P. Hanusa, *Polyhedron*, 2009, **28**, 2355-2358.
82. A. J. Dent, K. R. Seddon and T. Welton, *J. Chem. Soc., Chem. Commun.*, 1990, 315-316.
83. L. C. Fernandes, D. M. Correia, C. García-Astrain, N. Pereira, M. Tariq, J. M. S. S. Esperança and S. Lanceros-Méndez, *ACS Applied Materials & Interfaces*, 2019, **11**, 20316-20324.
84. M. C. A. Kuhn, A. A. M. Lapis, G. Machado, T. Roisnel, J.-F. Carpentier, B. A. D. Neto and O. L. Casagrande, *Inorg. Chim. Acta*, 2011, **370**, 505-512.
85. A. Chinnappan, A. H. Jadhav, H. Kim and W.-J. Chung, *Chem. Eng. J.*, 2014, **237**, 95-100.
86. B. Gilbert, H. Olivier-Bourbigou and F. Favre, *Oil Gas Sci. Technol. – Rev. IFP*, 2007, **62**, 745-759.
87. J. Estager, A. A. Oliferenko, K. R. Seddon and M. Swadźba-Kwaśny, *Dalton Trans.*, 2010, **39**, 11375-11382.
88. T. C. Berto, A. L. Speelman, S. Zheng and N. Lehnert, *Coord. Chem. Rev.*, 2013, **257**, 244-259.
89. R. P. Orenha and S. E. Galembeck, *J. Chem. Educ.*, 2014, **91**, 1064-1069.
90. D. M. P. Mingos, in *Nitrosyl Complexes in Inorganic Chemistry, Biochemistry and Medicine I*, ed. D. M. P. Mingos, Springer-Verlag, Berlin, Heidelberg, 2014, vol. 153, pp. 1-44.

91. H. Lewandowska, in *Nitrosyl Complexes in Inorganic Chemistry, Biochemistry and Medicine I*, ed. D. M. P. Mingos, Springer-Verlag, Berlin, Heidelberg, 2013, vol. 153, pp. 115-165.
92. C. Laurence and J. F. Gal, *Lewis Basicity and Affinity Scales: Data and Measurement*, John Wiley & Sons, Ltd, Chichester, 2009.
93. M. Méndez and A. Cedillo, *Comput. Theor. Chem.*, 2013, **1011**, 44-56.
94. K. O. Christe, D. A. Dixon, D. McLemore, W. W. Wilson, J. A. Sheehy and J. A. Boatz, *J. Fluorine Chem.*, 2000, **101**, 151-153.
95. R. F. Childs, D. L. Mulholland and A. Nixon, *Can. J. Chem.*, 1982, **60**, 801-808.
96. V. Gutmann, *Electrochim. Acta*, 1976, **21**, 661-670.
97. M. A. Beckett, G. C. Strickland, J. R. Holland and K. Sukumar Varma, *Polymer*, 1996, **37**, 4629-4631.
98. G. A. Olah, S. Kobayashi and M. Tashiro, *J. Am. Chem. Soc.*, 1972, **94**, 7448-7461.
99. S. Kobayashi, T. Busujima and S. Nagayama, *Chem.: Eur. J.*, 2000, **6**, 3491-3494.
100. V. Gutmann, *Pure Appl. Chem.*, 1979, **51**, 2197.
101. I. C. Quarmby and R. A. Osteryoung, *J. Am. Chem. Soc.*, 1994, **116**, 2649-2650.
102. V. Gutmann, *Pure Appl. Chem.*, 1971, **27**, 73-88.
103. U. Mayer, V. Gutmann and W. Gerger, *Monatshefte für Chemie / Chemical Monthly*, 1975, **106**, 1235-1257.
104. M. Schmeisser, P. Illner, R. Puchta, A. Zahl and R. van Eldik, *Chemistry – A European Journal*, 2012, **18**, 10969-10982.
105. M. Schmeisser and R. van Eldik, *Dalton Trans.*, 2014, **43**, 15675-15692.
106. M. Holzweber, R. Lungwitz, D. Doerfler, S. Spange, M. Koel, H. Hutter and W. Linert, *Chemistry – A European Journal*, 2013, **19**, 288-293.
107. K. Yoshifumi, F. Masanori, F. Tomotsumi and T. Masahide, *Chem. Lett.*, 2005, **34**, 338-339.
108. T. Fujisawa, M. Fukuda, M. Terazima and Y. Kimura, *The Journal of Physical Chemistry A*, 2006, **110**, 6164-6172.
109. H. Olivier-Bourbigou, F. Favre, A. Forestière and F. Hugues, in *Handbook of Green Chemistry*, ed. P. T. Anastas, Wiley-VCH, Weinheim, 2010, pp. 101-126.
110. S. Takahashi, L. A. Curtiss, D. Gosztola, N. Koura and M.-L. Saboungi, *Inorg. Chem.*, 1995, **34**, 2990-2993.
111. A. A. Fannin, D. A. Floreani, L. A. King, J. S. Landers, B. J. Piersma, D. J. Stech, R. L. Vaughn, J. S. Wilkes and J. L. Williams, *J. Phys. Chem.*, 1984, **88**, 2614-2621.
112. J. L. Gray and G. E. Maciel, *J. Am. Chem. Soc.*, 1981, **103**, 7147-7151.
113. S. Takahashi, M.-L. Saboungi, R. J. Klingler, M. J. Chen and J. W. Rathke, *J. Chem. Soc., Faraday Trans.*, 1993, **89**, 3591-3595.
114. D. C. Apperley, C. Hardacre, P. Licence, R. W. Murphy, N. V. Plechkova, K. R. Seddon, G. Srinivasan, M. Swadźba-Kwaśny and I. J. Villar-Garcia, *Dalton Trans.*, 2010, **39**, 8679-8687.

115. M. Currie, J. Estager, P. Licence, S. Men, P. Nockemann, K. R. Seddon, M. Swadźba-Kwaśny and C. Terrade, *Inorg. Chem.*, 2013, **52**, 1710-1721.
116. J.-Z. Yang, P. Tian, W.-G. Xu, B. Xu and S.-Z. Liu, *Thermochim. Acta*, 2004, **412**, 1-5.
117. C. Hardacre, R. W. Murphy, K. R. Seddon, G. Srinivasan and M. Swadźba-Kwaśny, *Aust. J. Chem.*, 2010, **63**, 845-848.
118. M. B. Alves, V. O. Santos jr, V. C. D. Soares, P. A. Z. Suarez and J. C. Rubim, *J. Raman Spectrosc*, 2008, **39**, 1388-1395.
119. M. B. Alves, A. P. Umpierre, V. O. Santos Jr, V. C. D. Soares, J. Dupont, J. C. Rubim and P. A. Z. Suarez, *Thermochim. Acta*, 2010, **502**, 20-23.
120. Y. Liu, G. Wu and M. Qi, *J. Cryst. Growth*, 2005, **281**, 616-622.
121. V. Lecocq, A. Graille, C. C. Santini, A. Baudouin, Y. Chauvin, J. M. Basset, L. Arzel, D. Bouchu and B. Fenet, *New J. Chem.*, 2005, **29**, 700-706.
122. S.-I. Hsiu, J.-F. Huang, I. W. Sun, C.-H. Yuan and J. Shiea, *Electrochim. Acta*, 2002, **47**, 4367-4372.
123. Y. Zou, H. Xu, G. Wu, Z. Jiang, S. Chen, Y. Huang, W. Huang and X. Wei, *J. Phys. Chem. B*, 2009, **113**, 2066-2070.
124. R. Kore, P. Berton, S. P. Kelley, P. Aduri, S. S. Katti and R. D. Rogers, *ACS Catal.*, 2017, **7**, 7014-7028.
125. S. P. Wicelinski, R. J. Gale and J. S. Wilkes, *Thermochim. Acta*, 1988, **126**, 255-263.
126. S. P. Wicelinski, R. J. Gale, K. M. Pamidimukkala and R. A. Laine, *Anal. Chem.*, 1988, **60**, 2228-2232.
127. L. Wang, J.-J. Zou, X. Zhang and L. Wang, *Fuel*, 2012, **91**, 164-169.
128. J. S. Wilkes, J. S. Frye and G. F. Reynolds, *Inorg. Chem.*, 1983, **22**, 3870-3872.
129. K. Matuszek, A. Chrobok, J. M. Hogg, F. Coleman and M. Swadźba-Kwaśny, *Green Chem.*, 2015, **17**, 4255-4262.
130. K. Qiao and Y. Deng, *J. Mol. Catal. A: Chem.*, 2001, **171**, 81-84.
131. J. A. Boon, J. A. Levisky, J. L. Pflug and J. S. Wilkes, *J. Org. Chem.*, 1986, **51**, 480-483.
132. D. S. Kim and W. S. Ahn, *Korean J. Chem. Eng.*, 2003, **20**, 39-43.
133. H. Q. N. Gunaratne, T. J. Lotz and K. R. Seddon, *New J. Chem.*, 2010, **34**, 1821-1824.
134. K. Yoo, V. V. Namboodiri, R. S. Varma and P. G. Smimiotis, *J. Catal.*, 2004, **222**, 511-519.
135. J. Zhang, C. Huang, B. Chen, P. Ren and M. Pu, *J. Catal.*, 2007, **249**, 261-268.
136. M. J. Earle, K. R. Seddon, C. J. Adams and G. Roberts, *Chem. Commun.*, 1998, 2097-2098.
137. Y. Chauvin, B. Gilbert and I. Guibard, *J. Chem. Soc., Chem. Commun.*, 1990, 1715-1716.
138. J. M. Hogg, F. Coleman, A. F. Ferrer-Ugalde, M. P. Atkins and M. Swadźba-Kwaśny, *Green Chem.*, 2015, **17**, 1831-1841.
139. O. Stenzel, R. Brüll, U. M. Wahner, R. D. Sanderson and H. G. Raubenheimer, *J. Mol. Catal. A: Chem.*, 2003, **192**, 217-222.
140. C. W. Lee, *Tetrahedron Lett.*, 1999, **40**, 2461-2464.

141. J. M. Hogg, L. C. Brown, K. Matuszek, P. Latos, A. Chrobok and M. Swadźba-Kwaśny, *Dalton Trans.*, 2017, **46**, 11561-11574.
142. K. Matuszek, S. Coffie, A. Chrobok and M. Swadźba-Kwaśny, *Catal. Sci. Technol.*, 2017, **7**, 1045-1049.
143. C. J. Adams, M. J. Earle and K. R. Seddon, *Chem. Commun.*, 1999, 1043-1044.
144. Y. Deng, F. Shi, J. Beng and K. Qiao, *J. Mol. Catal. A: Chem.*, 2001, **165**, 33-36.
145. X. Liang, G. Gong, H. Wu and J. Yang, *Fuel*, 2009, **88**, 613-616.
146. B. A. de Silveira Neto, M. B. Alves, A. A. M. Lapis, F. M. Nachtigall, M. N. Eberlin, J. Dupont and P. A. Z. Suarez, *J. Catal.*, 2007, **249**, 154-161.
147. J. R. Harjani, S. J. Nara and M. M. Salunkhe, *Tetrahedron Lett.*, 2002, **43**, 1127-1029.
148. B. A. da Silveira Neto, G. Ebeling, R. S. Gonçalves, F. C. Gozzo, M. N. Eberlin and J. Dupont, *Synthesis*, 2004, **2004**, 1155-1158.
149. J. K. Joseph, S. L. Jain, S. Singhal and B. Sain, *Ind. Eng. Chem. Res.*, 2011, **50**, 11463-11466.
150. R. Xia, R. Zhang, X. Meng, Z. Liu, J. Meng and C. Xu, *Pet. Sci.*, 2011, **8**, 219-223.
151. M. Y. Huang, J. C. Wu, F. S. Shieu and J. J. Lin, *Fuel*, 2011, **90**, 1012-1017.
152. P. Kumar, W. Vermeiren, J. P. Dath and W. F. Hölderich, *Appl. Catal., A*, 2006, **304**, 131-141.
153. M. Markiton, A. Chrobok, K. Matuszek, K. R. Seddon and M. Swadźba-Kwaśny, *RSC Adv.*, 2016, **6**, 30460-30467.
154. G. W. Parshall, *J. Am. Chem. Soc.*, 1972, **94**, 8716-8719.
155. Y. Chauvin, B. Gilbert and I. Guibard, *J. Chem. Soc., Chem. Commun.*, 1990, 1715-1716.
156. B. A. da Silveira Neto, G. Ebeling, R. S. Gonçalves, F. C. Gozzo, M. N. Eberlin and J. Dupont, *Synthesis*, 2004, **2004**, 1155-1158.
157. Y. J. Kim and R. S. Varma, *J. Org. Chem.*, 2005, **70**, 7882-7891.
158. Q. Wang, X. Lu, X. Zhou, M. Zhu, H. He and X. Zhang, *J. Appl. Polym. Sci.*, 2013, **129**, 3574-3581.
159. S. Cot, M. K. Leu, A. Kalamiotis, G. Dimitrakis, V. Sans, I. de Pedro and I. Cano, *ChemPlusChem*, 2019, **84**, 786-793.
160. F. Sce, I. Cano, C. Martin, G. Beobide, O. Castillo and I. de Pedro, *New J. Chem.*, 2019, **43**, 3476-3485.
161. B. Sarmah, R. Kore and R. Srivastava, *Inorg. Chem. Front.*, 2018, **5**, 1609-1621.
162. M. Jankowska-Wajda, O. Bartlewicz, A. Walczak, A. R. Stefankiewicz and H. Maciejewski, *J. Catal.*, 2019, **374**, 266-275.
163. K. Li, H. Choudhary, M. K. Mishra and R. D. Rogers, *ACS Catal.*, 2019, **9**, 9789-9793.
164. R. K. Kore, S. P. Kelley, P. Aduri and R. D. Rogers, *Dalton Trans.*, 2018, **47**, 7795.
165. Y. W. Tiong, C. L. Yap, S. Gan and W. S. P. Yap, *Renewable Energy*, 2020, **146**, 932-943.

166. M. Azizi, M. Nasr-Esfahani, I. Mohammadpoor-Baltork, M. Moghadam, V. Mirkhani, S. Tangestaninejad and R. Kia, *J. Org. Chem.*, 2018, **83**, 14743-14750.
167. E. Gutowski Keith, *Physical Sciences Reviews*, 2018, **3**.
168. S. Neil, Mercury-grabbing ionic liquids hit the gas, https://www.chemistryworld.com/news/mercury-grabbing-ionic-liquids-hit-the-gas/8363.article, (accessed 13/09, 2019).
169. PetroChina's first ionic liquid alkylation unit, https://www.hydrocarbonprocessing.com/news/2018/11/petrochinas-first-ionic-liquid-alkylation-unit, (accessed 13/09, 2019).
170. M. McCoy, *Chem. Eng. News*, 2016, **94**, 16.
171. J. Simley, Honeywell UOP and Chevron Win 2017 Platts Breakthrough Solution Award for Ionic Liquids Alkylation Technology, https://www.uop.com/?press_release=honeywell-uop-and-chevron-win-2017-platts-breakthrough-solution-award-for-ionic-liquids-alkylation-technology, (accessed 17/12, 2019).
172. W. L. F. Armarego and D. D. Perrin, *Purification of Laboratory Chemicals*, Butterworth-Heineman, Oxford (UK), 1997.
173. J. Dupont, C. S. Consorti, P. A. Z. Suarez and R. F. Souza, *Org. Synth.*, 2002, **79**, 236-237.
174. A.-L. Girard, N. Simon, M. Zanatta, S. Marmitt, P. Gonçalves and J. Dupont, *Green Chem.*, 2014, **16**, 2815-2825.
175. D. Ballivet-Tkatchenko, B. Nickel, A. Rassat and J. Vincent-Vaucquelin, *Inorg. Chem.*, 1986, **25**, 3497-3501.
176. V. Farmer and T. Welton, *Green Chem.*, 2002, **4**, 97-102.
177. A. M. Confer, A. C. McQuilken, H. Matsumura, P. Moënne-Loccoz and D. P. Goldberg, *J. Am. Chem. Soc.*, 2017, **139**, 10621-10624.
178. A. E. Servid, A. L. McKay, C. A. Davis, E. M. Garton, A. Manole, P. S. Dobbin, M. A. Hough and C. R. Andrew, *Biochemistry*, 2015, **54**, 3320-3327.
179. B. Benko and N. T. Yu, *Proc Natl Acad Sci U S A*, 1983, **80**, 7042-7046.
180. I. de Pedro, O. Fabelo, A. García-Saiz, O. Vallcorba, J. Junquera, J. A. Blanco, J. C. Waerenborgh, D. Andreica, A. Wildes, M. T. Fernández-Díaz and J. R. Fernández, *Phys. Chem. Chem. Phys.*, 2016, **18**, 21881-21892.
181. V. G. Charalampopoulos, J. C. Papaioannou, G. Kakali and H. S. Karayianni, *Carbohydr. Res.*, 2008, **343**, 489-500.
182. C. T. Tran and E. Kim, *Inorg. Chem.*, 2012, **51**, 10086-10088.
183. Z. J. Tonzetich, L. H. Do and S. J. Lippard, *J. Am. Chem. Soc.*, 2009, **131**, 7964-7965.
184. D. M. Murphy, in *Metal Oxide Catalysis*, eds. S. D. Jackson and J. S. J. Hargreaves, Wiley-VCH Verlag GmbH & Co. KGaA, 2009, pp. 1-50.
185. S. Begel, R. Puchta, J. Sutter, F. W. Heinemann, L. Dahlenburg and R. Eldik, *Inorg. Chem.*, 2015, **54**, 6763-6775.
186. K. Murata and D. E. Irish, *Spectrochim. Acta A*, 1988, **44**, 739-743.
187. I. Ben Hadj Sadok, F. Hajlaoui, K. Karoui, N. Audebrand, T. Roisnel and N. Zouari, *J. Phys. Chem. Solids*, 2019, **129**, 71-80.

188. https://www.sigmaaldrich.com/MSDS/MSDS/DisplayMSDSPage.do?country=GB&language=en&productNumber=229997&brand=ALDRICH&PageToGoToURL=https%3A%2F%2Fwww.sigmaaldrich.com%2Fcatalog%2Fproduct%2Faldrich%2F229997%3Flang%3Den, (accessed 05/08/2019).
189. K. Karoui, M. Ben Bechir, A. Bulou, K. Guidara and A. Ben Rhaiem, *J. Mol. Struct.*, 2016, **1114**, 161-170.
190. D. K. Singh, S. Cha, D. Nam, H. Cheong, S.-W. Joo and D. Kim, *ChemPhysChem*, 2016, **17**, 3040-3046.
191. S. Hayashi, R. Ozawa and H.-o. Hamaguchi, *Chem. Lett.*, 2003, **32**, 498-499.
192. Mettler and Toledo, Interpreting DSC curves, https://www.mt.com/dam/Analytical/MatcharApps/uc111.pdf, (accessed 29/07, 2019).
193. H. A. Patel, J. Byun and C. T. Yavuz, *ChemSusChem*, 2017, **10**, 1303-1317.
194. T. P. Senftle and E. A. Carter, *Acc. Chem. Res.*, 2017, **50**, 472-475.
195. M. Aresta, A. Dibenedetto and E. Quaranta, *J. Catal.*, 2016, **343**, 2-45.
196. M. Cokoja, M. E. Wilhelm, M. H. Anthofer, W. A. Herrmann and F. E. Kuhn, *ChemSusChem*, 2015, **8**, 2436-2454.
197. Q. He, J. W. O'Brien, K. A. Kitselman, L. E. Tompkins, G. C. T. Curtis and F. M. Kerton, *Catal. Sci. Technol.*, 2014, **4**, 1513-1528.
198. L. Xiao, D. Lv and W. Wu, *Catal. Lett.*, 2011, **141**, 1838-1844.
199. J. Sun, S. Zhang, W. Cheng and J. Ren, *Tetrahedron Lett.*, 2008, **49**, 3588-3591.
200. J. Gao, Q.-W. Song, L.-N. He, C. Liu, Z.-Z. Yang, X. Han, X.-D. Li and Q.-C. Song, *Tetrahedron*, 2012, **68**, 3835-3842.
201. H. Zhou, Y.-M. Wang, W.-Z. Zhang, J.-P. Qu and X.-B. Lu, *Green Chem.*, 2011, **13**, 644-650.
202. S. R. Choon, J. Hwang, B. L. Hong and J. J. Shim, *Bull. Korean Chem. Soc.*, 2007, **28**, 1060-1062.
203. J. Sun, J. Ren, S. Zhang and W. Cheng, *Tetrahedron Lett.*, 2009, **50**, 423-426.
204. L. Han, H.-J. Choi, S.-J. Choi, B. Liu and D.-W. Park, *Green Chem.*, 2011, **13**, 1023-1028.
205. Z.-Z. Yang, Y.-N. Zhao, L.-N. He, J. Gao and Z.-S. Yin, *Green Chem.*, 2012, **14**, 519-527.
206. S. Zhang, Y. Chen, F. Li, X. Lu, W. Dai and R. Mori, *Catal. Today*, 2006, **115**, 61-69.
207. J. Sun, S.-i. Fujita and M. Arai, *J. Organomet. Chem.*, 2005, **690**, 3490-3497.
208. J. Peng and Y. Deng, *New J. Chem.*, 2001, **25**, 639-641.
209. M. Jones and S. A. Fleming, in *Organic Chemistry*, W. W. Norton & Company, New York, 2014, ch. 11, pp. 502-506.
210. J.-W. Huang and M. Shi, *J. Org. Chem.*, 2003, **68**, 6705-6709.
211. H. Kawanami and Y. Ikushima, *Chem. Commun.*, 2000, 2089-2090.

212. Y.-M. Shen, W.-L. Duan and M. Shi, *Adv. Synth. Catal.*, 2003, **345**, 337-340.
213. L.-N. He, H. Yasuda and T. Sakakura, *Green Chem.*, 2003, **5**, 92-94.
214. G. Fiorani, W. Guo and A. W. Kleij, *Green Chem.*, 2015, **17**, 1375-1389.
215. N. Kihara, N. Hara and T. Endo, *J. Org. Chem.*, 1993, **58**, 6198-6202.
216. T. Yano, H. Matsui, T. Koike, H. Ishiguro, H. Fujihara, M. Yoshihara and T. Maeshima, *Chem. Commun.*, 1997, 1129-1130.
217. K. Yamaguchi, K. Ebitani, T. Yoshida, H. Yoshida and K. Kaneda, *J. Am. Chem. Soc.*, 1999, **121**, 4526-4527.
218. A. Decortes, A. M. Castilla and A. W. Kleij, *Angew. Chem. Int. Ed.*, 2010, **49**, 9822-9837.
219. Y. Chen, R. Qiu, X. Xu, C.-T. Au and S.-F. Yin, *RSC Adv.*, 2014, **4**, 11907-11918.
220. C. Martín, G. Fiorani and A. W. Kleij, *ACS Catal.*, 2015, **5**, 1353-1370.
221. M. North, R. Pasquale and C. Young, *Green Chem.*, 2010, **12**, 1514-1539.
222. X.-B. Lu and D. J. Darensbourg, *Chem. Soc. Rev.*, 2012, **41**, 1462-1484.
223. F. de la Cruz-Martínez, J. Martínez, M. A. Gaona, J. Fernández-Baeza, L. F. Sánchez-Barba, A. M. Rodríguez, J. A. Castro-Osma, A. Otero and A. Lara-Sánchez, *ACS Sustainable Chem. Eng.*, 2018, **6**, 5322-5332.
224. D. O. Meléndez, A. Lara-Sánchez, J. Martínez, X. Wu, A. Otero, J. A. Castro-Osma, M. North and R. S. Rojas, *ChemCatChem*, 2018, **10**, 2271-2277.
225. C. M. Miralda, E. E. Macias, M. Zhu, P. Ratnasamy and M. A. Carreon, *ACS Catal.*, 2012, **2**, 180-183.
226. M. Zhu, D. Srinivas, S. Bhogeswararao, P. Ratnasamy and M. A. Carreon, *Catal. Commun.*, 2013, **32**, 36-40.
227. J. Liang, Y.-Q. Xie, X.-S. Wang, Q. Wang, T.-T. Liu, Y.-B. Huang and R. Cao, *Chem. Commun.*, 2018, **54**, 342-345.
228. D.-H. Lan, L. Chen, C.-T. Au and S.-F. Yin, *Carbon*, 2015, **93**, 22-31.
229. D.-H. Lan, Y.-X. Gong, N.-Y. Tan, S.-S. Wu, J. Shen, K.-C. Yao, B. Yi, C.-T. Au and S.-F. Yin, *Carbon*, 2018, **127**, 245-254.
230. D.-H. Lan, F.-M. Yang, S.-L. Luo, C.-T. Au and S.-F. Yin, *Carbon*, 2014, **73**, 351-360.
231. J. A. Stewart, R. Drexel, B. Arstad, E. Reubsaet, B. M. Weckhuysen and P. C. A. Bruijnincx, *Green Chem.*, 2016, **18**, 1605-1618.
232. L. Yang and H. Wang, *ChemSusChem*, 2014, **7**, 962-998.
233. B.-H. Xu, J.-Q. Wang, J. Sun, Y. Huang, J.-P. Zhang, X.-P. Zhang and S.-J. Zhang, *Green Chem.*, 2015, **17**, 108-122.
234. F. D. Bobbink and P. J. Dyson, *J. Catal.*, 2016, **343**, 52-61.
235. D.-H. Lan, N. Fan, Y. Wang, X. Gao, P. Zhang, L. Chen, C.-T. Au and S.-F. Yin, *Chin. J. Catal.*, 2016, **37**, 826-845.
236. Z.-Z. Yang, Y.-N. Zhao and L.-N. He, *RSC Adv.*, 2011, **1**, 545-567.
237. W. Cheng, Q. Su, J. Wang, J. Sun and F. T. T. Ng, *Catalysts*, 2013, **3**, 878-901.
238. M. S. Sitze, E. R. Schreiter, E. V. Patterson and R. G. Freeman, *Inorg. Chem.*, 2001, **40**, 2298-2304.

239. L. Han, M.-S. Park, S.-J. Choi, Y.-J. Kim, S.-M. Lee and D.-W. Park, *Catal. Lett.*, 2012, **142**, 259-266.
240. D. Kim, Y. Moon, D. Ji, H. Kim and D. Cho, *ACS Sustainable Chem. Eng.*, 2016, **4**, 4591-4600.
241. M.-I. Kim, S.-J. Choi, D.-W. Kim and D.-W. Park, *J. Ind. Eng. Chem.*, 2014, **20**, 3102-3107.
242. R. O. Colclough, G. Gee, W. C. E. Higginson, J. B. Jackson and M. Litt, *J. Polym. Sci. A*, 1959, **34**, 171-179.
243. I. J. Villar-Garcia, E. F. Smith, A. W. Taylor, F. Qiu, K. R. J. Lovelock, R. G. Jones and P. Licence, *Phys. Chem. Chem. Phys.*, 2011, **13**, 2797-2808.
244. H. Wang, R. Yan, Z. Li, X. Zhang and S. Zhang, *Catal. Commun.*, 2010, **11**, 763-767.
245. F. Li, L. Xiao, C. Xia and B. Hu, *Tetrahedron Lett.*, 2004, **45**, 8307-8310.
246. G. Gurau, H. Rodríguez, S. P. Kelley, P. Janiczek, R. S. Kalb and R. D. Rogers, *Angew. Chem. Int. Ed.*, 2011, **50**, 12024-12026.
247. O. Holloczki, D. Gerhard, K. Massone, L. Szarvas, B. Nemeth, T. Veszpremi and L. Nyulaszi, *New J. Chem.*, 2010, **34**, 3004-3009.
248. M. Besnard, M. I. Cabaço, F. Vaca Chávez, N. Pinaud, P. J. Sebastião, J. A. P. Coutinho, J. Mascetti and Y. Danten, *J. Phys. Chem. A*, 2012, **116**, 4890-4901.
249. J. Blath, N. Deubler, T. Hirth and T. Schiestel, *Chem. Eng. J.*, 2012, **181-182**, 152-158.
250. A. a. K. Abdul-Sada, A. M. Greenway, P. B. Hitchcock, T. J. Mohammed, K. R. Seddon and J. A. Zora, *J. Chem. Soc., Chem. Commun.*, 1986, 1753-1754.
251. A. G. Avent, P. A. Chaloner, M. P. Day, K. R. Seddon and T. Welton, *J. Chem. Soc., Dalton Trans.*, 1994, 3405-3413.
252. J. D. Holbrey and K. R. Seddon, *J. Chem. Soc., Dalton Trans.*, 1999, 2133-2140.
253. G.-P. Wu, S.-H. Wei, X.-B. Lu, W.-M. Ren and D. J. Darensbourg, *Macromolecules*, 2010, **43**, 9202-9204.
254. G.-P. Wu, S.-H. Wei, W.-M. Ren, X.-B. Lu, B. Li, Y.-P. Zu and D. J. Darensbourg, *Energy Environ. Sci.*, 2011, **4**, 5084-5092.
255. T. Ema, Y. Miyazaki, S. Koyama, Y. Yano and T. Sakai, *Chem. Commun.*, 2012, **48**, 4489-4491.
256. T. Ema, Y. Miyazaki, J. Shimonishi, C. Maeda and J.-y. Hasegawa, *J. Am. Chem. Soc.*, 2014, **136**, 15270-15279.
257. F. Castro-Gómez, G. Salassa, A. W. Kleij and C. Bo, *Chem. Eur. J.*, 2013, **19**, 6289-6298.
258. *%ee determination by GC Chromatography was carried out by Dr. Israel Cano.*
259. M. B. Smith, *March's Advanced Organic Chemistry: Reactions, Mechanisms, and Structure*, John Wiley & Sons 7th Edition edn., 2013.
260. M. North and R. Pasquale, *Angew. Chem. Int. Ed.*, 2009, **48**, 2946-2948.
261. J.-Q. Wang, K. Dong, W.-G. Cheng, J. Sun and S.-J. Zhang, *Catal. Sci. Technol.*, 2012, **2**, 1480-1484.

262. S. Foltran, R. Mereau and T. Tassaing, *Catal. Sci. Technol.*, 2014, **4**, 1585-1597.
263. L. Wang, X. Jin, P. Li, J. Zhang, H. He and S. Zhang, *Ind. Eng. Chem. Res.*, 2014, **53**, 8426-8435.
264. C. J. Whiteoak, A. Nova, F. Maseras and A. W. Kleij, *ChemSusChem*, 2012, **5**, 2032-2038.
265. F. Chen, X. Li, B. Wang, T. Xu, S. L. Chen, P. Liu and C. Hu, *Chem. Eur. J.* , 2012, **18**, 9870-9876.
266. H.-H. Limbach, J. Miguel Lopez and A. Kohen, *Philos. Trans. of the Royal Soc. B*, 2006, **361**, 1399-1415.
267. J. W. Comerford, I. D. V. Ingram, M. North and X. Wu, *Green Chem.*, 2015, **17**, 1966-1987.
268. S. Marmitt and P. F. B. Gonçalves, *J. Comput. Chem.*, 2015, **36**, 1322-1333.
269. M. B. Smith and J. March, *March's Advanced Organic Chemistry: Reactions, Mechanisms, and Structure*, Wiley Hoboken (New Jersey, USA), 2007.
270. A. Bordet, L.-M. Lacroix, P.-F. Fazzini, J. Carrey, K. Soulantica and B. Chaudret, *Angew. Chem., Int. Ed.*, 2016, **55**, 15894-15898.
271. J. Wang, H. Z. Zhang, R. S. Li and C. Z. Huang, *TrAC, Trends Anal. Chem.*, 2016, **80**, 429-443.
272. L. Prati and A. Villa, *Acc. Chem. Res.*, 2014, **47**, 855-863.
273. A. Primo, A. Corma and H. García, *Phys. Chem. Chem. Phys.*, 2011, **13**, 886-910.
274. Y. Zhao, Z.-q. Deng and J. Li, *Sensors Actuators B Chem*, 2014, **202**, 557-567.
275. N. S. Abadeer and C. J. Murphy, *J. Phys. Chem. C*, 2016, **120**, 4691-4716.
276. X. Meng, T. Wang, L. Liu, S. Ouyang, P. Li, H. Hu, T. Kako, H. Iwai, A. Tanaka and J. Ye, *Angew. Chem. Int. Ed.*, 2014, **53**, 11478-11482.
277. F. K. Butt and A. S. Bandarenka, *J. Solid State Electrochem.*, 2016, **20**, 2915-2928.
278. I. Bilecka and M. Niederberger, *Nanoscale*, 2010, **2**, 1358-1374.
279. N. A. Khan and S. H. Jhung, *Coord. Chem. Rev.*, 2015, **285**, 11-23.
280. N. Tarasova, A. Zanin, K. Burdakov and P. Sobolev, *Polym. Adv. Technol.*, 2015, **26**, 687-695.
281. E. Calcio Gaudino, G. Cravotto, M. Manzoli and S. Tabasso, *Green Chem.*, 2019, **21**, 1202-1235.
282. A. de la Hoz, A. Díaz-Ortiz and P. Prieto, in *Alternative Energy Sources for Green Chemistry*, The Royal Society of Chemistry, 2016, pp. 1-33.
283. C. O. Kappe, *Angew. Chem. Int. Ed.*, 2004, **43**, 6250-6284.
284. D. M. P. Mingos and D. R. Baghurst, *Chem. Soc. Rev.*, 1991, **20**, 1-47.
285. C. Gabriel, S. Gabriel, E. H. Grant, E. H. Grant, B. S. J. Halstead and D. Michael P. Mingos, *Chem. Soc. Rev.*, 1998, **27**, 213-224.
286. C. O. Kappe, D. Dallinger and S. S. Murphree, in *Practical Microwave Synthesis for Organic Chemists: Strategies, Instruments, and Protocols*, Wiley-VCH Weinheim, 2008, pp. 11-42.

287. B. L. Hayes, in *Microwave Synthesis: Chemistry at the Speed of Light*, CEM Publishing, Matthews, 2002, pp. 11-29.
288. J. Hoffmann, M. Nüchter, B. Ondruschka and P. Wasserscheid, *Green Chem.*, 2003, **5**, 296-299.
289. R. Martínez-Palou, *Mol. Divers.*, 2010, **14**, 3-25.
290. J. Zhang, X. Xie, L. Li, X. Wu and C. Ma, *Heterocycles*, 2016, **92**, 1171-1185.
291. M. Deetlefs and K. R. Seddon, *Green Chem.*, 2003, **5**, 181-186.
292. R. S. Varma and V. V. Namboodiri, *Chem. Commun.*, 2001, 643-644.
293. V. V. Namboodiri and R. S. Varma, *Tetrahedron Lett.*, 2002, **43**, 5381-5383.
294. Y. Jin Kim and R. S. Varma, *Tetrahedron Lett.*, 2005, **46**, 1467-1469.
295. Y. J. Kim and R. S. Varma, *Tetrahedron Lett.*, 2005, **46**, 7447-7449.
296. S. Cot, M. K. Leu, A. Kalamiotis, G. Dimitrakis, V. Sans, I. de Pedro and I. Cano, *ChemPlusChem*, 2019, **84**, 786-793.
297. R. J. Giguere, T. L. Bray, S. M. Duncan and G. Majetich, *Tetrahedron Lett.*, 1986, **27**, 4945-4948.
298. R. Gedye, F. Smith, K. Westaway, H. Ali, L. Baldisera, L. Laberge and J. Rousell, *Tetrahedron Lett.*, 1986, **27**, 279-282.
299. M. V. Alexander, A. C. Khandekar and S. D. Samant, *J. Mol. Catal. A: Chem.*, 2004, **223**, 75-83.
300. J. Estager, J.-M. Lévêque, R. Turgis and M. Draye, *J. Mol. Catal. A: Chem.*, 2006, **256**, 261-264.
301. N. Srinivasan and A. Ganesan, *Chem. Commun.*, 2003, 916-917.
302. V. Singh, S. Kaur, V. Sapehiyia, J. Singh and G. L. Kad, *Catal. Commun.*, 2005, **6**, 57-60.
303. Z.-Z. Zhou, F.-Q. Ji, M. Cao and G.-F. Yang, *Adv. Synth. Catal.*, 2006, **348**, 1826-1830.
304. N. E. Leadbeater, H. M. Torenius and H. Tye, *Mol. Divers.*, 2003, **7**, 135-144.
305. A. Arfan, L. Paquin and J. P. Bazureau, *Russ. J. Org. Chem.*, 2007, **43**, 1058-1064.
306. A. K. Pathak, C. Ameta, R. Ameta and P. B. Punjabi, *J. Heterocycl. Chem.*, 2016, **53**, 1697-1705.
307. K. Kristof and K. Marijan, *Curr. Org. Chem.*, 2013, **17**, 448-456.
308. R. L. Vekariya, *J. Mol. Liq.*, 2017, **227**, 44-60.
309. H. Weingärtner, in *Ionic Liquids Further UnCOILed*, eds. N. V. Plechkova and K. R. Seddon, Wiley Hoboken, New Jersey, 2014.
310. R. Buchner and G. Hefter, *Phys. Chem. Chem. Phys.*, 2009, **11**, 8984-8999.
311. U. H. Choi, A. Mittal, T. L. Price, H. W. Gibson, J. Runt and R. H. Colby, *Macromolecules*, 2013, **46**, 1175-1186.
312. H. Guettaf, E. H. Belarbi, N. Benkhettou and B. Haddad, *Procedia Comput. Sci.*, 2016, **83**, 1044-1049.
313. G. Brodie, M. V. Jacob and P. Farrell, in *Microwave and Radio-Frequency Technologies in Agriculture*, deGruyter, 2016, pp. 155-174.

314. M. Kruger, M.-M. Huang, E. Brundermann, H. Weingartner and M. Havenith, *IEEE Trans. Terahertz Sci. Technol*, 2011, **1**, 313-320.
315. J. Sangoro, T. Cosby and F. Kremer, in *Dielectric Properties of Ionic Liquids*, ed. M. Paluch, Springer International Publishing 2016, ch. 2, pp. 29-51.
316. Z. Wojnarowska and M. Paluch, *J. Phys.: Condens. Matter*, 2015, **27**, 1-20.
317. G. Dimitrakis, I. J. Villar-Garcia, E. Lester, P. Licence and S. Kingman, *Phys. Chem. Chem. Phys.*, 2008, **10**, 2947-2951.
318. H. Weingärtner, *J. Mol. Liq.*, 2014, **192**, 185-190.
319. D. A. Turton, J. Hunger, A. Stoppa, A. Thoman, M. Candelaresi, G. Hefter, M. Walther, R. Buchner and K. Wynne, *J. Mol. Liq.*, 2011, **159**, 2-8.
320. J. Wallauer, M. Balabajew and B. Roling, in *Electrodeposition from Ionic Liquids*, eds. F. Endres, A. Abbott and D. MacFarlane, Wiley-VCH, Weinheim, 2017, pp. 373-399.
321. F. Kremer and A. Schönhals, in *Broadband Dielectric Spectroscopy*, Springer-Verlag, Berlin Heidelberg, 2003, pp. 1-96.
322. A. Kalamiotis, A. Ilchev, D. J. Irvine and G. Dimitrakis, *Sensors Actuators B Chem*, 2019, **290**, 34-40.
323. A. P. Gregory and R. N. Clarke, *Meas. Sci. Technol.*, 2007, **18**, 1372-1386.
324. J. P. Grant, R. N. Clarke, G. T. Symm and N. M. Spyrou, *J. Phys. E: Sci. Instrum.*, 1989, **22**, 757-770.
325. *Agilent 85070E Dielectric Probe Kit 200 MHz to 50 GHz*, Agilent Technologies.
326. H. Chang, G. Dimitrakis, F. Xu, C. Yi, S. Kingman and Y. Zhu, *Chem. Phys. Lett.*, 2013, **555**, 159-163.
327. M. Al-Harahsheh, S. Kingman, A. Saeid, J. Robinson, G. Dimitrakis and H. Alnawafleh, *Fuel Process. Technol.*, 2009, **90**, 1259-1264.
328. Z. Li and E. Li, presented in part at the The 2012 International Workshop on Microwave and Millimeter Wave Circuits and System Technology, 19-20 April 2012, 2012.
329. L. Shihe, C. Akyel and R. G. Bosisio, *IEEE T Microw Theory*, 1981, **29**, 1041-1048.
330. R. Hutcheon, M. d. Jong, F. Adams, G. Wood, J. McGregor and B. Smith, *J Microwave Power Electromagnetic Energy*, 1992, **27**, 93-102.
331. J. Robinson, S. Kingman, D. Irvine, P. Licence, A. Smith, G. Dimitrakis, D. Obermayer and C. O. Kappe, *Phys. Chem. Chem. Phys.*, 2010, **12**, 4750-4758.
332. Z. Chongmin, S. Takehiko, J.-K. Akiko, F. Emiko, K. Akiko, T. Mizuki and I. Yasuhiro, *Bull. Chem. Soc. Jpn.*, 2007, **80**, 2365-2374.
333. X. Chen, D. Song, C. Asumana and G. Yu, *J. Mol. Catal. A: Chem.*, 2012, **359**, 8-13.
334. T. Sasaki, M. Tada, C. Zhong, T. Kume and Y. Iwasawa, *J. Mol. Catal. A: Chem.*, 2008, **279**, 200-209.
335. C. Zhong, T. Sasaki, M. Tada and Y. Iwasawa, *J. Catal.*, 2006, **242**, 357-364.

336. A. J. Carmichael, C. Hardacre, J. D. Holbrey, M. Nieuwenhuyzen and K. R. Seddon, *Anal. Chem.*, 1999, **71**, 4572-4574.
337. D. F. Roeper, K. I. Pandya, G. T. Cheek and W. E. O'Grady, *J. Electrochem. Soc.*, 2011, **158**, F21-F28.
338. G. Widman, Interpreting TGA curves, https://www.mt.com/dam/non-indexed/po/ana/ta-usercom/51710099_UserCom13_TA_e.pdf, (accessed 29/07, 2019).
339. K. Mohomed, *Thermogravimetric Analysis (TGA) Theory and Applications*, TA Instruments.
340. G. Höhne, W. F. Hemminger and H.-J. Flammersheim, *Differential Scanning Calorimetry*, Springer Verlag, Berlin Heidelberg, 2003.
341. Horiba, http://www.horiba.com/br/scientific/products/raman-spectroscopy/raman-academy/, (accessed 02/09, 2019).
342. L. Kerr, K. Domijan, I. Cullen and B. Hennelly, *Photonics Lasers Med.*, 2014, **3**, 2193-0643.
343. I. R. Lewis and H. Edwards, *Handbook of Raman Spectroscopy: From the Research Laboratory to the Process Line*, CRC Press, 2001.
344. *The crystal structure determination was carried out by the Crystal Structure Service of the Faculty of Chemistry, University of Nottingham.*
345. A. Efimova, G. Hubrig and P. Schmidt, *Thermochim. Acta*, 2013, **573**, 162-169.
346. A. Wojakowska, E. Krzyżak and S. Plińska, *J. Therm. Anal. Calorim.*, 2007, **88**, 525-530.
347. A. F. Al-Hossainy, A. Ibrahim and M. S. Zoromba, *J. Mater. Sci.: Mater. Electron*, 2019, **30**, 11627-11642.
348. R. Łyszczek, H. Głuchowska, J. Sienkiewicz-Gromiuk, L. Mazur and B. Tarasiuk, *Polyhedron*, 2015, **99**, 132-140.
349. S. Zhang, N. Sun, X. He, X. Lu and X. Zhang, *J. Phys. Chem. Ref. Data*, 2006, **35**, 1475-1517.
350. P. Atkins, T. Overton, J. Rourke, M. Weller and F. Armstrong, in *Shriver and Atkins' Inorganic Chemistry*, Oxford University Press, Oxford, 2009, vol. 5th Edition, pp. 223-253.
351. L. Nataf, F. Aguado, I. Hernández, R. Valiente, J. González, M. N. Sanz-Ortiz, H. Wilhelm, A. P. Jephcoat, F. Baudelet and F. Rodríguez, *Phys. Rev. B*, 2017, **95**.
352. D. J. Lockwood, I. W. Johnstone, H. J. Labbe and B. Bria, *J. Phys. C: Solid State Phys.*, 1983, **16**, 6451-6474.
353. R. J. Newport, R. A. Howe and N. D. Wood, *J. Phys. C: Solid State Phys.*, 1985, **18**, 5249-5257.
354. I. J. Villar-Garcia, E. F. Smith, A. W. Taylor, F. Qiu, K. R. J. Lovelock, R. G. Jones and P. Licence, *Phys. Chem. Chem. Phys.*, 2011, **13**, 2797-2808.